UMONS - University of Mons
Faculty of Sciences
Atomic Physics and Astrophysics

UMONS
Université de Mons

Faculté
des Sciences

Study of plasma environment effects on radiative and non-radiative atomic processes involving the K inner-shell in ions of astrophysical interest

presented by

Jérôme Deprince

A dissertation submitted in fulfilment of the requirements of
the degree of *Docteur en Sciences*

May 2020

Jury

Prof. P. Quinet (University of Mons, Belgium - Supervisor)
Dr. P. Palmeri (University of Mons, Belgium - Supervisor)
Prof. M. Voué (University of Mons, Belgium - President)
Prof. C. Semay (University of Mons, Belgium - Secretary)
Dr. F. Delahaye (Observatoire de Paris, France - Referee)
Prof. S. Fritzsche (Helmholtz-Institut Jena, Germany - Referee)

Acknowledgments

First of all, I would particularly like to thank my two supervisors, Prof. Pascal Quinet and Dr. Patrick Palmeri, who helped me complete this PhD thesis work in the best possible conditions. The numerous fruitful discussions, their guidance, their availability, along with the good working atmosphere they created have undoubtedly and favorably contributed to the completion of my work.

I also want to thank my two work buddies Sébastien and Helena, with whom I have been sharing my office for the last few years, for the several productive discussions we had, the help they gave me when I needed it and, especially, for the enjoyable moments we used to share (both inside and outside our office) during these years. A good atmosphere is certainly helpful to complete such a long-term undertaking!

I would also like to thank my university friends for the entertaining moments we shared during lunch breaks or after the working day: Lucas, Ludovic, Antoine, Marie, Eleonore, David, ... just to mention some of them.

I am also really grateful to my close family and to my girlfriend Mélanie for their steady and unfailing support. They have been able to take my mind off things when I needed it most and to encourage me to complete this work. The love from my family has always been important to me, and they have endlessly been supporting me during my whole educational background through my PhD thesis work. Mélanie, for her part, has given me all the love I needed to overcome difficulties in the hardest moments, and especially helped me relax and get motivated to perform my work.

Besides, I would like to thank all my colleagues from our "American" collaboration team, namely Dr. Claudio Mendoza, Prof. Manuel Bautista, Dr. Tim Kallman and Dr. Javier Garcia. Each of them has somehow helped me during my nascent career. In particular, Claudio and Manuel kindly welcomed me at Western Michigan University in Kalamazoo for a two-month stay to help me learn to use a new computational method; Tim gave me a tour of the NASA Goddard Space Flight Center in Greenbelt during a stay over there; and, more recently, Javier invited me to perform a one-year postdoctoral research stay in his group at Caltech in Pasadena. I am thus also grateful to each of them.

Contents

Introduction

Since the European satellite EXOSAT was launched in 1983, X-ray space telescope performances have steadily improved considerably. Current satellites such as XMM-Newton and Chandra actually reach spectral resolutions that are hundred times better than the first missions aimed at the observation of X-rays from astrophysical sources. This progress will be even more emphasized with the future X-ray missions XRISM and ATHENA, whose launches are respectively scheduled for 2022 and for the early 2030s. Furthermore, the development of atomic physics computation methods that are becoming more and more sophisticated, along with the strong increase of computer power, enable the study of complex atomic processes in much more details. It is now possible to accurately evaluate fine effects that can even slightly modify the atomic parameters in order to carefully analyze and interpret the high-resolution spectra observed from astrophysical sources.

K-shell atomic processes in oxygen and iron ions are especially interesting for X-ray astronomy, as they supply very good diagnostic tools for astrophysical plasmas. In particular, iron fluorescent K lines play a key role in the study of X-ray astrophysical spectra. They are actually observed in most of the X-ray spectra from diverse celestial objects such as active galactic nuclei or accreting neutron stars and black holes. This is mainly due to the relatively high iron astrophysical abundance and to the efficiency of the fluorescence process in iron ions. The high resolutions reached by the instruments aboard the current satellites enable the use of these lines as powerful diagnostic tools of the physical conditions that occur in the astrophysical plasma from which they are emitted.

More particularly, the iron fluorescent K lines from accretion disks surrounding black holes are of crucial interest, since the redshifts and broadenings observed for these lines can only be explained by the presence of a strong gravitational field. As a consequence, these iron K lines can only originate from a region very close to the central black hole. Therefore, iron K lines from accretion disks around black holes turn out to be natural probes of the effects of special and general relativity in these regions, in addition to being important diagnostic tools of the plasma forming the disks. The study of the intensity and profile of iron K lines is actually the only known observational method that allows to infer several interesting features of the

black hole itself, such as its spin.

In order to model and interpret X-ray spectra from such astrophysical objects, and in light of the impressive resolutions achieved by current (and future) instruments aboard X-ray space telescopes, it is necessary to know the atomic data involved in K-line formation as accurately as possible. The computation of such data has been the subject of several works in the past; however, none of these takes into consideration the effects of the plasma environment on the corresponding atomic parameters. Nevertheless, recent simulations based on general relativity and magnetic hydrodynamics (Schnittman *et al.* 2013, Jiang *et al.* 2019) tend to support the existence of rather high densities in accretion disks surrounding black holes, up to $10^{21} - 10^{22}$ cm^{-3}. The effects of such a high-density plasma on the atomic parameters related to K-line emission have never been studied up to now. As recently highlighted by Smith & Brickhouse (2014) in a review article entitled *Atomic Data Needs for Understanding X-ray Astrophysical Plasmas*, the consideration of such effects is however essential to meet the accuracy requirements for the atomic data needed to correctly interpret astrophysical spectra observed by current X-ray satellites. This necessity will be even more exacerbated with the impending launches of XRISM and ATHENA within the next decade, whose on-board instruments will reach spectral resolutions never achieved before in X-ray astronomy.

Within this framework, our work aims to study the plasma environment effects on the radiative and non-radiative atomic parameters that characterize K lines in ions of astrophysical interest, such as iron and oxygen ions, for conditions such as those expected in the accretion disks surrounding black holes. For this purpose, we modeled the electronic structures of all the ionization stages of oxygen and iron (in the isolated atomic system case) by means of the multiconfiguration Dirac-Fock (MCDF) method as implemented in the GRASP2K (Jönsson *et al.* 2013) code. The effects of the plasma environment on the electronic structure and on the atomic processes involved in K-line formation were then evaluated by using a static Debye-Hückel potential within the RATIP computational program (Fritzsche 2001, 2012). For comparison purposes, we also used the multiconfiguration Breit-Pauli approximation as implemented in the AUTOSTRUCTURE (AST) code (Badnell 1997, 2011), in which a Debye-Hückel potential has also been considered to treat the plasma screening effects.

In the first Chapter, after some fundamental reminders of atomic physics about K-line formation by fluorescence, we present the general astrophysical context within which our work takes place. In particular, we highlight the importance of oxygen and iron K lines in X-ray astronomy.

Then, in Chapter 2, we present the theoretical concepts and computational methods used to model the atomic structures and parameters related to K-shell

processes for the ions considered in this work (oxygen and iron), namely the MCDF method as implemented in GRASP2K, the AUTOSTRUCTURE code and the RATIP program.

The method following which the plasma environment effects can be taken into account within the computation of atomic processes is described in Chapter 3. Several screening potential models (in particular, the Debye-Hückel one) are discussed in this chapter. The modifications implemented in the RATIP code to model plasma screening effects are also presented. In addition, we discuss the validity of our model by comparing several results that we obtained with available data deduced from experimental measurements or computed using independent theoretical approaches.

In Chapter 4, we present our results concerning the plasma environment effects on the atomic structures, radiative wavelengths, transition probabilities and Auger widths for all the ionization stages of oxygen. The methodology is carefully described to serve as a template for the rest of this work.

The Chapter 5 is dedicated to the study of plasma environment effects on the atomic structures and atomic parameters associated with K-shell processes in iron ions. The results obtained concerning ionization potentials, K-shell thresholds, radiative wavelengths and rates, and Auger widths are shown for Fe II – Fe XXV. The plasma environment influence on the K-shell photoionization cross section is also discussed in the case of Fe XXIV. This chapter ends with a discussion about the main astrophysical implications expected from the results obtained in our work.

Finally, we draw the general conclusions of our investigations and develop some interesting perspectives.

Chapter 1

The K lines in X-ray astrophysics

This first chapter aims to introduce the main motivations of this work by presenting the astrophysical context within which it is part of. After a brief atomic-physics reminder about the nature of K lines and their formation by fluorescence, we explain the importance of iron and oxygen K lines in X-ray astrophysics. In particular, we explain how such lines are emitted from accretion disks around black holes. We also discuss the structure of such interesting astrophysical objects as well as the physical conditions within it. Then, we give an insight of the work that has already been carried out concerning the computations of atomic parameters related to K-line emissions by ions of astrophysical importance such as iron and oxygen and, finally, we end this chapter by presenting several past, current and future missions and observatories dedicated to the recording of X-ray astrophysical spectra.

1.1 K-line formation by fluorescence

In atomic physics, the de-excitation electronic transitions of an ion in which a valence electron comes to fill a vacancy in the K shell[1] (atomic shell characterized by the quantum principal number $n = 1$) of the latter are called K lines. To create such an (highly-)excited K-vacancy state in an ion, that is the initial state of this kind of transition, a K-shell electron must have previously been excited to an upper shell (*e.g.* by photoabsorption) or pulled off by photoionization of the ion lying initially in the lower charge state. This process in which a K-vacancy state is created by light absorption and then followed by the ion de-excitation by emitting a K line is the so-called fluorescence phenomenon. The K lines formed by electronic transitions of the type 2p → 1s and 3p → 1s are respectively called Kα and Kβ lines.

---

[1] An ion in such a state is thus said to be in a "K-vacancy state".
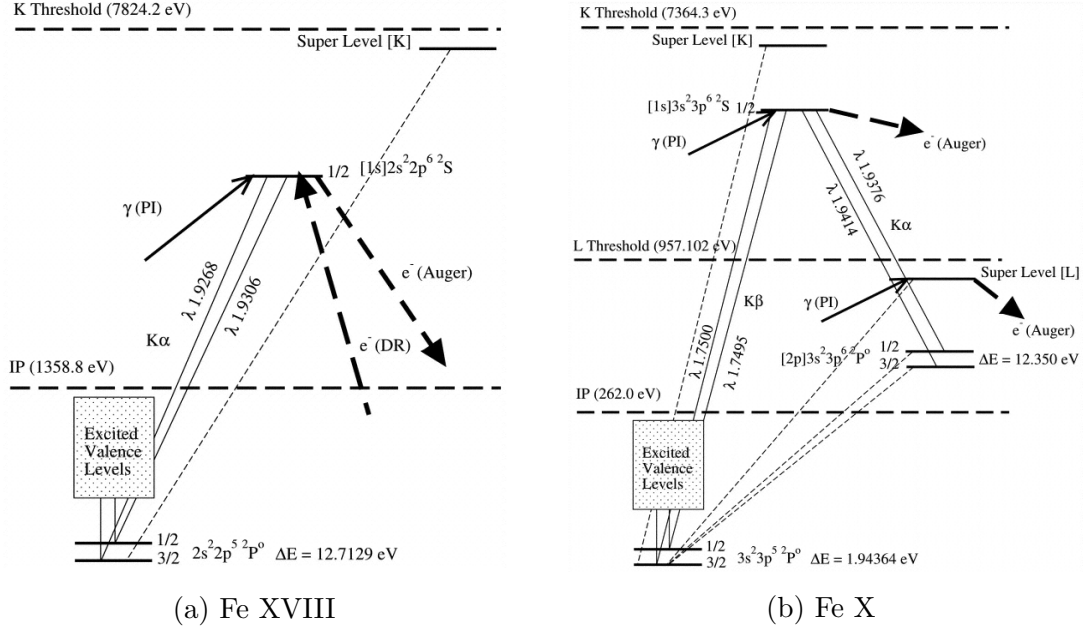
Figure 1.1: Grotrian diagrams for inner-shell processes in two iron ions (Kallman *et al.* 2004).

Actually, radiative de-excitation through K-line emission is not the only possible way to spontaneously de-excite an ion lying in a highly-excited K-vacancy state: the non-radiative Auger process is in competition with radiative K-line emission by fluorescence. In this process, a valence electron of the ion is spontaneously ejected into the continuum by autoionization, carrying the excess of energy and thus de-exciting the ion. Thereby, one can define the fluorescence yield, which expresses the branching ratio for the radiative de-excitation of an ion by fluorescence (for a specific radiative channel) among all the radiative and non-radiative (Auger) de-excitation channels, as

$$\omega_z^{\mathrm{K}}(p \to q) = \frac{A_z^{\mathrm{rad,K}}(p \to q)}{\sum_{r<p} A_z^{\mathrm{rad,K}}(p \to r) + \sum_s A_z^{\mathrm{a,K}}(p \to s)} \tag{1.1}$$

for an ion initially in a K-vacancy state and in the charge state z, where $A_z^{\mathrm{rad,K}}$ and $A_z^{\mathrm{a,K}}$ are respectively the transition rates for radiative and Auger decays. The sum over all the possible channels for the radiative and Auger de-excitations are respectively called the radiative and the Auger widths of a given K-vacancy state.

More precisely, the K lines that particularly interest us in this work are those emitted by iron ions (for reasons that will be developed in the next sections of this chapter). Two examples of Grotrian diagrams showing the inner-shell processes

6

that occur in Fe XVIII and Fe X are displayed in Figure 1.1. In the case of the ion Fe XVIII, the highly-excited K-vacancy state $[1s]2p^6\ ^2S_{1/2}$[2], which lies above the ionization potential (it is thus an autoionizing resonant state), can be populated by photoionization of the ground state $2p^6\ ^1S_0$ of Fe XVII. This former can then de-excite either by fluorescence through a Kα line or by autoionization through an Auger transition. For Fe X, the K-vacancy state $[1s]3p^6\ ^2S_{1/2}$, which can be populated by photoionization of the ground state $3p^6\ ^1S_0$ of Fe IX, can de-excite by radiative K-shell transitions toward one of the two valence levels $[2p]3p^6\ ^2P_{1/2,3/2}$ (Kα line) or toward the ground term $3p^5\ ^2P$ (Kβ line), or by non-radiative Auger decays. In these diagrams, the notation "IP" stands for "ionization potential", that is the minimal energy needed to ionize the ion (*i.e.* the difference between the ground level total energies of the latter and of the higher charge state). The K-shell threshold (also just named K threshold or K edge) is the minimal energy required to pull an electron off the K shell. Let us also notice that the "Super Level [K]" is actually a fictive level that takes into account all the levels that are not explicitly included in the model. Finally, let us highlight that the ionization potential and K threshold of an ion are two atomic parameters of particular interest in this work.

1.2 About the importance of iron K lines in astrophysics

Iron K lines are of indisputable importance in X-ray astronomy. They are observed in most X-ray spectra of various astrophysical objects such as active galactic nuclei (AGN), supernovae remnants, clusters of galaxies, X-ray binaries, accreting neutron stars and black holes, *etc.* (see, *e.g.*, Serlemitsos *et al.* 1973, Sanford *et al.* 1975, Serlemitsos *et al.* 1977, Pravdo *et al.* 1977, Cackett *et al.* 2010, Reynolds 2014). They appear in the energy range 5-10 keV of the X-ray band.

The reason why these lines are widely observed in astrophysical X-ray spectra is notably due to the relatively high iron abundance in the celestial bodies. Actually, the ^{56}Fe element is the most stable one of the periodic table, since its nuclear binding energy per nucleon is the highest one with respect to the other elements. This feature is commonly called the "iron peak" (see Figure 1.2). Therefore, the thermonuclear fusion reactions that take place in massive stars, supplying the required energy to balance the own weight of the latter through the radiation pressure generated by these reactions, finally lead to the formation of iron in the

---

[2]The notation $[nl]\ n'l'$ means that all the subshells with an energy lower than the $n'l'$ subshell are filled, except the subshell nl that has one vacancy in its K shell, *i.e.* there is one missing electron with respect to the filled nl subshell.
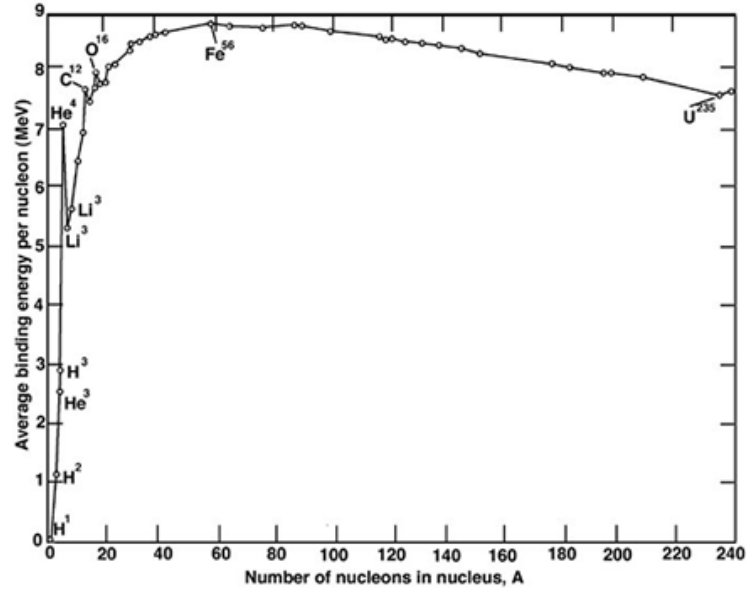
Figure 1.2: Evolution of the nuclear binding energy per nucleon depending on the number of nucleons.
(http://www.splung.com/nuclear/images/benergy/benergy.png)

stellar cores through various nuclear fusion reactions that take place in several steps and that produce more and more heavy elements (but we do not detail them in this work in order to not digress from the main subject). Since the thermonuclear fusion reactions are endothermic beyond the ^{56}Fe, once there basically remains only iron in the stellar core, there is no more fusion reaction that can supply the pressure radiation to balance the star weight, which results in the so-called "iron catastrophe": the gravitational collapse of the star core, which ejects a significant quantity of the star mass in the surrounding interstellar space (this phenomenon is accompanied by considerable light emission and is called a supernova). As some iron was present in significant quantity in the core of the star before the latter collapses, considerable iron traces (among the plentiful quantity of hydrogen and helium) are found in the nebula or in the dust and gas cloud formed by the matter that was ejected. Later in its evolution, a part of this nebula or dust and gas cloud can end up collapsing on itself, which leads to the formation of new stars that will consequently inherit the relatively high iron abundance of the initial cloud or nebula. Another part of those gas and dust that remained in the vicinity of the massive star remnant (namely a neutron star or black hole, depending on the initial mass of the star) can also finish by gathering around the latter and form an accretion disk of matter, which will be itself also composed of a rather

8

large quantity of iron. This accretion phenomenon, which actually results from a mechanism of angular momentum redistribution, along with the structure of such accretion disks will be discussed in much more details in Section 1.3.

Let us also note that the iron K lines are unique among commonly observed X-ray lines in that they can be emitted efficiently by gas over a wide range of temperatures and ionization states (Kallman *et al.* 2004), due to their large fluorescence yields (up to 0.39, Palmeri *et al.* 2003b). In addition, they are located in a relatively unconfused spectral region, which enables to clearly identify the iron K lines in the observed X-ray spectrum. They can thus be considered as powerful tools for astrophysical plasma diagnostics, that is the determination of the physical conditions (temperature and densities) and quantity of emitting element in the astrophysical plasma from which the radiative K lines are emitted. Such diagnostics can be performed by comparing the shape, position and intensity of the observed lines to the ones of a model spectrum, for which the physical conditions and other parameters such as the element abundances can be varied and thus adjusted to fit the observed spectrum.
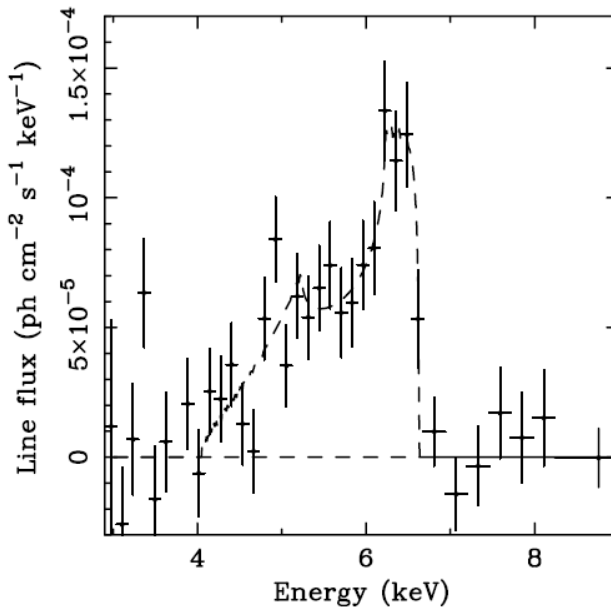

Figure 1.3: Broadened iron K line (where the continuum has been subtracted) from an observation recorded by ASCA (*Advanced Satellite for Cosmology and Astrophysics*, initially called Astro-D) of the Seyfert galaxy MCG–6–30–15 in July 1994 (Tanaka *et al.* 1995).

9

In particular, the iron fluorescence K lines coming from accretion disks around black holes are even more interesting. They actually turn out to be very useful natural probes of the regions close to the accreting black hole (see, *e.g.*, Reynolds & Nowak 2003 for a detailed review). Indeed, the iron K lines emitted by these sources have observed widths and shifts that imply an origin very close to the central black hole, namely at a few Schwarzchild radii from the center of the latter (Tanaka *et al.* 1995, Reis & Miller 2013), which allows to study the inner part of the accretion disk. Such broadened and shifted iron K lines are identified in most X-ray spectra of AGN and galactic black holes (Reynolds 2014). A very famous example of a broadened iron K-line complex is illustrated in Figure 1.3. This X-ray spectrum was recorded by Tanaka *et al.* (1995) from the Seyfert galaxy MCG-6-30-15 (which is an active galaxy) and is historically the first clear and well-resolved observation of such a line. This iron K line that is normally located at the energy of 6.4 keV is here clearly broadened and redshifted.

The broadening and shift of those iron K lines emitted by black hole accretion disks are due to special and general relativistic effects caused by the intense gravitational field of the central black hole. Firstly, as the emitting plasma is assumed to be located very close to the black hole event horizon, the velocities of the emitting ions are actually very high (non-negligible with respect to the velocity of light). For instance, Tanaka *et al.* (1995) inferred from the width of the observed ionized iron K lines in the X-ray spectrum of the Seyfert galaxy MCG-6-30-15 that the velocity of the emitting particles was about 100 000 km.s^{-1}. Therefore, the very high velocity distribution of the ions that emit light in all the direction provokes a relativistic Doppler broadening of the corresponding line shape. The latter is due to the distribution and superposition of the various relativistic Doppler shifts of the emitted photon wavelengths depending on the emitting ion position within the accretion disk and depending on the fact that this ion approaches or moves away with respect to the observer, due to the accretion disk rotation. Let us also note that the relatively high density that is not uniform within the accreting material (this will be discussed in Section 1.3) in the inner part of the disk combined with friction and turbulence phenomena are also responsible for a second type of line broadening, namely the so-called "collisional broadening", also named "pressure broadening". This effect is due to the various collisions undergone by the emitting ions and to the proximity of the latter with respect to the other plasma particles (ions and electrons) that disturb it and that can cause changes in its atomic structure (see Chapter 3 for more details), resulting in the superposition of various shifts (due to the density and iron ionization stage distribution within the accretion disk) that results in a broadened profile. Secondly, the gravitational redshift predicted by the general relativity theory is also in great part responsible for the observed shifts of iron K lines. Due to the radial distribution of the emitting iron
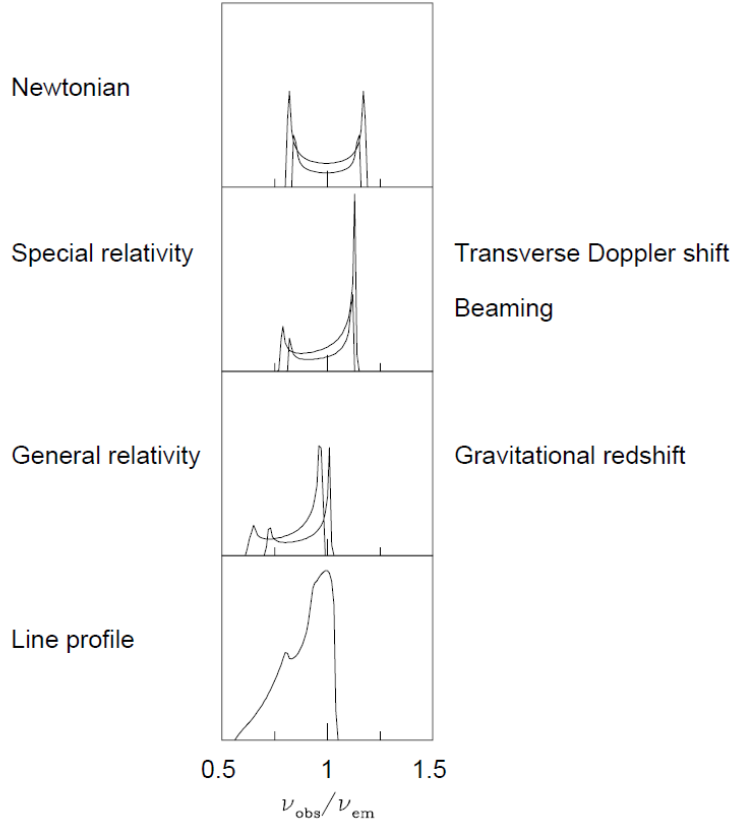
Figure 1.4: Effects that result in the distorted profile of the iron K-line complex emitted by accreting black hole (from Fabian *et al.* 2000).

ions within the disk, the latter are subject to various intensity of the central black hole gravitational field (the emitting ions that are closer to the black hole are more disturbed than the ones located farther). Thereby, the radial distribution of line gravitational redshifts also provokes a broadening of the iron K-line profile. These different effects that shift and broaden the iron K-line complex are isolated and summarized in Figure 1.4 (Fabian *et al.* 2000).

As a consequence, the study of the intensity and profile of the iron K-line complex, in addition to be a powerful plasma diagnostic tool, can also help investigate the effects of the special relativity and the gravitational effects due to the general relativity in the emitting regions within the "strong field" regime. The importance of studying the X-ray iron K lines emitted by accreting black holes is thus clearly emphasized since such information for regions so close to black holes undergoing such an intense gravitational field is not available by other known techniques up
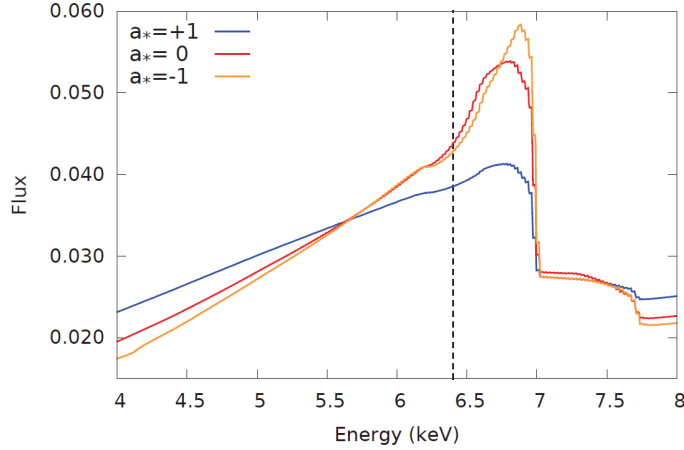
Figure 1.5: Spin effect on the relativistically distorted Fe K line (for a disk inclination of 40°) from Garcia *et al.* (2018).

to now.

Furthermore, and even more interesting again, the study of the iron K-line broadened and shifted profile from such sources turns out to be a particularly useful technique to estimate the spin of the central black hole (see Miller *et al.* 2002, 2009, and Miller 2007 or Reynolds and Nowak 2003 for a detailed review). The latter, noted a, is defined as the dimensionless angular momentum of the black hole, J, that is $a = cJ/GM^2$, where c is the light velocity in the vacuum, G is the Newton gravitational constant and M is the black hole mass. The black hole spin can actually be derived by fitting the observed broadened iron K-line complex to a model spectrum, by assuming that the radiative emission that comes from the inner part of the accretion disk is located at the innermost stable circular orbit (ISCO) of the central black hole (Steiner *et al.* 2012). Since the radius of the ISCO (R_{ISCO}) is a monotonic function of the black hole spin, fitting the model spectrum to the observed data helps determine R_{ISCO} and, as a consequence, allows to estimate the black hole spin (Miller 2007). Actually, the smallest R_{ISCO} is, the closest to the central black hole the emitting ions are located and, thereby, the most distorted the irons K lines are. This can be illustrated by Figure 1.5 from Garcia *et al.* (2018), which shows the spin effect on the relativistically blurred iron K line (for a disk inclination of 40°). In passing from extreme retrograde spin ($a = -1$) to extreme prograde ($a = 1$), R_{ISCO} shrinks from 9 R_G to 1 R_G (where $R_G = GM/c^2$ is the gravitational radius) and, as a consequence, the emitting ions are located closer to the central black hole and the iron K line broadens dramatically.

The determination of the black hole spin is of particular importance in order

to study the formation and evolution story of this fascinating compact object. Actually, on the one hand, the spin of a supermassive black hole is a key element to help distinguish the right evolution scenario of the black hole among the various existing ones (Berti & Volonteri 2008). On the other hand, the spin of a stellar-mass black hole is connected to the angular momentum of the initial star that has ended up as a black hole. The knowledge of the black hole spin thus offers an interesting window to study supernovae (Miller *et al.* 2011).

1.3 Black hole accretion disk structure and X-ray emission mechanism

The accretion phenomenon, which leads to the formation of a flat accretion disk around a compact object such as a black hole, is mainly explained by an angular momentum transport and redistribution mechanism. Actually, the matter that is located in the vicinity of the compact object is attracted in its direction by gravitational interaction and ends up orbiting around it and forming a flat disk structure in rotation (due to the various initial velocities of the particles). The gravitational energy of the disk components is then dispersed in the form of X-ray radiations due to the viscous friction and turbulences within the plasma forming the disk. While those components are losing gravitational potential energy, they
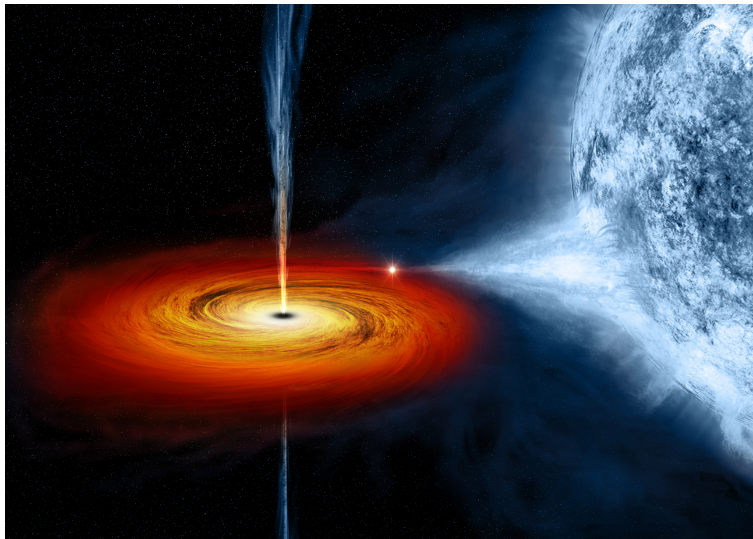

Figure 1.6: Artistic view representing the accreting black hole Cygnus X-1 (http://chandra.harvard.edu/photo/2011/cygx1/cygx1_ill.jpg).

fall in a spiral and, as a consequence, their angular momentum decreases. Thereby, in order to ensure the conservation of the angular momentum, the latter must be redistributed. As a result, the angular momentum of the matter that was lying a little farther must increase, which makes the latter also beginning to orbit around the compact object. This angular momentum transport and redistribution mechanism mainly explains the accretion phenomenon and thus the formation of accretion disks around black holes or neutron stars. Furthermore, the accretion phenomenon is also a very efficient process that converts a mass flow in luminosity, and is assumed to explain the very intense luminosity that characterizes the AGN, which have an accreting supermassive black hole in their center.

As above-mentioned, the origin of the angular momentum transport mechanism, which leads to the formation of an accretion disk, arises from the dissipation of gravitational energy through X-ray emissions that are due to viscosity and turbulences within the plasma formed by the accreting material. The latter are partly caused by the magnetohydrodynamics (MHD) instabilities, also called magneto-rotational instabilities (MRI), which stems from the intense and highly irregular and non-homogeneous magnetic fields that take place within the rotating plasma forming the accretion disk. It is widely assumed that the MRI are the leading candidates to explain the origin of the angular momentum redistribution mechanism that leads to the formation of the accretion disks around the compact objects (Balbus & Hawley 1991).

The X-ray iron K-line emission from accreting black holes is not compatible with a thermal emission from the accretion disk (Reynolds & Nowak 2003). Such an emission does not produce X-rays that are energetic enough to ionize iron ion K shell (and thus creating the K-vacancy states that are the initial states of the K lines through the fluorescence phenomenon). The emission of iron fluorescent K lines can however be explained by the reflection model (see Fabian & Ross 2010 for a review), that is widely accepted nowadays. In this model, the iron K lines emitted from the accretion disk are assumed to be produced by converting *via* fluorescence (as explained in Section 1.1) a X-ray continuum emission generated by an external source that illuminates the disk. More precisely, they are supposed to be emitted through K-shell fluorescence induced by K-shell photoionization generated by such an external X-ray continuum. Such a fluorescent emission of the iron ions located within the disk after that the latter has absorbed a continuum emission of X-rays that illuminates it gives the picture of a "reflection" of this X-ray radiation by the disk.

There exist several hypotheses for the mechanisms that explain how the accretion disk can be illuminated by X-rays that are energetic enough to be able to photoionize the iron K shell and create K-vacancy states in iron ions. One of those hypotheses supposes that radiations emitted for instance during eruptions or flares

within the accretion disk (similar to the solar eruptions) due to magnetic field instabilities can be accelerated by reflection in a hot and compact corona around the accreting black hole (Reis & Miller 2013) and could finally irradiate the disk in return. The name of "corona" is a reference to the stellar corona (such as the solar one) that is a hot and not very dense plasma surrounding stars. The origin and the properties of such a corona around accreting black holes remain however to be determined. The production of a continuous flux of high-energy X-rays by the corona is assumed to arise from inverse Compton scattering of lower energy X-ray photons (emitted for instance during flares within the accetion disk plasma) through the hot corona, which would produce X-ray photons with a sufficient energy to photoionize the iron ion K shell (Liang & Price 1977, Haardt & Maraschi 1991). Another plausible source of high-energy X-rays that illuminate the disk stems from the synchrotron radiations within the relativistic jets of matter and light emitted at the black hole poles (Reis & Miller 2003). Such radiations are notably emitted in the X-ray band by the acceleration of charged particles that spin around the magnetic field lines in a spiral (which focuses the jet) and that can reach energies greater than the iron ion K-shell ionization threshold. X-ray photons of lower energies in the synchrotron radiation emitted from the relativistic jets can by the way also be accelerated by inverse Compton scattering in the corona (as explained above) to reach the required energy to photoionize the K shell of iron ions.

The spatial limit between the corona and the accretion disk of a black hole is defined thanks to the optical depth. As a reminder, the optical depth, noted τ, is a dimensionless factor that characterizes the absorption of a radiation flux through a given medium. For a given incident radiation flux with an initial intensity I_0, the intensity I measured after its way through the medium is related to I_0 through an exponentially decreasing law that depends on the optical depth τ as

$$I = I_0 \, e^{-\tau}. \tag{1.2}$$

The optical depth also enables to define the opacity of the medium traversed by the radiation, κ, by means of the relation

$$\tau = \int \kappa \, \mathrm{d}s, \tag{1.3}$$

where the curvilinear integral is carried out along the geometrical path followed by the radiation. The optical depth thus allows to distinguish the optically thick accretion disk ($\tau > 1$) to the optically thin corona ($\tau < 1$).

Recently, Schnittman *et al.* (2013) performed a MHD simulation (within a general relativistic framework) coupled to a radiative transport code in order to model the accretion disk dynamics in the case of stellar-mass black holes, within the

(a) Electron density profile

(b) Temperature profile
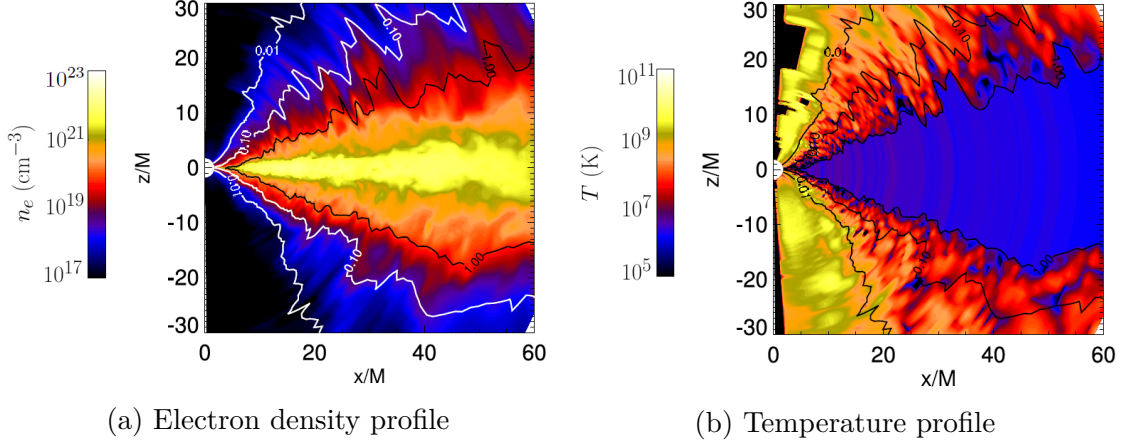
Figure 1.7: Electron density (1.7a) and temperature (1.7b) profile estimated from the simulation (at a given time) of the cross-section in the (r, z) plane of the accretion disk and corona of a black hole that has a mass $M = 10M_\odot$ and an accretion rate $\dot{m} = 0, 1$ carried out by by Schnittman *et al.* (2013).

assumption of the reflection model discussed above. The results of their simulation reproduce the main "reflection" features as those observed in accreting black hole X-ray spectra, particularly the distorted iron K lines. Let us also mention that a coronal radiation distribution has successfully been used in their simulation to model the high-energy X-rays that illuminate the disk and ionize the K shell of iron ions. Thereby, the results obtained by the simulations of Schnittman *et al.* (2013) confirm the hypothesis of the reflection model as principal mechanism that leads to the production of iron K lines by fluorescence in accretion disk around black holes.

   Furthermore, these simulations allowed to obtain an estimate of the density and temperature profiles of the accretion disk and corona around a stellar-mass black hole. An example of such profiles for a cross-section of the plane $(r, z = r\cos\theta, \phi = 0)$ of a black hole of ten solar masses $(M = 10M_\odot)$ with a typical accretion rate[1] of 10% $(\dot{m} = 0.1)$ is displayed in Figure 1.7. The latter is inspired by the one found in Schnittman *et al.* (2013), with the scales that have been converted from keV to K and from g/cm^{-3} to cm^{-3}, respectively for the temperature and the electron density profiles (the latter being more convenient to be expressed as a particle density instead of a mass density for the necessity of this work). The $z = 0$ plane corresponds to the accretion disk plane. The contour solid lines represent the

---

[1]The accretion rate $\dot{m}$ represents the efficiency with which the accreting black hole converts the accreted mass flow in luminosity. Formally, it corresponds to the ratio between the produced luminosity, L, to the Eddington luminosity L_{Edd} (defined as the maximal luminosity that a star can radiate without being broken up), that is $\dot{m} = L/L_{\text{Edd}}$.

surfaces of equal optical depth, with $\tau = 1$ that corresponds to the spatial limit between the optically thick accretion disk ($\tau > 1$) and the optically thin corona ($\tau < 1$).

The region of interest for this work is the optically thick accretion disk, from where the distorted iron fluorescent K lines should originate. Therefore, from the MHD simulation results of Schnittman *et al.* (2013), we can have an estimate of the order of magnitude for the physical conditions (temperature and electron density) within the accretion disk of a black hole. By looking at Figure 1.7a, one can see that the simulations revealed that the electron density should range from 10^{18} to about 10^{22} cm^{-3} in the accretion disk ($\tau > 1$), while Figure 1.7b indicates that the temperature should be included between 10^5 and 10^7 K. As a result, these MHD simulations of Schnittman *et al.* (2013) revealed that the electron density within the accretion disk can be as high as 10^{21} - 10^{22} cm^{-3}, which is quite high for a photoionized astrophysical plasma. The region of the accretion disk black hole that is responsible for the emission of iron fluorescent K lines appearing distorted in the X-ray spectrum is thus a plasma characterized by a rather high density.

1.4 Atomic data requirement to model the iron K lines

In order to perform a correct diagnostic of the distorted Fe K-shell complex observed in most X-ray accreting black hole spectra and, thereby, to possibly deduce very interesting features of the emitting region as well as of the black hole itself (see Section 1.3), the model spectrum needs to incorporate the most accurate and reliable atomic data, for all the processes that are involved in K-line emission by fluorescence and for all the possible physical conditions within the emitting region. For instance, the rates at which the radiation can be absorbed and emitted by the ions of interest, along with the various ionization limits to obtain the ionization balance (that allows to determine which ionization stages are present in the plasma), are atomic data of indisputable importance to model an astrophysical X-ray spectrum that aims to be fitted to the observed one for diagnostic purposes.

Plenty of atomic data involved in iron K-line emission have already been computed in the last two decades. Among the most relevant ones, we can note that the radiative wavelengths and rates, Auger transition rates, ionization potentials, K thresholds and K-shell photoionization cross sections for K-vacancy states in all the iron ions have been calculated by Bautista *et al.* (2003), Palmeri *et al.* (2003a), Mendoza *et al.* (2004) and Palmeri *et al.* (2003b). These four references concern the atomic data related to K-vacancy states in Fe XXIV, Fe XVIII–Fe XXV, Fe X–Fe XVII, and Fe II–Fe IX, respectively. All these atomic data are

required to model the X-ray spectra of accreting black holes and, in particular, to model the distorted iron K lines. They were computed by using two main methods, namely the pseudo-relativistic Hartree-Fock method (HFR, which is the non-relativistic counterpart of the MCDF method that is detailed in Section 2.1 of Chapter 2) and the AUTOSTRUCTURE program (that is presented in Section 2.2 of Chapter 2).

Kallman *et al.* (2004) present a model that aims to determine the level population from the collisional-radiative equations simplified for "model atoms" using the atomic data above-mentioned. This model and all the atomic data from the papers aforesaid have been included in the XSTAR code (Kallman & Bautista 2001, Bautista & Kallman 2001), which is a standard code used by NASA to model X-ray spectra emitted by photoionized astrophysical plasmas[1]. In addition to the X-ray spectrum, this code allows to determine the ionization and thermal balances of the astrophysical plasma, along with the opacity of the latter (*i.e.* its absorption properties) depending on the physical conditions within the plasma. More precisely, XSTAR computes the level populations, the ionic fractions of the plasma components, the temperature, the opacity and the emissivities for a photoionized plasma with a given composition. It uses a complete collisional-radiative model in which the population of all the involved atomic levels is explicitly calculated, by taking into account all the radiative and collisional atomic processes that can populate and depopulate each level. The XILLVER program (Garcia & Kallman 2010, Garcia *et al.* 2013), that is based on the XSTAR code, aims to model X-ray spectra from accreting black holes within the framework of the reflection model described in Section 1.3, and can thus model the distorted iron K lines. This program can actually be seen as an extension of XSTAR as it uses all the properties that can be computed by XSTAR (and that was mentioned above) in the particular case of X-ray spectra from accreting black holes. Thereby, all the above-mentionned atomic data that are implemented in XSTAR are also used in XILLVER.

However, the atomic data that are used in XSTAR (and XILLVER) to model X-ray spectra (and which are listed above) were computed using an isolated ion approximation, namely without considering that the emitting ions are actually embedded in a plasma. The plasma environment effects on such atomic data are thus neglected (such plasma effects are detailed in Chapter 3). Nevertheless, as discussed in Section 1.3, the densities expected in the plasma forming the accreting material that is responsible for the K-line emission are actually rather high, since they can be as high as 10^{22} cm^{-3} (Schnittman *et al.* 2013, Jiang *et al.* 2019). For such a high density, one can expect that the emitting ions embedded in the plasma can be disturbed by the presence of the other electrons and ions within the plasma

---

[1]Program publicly available at http://heasarc.gsfc.nasa.gov/docs/software/xstar/xstar.html.

that are in their close vicinity and interact with them, so that their atomic structure can be affected. This could provoke changes in the ionization balance and have an influence on the atomic processes involved in light emission (see Chapter 3). Incidentally, Smith & Brickhouse (2014) have recently published a review entitled *Atomic Data Needs for Understanding X-ray Astrophysical Plasmas* where they highlighted the necessity to take the effects of high-density plasma environment into account while modeling astrophysical X-ray spectra, in particular in light of the resolution achieved by the new era of X-ray satellites (see Section 1.6). Moreover, Garcia *et al.* (2016) emphasized the incompleteness of the atomic data available at the moment to model X-ray reflection spectra from accreting black holes due to high-density effects. They showed in their paper that electron densities higher than 10^{18} cm^{-3} should affect the X-ray spectrum of accreting compact objets in several ways (modifications in the ionization balance, in the emission line spectrum, in the continuum photoelectric absorption, *etc.*). They concluded by saying that *"at such densities, much of the rate data in current atomic data bases is inapplicable and new atomic calculations are sorely needed"* and that *"the development of accurate high-density reflection models is now a priority given the high-resolution data"*.

Furthermore, the accuracy of the spin estimates by using the method described above is called into question because of inconsistencies observed in the results (Garcia *et al.* 2016, Garcia *et al.* 2018). Actually, fitting the data over the model X-ray
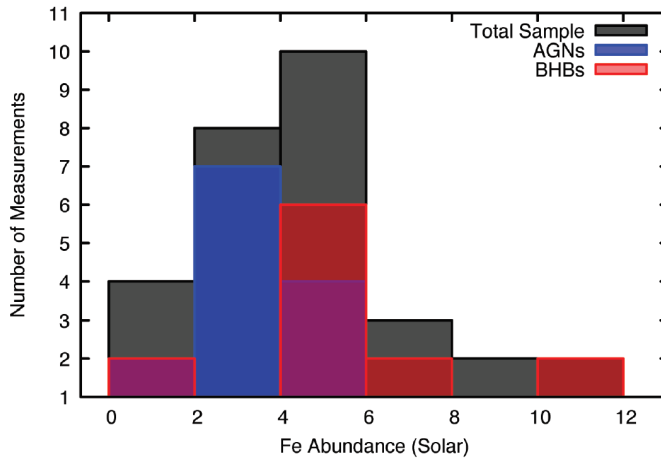

Figure 1.8: Histogram from Garcia *et al.* (2018) of iron abundance determinations using reflection spectroscopy for both 13 AGN (Active Galactic Nuclei) and 9 BHBs (Black-Hole Binaries). Values a few times the solar standard are routinely found.

spectrum requires uncommonly high iron abundances, typically several times the solar value. Figure 1.8 shows a compilation of the iron abundances reported by Garcia *et al.* (2018) by using reflection models as implemented in XILLVER for 13 AGNs and 9 stellar-mass black hole binaries. The trend is clear in both cases for abundances a few times over the solar value. Since no plausible physical explanation has been concurrently proffered for these black-hole systems to be so iron rich (it is unlikely that supersolar abundances are realistic since metal enrichment mechanisms in these two types of systems are expected to be very different), the most likely explanation for the supersolar iron abundances is model shortfall at very high densities (higher than 10^{18} cm^{-3}) due to atomic data shortcomings in this regime, as aforementioned. Moreover, very recent analyses of the reflection spectra from AGNs and black-hole binaries (BHB) appear to indicate that the high-density effects are acting positively to resolve the mystery of the high iron abundances leading to substantially lower observed values (Tomsick *et al.* 2018; Jiang *et al.* 2019).

In conclusion, it is now clear that the isolated ion approximation on which the atomic data implemented in the astrophysical models relies should not be valid anymore in high-density plasma, typically for the densities that are expected in accretion disk around black holes (higher than 10^{18} cm^{-3}). The main motivation of this work, namely the attempt to provide new atomic data that take high-density plasma effects into account in order to address this shortcoming, is thus clearly highlighted.

1.5 About the importance of oxygen K-shell processes in astrophysics

Oxygen is one of the most abundant elements in astrophysical media after hydrogen and helium (Meyer *et al.* 1998) and thus plays a key role in the understanding of the chemical evolution of galaxies (Pilyugin 2001). Besides, oxygen ions also have their importance for X-ray astrophysics, especially for atomic processes involving the K shell. The oxygen K-shell absorption actually supplies a very good diagnostic tool for astrophysical plasmas. For instance, O VII and O VIII edges are observed in the X-ray spectra of many Seyfert 1 galaxies, which have been used by Lee *et al.* (2001) to reveal the existence of a dusty warm absorber (hot ionized gas responsible for absorption in AGN X-ray spectra) in the galaxy MCG6-30-15, whereas inner-shell transitions of O III - O VI detected in the spectrum of NGC 5548 by Steenbrugge *et al.* (2003) also indicate the presence of a warm absorber. Redshifted emission lines from O VIII and O VII were also observed in the high-resolution X-ray spectrum of NGC 5548 by Kaastra *et al.* (2000). Moreover, a

gravitationally redshifted O VIII Lyα line observed in absorption in the spectrum of the bursting neutron star EXO 0748-676 shows multiple components consistent with a Zeeman splitting in a magnetic field (Loeb 2003). Furthermore, observations of the O I edge in the spectrum of the black-hole binary LMCX-3 by Page *et al.* (2003) lead to upper limits of the neutral and ionized column densities, while high-resolution spectroscopy of the interstellar O K edge in X-ray binaries carried out by Juett *et al.* (2004) enables to rule out oxygen features from dust and molecular components and thus to provide first estimates of the O ionization fractions.

This is why, similarly to iron ions, a lot of atomic data related to K-shell atomic processes in oxygen ions have been computed in the last decades, notably by Garcia *et al.* (2005), which reported the radiative wavelengths and rates, Auger transition rates, ionization potentials, K thresholds and K-shell photoionization cross sections for K-vacancy states in all the ionization stages of oxygen ions. Besides, these data are also implemented in the XSTAR and XILLVER codes.

However, similarly to the iron ion case, the plasma high-density effects were not taken into account in the calculation of these parameters. For the reasons highlighted above, in order to model at best the oxygen features within the astrophysical X-ray spectra of accreting sources, it is also required to estimate the plasma environment effects on all the data involved in K-shell atomic processes that occur in oxygen ions.

1.6   X-ray observatories

As the Earth's atmosphere is completely opaque to X-rays, telescopes for X-ray astronomy need to operate from the upper atmosphere (with sounding balloons, as in the X-ray astronomy beginnings) or, preferably, directly from space. The current detectors of astrophysical X-rays are thus satellites that are orbiting around Earth. In the recent past, a large number of spatial X-ray observation missions (of which several are still in activity) have been launched by NASA (*National Aeronautics and Space Administration*), ESA (*European Space Agency*) or even JAXA (*Japan Aerospace Exploration Agency*). In this section, we briefly describe some of the most important past, current and future X-ray missions, among which some are particularly focused on the observation of X-ray spectra from accreting sources.

The first two most important X-ray observatories were the European satellite EXOSAT (European X-ray Observatory Satellite), that was launched in May 1983 and operated until April 1986, and the Japanese satellite Ginga (which means "Galaxy" in Japanese, and which was initially named Astro-C), launched in February 1987 and in activity until November 1991. Those satellites were respectively operating in the 2-20 keV and 1-50 keV energy bands and were equipped by spectrometers with a resolution of about 600 eV at the energy of 6 keV (the typical

energy of iron K lines). EXOSAT was the first satellite that provided the first clear observations of the distorted iron K lines and reflection features in the X-ray spectra of accreting sources (Fabian *et al.* 1989, Nandra *et al.* 1989). However, in light of the poor spectral resolution of the instruments on board the satellite, such observations did not allow a detailed study of the relativistic effects that broaden and shift the lines.

The launch of the Japanese satellite ASCA (*Advanced Satellite for Cosmology and Astrophysics*, initially named Astro-D and for which NASA has significantly contributed) in February 1993 (and which operated until March 2001) finally made it possible to study in a deeper way the distorted iron K lines. Actually, the spectral resolution of two (of the four) X-ray spectrometers on-board this satellite was about 120 eV at the energy of 6 keV, which allows to resolve the iron K-line profile in the observed X-ray spectra and thus to discern the relativistic broadening features of the lines. One of the most relevant examples is the observation of the distorted iron K lines by Tanaka *et al.* (1995) within the X-ray spectrum of the Seyfert galaxy MCG-6-30-15 recorded by ASCA (see Figure 1.3 in Section 1.2), which was historically the first clear observation of such a line that allowed to study the relativistic effects that broaden and shift this famous line.

Currently, there are (among others) two widely-exploited and well-known X-ray observatories that are still in activity, namely the Chandra X-ray Observatory (initially called AXAF for *Advanced X-ray Astronomy Facility*) that was launched in July 1999 by NASA, and XMM-Newton (where XMM stands for *X-ray Multi-Mirror*), that was put into orbit in December 1999 by ESA. They respectively operate in the 0.1-10 keV and in the 0.1-12 keV X-ray energy bands (which include the typical emission energy of the iron K lines in both cases). The diffraction grating spectrometer of Chandra allows the observation of X-rays at high spectral resolution, namely about 30 eV (at 6 keV). The XMM-Newton's one has a lower resolution (about 130 eV at 6 keV, which is comparable to the ASCA spectrometer) than Chandra, but it is complementary to the latter in the sense that its telescope effective collecting area is much bigger than the Chandra's one, thus providing a better signal-to-noise ratio. Both Chandra and XMM-Newton have thus become two of the most important astrophysical satellites to observe X-rays from accreting sources, and they are actually commonly used to observe the same source together in a joint analysis in order to obtain high-resolution X-ray spectra with a rather good signal-to-noise ratio.

Another current (and more recent) X-ray mission is the NuSTAR telescope (Nuclear Spectroscopic Telescope ARray) that operates in the range 3 - 79 keV, so for higher energies than Chandra and XMM-Newton (still including the Fe K line emission energy), and which was successfully launched in June 2012. It is the first focusing hard X-ray satellite in orbit, providing more than two orders of mag-

nitude improvement in sensitivity as compared to previous high-energy missions working at similar energies (Harrison *et al.* 2013). It aims to study high-energy astrophysical X-rays such as those emitted by accreting black holes, supernova explosions, neutron stars, *etc.* In particular, several black hole spin estimations have been performed by using NuSTAR high-resolution data (see, *e.g.*, Kara *et al.* 2015, Garcia *et al.* 2016, Xu *et al.* 2018).

Astro-E was a Japanese X-ray mission that had on board an X-ray microcalorimeter (developed by NASA) instead of a spectrometer. This detector allows to obtain very high spectral resolution, much better than the typical grating spectrometer resolutions. Such a microcalorimeter actually measures the tiny increase of temperature caused by the heat produced when an X-ray photon interacts with the detector medium, and enables to reach a spectral resolution of about 7 eV (at the energy of 6 keV) in the case of the Astro-E's microcalorimeter. Unfortunately, a loss of control of the satellite happened during the launch in February 2000 and Astro-E crashed on Earth. However, a copy of Astro-E, named Astro-E2, was successfully launched in July 2005 and was then renamed Suzaku on that occasion. Sadly, two weeks after it was put into orbit, a dysfunction of the high-resolution microcalorimeter cooling system provoked a definitive shutdown of this detector. The other two instruments were not affected by this problem, so they have been keeping collecting data and are still in activity at the moment. Nevertheless, their spectral resolution is much less competitive compared to the microcalorimeter one (respectively 12 eV and 130 eV at 6 keV).

Very recently, on the 17th of February 2016, the Astro-H satellite was successfully launched by JAXA, and was renamed Hitomi. This mission had on board an
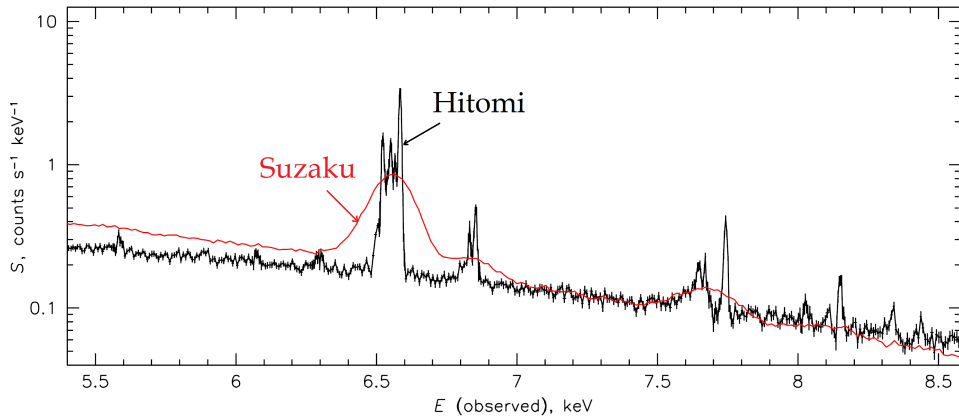
Figure 1.9: X-ray observation of the Perseus cluster core (figure from The Hitomi Collaboration 2016).

X-ray microcalorimeter that was developed by NASA and that achieved a spectral resolution better than 7 eV (at 6 keV). Once again, accidentally, JAXA lost the control of the satellite a few weeks after it was launched. Hitomi just had the time to record one X-ray spectrum from the core of the Perseus cluster (The Hitomi Collaboration 2016), with very promising results. Indeed, as one can see in Figure 1.9, the iron K line complex (around 6.5 keV) is much better resolved with the Hitomi's X-ray microcalorimeter than it was in the spectrum observed previously with Suzaku.

In light of those promising results obtained by Hitomi's X-ray micro-calorimeter just before it became unusable, JAXA and NASA decided to schedule a new X-ray mission with the same features as Hitomi for early 2022, called XRISM (*X-Ray Imaging and Spectroscopy Mission*). It will be equipped by an X-ray microcalorimeter similar to the Hitomi's one, operating in the 0.3 - 12 keV X-ray energy band with an energy resolution ≤ 7 eV (Guainazzi & Tashiro 2018; Tashiro *et al.* 2018).

In the long term, a future X-ray mission is scheduled for the early 2030s by ESA: the ATHENA mission (*Advanced Telescope for High ENergy Astrophysics*). This satellite will be equipped by an X-ray microcalorimeter (named X-IFU, which stands for *X-ray Integral Field Unit*) that should at least achieve the unprecedented spectral resolution of 2.5 eV (at the energy of 6 keV), with the objective to even reach 1.5 eV (Nandra *et al.* 2013; Guainazzi & Tashiro 2018). Besides, the effective collecting area should be at least ten times bigger than Chandra's. This high-resolution X-ray detector would undoubtedly enable to resolve the distorted fluorescence Fe K complex like never before, and would thus allow to deeply study the features of the relativistically broadened and shifted profile of these iron K lines that come from accreting sources.

With the advent of spatial missions equipped by this new era of X-ray detectors (namely the X-ray microcalorimeters) that achieve (or should achieve) unprecedented high spectral resolutions, all the microphysics effects that can affect the shape and intensity of the lines have to be considered in the theoretical models that compute X-ray spectra in order to perform a correct diagnostic from the high-resolution observed data, and thus to study the relativistic distortion of the iron K lines (in order to estimate the black hole spin in the case of accreting black hole, for instance). This is why, in light of the high densities that are expected in accretion disks surrounding black holes and that can affect the shape of the accreting black hole X-ray spectrum (see Section 1.3 and Section 1.4), it is sorely and urgently needed to consider the high-density plasma effects while computing the atomic data aimed at being implemented in the astrophysical modeling codes. Therefore, our work precisely tends to meet this requirement.

Chapter 2

Theory and computational methods

In this chapter, we present the theoretical methods used in this work to model the atomic structure of the considered ions. The main approach that we systematically use in our investigations is the multiconfiguration Dirac-Fock (MCDF) method, the purely relativistic version of the Hartree-Fock method. The MCDF method is described in Section 2.1 and is implemented in the GRASP2K computational code (Jönsson *et al.* 2013). Another approach that is used for comparison purpose in this work is the Breit-Pauli relativistic approximation as implemented in the AUTOSTRUCTURE program (Badnell 1997, 2011). The main concepts of this method are briefly described in Section 2.2.

Let us remark that all the expressions given in this manuscript (unless explicitly mentioned) are expressed in the Hartree atomic unit system, namely in the unit system where

$$m_e = 1 \,;\, \hbar = 1 \,;\, e = 1 \,;\, 4\pi\epsilon_0 = 1 \,,$$

m_e denoting the electron mass, e its charge and ϵ_0 the vacuum permittivity.

2.1 Multiconfiguration Dirac-Fock method

The MCDF approach consists in solving approximately the Dirac equation for each bound electron of the considered atom by using the central field approximation (*i.e.* considering that all the electrons move independently with respect to each other in a spherically symmetric effective potential).

In this multiconfiguration method, each atomic state is described as a linear combination of well-chosen basis states. Then, by requiring a functional of the energy to be stationary with respect to small variations of the spin-orbital radial

parts, we obtain a coupled integro-differential equation system (called the Dirac-Fock equations) that can be solved in an iterative way using the self-consistent field (SCF) method.

Finally, an estimate of the energy levels and atomic states are respectively given by the eigenvalues and the eigenstates of the Hamiltonian. They are obtained by diagonalizing the latter at every iteration. Let us also note that some corrections due to quantum electrodynamics (QED) are perturbatively added to the Hamiltonian of the system, such as the transverse Breit interaction, the vacuum polarization and the electron self-energy.

We begin this section by giving a brief reminder about a few fundamental notions of relativistic quantum mechanics and by introducing the notation that we use in this manuscript. Then we describe the theoretical founding principles of the MCDF method. Afterward, the origin of the corrective terms linked to QED is briefly described. Finally, we present the computational program used in this work to model the ion atomic structures, namely the GRASP2K code, in which the MCDF method is implemented.

2.1.1 The hydrogen atom problem in relativistic quantum mechanics

Following the relativistic quantum mechanics theory, the wave equation that determines the behavior of a free electron is given by the Dirac equation:

$$(i\,\gamma^{\mu}\partial_{\mu} - c)\,\psi = 0, \tag{2.1}$$

where, in the Dirac representation, the four operators γ^{μ} are given by the matrices

$$\gamma^0 = \begin{pmatrix} \mathbb{1} & 0 \\ 0 & -\mathbb{1} \end{pmatrix}, \qquad \gamma^i = \begin{pmatrix} 0 & \sigma^i \\ -\sigma^i & 0 \end{pmatrix}, \tag{2.2}$$

with $i = 1, 2, 3$ and where σ^i are the usual 2×2 Pauli matrices.

A solution of the Dirac equation is a 4-component spinor named Dirac spinor.

The hydrogen atom problem, that is the search for stationary states of an electron in a Coulomb potential (having a spherical symmetry) generated by the nucleus, amounts to find the eigenstates of the Dirac Hamiltonian[1]

$$h_D = c\vec{\alpha}.\vec{p} + (\beta - 1)c^2 + V_{\text{nucl}}(r), \tag{2.3}$$

---

[1] The rest energy of the electron, c^2, is subtracted from the Hamiltonian in order to shift the null energy state and coincide the usual non-relativistic conventions in atomic physics.

where α^i, $i = 1, 2, 3$, and β are defined using the Dirac matrices γ^μ (2.2) such as

$$\alpha^i = \gamma^0 \gamma^i, \qquad \beta = \gamma^0. \tag{2.4}$$

Assuming the nucleus to be point-like (*i.e.* having an infinite mass), the nuclear potential can simply be written as $V_{\text{nucl}}(r) = -Z/r$.

The eigenvectors of the Dirac Hamiltonian (2.3) are called spin-orbitals. In spherical coordinates (r, θ, φ), they can be written as

$$\psi(r, \theta, \varphi) = \frac{1}{r} \begin{pmatrix} P_{n,\kappa}(r) \chi_{\kappa,m}(\theta, \varphi) \\ i Q_{n,\kappa}(r) \chi_{-\kappa,m}(\theta, \varphi) \end{pmatrix}, \tag{2.5}$$

where $P_{n,\kappa}(r)$ and $Q_{n,\kappa}(r)$ are respectively the great and the small radial components that are solutions of the radial equation system

$$\begin{pmatrix} (c^2 - Z/r - E_{n,\kappa}) & c \left(-\dfrac{\mathrm{d}}{\mathrm{d}r} + \dfrac{\kappa}{r} \right) \\ c \left(\dfrac{\mathrm{d}}{\mathrm{d}r} + \dfrac{\kappa}{r} \right) & (-c^2 - Z/r - E_{n,\kappa}) \end{pmatrix} \begin{pmatrix} P_{n,\kappa}(r) \\ Q_{n,\kappa}(r) \end{pmatrix} = \begin{pmatrix} 0 \\ 0 \end{pmatrix}, \tag{2.6}$$

in which n is the principal quantum number (the quantum number κ will be as for it properly defined latter) and where the 2-component spinors $\chi_{\kappa,m}$ are the spin-orbital angular parts. The latter are eigenvectors of the operators $\vec{j}^2$, j_3, $\vec{l}^2$ and $\vec{s}^2$ ($\vec{l}$, $\vec{s}$ and $\vec{j} = \vec{l} + \vec{s}$ being respectively the orbital angular momentum, spin and total angular momentum operators acting on a two-dimensional spinor space) with the eigenvalues $j(j+1)$, m, $l(l+1)$ and $s(s+1)$, with $j = 1/2, 3/2, 5/2, ...$, $-j \leq m \leq j$ and $l = j \pm 1/2$, respectively. The spinors $\chi_{\kappa,m}$ are also eigenvectors of the operator

$$K = - \left(1 + \vec{\sigma}.\vec{l} \right) \tag{2.7}$$

with the eigenvalues

$$\kappa = \left(j + \frac{1}{2} \right) \eta \quad \text{while } l = j + \frac{1}{2}\eta, \quad \text{with } \eta = \pm 1, \tag{2.8}$$

which allows to label the angular parts $\chi_{\kappa,m}$ in such a way. The spinors $\chi_{\kappa,m}$ can be developed on the spherical harmonic basis $\{Y_l^m(\theta, \varphi) \mid m = -l, -l+1, ..., l\}$. Their expression is given by Grant (2007) as

$$\chi_{\kappa,m}(\theta, \varphi) = \sum_{\sigma = \pm \frac{1}{2}} (l, m - \sigma, 1/2, \sigma \mid l, 1/2, j, m) Y_l^{m-\sigma}(\theta, \varphi) \phi_\sigma, \tag{2.9}$$

where ϕ_σ are two 2-component basis spinors, that is

$$\phi_{1/2} = \begin{pmatrix} 1 \\ 0 \end{pmatrix} \quad \text{and} \quad \phi_{-1/2} \begin{pmatrix} 0 \\ 1 \end{pmatrix}. \tag{2.10}$$

27

2.1.2 Basic principles of the MCDF method

Dirac-Coulomb Hamiltonian and atomic state functions

The relativistic Hamiltonian for a N-electron atom is given by the Dirac-Coulomb Hamiltonian

$$H_{DC} = \sum_{i=1}^{N} h_D(\vec{r}_i) + \sum_{i>j} \frac{1}{r_{ij}}, \tag{2.11}$$

where $h_D(\vec{r}_i)$ is the monoelectronic Dirac Hamiltonian (2.3) for the ith electron.

Within the central field approximation, each single electron is assumed to move independently with respect to the other ones in a spherically symmetric effective potential, $V(r)$, generated by the nucleus and by the mean effect of the $N-1$ other electrons (through a mean central potential, let us call it $U(r)$). This allows us to replace the monoelectronic Dirac Hamiltonian (2.3) by the operator

$$\tilde{h}_D = c\vec{\alpha}.\vec{p} + (\beta - 1)c^2 + V(r), \tag{2.12}$$

where $V(r) = -Z/r + U(r)$. The total Dirac-Coulomb Hamiltonian of the system (2.11) can thus be approximated by the following Hamiltonian:

$$H = \sum_{i=1}^{N} \tilde{h}_D(\vec{r}_i). \tag{2.13}$$

In light of the spherical symmetry of this Hamiltonian, the spin-orbitals can be written as (2.5). Thereby, only the radial parts $P(r)$ and $Q(r)$ remain to be computed in order to completely determine the electronic spin-orbitals.

The starting point of the MCDF method is to develop each atomic state function (ASF), $\Psi(P, J, M)$, that describes an atomic state of parity P and characterized by a total angular momentum quantum number J (with its projection M), as a linear combination of configuration state functions (CSF) with the same parity and angular momentum, $\Phi(\gamma, P, J, M)$, where γ contains all the information required to define the CSF in a unequivocal way (*e.g.* the coupling scheme, the orbital occupation quantum number, *etc.*):

$$\Psi(P, J, M) = \sum_{r=1}^{n_c} c_r \Phi(\gamma_r, P, J, M), \tag{2.14}$$

where c_r are the mixing coefficients and n_c is the number of CSFs explicitly introduced in the chosen model. These mixing coefficients have to satisfy the normalization condition

$$\sum_{r=1}^{n_c} |c_r|^2 = 1. \tag{2.15}$$

Each CSF is given as a linear combination of Slater determinants[2] built from the spin-orbitals (2.5) whose radial parts are optimized self-consistently by solving the MCDF equations (see section 2.1.2).

Construction of the Hamiltonian matrix in the chosen CSF basis

The first step consists in constructing the Hamiltonian matrix that has to be implemented in the method. The matrix elements of the Hamiltonian of the system can be expressed from angular coefficients (depending only of the CSF angular parts) and mono- and bielectronic radial integrals (Grant 2007).

The expression of the monoelectronic radial integral, $I(ab)$, for an electron initially on an spin-orbital a[3], is given by

$$
I(ab) = \delta_{\kappa_a \kappa_b} \int_0^\infty \left[c\, Q_a^*(r) \left(\frac{\mathrm{d}}{\mathrm{d}r} + \frac{\kappa_b}{r} \right) P_b(r) - c\, P_a^*(r) \left(\frac{\mathrm{d}}{\mathrm{d}r} - \frac{\kappa_b}{r} \right) Q_b(r) \right.
$$
$$
\left. - 2c^2 Q_a^*(r) Q_b(r) + V_{\mathrm{nucl}}(r) \left[P_a^*(r) P_b(r) + Q_a^*(r) Q_b(r) \right] \right] \mathrm{d}r.
$$
$$(2.16)$$

The bielectronic radial integral is expressed as a generalized relativistic Slater integral and is represented by $R^k(abcd)$:

$$
R^k(abcd) = \int_0^\infty \left[\left(P_a^*(r) P_c(r) + Q_a^*(r) Q_c(r) \right) \frac{1}{r} Y^k(bd; r) \right] \mathrm{d}r, \qquad (2.17)
$$

with the relativistic Hartree function Y defined as

$$
Y^k(bd; r) = r \int_0^\infty U^k(r, s) \left(P_b^*(s) P_d(s) + Q_b^*(s) Q_d(s) \right) \mathrm{d}s, \qquad (2.18)
$$

where

$$
U^k(r, s) = \begin{cases} \dfrac{r^k}{s^{k+1}} & \text{if } r \leq s \\[2mm] \dfrac{s^k}{r^{k+1}} & \text{if } r > s. \end{cases} \qquad (2.19)
$$

This bielectronic integral describes the electrostatic interaction between two electrons that can belong to different configurations in the most general case (which expresses the so-called interaction configuration). The direct radial integral, $F^k(ab)$,

---

[2] A Slater determinant allows to write the atomic state wavefuction as a product of antisymmetrized monoelectronic spin-orbitals, which makes sure of the wavefunction antisymmetry with respect to the exchange of two electrons and thus satisfy to the Pauli exclusion principle.

[3] Notation : the (spin-)orbital a is the one that is characterized by the quantum numbers (n_a, κ_a).

and the exchange one, $G^k(ab)$, are two particular cases of Slater integral in a monoconfiguration case. They express, respectively, the direct and the exchange (as the particles are indiscernible) electrostatic interaction between two electrons belonging to the same configuration. They are given by

$$F^k(ab) = R^k(abab), \tag{2.20}$$
$$G^k(ab) = R^k(abba). \tag{2.21}$$

The diagonal elements of the Hamiltonian matrix, in the chosen CSF basis, can be written as (Grant 2007):

$$H_{rr} = \sum_{a=1}^{n_o} \left(q_r(a)I(aa) + \sum_{b \geq a}^{n_o} \left[\sum_{k=0,2,...}^{k_0} f_r^k(ab)F^k(ab) + \sum_{k=k_1,k_1+2,...}^{k_2} g_r^k(ab)G^k(ab) \right] \right), \tag{2.22}$$

where n_o is the (spin-)orbital number, $q_r(a)$ the occupation number of the orbital a (*i.e.* the number of electrons that belong to the subshell that has the quantum numbers (n_a, κ_a)) of the CSF r, and where $f_r^k(ab)$ and $g_r^k(ab)$ are angular coefficients whose general expressions are defined in Grant (2007). The latter depend of the coupling scheme between equivalent electrons (*i.e.* electrons belonging to the same subshell) and between non-equivalent electrons, and depend consequently of the occupation number of each subshell. The standard coupling scheme used in the MCDF method in order to build the CSF is a jj coupling scheme defined in the following way:

- First, all the electrons of a same subshell a, having an occupation number $q(a) \leq 2j_a + 1$, are coupled between them following a jj coupling scheme in order to give an angular momentum J_a to every subshell.

- Then, the successive subshells a and b having an angular momentum J_a and J_b are jj-coupled in order to give an intermediary angular momentum X_1 that is in turn jj-coupled with the angular momentum J_c of the following subshell c to obtain an intermediary angular momentum X_2, *etc.* and this until the coupling of the last occupied subshell for finally obtaining a total angular momentum J. This scheme can be represented as follow:

$$(...((J_aJ_b)X_1J_c)X_2...)J. \tag{2.23}$$

The summation bounds k_0, k_1 and k_2 in (2.22) are given by:

$$k_0 = (2j_a - 1)\,\delta_{ab}, \tag{2.24}$$

$$k_1 = \begin{cases} |j_a - j_b| & \text{if } \kappa_a\kappa_b > 0 \\ |j_a - j_b| + 1 & \text{if } \kappa_a\kappa_b < 0, \end{cases} \tag{2.25}$$

$$k_2 = \begin{cases} j_a + j_b & \text{if } j_a + j_b + k \text{ is even} \\ j_a + j_b - 1 & \text{else.} \end{cases} \tag{2.26}$$

The off-diagonal elements $(r \neq s)$ of the Hamiltonian matrix in the chosen CSF basis, which express the configuration interaction between the different CSFs, can be written following the general form:

$$H_{rs} = \sum_{a,b} t_{rs}(ab)I(ab)\delta_{\kappa_a\kappa_b} + \sum_k \sum_{a,b,c,d} v_{rs}^k(abcd)R^k(abcd), \tag{2.27}$$

where $t_{rs}(ab)$ and $v_{rs}^k(abcd)$ are coupling angular coefficients of the same type as those appearing in (2.22), which also depend on the coupling scheme and on the subshells a, b, c and d that contribute to H_{rs}. The general expression of these coefficients in the various cases (filled or unfilled subshell, equivalent or non-equivalent electrons, *etc.*) are given in Grant (2007).

The MCDF equations

In order to optimize the spin-orbital radial parts $P(r)$ and $Q(r)$ (2.5), we solve a system of integro-differential equations obtained by applying a variational principle to an energy functional requiring the latter to be stationary with respect to small variations of the radial parts. The Lagrange multiplier method is used to require the orthogonality for the spin-orbitals. Let us consider the energy functional

$$\mathcal{E} = \sum_{r=1}^{n_c} \sum_{s=1}^{n_c} d_{rs}H_{rs} + \sum_a \sum_b (1 - \delta_{ab})\bar{q}(a)\epsilon_{ab}\,(a|b), \tag{2.28}$$

where ϵ_{ab} are Lagrange multipliers that ensure the orthogonality between the spin-orbital radial parts, where $\bar{q}(a)$ is called the generalized occupation number and is defined as

$$\bar{q}(a) = \sum_{r=1}^{n_c} d_{rr}q_r(a), \tag{2.29}$$

and where

$$(a|b) = \int_0^\infty \Big(P_a^*(r)P_b(r) + Q_a^*(r)Q_b(r) \Big)\mathrm{d}r. \tag{2.30}$$

31

The d_{rs} coefficients are generalized statistical weights that can be expressed in different ways, leading to diverse variants of the energy functional $\mathcal{E}$ (2.28):

- OL (Optimal Level) mode: in this mode, only one particular level is optimized. For an atomic state i, the generalized weights are given by

$$d_{rs} = c_{ri}c_{si}, \tag{2.31}$$

  where c_{ji} denotes the mixing coefficient of the ASF labeled i that corresponds to the CSF labeled j. The spin-orbitals obtained by this method are thus different if the optimization is carried out for different levels.

- EOL (Extended Optimal Level) mode: this option makes it possible to optimize a set of chosen levels at the same time. The generalized weights can thus be written as

$$d_{rs} = \frac{1}{n_L} \sum_{i=1}^{n_L} c_{ri}c_{si}, \tag{2.32}$$

  where n_L is the number of chosen levels ($n_L < n_c$). In this case, the same set of spin-orbitals is used to describe the set of ASF corresponding to the levels that have been chosen for building the energy functional $\mathcal{E}$.

- AL (Average Level) mode: in this option, the trace of the Hamiltonian matrix is optimized. The generalized weights are thus independent of the mixing coefficients and each CSF is weighted by its statistical weight:

$$d_{rs} = \delta_{rs} \frac{2J_r + 1}{\sum_{t=1}^{n_c} (2J_t + 1)}. \tag{2.33}$$

  Unlike the OL and EOL modes, this option allows a global optimization on all the energy levels.

- EAL (Extended Average Level) mode: this mode is the same as the AL mode except that the a weighted trace of the Hamiltonian matrix is optimized. The weights can thus be freely chosen by the user (and are consequently independent of the mixing coefficients).

By applying a variational principle to the functional energy $\mathcal{E}$ (2.28) for a spin-orbital a, a system of coupled integro-differential equations is obtained. The latter

are called the multiconfiguration Dirac-Fock equations and are given by

$$
\begin{cases}
-\dfrac{Z - Y(a;r)}{r}P_a(r) + c\left(-\dfrac{\mathrm{d}}{\mathrm{d}r} + \dfrac{\kappa_a}{r}\right)Q_a(r) - \epsilon_{aa}P_a(r) = -X_{+1}(a;r) \\[2mm]
c\left(\dfrac{\mathrm{d}}{\mathrm{d}r} + \dfrac{\kappa_a}{r}\right)P_a(r) + \left(-2c^2 - \dfrac{Z - Y(a;r)}{r}\right)Q_a r - \epsilon_{aa}Q_a(r) = -X_{-1}(a;r)
\end{cases},
$$

$$(2.34)$$

with the normalization condition

$$
\int_0^\infty \left(P_a^*(r)P_a(r) + Q_a^*(r)Q_a(r)\right)\,\mathrm{d}r = 1,
\tag{2.35}
$$

where $Y(a;r)$ is the direct interaction potential and X_β, $\beta = \pm1$, is the exchange interaction potential. Their expression are respectively given by

$$
Y(a;r) = \sum_k \sum_{b=1}^{n_o}\left[y^k(ab)Y^k(bb;r) - \sum_{c=1}^{n_o}y^k(abac)Y^k(bc;r)\right],
\tag{2.36}
$$

where

$$
y^k(ab) = \frac{1 + \delta_{ab}}{\bar{q}(a)}\sum_{r=1}^{n_c}d_{rr}f_r^k(ab),
\tag{2.37}
$$

$$
y^k(abac) = \frac{1}{\bar{q}(a)}\sum_{r=1}^{n_c}\sum_{s=1}^{n_c}d_{rs}v_{rs}^k(abac),
\tag{2.38}
$$

and by

$$
X_\beta(a;r) = -\sum_{b\neq a}\delta_{\kappa_a\kappa_b}\,\epsilon_{ab}\,R_{\gamma_b,\beta\kappa_b}(r)
$$

$$
+ \sum_k\left[\sum_{b\neq a}x^k(ab)\frac{Y^k(ba;r)}{r}R_{\gamma_b,\beta\kappa_b}(r)\right.
\tag{2.39}
$$

$$
\left.- \sum_{bcd}\left(1 - \delta_{ac}\,x^k(abcd)\frac{Y^k(bd;r)}{r}R_{\gamma_c,\beta\kappa_c}(r)\right)\right],
$$

with

$$
R_{\gamma,\beta\kappa}(r) = \begin{cases} P_{\gamma,\kappa}(r) & \text{if } \beta = +1 \\ Q_{\gamma,\kappa}(r) & \text{if } \beta = -1, \end{cases}
\tag{2.40}
$$

and where

$$
x^k(ab) = \frac{1}{\bar{q}(a)}\sum_{r=1}^{n_c}d_{rr}g_r^k(ab),
\tag{2.41}
$$

$$
x^k(abcd) = \frac{1}{\bar{q}(a)}\sum_{r=1}^{n_c}\sum_{s=1}^{n_c}d_{rs}v_{rs}^k(abcd).
\tag{2.42}
$$

33

Those coupled equations can only be solved by an iterative method. The self-consistent field (SCF) method is thus used to obtain the radial parts $P(r)$ and $Q(r)$ of each spin-orbital (2.5). This method consists in (i) choosing a starting set of radial parts $P(r)$ and $Q(r)$ (*e.g.* the spin-orbital radial parts corresponding to the screened hydrogenoïd atom), (ii) computing all the terms that appear in the MCDF equations for this set of radial parts and then (iii) solving the MCDF equations to obtain new radial parts. The steps (i), (ii) and (iii) are repeated in an iterative procedure until a certain convergence criterion is achieved. Nevertheless, let us remark that the number of the spin-orbital radial parts is much bigger in the relativistic case compared to the non-relativistic one, which makes this process much longer and more complex in the former case than in the latter one.

Solving the eigenvalue equation by the configuration interaction method

Once the spin-orbital are optimized as described above, the mixing coefficients can be determined thanks to the configuration interaction method. The energy of an atom in the state Γ described by an ASF having the form (2.14) is given by

$$E_\Gamma = \vec{c}_\Gamma^{\,\dagger} H \vec{c}_\Gamma, \tag{2.43}$$

where H is the Hamiltonian matrix in the chosen CSF basis and where $\vec{c}_\Gamma$ is a column vector whose components are the ASF mixing coefficients related to the atomic state Γ: $(c_{\Gamma,1}, ..., c_{\Gamma,n_c})$, with the normalization condition (2.15) that reads, with those notations, as $\vec{c}_\Gamma^{\,\dagger} \vec{c}_\Gamma = 1$.

The search for the stationary states of the system (*i.e.* the Hamiltonian eigenstates) is thus equivalent to solve the following eigenvalue problem:

$$H \vec{c}_\Gamma = E_\Gamma \vec{c}_\Gamma. \tag{2.44}$$

For a given atomic state, the eigenvalues and eigenvectors obtained by diagonalizing the Hamiltonian thus correspond respectively to the atomic energy levels and ASF mixing coefficients and consequently allow to completely describe this atomic state.

2.1.3 Quantum electrodynamics corrections

The Coulomb interaction term is not sufficient to describe the interactions between the bound electrons of an atom. Actually, in a relativistic context, it is necessary to take into account corrections due to the quantum electrodynamics (QED) theory. The most important ones are the transverse interaction (first-order correction), the vacuum polarization and the electron self-energy (SE) corrections (second-order corrections). The latter are added in a perturbative way to the Hamiltonian for solving the eigenvalue equation in order to correct the energy levels and the ASF representation (through the correction of the mixing coefficients).

(a) electron-electron scattering (transverse interaction)

(b) Vacuum polarization

(c) Self-energy
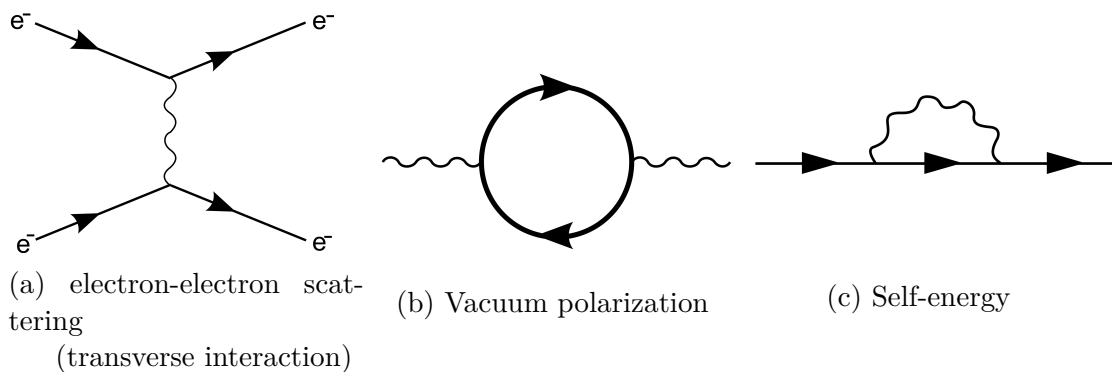
Figure 2.1: Feynman diagrams representing the QED phenomena taken into account as perturbative corrections in the MCDF method.

Breit transverse interaction

In QED, the electron-electron scattering is described as the exchange of a virtual photon (gauge boson of the electromagnetic interaction), whose Feynman diagram (of the first order) is represented in Figure 2.1a. The correction to the instantaneous Coulomb interaction term between two bound electrons of an atom due to this photon exchange is called the transverse interaction. This effect is modeled by means of a transverse interaction Hamiltonian operator that is added to the Dirac-Coulomb Hamiltonian of the system. The expression of this correction to the Hamiltonian is obtained by assuming that the energy of the photon that is exchanged between an electron lying on an orbital i and another one lying on an orbital j is equal to the difference between the binding energy of these two orbitals. The expression of the transverse interaction operator is thus given by Grant (2007) as

$$B_{ij}^T = -\vec{\alpha}_i.\vec{\alpha}_j \frac{e^{i\omega_{ij}r_{ij}/c}}{r_{ij}} - \left(\vec{\alpha}_i.\vec{\nabla}_{ij}\right)\left(\vec{\alpha}_j.\vec{\nabla}_{ij}\right)\frac{e^{i\omega_{ij}r_{ij}/c}-1}{\omega_{ij}^2 r_{ij}/c^2}, \qquad (2.45)$$

where $\vec{\alpha}_i = (\alpha_i^1, \alpha_i^2, \alpha_i^3)$ is a vector whose components are the three Dirac matrices α^k acting on an electron lying on an orbital i, $r_{ij} = |\vec{r}_i - \vec{r}_j|$, and where ω_{ij} is the emitted photon frequency, *i.e.* $\hbar\omega_{ij} = |E_i - E_j|$, E_i and E_j being the respective binding energy of the orbitals i and j.

Vacuum polarization

The QED theory predicts that a vacuum fluctuation of energy ΔE can give rise to the creation of an electron-positron pair that will annihilate after a time interval Δt satisfying the Heisenberg uncertainty principle: $\Delta E.\Delta t \gtrsim \hbar$. The Feynman diagram that represents such a phenomenon (which is a second-order diagram) is

shown in Figure 2.1b. Thereby, dipoles spontaneously appear from the vacuum during a very short time, which affects the surrounding electromagnetic field. Actually, an electron interacting with these dipoles would modify the spatial repartition of the latter, which provokes a "vacuum polarization" giving rise to the modification of the electromagnetic field generated by the electron as its charge is screened. As a consequence, the electronic structure of an atom would also be affected. This correction is taken into account in the MCDF method through an effective potential modeling the vacuum polarization around a point-like charge, such as the Uehling potential (see Greiner & Reinhardt 2002), which is perturbatively added to the Hamiltonian of the system (Grant 2007).

Self-energy

The electron self-energy is another QED second-order correction taken into account in the MCDF method (Grant 2007). This correction is due to the fact that an electron can spontaneously emit a virtual photon having an energy ΔE and then reabsorb it after a time interval Δt such as $\Delta E.\Delta t \gtrsim \hbar$. The Feynman diagram describing this phenomenon is illustrated in Figure 2.1c. This effect contributes to the electron mass-energy (this explains its name) due to the interaction between the electron and its own electromagnetic field, thereby also modifying the electronic structure of atoms. The electron self-energy can be computed in the framework of the QED renormalization (see Greiner & Reinhardt 2002).

2.1.4   The GRASP2K and RATIP computational codes

GRASP2K

The GRASP2K (*General purpose Relativistic Atomic Structure Program 2000*, Jönsson *et al.* 2013) program is used to obtain the spin-orbital wavefunctions of an atomic system using the MCDF method, as described above. It consists of several modules that we present in this section.

After having entered all the information about the nucleus of the element that we aim to model in the ISO module, the RCSL program is used to generate the list of the CSFs that we want to explicitly include in our configuration interaction model. In order to do this, the list of (relativistic) orbitals and configurations that we want to incorporate in the multiconfiguration expansion can be introduced by considering multiple electron excitations from reference configurations to a given set of active orbitals (this is known as the active space (AS) method).

Then, the MCP module can compute all the angular coefficients involved in the expression of the Hamiltonian matrix elements (2.22) and (2.27), by using the expression given in Grant (2007) in the case of the CSFs found in the list generated

at the previous step.

The initial spin-orbital radial parts (that aim to be used as initial functions in the iterative process of the SCF method) can then be obtained thanks to the ERWF module. Diverse types of orbitals can be chosen, namely: screened hydrogenoid type orbitals, orbitals generated in a Thomas-Fermi potential (free electrons confined in a box), or orbitals coming from a previous calculation.

Finally, the RSCF program is used to obtain the optimized spin-orbitals. In order to compute them, the SCF method is used to iteratively solve the coupled integro-differential MCDF equations (2.34) by using either the (E)OL or the (E)AL options. In this purpose, the RSCF code first computes the interaction radial integrals (2.16) and (2.17) along with all the terms appearing in the MCDF equations using the initial radial parts generated by the ERWF module in order to obtain new ones. This step is then carried out again and again in an iterative process until the spin-orbital radials parts have converged. The program stops when a certain criterion of convergence is satisfied, namely when the biggest relative variation of the spin-orbital radial part value calculated on each integration grid point between two successive steps is lower than a threshold value (10^{-8} by default). Once the convergence is obtained, the spin-orbitals are built by means of the optimized radial parts and by using their expression (2.5), and the CSFs are thus given by Slater determinants built with those optimized spin-orbitals. The Hamiltonian matrix in the chosen CSF basis is then constructed element by element by using the expression of its diagonal (2.22) and off-diagonal (2.27) elements for being diagonalized in the RCI program in order to obtain the atomic energy levels and mixing coefficients for each ASF, that are respectively eigenvalues and eigenvectors of the Hamiltonian matrix (see 2.44). This allows to completely determine the expression of the wavefunction for each ASF, through its multiconfiguration development. The QED corrections described in Section 2.1.3 are finally added perturbatively to the Hamiltonian in order to obtain the corrected energy levels and mixing coefficients after diagonalization.

RATIP

The RATIP (*Relativistic Atomic Transition and Ionization Properties*) program has been developed by Fritzsche (2001, 2002) to compute the atomic structure and properties of atoms (and ions). It can be considered as an extension of the GRASP2K (or GRASP92, which was the previous version of GRASP2K) as it uses the spin-orbitals computed beforehand with the latter. RATIP is also built as a suite of programs, just as GRASP2K.

The RELCI code uses the GRASP2K spin-orbitals to build the Hamiltonian matrix in the chosen CSF basis (taking into account the QED effects described in Section 2.1.3) and then to diagonalize it in order to obtain the energy levels

of the atomic system and the mixing coefficients of each ASF, which completely determines each ASF of the atomic system.

The EINSTEIN program aims to compute the radiative parameters associated with the modeled atomic system. It can compute the radiative wavelengths and transition rates (Einstein coefficients). The REOS module is an alternative version of EINSTEIN where relaxed spin-orbitals can be used, namely orbitals that are different for the initial and the final states.

Many other modules exist in RATIP, but let us highlight two other ones that are used in this work, namely the AUGER and PHOTO modules, which are used to respectively compute the Auger rates and photoionization cross sections for given channels. Those processes will be described in more details in Section 2.3. It is also worth mentioning that the RATIP program has recently been modified to take into account some new effects that will be described in details in Chapter 3.

2.2 AUTOSTRUCTURE method

AUTOSTRUCTURE (AST) is an extension by Badnell (1997, 2011) of the atomic structure program SUPERSTRUCTURE (Eissner *et al.* 1974). As it is used in this work for comparison purpose, a brief description of the fundamental principles of this method is given in this section.

AST is a multiconfiguration method designed for computing the fine-structure level energies, the radiative and Auger rates of an ion based on a Breit-Pauli relativistic Hamiltonian. The latter is given by

$$H_{\mathrm{bp}} = H_{\mathrm{nr}} + H_{\mathrm{1b}} + H_{\mathrm{2b}} \tag{2.46}$$

for an $N-$electron system, where H_{nr} is the usual non-relativistic Hamiltonian, and H_{1b} and H_{2b} are respectively the one-body and two-body operators. The one-body corrections, given by

$$H_{\mathrm{1b}} = \sum_{i=1}^{N} f_i(\mathrm{mass}) + f_i(\mathrm{d}) + f_i(\mathrm{so}), \tag{2.47}$$

describe the non-fine structure mass-variation, $f_i(\mathrm{mass})$, the one-body Darwin correction, $f_i(\mathrm{d})$ and the spin-orbit interaction, $f_i(\mathrm{so})$. The two-body corrections, usually referred to as the Breit interaction, include fine-structure terms (spin-other orbit and mutual spin-orbit interaction, $g_{ij}(\mathrm{so})$, and spin-spin interaction, $g_{ij}(\mathrm{ss})$) and non-fine structure terms (spin-spin contact interaction, $g_{ij}(\mathrm{css})$, Darwin cor-

rection, $g_{ij}(d)$, and orbit-orbit interaction, $g_{ij}(oo)$):

$$H_{2b} = \sum_{i>j}^{N} g_{ij}(so) + g_{ij}(ss) + g_{ij}(css) + g_{ij}(d) + g_{ij}(oo). \qquad (2.48)$$

The expressions of these one- and two-body corrections are given by Eissner *et al.* (1974):

$$f_i(\text{mass}) = -\frac{1}{4}\alpha^2 \nabla_i^4, \qquad (2.49)$$

$$f_i(d) = -\frac{1}{4}Z\alpha^2 \nabla_i^2 \frac{1}{r_i}, \qquad (2.50)$$

$$f_i(so) = -\frac{Z\alpha^2}{r_i^3}\vec{l_i} \cdot \vec{s_i}, \qquad (2.51)$$

$$g_{ij}(so) = -\alpha^2 \left[\left(\frac{\vec{r}_{ij}}{r_{ij}^3} \times \vec{p_i} \right) \cdot (\vec{s_i} + 2\vec{s_j}) + \left(\frac{\vec{r}_{ij}}{r_{ij}^3} \times \vec{p_j} \right) \cdot (\vec{s_j} + 2\vec{s_i}) \right] (2.52)$$

$$g_{ij}(ss) = 2\alpha^2 \left[\frac{\vec{s_i} \cdot \vec{s_j}}{r_{ij}^3} - 3\frac{(\vec{s_i} \cdot \vec{r}_{ij})(\vec{s_j} \cdot \vec{r}_{ij})}{r_{ij}^5} \right], \qquad (2.53)$$

$$g_{ij}(css) = -\frac{16\pi}{3}\alpha^2 \vec{s_i} \cdot \vec{s_j}\, \delta^3(\vec{r}_{ij}), \qquad (2.54)$$

$$g_{ij}(d) = \frac{1}{2}\alpha^2 \nabla_i^2 \left(\frac{1}{r_{ij}} \right), \qquad (2.55)$$

$$g_{ij}(oo) = -\frac{\alpha^2}{r_{ij}} \left(\vec{p_i} \cdot \vec{p_j} + \frac{\vec{r}_{ij} \cdot (\vec{r}_{ij} \cdot \vec{p_j})\vec{p_i}}{r_{ij}^3} \right), \qquad (2.56)$$

where α is the fine-structure constant, Z is the atomic number, $\vec{r}_{ij} = \vec{r_i} - \vec{r_j}$ and $r_{ij} = |\vec{r}_{ij}|$. Let us note that, in AST, the one- and two-body operators have been fully implemented up to order $\alpha^2 Z^4$.

Since AST is a multiconfiguration method, the LS atomic wavefunctions are represented as

$$\Psi(LS) = \sum_i c_i \Phi_i, \qquad (2.57)$$

where the basis functions Φ_i are antisymmetrized products of orthonormal non-relativistic orbitals,

$$\phi_{nlm}(r,\theta,\phi) = \frac{1}{r}P_{nl}(r)Y_{lm}(\theta,\phi)\sigma(1/2,\chi), \qquad (2.58)$$

where $P_{nl}(r)$ is the radial part of the mono-electronic orbital, $Y_{lm}(\theta,\phi)$ the spherical harmonics and $\sigma(1/2,\chi)$ a spin basis function that depends on the spin coordinate

39

χ. The radial orbitals $P_{nl}(r)$ are solutions of the homogeneous radial equation

$$\left[\frac{\mathrm{d}^2}{\mathrm{d}r^2} - \frac{l(l+1)}{r^2} + V^{\mathrm{TFDA}}(r) + \epsilon_{nl} \right] P_{nl}(r) = 0, \qquad (2.59)$$

with the appropriate boundary conditions, and where

$$V^{\mathrm{TFDA}}(r) = -\frac{2Z_{\mathrm{eff}}^{\mathrm{TFDA}}(\lambda_{nl}r)}{r} \qquad (2.60)$$

is the scaled statistical Thomas-Fermi-Dirac-Amaldi (TFDA) model potential (Eissner & Nussbaumer 1969), λ_{nl} is the scaling parameter corresponding to the $P_{nl}(r)$ radial orbital, and $Z_{\mathrm{eff}}^{\mathrm{TFDA}}$ is the TFDA effective charge that has to obey to the boundary conditions

$$\lim_{r \to 0} Z_{\mathrm{eff}}^{\mathrm{TFDA}}(\lambda_{nl}r) = Z, \qquad (2.61)$$

$$\lim_{r \to \infty} Z_{\mathrm{eff}}^{\mathrm{TFDA}}(\lambda_{nl}r) = Z - N + 1, \qquad (2.62)$$

and which expresses the screening degree of the nuclear charge by the statistical gas formed by the $(N-1)$ other bound electrons of the atomic system.

The intermediate coupling (IC) atomic state functions are in turn obtained by diagonalizing the Breit-Pauli Hamiltonian (2.46), so that the relativistic fine-structure levels and rates can be computed.

2.3   Computation of atomic parameters

Once the electronic structure of an atom is modeled (either by using the MCDF or the AST method), the parameters related to diverse atomic processes can be computed. A few definitions, theoretical concepts and approximations used to calculate the atomic parameters for the processes considered in this work are given in the following sections.

2.3.1   Radiative parameters

An atom in an excited state can de-excite itself by emitting a photon whose energy is characteristic of the atomic transition and given by the difference between the energy of the upper (excited) level, E_b, and the energy of the lower one, E_a: $\Delta E_{ab} = E_b - E_a$. The radiation is often characterized by its radiative wavelength that is given by

$$\lambda_{ab} = \frac{hc}{\Delta E_{ab}}, \qquad (2.63)$$

where h is the Planck constant and c the light velocity in the vacuum. λ_{ab} is in general given in nanometers (nm) or in Ångströms (Å).

Another feature of a radiation is the radiative transition probability, which expresses the spontaneous radiative emission rate of a photon by the atom by unit of time for a given transition (radiative de-excitation). In a non-relativistic approach (such as AST), the spontaneous radiative emission probability (or transition probability) for an electric dipole transition (E1) from an upper level b to a lower level a is given by Cowan (1981), in unit of s^{-1}, as

$$A_{ab} = \frac{64\pi^2 e^2 a_0^2 \sigma_{ab}^3}{3h} \sum_q \left| \langle a | P_q^1 | b \rangle \right|^2, \tag{2.64}$$

where σ_{ab} is the wavenumber of the transition (*i.e.* the inverse of the transition wavelength) and where

$$P_q^1 = \sum_i^N r_i C_q^1(\theta_i, \varphi_i) \tag{2.65}$$

is the (q^{th} component of the) classical dipole moment of the atom, in which the C_q^1 factors are proportional to the spherical harmonic Y_q^1 such as

$$C_q^1(\theta, \varphi) = \sqrt{\frac{4\pi}{3}} Y_q^1(\theta, \varphi). \tag{2.66}$$

In a fully-relativistic approach (such as the MCDF method), the radiative transition probabilities relative to a given transition can be derived from the relativistic line strengths, that is the matrix elements of an electromagnetic transition operator (given by a multipole development) between the ASFs corresponding to the two atomic states involved in the transition. The expression of the relativistic transition probability for a given transition from a upper level b to a lower level a is given by Grant (1974, 2007) as:

$$A_{ab} = 2\alpha\omega \frac{2j_a + 1}{2K + 1} \begin{pmatrix} j_b & K & j_a \\ \frac{1}{2} & 0 & -\frac{1}{2} \end{pmatrix}^2 |M_{ab}|^2, \tag{2.67}$$

where α is the fine-structure constant, ω is the angular frequency associated with the transition ($\hbar\omega = E_b - E_a$ is the energy of the photon spontaneously emitted during the transition), K is the electric or magnetic multipole order of the transition (*e.g.* $K = 1$ for an allowed transition, *i.e.* an electric dipole transition E1). The symbol into bracket is a 3-j Wigner symbol, linked to Clebsh-Gordan coefficients by the relation

$$\begin{pmatrix} j_1 & j_2 & j_3 \\ m_1 & m_2 & m_3 \end{pmatrix} = \frac{(-1)^{j_1 - j_2 - m_3}}{\sqrt{2j_3 + 1}} \left(j_1 \, m_1 \, j_2 \, m_2 \, | \, j_3 \, (-m_3) \right). \tag{2.68}$$

In Equation (2.67), M_{ab} is a function of ω that depends on the electric or magnetic feature of the transition along with the chosen gauge. For practical reasons (related to the computation of the transition operator between two atomic states), in atomic physics, it is usual to choose different gauges with respect to the well-known Lorentz gauge for the potential quadrivector. The Babushkin or Coulomb gauges are frequently used. Actually, in one hand, in the framework of the non-relativistic quantum mechanics theory, the transition operator between the initial and the final states can be expressed either in the position representation (named "length gauge") or in the momentum representation ("velocity gauge"); and at the non-relativistic limit, the relativistic transition operator represented in the Babushkin gauge comes down to the non-relativistic transition operator represented in the length gauge. In an analogous way, the relativistic transition operator expressed in the Coulomb gauge comes down to the transition operator in the length gauge at the non-relativistic limit. In another hand, the transition probabilities are usually computed in both the Babushkin and Coulomb gauges, so that the results obtained in both cases can be compared : the gauge invariance of the electromagnetic theory guarantees that the results expressed in both gauges must theoretically be the same. Thereby, a good agreement between the numerical results obtained in both gauges is (among others) a useful criterion to evaluate the reliability of the transition rates.

In the case of electric multipolar transitions, M_{ab} depends linearly of the gauge parameter, noted G, which is null in the Coulomb gauge and is equal to $[(K + 1)/K]^{1/2}$ in the Babushkin gauge. Its expression is given by Grant (2007) as

$$M_{ab}(\omega, G) = M_{ab}(\omega, 0) + G\tilde{M}_{ab}(\omega), \tag{2.69}$$

where

$$
\begin{aligned}
M_{ab}(\omega, 0) = -i^k \Bigg\{ & \left(\frac{K}{K+1}\right)^{1/2} \left[(\kappa_a - \kappa_b)I^+_{K+1} + (K+1)I^-_{K+1}\right] \\
& - \left(\frac{K+1}{K}\right)^{1/2} \left[(\kappa_a - \kappa_b)I^+_{K-1} + KI^-_{K-1}\right] \Bigg\},
\end{aligned}
\tag{2.70}
$$

and

$$
\begin{aligned}
\tilde{M}_{ab}(\omega) = -i^k \Big\{ & (\kappa_a - \kappa_b)I^+_{K+1} + (K+1)I^-_{K+1} \\
& + (\kappa_a - \kappa_b)I^+_{K-1} + KI^-_{K-1} - (2K+1)J_K \Big\},
\end{aligned}
\tag{2.71}
$$

with the integrals $I^\pm_K$ and J_K that are defined as

$$I^\pm_K = \int_0^\infty \left[P_a^*(r)Q_b(r) \pm Q_a^*(r)P_b(r)\right] j_K(\omega r/c)\,\mathrm{d}r, \tag{2.72}$$

$$J_K = \int_0^\infty [P_a^*(r)P_b(r) + Q_a^*(r)Q_b(r)] \, j_K(\omega r/c) \, \mathrm{d}r, \qquad (2.73)$$

where $P(r)$ and $Q(r)$ are respectively the great and the small components of the spin-orbital radial parts (*c.f.* section 2.1.1) and where $j_K(\omega r/c)$ is a spherical Bessel function.

2.3.2 Continuum processes : the distorted wave approximation

An atom in a highly-excited state can also de-excite itself by autoionization through the Auger process[1] (phenomenon in which an electron is spontaneously emitted in the continuum by carrying the excess of energy) or can be photoionized by emitting an electron after having absorbed a photon (that has an energy greater than the electron binding energy). In both cases, these processes involve an electron from the continuum. In both approaches described in this chapter (MCDF and AST), continuum (spin-)orbitals are modeled using the distorted-wave (DW) approximation[2]. The latter consists in not including the coupling among channels: only the initial and final channels are considered in the continuum problem. The DW approximation is thus valid when the coupling among channels other than the initial and the final states is weak. For instance, in highly-charged ions, the Coulomb central potential dominates the electron-electron interaction, thus the coupling among all the channels is weak and DW may be valid. As a result, resonance effects (which arise due to the coupling among channels) are not considered in the DW approximation, but they can be added perturbatively in diverse ways.

In the DW approximation, the scattering state $|\psi_t\rangle = |\psi(P_t J_t M_t)\rangle$ that represents the $(N+1)$-electron system composed of the final N-electron ion in the bound state $|\psi_f\rangle = |\psi(P_f J_f M_f)\rangle$ and of the outgoing continuum electron of energy ϵ and angular momentum κ is thus described as

$$|\psi(P_t J_t M_t)\rangle = |\psi(P_f J_f M_f)\rangle \, |\phi(\epsilon \kappa)\rangle . \qquad (2.74)$$

The radial parts $P_\kappa(r)$ and $Q_\kappa(r)$ of the continuum electron relativistic orbital $|\phi(\epsilon \kappa)\rangle$ are obtained within the frozen core approximation by solving the following

---

[1]This process can occur if the atom is in a highly-excited state lying above its ionization potential on a so-called "autoionization state".

[2]Let us however note that, as those processes have only been modeled by using the MCDF/RATIP method in this work, they are only described in the relativistic framework in the next paragraphs.

MCDF equations (Grant 2007):

$$\begin{cases} \left(\dfrac{\mathrm{d}}{\mathrm{d}r} + \dfrac{\kappa}{r}\right) P_\kappa(r) = \left[2c + \dfrac{1}{c}(\epsilon - V_{\mathrm{fc}}(r))\right] Q_\kappa(r) + X_Q(r) \\[2ex] \left(\dfrac{\mathrm{d}}{\mathrm{d}r} - \dfrac{\kappa}{r}\right) Q_\kappa(r) = -\dfrac{1}{c}(\epsilon - V_{\mathrm{fc}}(r)) P_\kappa(r) - X_P(r) \end{cases}, \qquad (2.75)$$

where the frozen core direct potential $V_{\mathrm{fc}}(r)$ and exchange potentials $X_P(r)$ and $X_Q(r)$ of the final ionic bound state $|\psi_f\rangle$ are constructed as in Section 2.1.2 (see Equation (2.36) and Equation (2.39)).

Auger process (autoionization)

An inner-shell excited bound state of an atom/ion can experience an autoionization (spontaneous emission of an Auger electron) if the initial level is a resonant state that is energetically embedded into the continuum of the next higher charge state. The electron emission from such a state then arises from the coupling to one or several scattering states. The Auger transition amplitude for the autoionization of an excited bound state $|\psi_i(P_i J_i M_i)\rangle$ having a total angular momentum J_i with a projection M_i and a parity P_i into the final scattering state $|\psi_t\rangle = |\psi(P_t J_t M_t)\rangle$, arising from the coupling of the bound state $|\psi_f\rangle = |\psi(P_f J_f M_f)\rangle$ of the final ion with the partial wave of the outgoing electron of energy ϵ and angular momentum κ (defined as 2.8), is given by Fritzsche (2012) as

$$V_{J_f l j J_t} = \langle (\psi_f, \epsilon\kappa) P_t J_t \, ||V|| \, \psi_i(P_i J_i) \rangle \, \delta_{J_i J_t} \delta_{M_i M_t} \delta_{P_i P_t}, \qquad (2.76)$$

by assuming to have a common set of orthonormal orbitals for both the initial $|\psi_i\rangle$ and final $|\psi_f\rangle$ bound states. In this case, the transition operator V simplifies to the electron-electron interaction operator, namely $V = V^{\mathrm{Coulomb}} + V^{\mathrm{Breit}}$ within the framework of the Dirac-Coulomb-Breit Hamiltonian (see Fritzsche 2012).

Photoionization

For a given channel, the photoionization cross section of an initial bound state $|\psi_i(P_i J_i)\rangle$ with N electrons into some final state $|\psi_f(P_f J_f)\rangle$ of the $(N-1)$-electron system is proportional to the squared transition amplitude. The photoionization E1 transition amplitude for such a process into some final scattering state $|\psi_t\rangle = |\psi(P_t J_t)\rangle$ is described thanks to the *bound-free* transition amplitude that is given by Fritzsche (2012) as

$$M^{\mathrm{E1}}_{J_i \to J_f l j J_t} = i^{-l} e^{-i\Delta_k} \left\langle (\psi_f, \epsilon\kappa) P_t J_t \left|\left| \sum_i \vec{\alpha}_i \cdot \vec{A}^{\mathrm{E1}}_i(\vec{k}) \right|\right| \psi_i(P_i J_i) \right\rangle, \qquad (2.77)$$

44

where $\vec{\alpha}_i$ denotes the vector of the Dirac matrices, $\vec{A}_i^{\mathrm{E1}}(\vec{k})$ is the vector potential of the E1 radiation that interacts with the atomic system, ϵ and κ are respectively the energy and the momentum of the outgoing continuum electron and Δ_k is the phase that includes both the Coulomb phase as well as the non-Coulombic phase shift (due to the bound-state potential in which the continuum orbitals are generated). The analytical expression of the photoionization cross section can be found in Grant (2007).

Chapter 3

Consideration of plasma environment effects in the computation of atomic structure and processes

The purpose of this chapter is to present how the plasma environment in which an ion is embedded can modify its electronic structure and atomic processes. In this context, different models that aim to include these effects in the atomic structure modeling are presented. In particular, the way in which the RATIP program (described in Section 2.1.4) has been modified to take into account the effects of the plasma environment is explained in this chapter.

3.1 Plasma screening effect

As a reminder, a plasma is a (partially or completely) ionized gas. It thus consists of charged particles (positive ions and electrons, with possibly a few remaining neutral atoms) that interact amongst themselves through the Coulomb force. The matter in such a plasma state is torn between two opposite trends : the disorder due to the thermal agitation and the organization due to the collective aspect of the Coulomb interaction. When the first trend is the dominant one, the plasma rather tends to behave as a gas, whereas when the other trend dominates, the plasma rather has liquid aspects. The compromise between these two opposite trends can be somewhat quantified thanks to a non-dimensional parameter called the "plasma coupling parameter", that is defined as the ratio between the mean electrostatic potential energy between two particles to the plasma mean kinetic energy (which expresses the thermal agitation within the plasma). An expression

of this coupling parameter is given by Saha & Fritzsche (2007) as

$$\Gamma_{ab} = \frac{Z_a Z_b}{k_B T d_{ab}}, \tag{3.1}$$

where Z_a (Z_b) is the charge of the ionic species a (b), k_B is the Boltzmann constant and d_{ab} is the mean distance between the two particles, which depends on the plasma density. In the case of an astrophysical plasma (case considered in this work), which is mainly composed of hydrogen, the global mean charge of the plasma is very close to unity ($Z \approx 1$), so that the coupling parameter can be approximated by

$$\Gamma_{ab} = \frac{1}{k_B T d_{ab}}. \tag{3.2}$$

Such a coupling parameter can also be defined to estimate the coupling between the plasma electrons: its expression is thus the same as the one given in (3.2).

In the case of a plasma for which the coupling parameter is lower than unity ($\Gamma < 1$), this plasma is said to be a lowly-coupled plasma (in which the thermal agitation is the dominant trend). Conversely, if $\Gamma > 1$, the collective aspect due to the Coulomb interaction is dominant and thus the plasma is said to be strongly coupled. Although a plasma is a group of electrically-charged particles, the competition between the thermal agitation and the collective Coulomb interactions allows the plasma to remain ionized while being neutral on the whole, given the creation of conditions that are opposed to the charge separation within it. The latter gives rise to one of the most important features of a plasma: the screening effect, *i.e.* the local decreasing of the electrical fields within the plasma. Actually, the charge of an ion embedded within the plasma can be screened by the other surrounding particles (mainly the electrons) of the plasma. Thereby, the ion effective charge is lower than its real one, reducing incidentally the electrical field produced by the ion.

Obviously, the plasma screening effect can modify the atomic structure of the ions embedded in the plasma and can thus also affect the various atomic processes that occur within it. In fact, the changes in the ion effective nuclear charge due to the screening can modify the electronic structure and thus the associated atomic process rates. The electrostatic interactions that bound the electrons to the nucleus of an ion can be screened by an electron (or several ones) located in the close vicinity of this ion (or even within its own atomic structure), which can reduce the binding energy of the bound electrons. Thereby, the energy levels of an ion embedded in a plasma can be shifted due to the screening effect (Rogers *et al.* 1970). As a consequence, the transition energies of the lines emitted by an ion within a plasma can also be shifted. The wavefunctions of two nearby ions can also overlay and thus disturb each other if the ions are close enough, which can

give rise to the so-called pressure ionization effect (Nantel *et al.* 1998), that is the truncation of the highest excited states (which limits the amount of bound states and, by the way, the amount of energy levels). This is due to the fact that a (highly-excited) level cannot physically belong to both the nearby ions at the same time, so it cannot be a bound state of an ion while it is included in the volume of the other one. The combination of the screening effect (that shifts the energy levels) and of the pressure ionization phenomenon leads to the so-called continuum lowering, namely the decrease of the number of bound states due to the truncation of the states with high principal quantum numbers n (*i.e.* the most excited states). For example, Bautista *et al.* (1998) showed that only the states with $n \leq 30$ should be bound for a plasma composed of iron with a temperature of 10^6 K and a density of 10^{20} cm^{-3}. Such a truncation of the highest excited states may modify the ionization balance of the plasma (which determines the presence and absence of the diverse ionization stages of a given ionic species depending on the physical conditions of the medium) since the amount of levels to be summed in order to obtain the partition function would be limited. Moreover, it is obvious that the highest the density of the plasma is, the most important the above-mentioned effects are.

3.2 Modeling of the plasma screening effect

In this section, we present different models of plasma screening and the way in which this effect can be taken into account to model the electronic structure of an atom or ion. In particular, we describe how this effect has been included in the MCDF method as implemented in the RATIP code.

3.2.1 Screening effect modeling in the MCDF method

Plasma screening effects can be perturbatively introduced in the MCDF modeling of an atomic structure by modifying the Hamiltonian of the system during the configuration interaction (CI) process in which the Hamiltonian is diagonalized as described in Section 2.1.2. The screening of the electron–nucleus interaction can be taken into account by replacing the nuclear potential (electron–nucleus interaction potential), $V_{\text{nucl}}(r)$, which appears in the monoelectronic Dirac Hamiltonian (2.3) by a potential that takes the screening of the nuclear charge into account (Saha & Fritzsche 2006, 2007), that is

$$h_D^{\text{plasma}} = c\vec{\alpha}.\vec{p} + (\beta - 1)c^2 + V_{\text{n-e}}^{\text{plasma}}(r, \gamma), \tag{3.3}$$

where $V_{\text{n-e}}^{\text{plasma}}(r, \gamma)$ represents the modified nuclear potential that takes into account the screening of the electron–nucleus interaction by the plasma electrons,

and where γ contains all the useful information to describe the plasma screening depending on the model and on the physical conditions within the plasma. Different potential models that consider plasma screening effects are presented in the following sections. Obviously, in that case, the total Hamiltonian of the system, namely the Dirac-Coulomb Hamiltonian (2.11), is consequently modified and reads as

$$H_{DC}^{\text{plasma}} = \sum_{i=1}^{N} h_D^{\text{plasma}}(r_i, \gamma) + \sum_{i>j} \frac{1}{r_{ij}}. \qquad (3.4)$$

The screening of the electron–electron interaction can also be modeled, either completely or partially depending on the screening model. Actually, according to the model, this effect can already be taken into account in the electron–nucleus screened potential $V_{\text{n-e}}^{\text{plasma}}(r, \gamma)$ that appears in Equation (3.3). Otherwise, it is possible to explicitly introduce the screening of the electron–electron interaction by changing the $1/r_{ij}$ terms that describe the Coulomb interaction between every electron pair in (3.4) and replace them with a screened potential for the electron–electron interaction, $V_{\text{e-e}}^{\text{plasma}}(r, \gamma)$, similarly to the electron–nucleus screening case (Saha & Fritzsche 2006). Thereby, Equation (3.4) would read as

$$H_{DC}^{\text{plasma}} = \sum_{i=1}^{N} h_D^{\text{plasma}}(r_i, \gamma) + \sum_{i>j} V_{\text{e-e}}^{\text{plasma}}(r_{ij}, \gamma). \qquad (3.5)$$

3.2.2 Debye-Hückel potential model

A first model of screened potential is the Debye-Hückel (DH) one. It has been proposed by these two scientists in order to explain why electrolyte behavior diverts from the ideal solution one in chemistry (Debye & Hückel 1923). This potential model is also suitable to describe the plasma screening effects (*e.g.*, Saha & Fritzsche 2006) as it consists in modeling the screening of the electrical fields produced by electrical charges in interaction. In this section, we develop the way and give the approximations in which this potential can be obtained. The following reasoning is made for the screening of the electron–nucleus interaction by the plasma electrons for a given bound electron of an ion. The development would be pretty much the same for the electron–electron interaction screening (provided one would consider that $Z = 1$ thereafter).

Let us consider a point-like electrical charge Z within a plasma, which is located at the origin of a spherical coordinate system. This charge actually models the nuclear charge of an ion embedded in the plasma. The (static) Debye-Hückel model consists in describing how the electrostatic potential $\phi(r)$ produced by this charge is modified due to the screening by the surrounding electrons of the plasma for a weakly-coupled plasma, that is for a plasma with $\Gamma \ll 1$. Within this limit, the

electrostatic interaction energy between this charge and a plasma electron is much weaker than the mean kinetic energy of the plasma electrons, *i.e.* $\phi(r) \ll k_b T_e$. In this case, the correlation effects can thus be treated as perturbations and the potential can be expressed in the first order of $\phi(r)/(k_b T_e)$. Also, under such physical conditions, we can consider that the particles obey a classic Maxwell-Boltzmann statistic distribution since the electronic temperature is much larger than the Fermi temperature of the system. Thereby, the distribution (per unit of volume) of plasma electrons that disturb the electrical field produced by the central point-like charge Z, that is the electronic density at a distance r from the origin of coordinates, $n_e(r)$, is given, at the first order, by

$$n_e(r) = n_{e0} \exp\left(\frac{\phi(r)}{k_B T_e}\right) \approx n_{e0}\left(1 + \frac{\phi(r)}{k_B T_e}\right), \tag{3.6}$$

where n_{e0} is the plasma mean electronic density[1]. A solution for the electrostatic potential $\phi(r)$ can be obtained by solving the Poisson equation

$$\Delta\phi(r) = -4\pi\left[Z\delta(r) - n_e(r)\right]. \tag{3.7}$$

By assuming that $\phi(r)$ presents a spherical symmetry, a solution of the Poisson equation (3.7) for $\phi(r)$ can easily be found (see Piel 2010) and has the form

$$\phi(r) = \frac{Z}{r}\,e^{-r/\lambda_D}, \tag{3.8}$$

where the parameter

$$\lambda_D = \sqrt{\frac{k_B T_e}{4\pi n_{e0}}}, \tag{3.9}$$

which has the dimension of a length, is named the Debye length. The latter represents the distance scale from which the plasma electrons screen efficiently the electrical field produced by the point-like charge Z. Actually, compared to the Coulomb potential $\phi_{\text{Coul}} = Z/r$, the Debye-Hückel screened potential $\phi(r)$ produced by the nuclear charge Z exponentially decreases with the distance from the latter (see Figure 3.1), so that it significantly differs from the Coulomb one for $r > \lambda_D$. Thereby, beyond this distance λ_D, the potential generated by the point-like charge is screened by the plasma electrons. The Debye length obviously depends on the physical conditions within the plasma, namely the temperature and the density. As a result, and logically, the higher the plasma electronic density is, the bigger the number of plasma electrons in the same volume is, and thus the smaller the Debye length is, which means that the more the electrical field

---

[1]Mathematically, $n_{e0} = \lim\limits_{r \to \infty} n_e(r)$ since $\lim\limits_{r \to \infty} \phi(r) = 0$. n_{e0} thus coincides with the plasma mean density.
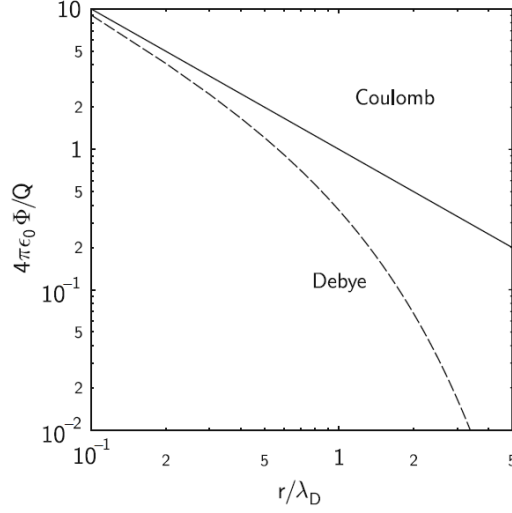
Figure 3.1: Comparison between the Coulomb potential and the screened Debye-Hückel potential produced by a point-like charge Q at the origin of the system coordinates (Piel 2010). Let us remark the use of the international unit system that explains the $4\pi\epsilon_0$ factor, which is equal to 1 in the atomic unit system that is used in this work.

produced by the charge Z is screened. One can also define the plasma screening parameter μ as the inverse of the Debye length λ_D, that is

$$\mu = \frac{1}{\lambda_D} = \sqrt{\frac{4\pi n_e}{k_B T_e}}. \tag{3.10}$$

As mentioned before, the same kind of reasoning can be applied in order to model the electron–electron interaction screening. Therefore, the (static) Debye-Hückel interaction potential of an atomic system embedded in a plasma is obtained by summing the screened potential for both the electron–nucleus and the electron–electron interactions:

$$
\begin{aligned}
V^{\mathrm{DH}}(r,\mu) &= -\sum_{i=1}^{N} \frac{Z\, e^{-\mu r_i}}{r_i} + \sum_{i>j}^{N} \frac{e^{-\mu r_{ij}}}{r_{ij}} \\
&= \sum_{i=1}^{N} V_{\mathrm{n\text{-}e}}^{\mathrm{DH}}(r_i,\mu) + \sum_{i>j}^{N} V_{\mathrm{e\text{-}e}}^{\mathrm{DH}}(r_{ij},\mu),
\end{aligned}
\tag{3.11}
$$

where N is the number of bound electrons, r_i is the distance of the ith electron with respect to the nucleus and $r_{ij} = |r_i - r_j|$ is the distance separating the

i^{th} and the jth electrons. Thereby, the plasma screening effects in many-particle computations result from the net effect in screening the electron–nucleus and the electron–electron interactions: while the first one usually destabilizes the electron binding, the second one tends to counteracts this trend (Saha & Fritzsche 2006).

The Debye-Hückel potential has been widely used in order to study the plasma screening effects on certain atomic properties, in a non-relativistic context, for hydrogenoid ions (Iafrate & Mendelsohn 1969, Saha *et al.* 2002), He-like ions (Kar & Ho 2004) and electrons with a few bound electrons (Gupta & Rajagopal 1981). It has also been used in a relativistic framework by Saha & Fritzsche (2006) to study the spectral properties involving valence electrons in Be-like ions, by using the method we describe in the next paragraph.

Such a Debye-Hückel screening potential can be pertubatively introduced within the MCDF method described in chapter 2 in order to take into account the plasma effects. Basically, a Debye-Hückel potential has to be considered instead of a Coulomb one in the configuration interaction process. As explained in section 3.2.1, theoretically, the generic screened potentials $V_{\text{n-e}}^{\text{plasma}}(r_i, \gamma)$ and $V_{\text{e-e}}^{\text{plasma}}(r_{ij}, \gamma)$ appearing in (3.3) and (3.5) have to be replaced by the respective Debye-Hückel potentials for the electron–nucleus and electron–electron interactions, *i.e.* $V_{\text{n-e}}^{\text{DH}}(r_i, \mu)$ and $V_{\text{e-e}}^{\text{DH}}(r_{ij}, \mu)$, respectively, where the screening parameter μ contains all the information about the physical conditions within the plasma. In this case, as described by Saha & Fritzsche (2006) the modified Dirac-Coulomb Hamiltonian that considers plasma screening effects within the Debye-Hückel model is given by

$$H_{DC}^{\text{DH}} = \sum_{i=1}^{N} h_D^{\text{DH}}(r_i, \mu) + \sum_{i>j} V_{\text{e-e}}^{\text{DH}}(r_{ij}, \mu), \qquad (3.12)$$

where the modified monoelectronic Dirac Hamiltonian reads as

$$h_D^{\text{DH}} = c\vec{\alpha}.\vec{p} + (\beta - 1)c^2 + V_{\text{n-e}}^{\text{DH}}(r_i, \mu). \qquad (3.13)$$

Numerically, the DH potential for the electron–nucleus screening is quite easy to implement, as it is a radial potential, just as the Coulomb one. However, the DH potential for the electron–electron screening in many-particle computations is much more complicated to implement, as angular terms are involved. Saha & Fritzsche (2006) described how this angular part of the DH screening can be evaluated in the way it is actually implemented in the modified RATIP code (Fritzsche 2012, see Section 3.2.4) that perturbatively takes into account the plasma screening effects. They showed that the modified two-particle integrals due to plasma screening effects can be derived by rewriting the electron–electron DH potential appearing in equation (3.12) in terms of the larger ($r_> = \max(r_i, r_j)$) and smaller

radii ($r_< = \min(r_i, r_j)$) of the one-particle radii r_i and r_j as

$$V_{\text{e-e}}^{\text{DH}}(r_{ij}, \mu) = -\mu \sum_{l=0}^{\infty} (2l+1) j_l(i\mu r_<) h_l^1(i\mu r_>) P_l(\cos\theta_{ij}), \qquad (3.14)$$

where j_l represents a Bessel function, h_l^1 a Hankel function of the first kind, and $P_l(\cos\theta)$ a Legendre polynomial that depends on the angle θ_{ij} between the two position vectors $\vec{r}_i$ and $\vec{r}_j$. The detailed development can be found in Burke & Joachain (1995).

Let us note that a similar form of potential can be used to model screening effects in a degenerate plasma, namely when the distances between the plasma particles are in the order of magnitude of the de Broglie wavelength (or even smaller). In this case, the Fermi-Dirac statistics have to be used instead of the Maxwell-Boltzmann one in the reasoning described above. Still within the hypothesis of a weakly-coupled plasma (*i.e.* $\Gamma \ll 1$), as in the Debye-Hückel approximation, the plasma electron distribution can be linearized and the same kind of screened potential is thus obtained, except that the characteristic screening length is given by the Thomas-Fermi screening length (instead of the Debye-Hückel one) whose expression is given, within the approximation of low temperatures, by

$$\lambda_{\text{TF}} = \sqrt{\frac{1}{2}\left(\frac{T}{3n_e}\right)^{1/3}}. \qquad (3.15)$$

Such a potential is called a screened Thomas-Fermi potential.

The scaled statistical Thomas-Fermi-Dirac-Amaldi (TFDA) potential used within the multiconfiguration Breit-Pauli method as implemented in AUTOSTRUCTURE (see Section 2.2) can also be modified and screened to take the plasma environment effects into account for an atom embedded in a weakly-coupled plasma. In this case, the TFDA effective charge $Z_{\text{eff}}^{\text{TFDA}}$ appearing in eq. (2.60) has to be screened in the framework of a Debye-Hückel potential model, so that the DH screened TFDA would read as

$$V_{\text{DH}}^{\text{TFDA}}(r) = -\frac{2Z_{\text{eff}}^{\text{TFDA}}(\lambda_{nl}r)e^{-\mu r}}{r}, \qquad (3.16)$$

where μ is the plasma screening length as defined in eq. (3.10), that is the inverse of the Debye length.

3.2.3 Ion-sphere potential model

For a high-density and low-temperature plasma for which the coupling parameter $\Gamma > 1$ (namely for a strongly-coupled plasma), a model based on a screening length (such as the Debye-Hückel or Thomas-Fermi models described in Section 3.2.2) is not valid since the approximation allowing the linearization of the plasma electron distribution does not stand in this case. Without this hypothesis, the Poisson equation for the electrostatic potential does not admit any analytical solution.

However, another type of approach has been proposed by Ichimaru (1982) to model strongly-coupled plasma: the ion-sphere model, that is a lattice-type interaction potential such as applied in solid state physics. In this model, it is assumed that each ion embedded in the plasma is confined in a small sphere (the so-called ion-sphere) of radius R_0 in which the plasma electrons are uniformly distributed. R_0 depends on the plasma electron density n_e since it is determined in such a way that the ionic charge is completely neutralized, *i.e.* so that the combination of the ion bound electrons and the plasma background electrons guarantee together the neutrality of the ion-sphere. In this case, if all the electrons inside the ion-sphere strongly interact with the embedded ion that has N_b bound electrons, it means that there are exactly $N_f = Z - N_b$ uniformly free plasma electrons inside the ion-sphere that has a radius

$$R_0 = \left[\frac{3(Z - N_b)}{4\pi n_e} \right]^{1/3}. \tag{3.17}$$

Within these hypotheses, the electrostatic interaction potential of the ion bound electrons is given by Saha & Fritzsche (2007) as

$$V^{\text{IS}}(r_i, R_0) = \begin{cases} -\dfrac{Z}{r_i} + \dfrac{Z - N_b}{2R_0}\left[3 - \left(\dfrac{r_i}{R_0}\right)^2 \right] & \text{if } r_i < R_0 \\ 0 & \text{if } r_i \geq R_0 \end{cases}, \tag{3.18}$$

where r_i is the distance between the ith electron and the nucleus (assumed point-like and at the center of the coordinate system). This ion-sphere (IS) potential (3.18) is built in such a way that it vanishes at the IS radius ($r = R_0$) and it is reduced to the Coulomb potential in the nucleus vicinity, *i.e.* $\lim_{r \to 0} rV(r, R_0) = Z$. As a consequence, the main default of the IS potential is that those requirements and assumptions make it discontinuous in $r = R_0$.

Moreover, since the ion-sphere is globally neutral (the effective electric field produced by the ion is neutralized outside the IS), the only electrical field experienced by the ion bound electrons is the one that results from the charge within the IS. Thereby, only the electron–electron correlations "within the ion-sphere" are

taken into account in this model, the correlations with the outside electrons are thus not considered.

The first term that appears in the IS potential (3.18) is an electron–nucleus Coulomb interaction term for a hydrogenoid ion. As a result, the IS potential (3.18) should be more suitable to model high-density plasma effects for ions with only a few bound electrons. The second term is a repulsive correction to the Coulomb term due to the interaction of the bound electrons with the plasma electron within the ion-sphere.

The ion-sphere model has been widely used to study dense plasma effects on spectral properties of hydrogenoid ions (*e.g.*, Yan & Ichimaru 1986, Ray 2000, Sil *et al.* 2005) and ions with a few bound electrons such as Be-like ions within a relativistic framework (Saha & Fritzsche 2007). More recently, advanced models based on IS theory have also been used to study high-density plasma effects on ions with a few bound electrons (*e.g.*, Belkhiri & Poirier 2014, Belkhiri *et al.* 2015).

In order to perturbatively model plasma effects within the MCDF method by means of an ion-sphere potential, as explained in Section 3.2.1 and just as for the Debye-Hückel potential model, the Coulomb nuclear potential has to be replaced by the ion-sphere potential in the Dirac monoelectronic Hamiltonian in the CI procedure (Fritzsche & Saha 2007). Thereby, the modified Dirac Hamiltonian would read as

$$h_D^{\mathrm{IS}} = c\vec{\alpha}.\vec{p} + (\beta - 1)c^2 + V^{\mathrm{IS}}(r_i, R_0), \tag{3.19}$$

which would thus modify the Dirac-Coulomb Hamiltonian such as

$$H_{DC}^{\mathrm{IS}} = \sum_{i=1}^{N} h_D^{\mathrm{IS}}(r_i, R_0) + \sum_{i>j} \frac{1}{r_{ij}}. \tag{3.20}$$

Let us remark that, unlike the Debye-Hückel potential model, the electron–electron correlations are here (partially[2]) already taken into account in (3.19). The electron–electron Coulomb repulsion terms in (3.20) thus do not have to be modified in the IS model.

3.2.4 The PLASMA modules of the RATIP and AUTO-STRUCTURE programs

The RATIP program, which has been presented in Section 2.1.4, has been recently developed and improved by Fritzsche (2012) to take the plasma environment effects into account in the computation of atomic structures and properties. In this purpose, the PLASMA module has been implemented. The latter is a modification of the RELCI module, in which plasma effects are modeled in a perturbative way

---

[2]Only inside the ion-sphere.

such as explained in previous sections, by means of a Debye-Hückel or an ion-sphere potential that is perturbatively introduced (in place of the Coulomb potential) in the Hamiltonian, which is still corrected by the QED effects mentioned in Section 2.1.3 such as in RELCI. After diagonalization of the perturbed Hamiltonian (that takes into account plasma screening effects), the corrected mixing coefficients representing the modified atomic structure can be used to compute the various atomic process rates that can be calculated by using the existing modules implemented in RATIP (see Section 2.1.4), such as the radiative and Auger parameters, or the photoionization cross sections. The influence of the screening effects due to the plasma environment on these atomic properties can thus be estimated by the new version of the RATIP program, choosing either a Debye-Hückel or an ion-sphere potential depending on the physical conditions within the plasma.

Let us also note that the AUTOSTRUCTURE program, which is described in Section 2.2, has also recently been adapted to take plasma screening effects into account (Badnell, Bautista and Mendoza, private communication 2017), similarly to the module PLASMA of the RATIP code, by screening the TFDA scaled statistical potential within the famework of a Debye-Hückel model (see Equation 3.16) as explained at the end of Section 3.2.2. This modified AST program is used in this work in the aim of comparing with the results obtained by the MCDF/RATIP method in a few selected cases.

3.3 The Debye-Hückel potential to model accretion disk plasmas: validation of our theoretical method

In Chapter 1, we discussed the physical conditions characterizing the plasma of an accretion disk around a black hole. As a reminder, advanced MHD simulations performed by Schnittman *et al.* (2013) revealed that the temperature within the plasma should range from 10^5 to 10^7 K and that the electron density should be between 10^{18} and 10^{22} cm^{-3} in the K-line emitting regions. For these physical conditions, the plasma coupling parameter Γ given in (3.2) takes the values $0.0003 \leq \Gamma \leq 0.6$. As a consequence, the coupling parameter is (much) lower than unity in most cases (even though it is not so far from it for the most "extreme" values of plasma conditions, namely a temperature of 10^5 K and electron density of 10^{22} cm^{-3}, but still lower than 1). Such a plasma can thus be considered as a weakly-coupled one and, as a consequence, the Debye-Hückel potential discussed in Section 3.2.2 should be suitable to model the effect of such a plasma environment.

Nevertheless, although many papers report that the screening effects can be

appropriately described using the Debye-Hückel model for weakly-coupled plasma (*e.g.*, Murillo & Weisheit 1998, Saha & Fritzsche 2006), one could understandably wonder if this model is still reliable for the most "extreme" physical conditions considered in this work, for which the coupling parameter is close (but still lower) than one, as mentioned above. However, in a very recent paper, Das *et al.* (2016) showed that, for physical conditions in the intermediate region between weakly and strongly coupled plasmas (*i.e.* $\Gamma \approx 1$), both Debye-Hückel and ion-sphere models reasonably agree with each other.

Moreover, in order to test our method using a Debye-Hückel potential for a high-density plasma, we computed the redshift of the Ti He-α line (1s^2 ^{1}S$_0$ - 1s2p ^{1}P$_1$) observed by Khattak *et al.* (2012) and that was theoretically reproduced by Belkhiri *et al.* (2015) using an advanced ion-sphere model with a Fermi-Dirac distribution. Actually, in this experiment, Khattak *et al.* measured a 3.4 ± 1.0 eV redshift of this K line in a plasma characterized by a temperature of 3000 eV and an electron density of 4.2×10^{24} cm^{-3}, which corresponds to a plasma screening parameter $\mu = 0.27$ a.u. In the same physical conditions, we used our MCDF/RATIP method with a Debye-Hückel potential to compute this shift due to plasma effects. In order to model the atomic structure of Ti XXI, we considered a CI model with the $n = 2$ spectroscopic configurations and correlations obtained by single and double excitations from $\{1s^2, 1s2s, 1s2p\}$ to $n = 3$ and $n = 4$ orbitals (354 CSFs in total). Using our model, we computed a redshift of 3.3 eV, which is in very good agreement with the experimental shift measured by Khattak *et al.* We can thus be quite confident in using our model with a screening parameter up to $\mu = 0.27$ a.u. We also note from Table 1 of Belkhiri *et al.* that the Fermi-Dirac distribution considered in the ion-sphere model used by these authors agrees very well with the Maxwell-Boltzman distribution for weakly-coupled plasmas ($n_e = 10^{24}$ cm^{-3}, $T = 100$ eV $-$ 1000 eV), a significant discrepancy being only observed in the case of strongly-coupled plasma ($n_e = 10^{24}$ cm^{-3}, $T = 1$ eV).

Another test of our method using a DH potential for a plasma with a rather high density has been carried out to compute the Ne X Lyman-α line shift as Nguyen *et al.* (1986) did in the case of a plasma with an electron density of 6×10^{24} cm^{-3} and a temperature of 500 eV. In their theoretical study, they obtained a redshift of about 25–26 eV using different models, which were based on the quantum-mechanical impact theory including the boundary depression effect, on the quantum-mechanical impact theory using the volume averaged electron density and on the confined atom in self-consistent field. With the Debye-Hückel potential as implemented in our method, and in the same conditions, with the same kind of CI model as the one used above ($n = 2$ spectroscopic configurations plus $n = 3$ and $n = 4$ correlations), we found a redshift of 24.5 eV, which is in very good

agreement with the results obtained by Nguyen *et al* (1986).

A last test has been made to reproduce the results obtained very recently by Gu & Beiersdorfer (2020). They used the FAC (*Flexible Atomic Code*) program (Gu 2008), in which three forms of plasma screening potential are implemented (the Debye-Hückel, ion-sphere and Stewart & Pyatt[1] potentials), in order to estimate the lowering of the ionization potential of He-like Ar and to compute the redshift of the Kβ transition in the same ion (Ar XVII) for plasma conditions characterized by an electron density $n_e = 10^{23}$ cm^{-3} and by temperatures ranging from 10^2 to 10^4 eV. For the lowest temperature considered (100 eV), their calculations show an ionization potential lowering of about 110 eV using the IS and SP models, while the lowering obtained using the DH potential is four times bigger. The same conclusion is found for the Kβ line shift as they found an overestimation of two order of magnitude while using the DH potential with respect to the results obtained with the IS and SP models (about 2–3 eV), and they thus conclude that the DH potential performs rather poorly for such plasma conditions. However, our computations completely disprove their conclusion and rule out their hypothesis following which the DH potential is not suitable to model a plasma characterized by such physical conditions. This may be due to a misinterpretation of the screening parameter (or Debye length) used in the model by their part. Actually, using our MCDF/RATIP method with a DH potential characterized by a screening parameter $\mu = 0.225$ a.u. (corresponding to $n_e = 10^{23}$ cm^{-3} and $T = 100$ eV), and with a CI model involving configurations that include orbitals up to $n = 4$, we obtained an ionization potential lowering of 103.14 eV for the He-like Ar, which is in good agreement with the results obtained by Gu & Beiersdorfer (2020) using IS and SP models, and contradicts the overestimation that they observed with their DH potential. We also obtained a redshift of 3.72 eV of the Kβ line, which is in rather good agreement with the IS and SP results of Gao & Beiersdorfer (2020). Here again, this completely contradicts the overestimation of 2 order of magnitude that they found while using their DH model, and shows that the Debye-Hückel potential actually performs rather well for these plasma conditions in the way it is implemented in our MCDF/RATIP method.

Furthermore, the necessity to consider the screening of the electron–electron interaction has also been a matter of controversy. Actually, as an example, Chang & Fang (2013) suggested that the screening between atomic electrons would require an unlikely qualitative picture, *i.e.* a substantial presence of the positive ions between atomic electrons, in spite of the relatively low mobility for the much heavier ions. In contrast with this speculative assumption, it is interesting to

---

[1]The Stewart & Pyatt (SP) model (Stewart & Pyatt 1966) is a screening potential built in such a way that the Debye-Hückel and the ion-sphere potentials result as approximate limiting cases respectively for $\Gamma \ll 1$ and for $\Gamma \gg 1$.

note that, according to Zhang & Winkler (1996) for example, it seems plausible to assume that local fluctuations of the uniform Debye screening are not only possible but rather the rule: *"If that is so, it may be argued that the electrons, being light particles, can be more efficient in taking advantage of such local fluctuations than an electron-ion pair which has one less mobile partner. In particular, it may be argued that electron pairs will preferably move into regions with higher screening potential because this will lower the energy of the system and that electron pairs are more efficient to do so than electron–ion pairs"*. The importance of screening effects on electron-electron interaction has also been highlighted very recently by Das *et al.* (2016) who found a significant influence of such effects on the ionization potential depressions and excitation energies in Al ions, the neutral and lowly ionized species being more affected than the highly ionized ones, the former having more electrons than the latter. In the same paper, more stability of the atomic systems were also predicted when the screening effects on the electron–electron interactions are taken into account. Many other papers showed the importance of the Debye screening effects on both the electron–nucleus and the electron–electron interactions. Among these papers, we can mention for instance Winkler (1996), Kar & Ho (2004), Kar & Ho (2005), Saha & Fritzsche (2006), Xie *et al.* (2012), Certik & Winkler (2013), *etc.*

We also wanted to test the importance of the screening effect on the electron–electron interactions using our MCDF/RATIP method. For this reason, we computed the line shifts that were measured for two different ionic species with and without the screening of the electron–electron interaction. The first example concerns neutral sodium (Na I) for which we performed MCDF/RATIP calculations including intravalence and core-valence correlations up to $n = 4$ in order to compare with some experimental line shifts taken from the compilation of Konjevic *et al.* (2002) and originally measured by Sreckovic *et al.* (1996) in a plasma with $T = 38000$ K and $n_e = 3.5 \times 10^{17}$ cm^{-3} (corresponding to a screening parameter $\mu = 0.0023$ a.u.). For the valence-shell 3s - 3p doublet at 5889.95/5895.90 Å, we respectively found line shifts of 4.42 Å and 4.50 Å when considering the Debye screening only on the electron–nucleus interaction, while these values were reduced to 0.43 Å and 0.51 Å when the screening on the electron–electron interactions was also considered. These last results are in very good agreement with the experimental values measured by Sreckovic *et al.*, namely 0.38 ± 0.09 Å and 0.41 ± 0.09 Å, while the results obtained if we neglect the electron–electron screening effect differ by one order of magnitude from them.

The second example is related to singly ionized oxygen (O II) for which MCDF/ RATIP calculations were carried out by including intravalence and core-valence correlation up to $n = 5$, in order to reproduce the experimental line shifts of 0.03 ± 0.02 Å and 0.05 ± 0.02 Å measured for the 2p^{2}3s ^{4}P$_{3/2}$ – 2p^{2}3p ^{4}D$_{5/2}$ (4641.81

Table 3.1: Values of the plasma screening parameter μ (in a.u.) depending on the plasma temperature T (in K) and on the electron density n_e (in cm^{-3})

n_e / T	10^{18}	10^{19}	10^{20}	10^{21}	10^{22}
10^5	0.002	0.008	0.024	0.077	0.242
10^6	0.001	0.002	0.008	0.024	0.077
10^7	0.000	0.001	0.002	0.008	0.024

Å) and 2p^{2}3s ^{4}P$_{1/2}$ – 2p^{2}3p ^{4}D$_{3/2}$ (4638.85 Å) transitions of O II ions embedded in a plasma with a temperature of 54000 K and an electron density of 2.8×10^{17} cm^{-3} (Djenize *et al.* 1998; Konjevic *et al.* 2002), corresponding to $\mu = 0.0017$ a.u. Here also, we conclude that these experimental values can only be reproduced when considering the Debye screening on both the electron–nucleus and electron–electron interactions, since we deduced line shifts of 0.05 Å and 0.05 Å in that case for both transitions, respectively, while much larger values (0.26 Å and 0.25 Å, respectively) were found when neglecting the screening on the electron–electron interactions.

In conclusion, in the previous paragraphs we have shown that (*i*) the Debye-Hückel potential seems to be suitable for weakly-coupled plasma also if the coupling parameter Γ is close to (but still lower than) unity and, moreover, we have been able to reproduce experimental results by using our model with a screening parameter $\mu = 0.27$ a.u., so we can be quite confident to use our method for weakly-coupled plasma with screening parameters up to this value; (*ii*) the Debye screening of the electron–electron interaction has to be taken into account while modeling plasma screening effects in order to obtain a good agreement with experiments. By the way, some of the tests discussed above have been compiled and recently published in Deprince *et al.* (2019a).

Finally, as the choice of Debye-Hückel potential model has now been fully justified, let us consider the values taken by the plasma screening parameter μ for the physical conditions considered in this work, namely the typical conditions within the plasma of a black hole accretion disk (which were discussed in chapter 1, see Schnittman *et al.* 2013): $T = 10^5 - 10^7$ K and $n_e = 10^{18} - 10^{22}$ cm^{-3}. For these values of temperature and electron density, as one can note by looking at Table 3.1, the screening parameter μ ranges between (almost) 0 a.u. (which actually corresponds to the isolated ion case) and 0.24 a.u, the latter corresponding to the most "extreme" plasma conditions considered in this work, namely the weakest temperature (10^5 K) along with the highest electron density ($n_e = 10^{22}$ cm^{-3}).

Obviously, the screening parameter μ can have the same value for different couples of electron density and temperature values (n_e, T). Let us also remind that we have shown above in this section that we can be confident in using our MCDF/RATIP method with a Debye-Hückel potential for weakly-coupled plasma characterized by a screening parameter up to $\mu = 0.27$ a.u. This is the reason why, in this work, and in light of the typical physical conditions expected within the plasma forming black hole accretion disks, we decided to study the effects of the plasma environment by means of a Debye-Hückel potential with a screening parameter that can take the values $0 \leq \mu \leq 0.25$ a.u. In particular, we focused our study on the plasma screening parameter values of $\mu = 0$ a.u., $\mu = 0.1$ a.u. and $\mu = 0.25$ a.u., which respectively correspond to the isolated-ion case, physical conditions such as $T = 10^5$ K and $n_e = 10^{21}$ cm^{-3} (or $T = 10^6$ K and $n_e = 10^{22}$ cm^{-3}) and physical conditions corresponding to $T = 10^5$ K and $n_e = 10^{22}$ cm^{-3}.

Chapter 4

Plasma environment effects on the atomic parameters involving the K shell in oxygen ions

In this chapter, we aim to study the effects of plasma environment on the atomic parameters that involve the K-shell in all the ionization stages of oxygen, for physical conditions such as those expected in accretion disks around black holes. This consists in a very good test of our method before concentrating on the iron ions since oxygen ions have a much less complex structure compared to iron. Moreover, the fewer number of electrons and existing ionization stages with respect to iron enables to estimate the plasma effects on the whole isonuclear sequence of oxygen more easily and quickly, in order to test our method. Furthermore, oxygen ions are also of astrophysical importance, especially for the atomic processes involving the K inner-shell, as explained in Section 1.5. For these reasons, before investigating plasma effects on K-shell processes in iron ions, we first want to test our MCDF/RATIP method to estimate the importance of the plasma environment effects on K-shell atomic processes in oxygen ions, and compare some of our results with those obtained using the modified AST program.

4.1 Models and computations for the isolated ions

The active space (AS) method was used to obtain the MCDF multiconfiguration expansion for O I – O VII, in which electrons from reference configurations are excited to a given active set of orbitals. For these oxygen ions, the AS was built up by considering all the single and double electron excitations from the reference configurations as reported in Table 4.1 to configurations including $n = 2$ and $n = 3$

orbitals. The number of CSFs included in the model of each ion is also given in this table. In order to take into account core-relaxation effects[1] on the K-vacancy states (Garcia *et al.* 2005), we used non-orthogonal orbitals optimized separately in two distinct level groups: a first group of exclusively valence levels where the K shell is full; and a second group of levels with at least a single K vacancy (one hole in the K inner-shell).

In the isolated atom approximation, the relativistic orbitals, along with the mixing coefficients, were optimized using the GRASP2K package (see Section 2.1.4) with the extended average level (EAL) option, where the $(2J + 1)$-weighted trace of the Dirac–Coulomb Hamiltonian is minimized to determine energy levels, transition wavelengths, and radiative and Auger rates. For the ionization potentials (IPs) and K thresholds, distinct optimizations were carried out: the orbitals were respectively optimized on the ground level and on the lowest K-vacancy level of each ion using the optimal level (OL) option of GRASP2K, in order to have a better estimation of the levels directly involved in the determination of the ioniza-

Table 4.1: Reference configurations used to build up the MCDF active space (AS) for O I – O VII and corresponding total number of CSFs within the model.

Ion	Reference configurations	Number of CSFs
O I	$1s^2 2s^2 2p^4$, $1s^2 2s 2p^5$, $1s^2 2p^6$, $1s 2s^2 2p^5$, $1s 2s 2p^6$	5280 CSFs
O II	$1s^2 2s^2 2p^3$, $1s^2 2s 2p^4$, $1s^2 2p^5$, $1s 2s^2 2p^4$, $1s 2s 2p^5$, $1s 2p^6$	6728 CSFs
O III	$1s^2 2s^2 2p^2$, $1s^2 2s 2p^3$, $1s^2 2p^4$, $1s 2s^2 2p^3$, $1s 2s 2p^4$, $1s 2p^5$	6341 CSFs
O IV	$1s^2 2s^2 2p$, $1s^2 2s 2p^2$, $1s^2 2p^3$, $1s 2s^2 2p^2$, $1s 2s 2p^3$, $1s 2p^4$	3986 CSFs
O V	$1s^2 2s^2$, $1s^2 2s 2p$, $1s^2 2p^2$, $1s 2s^2 2p$, $1s 2s 2p^2$, $1s 2p^3$	1828 CSFs
O VI	$1s^2 2s$, $1s^2 2p$, $1s 2s 2p$, $1s 2p^2$	479 CSFs
O VII	$1s^2$, $1s 2s$, $1s 2p$	98 CSFs

---

[1]The 1s orbital can actually have a shape that is slightly different depending on the fact that it is completely filled ($1s^2$) or not (K-vacancy state). This effect is known as the "core-relaxation effect" since the shape of the 1s orbital can change between the initial K-vacancy state and the final valence state in a K line emission.

tion limits.

The ionization potentials (IPs) of O I - O VII computed with MCDF/RATIP for the isolated ion case are given in Table 4.2 and compared with the values from the NIST (*National Institute of Standards and Technology*) atomic database (Kramida *et al.* 2019). As one can see when looking at this table, the results obtained in our work are in very good agreement with NIST values, the latter being reproduced to within 1% (or even much better, within 0.3% in the majority of cases) except for O I, for which a 4% accuracy was reached due to the well-known slow convergence of the CI expansion for neutrals. Furthermore, by using our MCDF/RATIP method we obtained a K threshold of 543.58 eV for the neutral oxygen, which is in excellent agreement (0.2%) with the value of 544.544 eV deduced by Gorczyka *et al.* (2013) while fitting the K-shell photoionization cross-section data from Henke *et al.* (1993).

The radiative wavelengths of the most intense K lines (characterized by transition rates greater than 10^{11} s^{-1}) calculated in our work with the MCDF/RATIP method are reported in Table 4.3. They are compared with the values obtained by Garcia *et al.* (2005) using both the pseudo-relativistic Hartree-Fock (HFR) method (that is the non-relativistic counterpart of the MCDF method, which is based on the Schrödinger equation and perturbatively corrected by several relativistic effects) and the multiconfiguration Breit-Pauli approximation as implemented in the AUTOSTRUCTURE (AST) program (which is briefly described in Section 2.2). The few available experimental data for such wavelengths are also listed in this table. They are deduced from Auger electron spectrometry (Krause 1994, Caldwell *et al.* 1994), spectroscopy of a Seyfert galaxy (Steenbrugge *et al.*

Table 4.2: Comparison between the ionization potentials (in eV) of O I - O VII computed in this work with MCDF/RATIP for the isolated ion case and the most accurate values published in the NIST atomic database.
.

Ion	NIST[a]	MCDF/RATIP
O I	13.618054 ± 0.000007	13.07
O II	35.12111 ± 0.00006	35.00
O III	54.93554 ± 0.00012	54.80
O IV	77.41350 ± 0.00025	77.31
O V	113.8989 ± 0.0005	112.81
O VI	138.1189 ± 0.0021	138.04
O VII	739.32679 ± 0.00006	739.86

[a] Kramida *et al.* (2019)

2003), electron beam ion trap measurements (Schmidt *et al.* 2004), spectroscopic tables (Moore 1998) and spectroscopic measurements (Engström & Litzen 1995). By looking at this table, one can see that the wavelengths that we computed in our work are in good agreement with those previously obtained by Garcia *et al.* (2005) using both the HFR and AST methods, since they differ by less than 1% on average (even less than 0.5% in most cases). More precisely, the present K-line wavelengths appear to be shorter by 0.1% for the highly charged ions to little less than 1% for the lower ionization stages. In addition, they are in excellent agreement with the few experimental spectroscopic data available. For instance, our predicted wavelength for the strong $K\alpha$ line in O VII agrees within less than 0.2% with the measurements made by Engström & Litzen (1995), and the same agreement is found for all the strong K lines in O VI when compared with the data available in the spectroscopic tables of Moore (1998) and with the electron beam ion trap measurements by Schmidt *et al.* (2004), while our values differ by about 0.5% from those reported by the latter for K lines in O III, O IV and O V. Our values are also in very good agreement (within 0.5-0.8%) with those obtained using Auger electron spectrometry by Krause (1994) and Caldwell *et al.* (1994) in O I and O II and with those deduced by the spectroscopy of NGC 5548 by Steenbrugge *et al.* (2003) in O III. In conclusion, the K-line wavelengths that we computed in our work are in very good agreement (within 1% or even better) with both the few experimental values available in the literature and the calculations performed by Garcia *et al.* (2005) using two different methods.

Table 4.3: Comparison between the K-line radiative wavelengths (in Å) calculated with our MCDF/RATIP method (isolated ion case) with the few available experimental data and with the wavelengths obtained by Garcia *et al.* (2005) using both the pseudo-relativistic Hartree-Fock (HFR) and the AUTOSTRUCTURE (AST) methods.

Ion	Transition	Exp.	MCDF/RATIP[a]	HFR[b]	AST[b]
O I	[1s]2p^5 ^{1}P$_1$ - 2p^4 ^{1}D$_2$		23.3180	23.45	23.44
	[1s]2p^5 ^{3}P$_1$ - 2p^4 ^{3}P$_2$		23.3752	23.47	23.44

[a] This work.

[b] Computations from Garcia *et al.* (2005).

[c] Auger electron spectrometry (Krause 1994, Caldwell *et al.* 1994).

[d] Spectroscopy of the Seyfert galaxy NGC 5548 (Steenbrugge *et al.* 2003).

[e] Electron beam ion trap measurements (Schmidt *et al.* 2004).

[f] Spectroscopic tables (Moore 1998).

[g] Spectroscopic measurements (Engström & Litzen 1995).

Table 4.3: (continued)

Ion	Transition	Exp.	MCDF/RATIP[a]	HFR[b]	AST[b]
	$[1s]2p^5\ ^3P_0$ - $2p^4\ ^3P_1$		23.3753	23.47	23.44
	$[1s]2p^5\ ^3P_1$ - $2p^4\ ^3P_1$	23.52[c]	23.3759	23.47	23.45
	$[1s]2p^5\ ^3P_1$ - $2p^4\ ^3P_0$	23.52[c]	23.3763	23.47	23.45
	$[1s]2p^5\ ^3P_2$ - $2p^4\ ^3P_2$	23.52[c]	23.3763	23.47	23.45
	$[1s]2p^5\ ^3P_2$ - $2p^4\ ^3P_1$	23.52[c]	23.3770	23.47	23.45
	$[1s]2p^5\ ^1P_1$ - $2p^4\ ^1S_0$		23.3940	23.53	23.52
O II	$[1s]2p^4\ ^2P_{1/2}$ - $2p^3\ ^2D_{3/2}$		23.1144	23.25	23.25
	$[1s]2p^4\ ^2P_{3/2}$ - $2p^3\ ^2D_{3/2}$		23.1159	23.25	23.25
	$[1s]2p^4\ ^2P_{3/2}$ - $2p^3\ ^2D_{5/2}$		23.1159	23.28	23.29
	$[1s]2p^4\ ^2S_{1/2}$ - $2p^3\ ^2P_{1/2}$	23.29[c]	23.1204	23.28	23.29
	$[1s]2p^4\ ^2S_{1/2}$ - $2p^3\ ^2P_{3/2}$	23.29[c]	23.1204	23.28	23.29
	$[1s]2p^4\ ^2D_{5/2}$ - $2p^3\ ^2D_{3/2}$		23.1636	23.29	23.29
	$[1s]2p^4\ ^2D_{5/2}$ - $2p^3\ ^2D_{5/2}$		23.1636	23.29	23.29
	$[1s]2p^4\ ^2D_{3/2}$ - $2p^3\ ^2D_{3/2}$		23.1638	23.29	23.29
	$[1s]2p^4\ ^2D_{3/2}$ - $2p^3\ ^2D_{5/2}$		23.1638	23.29	23.29
	$[1s]2p^4\ ^2P_{1/2}$ - $2p^3\ ^2P_{1/2}$		23.1759	23.34	23.34
	$[1s]2p^4\ ^2P_{1/2}$ - $2p^3\ ^2P_{3/2}$		23.1759	23.34	23.34
	$[1s]2p^4\ ^2P_{3/2}$ - $2p^3\ ^2P_{1/2}$	23.36[c]	23.1774	23.34	23.35
	$[1s]2p^4\ ^2P_{3/2}$ - $2p^3\ ^2P_{3/2}$	23.36[c]	23.1774	23.34	23.35
	$[1s]2p^4\ ^4P_{1/2}$ - $2p^3\ ^4S_{3/2}$		23.2124	23.35	23.35
	$[1s]2p^4\ ^4P_{3/2}$ - $2p^3\ ^4S_{3/2}$		23.2131	23.35	23.35
	$[1s]2p^4\ ^4P_{5/2}$ - $2p^3\ ^4S_{3/2}$		23.2143	23.35	23.35
	$[1s]2p^4\ ^2D_{5/2}$ - $2p^3\ ^2P_{3/2}$	23.36[c]	23.2254	23.32	23.31
	$[1s]2p^4\ ^2D_{3/2}$ - $2p^3\ ^2P_{1/2}$	23.36[c]	23.2256	23.32	23.31
	$[1s]2p^4\ ^2D_{3/2}$ - $2p^3\ ^2P_{3/2}$	23.36[c]	23.2256	23.32	23.31
O III	$[1s]2p^3\ ^1P_1$ - $2p^2\ ^1D_2$		22.8154	22.99	23.00

[a] This work.

[b] Computations from Garcia *et al.* (2005).

[c] Auger electron spectrometry (Krause 1994, Caldwell *et al.* 1994).

[d] Spectroscopy of the Seyfert galaxy NGC 5548 (Steenbrugge *et al.* 2003).

[e] Electron beam ion trap measurements (Schmidt *et al.* 2004).

[f] Spectroscopic tables (Moore 1998).

[g] Spectroscopic measurements (Engström & Litzen 1995).

Table 4.3: (continued)

Ion	Transition	Exp.	MCDF/RATIP[a]	HFR[b]	AST[b]
	$[1s]2p^3\ ^3S_1$ - $2p^2\ ^3P_0$	23.00^d	22.8748	23.06	23.07
	$[1s]2p^3\ ^3S_1$ - $2p^2\ ^3P_1$		22.8754	23.06	23.07
	$[1s]2p^3\ ^3S_1$ - $2p^2\ ^3P_2$		22.8766	23.06	23.07
	$[1s]2p^3\ ^3P_1$ - $2p^2\ ^3P_0$		22.8897	23.06	23.06
	$[1s]2p^3\ ^3P_2$ - $2p^2\ ^3P_1$		22.8902	23.02	23.03
	$[1s]2p^3\ ^3P_0$ - $2p^2\ ^3P_1$		22.8903	23.02	23.03
	$[1s]2p^3\ ^3P_1$ - $2p^2\ ^3P_1$		22.8903	23.02	23.03
	$[1s]2p^3\ ^1D_2$ - $2p^2\ ^1D_2$		22.8908	23.02	23.03
	$[1s]2p^3\ ^3P_2$ - $2p^2\ ^3P_2$		22.8914	23.02	23.03
	$[1s]2p^3\ ^3P_1$ - $2p^2\ ^3P_2$		22.8915	23.02	23.03
	$[1s]2p^3\ ^1P_1$ - $2p^2\ ^1S_0$		22.9227	23.09	23.09
	$[1s]2p^3\ ^3D_1$ - $2p^2\ ^3P_0$	23.17^d	22.9663	23.09	23.09
	$[1s]2p^3\ ^3D_2$ - $2p^2\ ^3P_1$		22.9669	23.09	23.09
	$[1s]2p^3\ ^3D_1$ - $2p^2\ ^3P_1$		22.9669	23.09	23.09
	$[1s]2p^3\ ^3D_3$ - $2p^2\ ^3P_2$		22.9680	23.09	23.10
	$[1s]2p^3\ ^3D_2$ - $2p^2\ ^3P_2$		22.9681	23.09	23.09
	$[1s]2p^3\ ^3D_1$ - $2p^2\ ^3P_2$		22.9682	23.09	23.09
O IV	$[1s]2p^2\ ^2S_{1/2}$ - $2p\ ^2P_{1/2}$		22.5066	22.65	22.66
	$[1s]2p^2\ ^2S_{1/2}$ - $2p\ ^2P_{3/2}$		22.5087	22.66	22.66
	$[1s]2p^2\ ^2P_{3/2}$ - $2p\ ^2P_{1/2}$		22.5567	22.75	22.74
	$[1s]2p^2\ ^2P_{1/2}$ - $2p\ ^2P_{1/2}$		22.5587	22.75	22.74
	$[1s]2p^2\ ^2P_{3/2}$ - $2p\ ^2P_{3/2}$		22.5588	22.75	22.74
	$[1s]2p^2\ ^2P_{1/2}$ - $2p\ ^2P_{3/2}$		22.5609	22.75	22.74
	$[1s]2p^2\ ^2D_{3/2}$ - $2p\ ^2P_{1/2}$		22.6310	22.78	22.77
	$[1s]2p^2\ ^2D_{5/2}$ - $2p\ ^2P_{3/2}$		22.6330	22.78	22.77
	$[1s]2p^2\ ^2D_{3/2}$ - $2p\ ^2P_{3/2}$	22.74^d	22.6331	22.78	22.77

[a] This work.

[b] Computations from Garcia *et al.* (2005).

[c] Auger electron spectrometry (Krause 1994, Caldwell *et al.* 1994).

[d] Spectroscopy of the Seyfert galaxy NGC 5548 (Steenbrugge *et al.* 2003).

[e] Electron beam ion trap measurements (Schmidt *et al.* 2004).

[f] Spectroscopic tables (Moore 1998).

[g] Spectroscopic measurements (Engström & Litzen 1995).

Ion	Transition	Exp.	MCDF/RATIP[a]	HFR[b]	AST[b]
O V	$[1s]2p\ ^1P_1$ - $2s^2\ ^1S_0$	22.374^e	22.2088	22.37	22.36
O VI	$[1s]2s2p\ ^2P_{3/2}$ - $2s\ ^2S_{1/2}$	21.82^f	21.7832	21.83	21.80
	$[1s]2s2p\ ^2P_{1/2}$ - $2s\ ^2S_{1/2}$	21.82^f	21.7836	21.83	21.80
	$[1s]2s2p\ ^2P_{3/2}$ - $2s\ ^2S_{1/2}$	22.0194^e	21.9706	22.03	22.02
	$[1s]2s2p\ ^2P_{1/2}$ - $2s\ ^2S_{1/2}$	22.0194^e	21.9730	22.04	22.02
O VII	$1s2p\ ^1P_1$ - $1s^2\ ^1S_0$	21.6020^g	21.5642	21.61	21.62

[a] This work.

[b] Computations from Garcia *et al.* (2005).

[c] Auger electron spectrometry (Krause 1994, Caldwell *et al.* 1994).

[d] Spectroscopy of the Seyfert galaxy NGC 5548 (Steenbrugge *et al.* 2003).

[e] Electron beam ion trap measurements (Schmidt *et al.* 2004).

[f] Spectroscopic tables (Moore 1998).

[g] Spectroscopic measurements (Engström & Litzen 1995).

Regarding the radiative rates, our MCDF/RATIP results agree on average within 10% with those obtained by Garcia *et al.* (2005), except for a few weak transitions and for a few transitions for which a huge disagreement between HFR and AST was observed in the calculations of Garcia *et al.* For instance, it is the case of the $[1s]2p^4\ ^2P_{3/2}$ - $2p^3\ ^2P_{3/2}$ K line in O II, for which there is a difference of a factor greater than 2 between the results obtained by HFR and AST. In this case, our MCDF/RATIP results seem to confirm the value computed with HFR (we thus not consider the AST value for this transition in our further comparison). For the most intense transitions (with transition probabilities greater than 10^{12} s^{-1}), we actually found an agreement that is better than 5% on average with the results obtained by Garcia *et al.* (2005) using both HFR and AST. This is thus a satisfactory agreement since cancellation effects (*i.e.* cancellations in the transition amplitude computation that result in a nonphysical weaker radiative rate and that typically appear in mutliconfiguration computations) may affect the weakest transition probabilities computed either by MCDF/RATIP, HFR or AST, and in light of the typical uncertainties of computed radiative rates ($\sim 5 - 10\%$, see *e.g.* Palmeri *et al.* 2003b; Hartman *et al.* 2010). To illustrate the discrepancy between our radiative rates and those obtained by Garcia *et al.* (2005), we plotted the ratio of the transitions probabilities computed in this work with the MCDF/RATIP method to the ones calculated by Garcia *et al.* using both HFR and AST methods
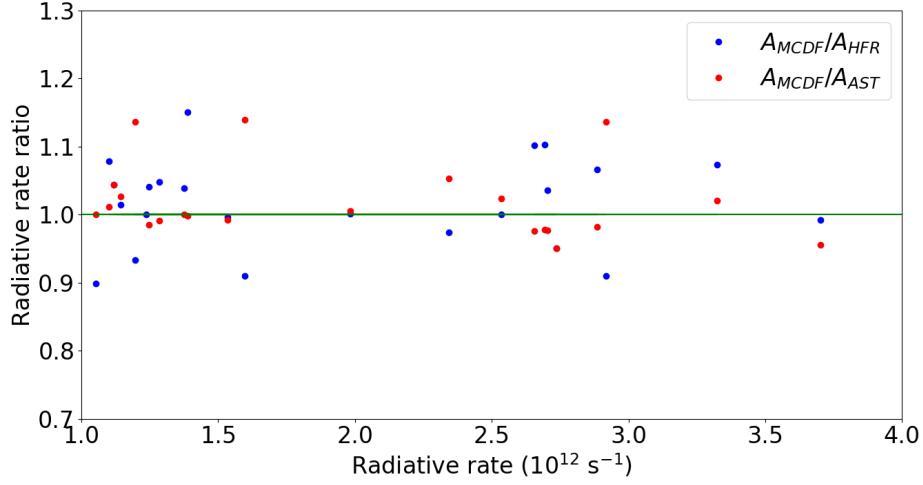
Figure 4.1: Ratio between the radiative rates computed by MCDF/RATIP (this work) and those obtained by Garcia *et al.* (2005) using HFR (*blue points*) and AST (*red points*) methods.

for the most intense transitions. This plot is displayed in Figure 4.1. It turned out that the mean ratio is of 1.02 in both cases, with a standard deviation of 6.5% and 5% for the comparison with HFR and AST, respectively. This reveals the good overall agreement between our data and those obtained by Garcia *et al.* (2005) concerning the radiative rates for the isolated ions.

As it can be seen in Figure 4.2, where are plotted the ratios between the most intense ($A^a > 10^{14}$ s^{-1}) Auger widths (*i.e.* the sum of all the Auger rates related to autoionization transitions that depopulate a given level) that we computed with MCDF/RATIP and those calculated with both the HFR and the AST methods by Garcia *et al.* (2005), the discrepancy is more important than for the radiative rates. Actually, we obtain a relative difference of about 25% and 18%, respectively, compared to the HFR and AST results of Garcia *et al.*, and a mean ratio of 1.24 and 1.13 with a standard deviation of 19% and 16%. However, the scattering of the results between the HFR and AST Auger widths obtained by Garcia *et al.* was also important as they found a $\sim 20\%$ mean difference between the HFR and AST Auger widths, so the general agreement with the Auger results of Garcia *et al.* can be judged as satisfactory. Besides, the biggest differences are observed for the neutral oxygen: this might illustrate the difficulty encountered to compute accurate rates at the neutral end of an isonuclear sequence. Moreover, let us also emphasize that our computations are fully relativistic, unlike HFR and AST, and that much more electronic correlations have been included in our models: this may

70
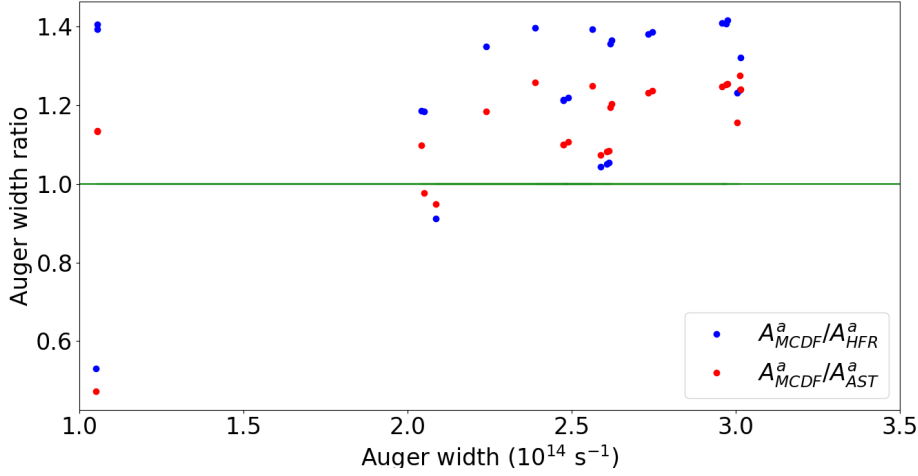
Figure 4.2: Ratio between the Auger widths computed by MCDF/RATIP (this work) and those obtained by Garcia *et al.* (2005) using HFR (*blue points*) and AST (*red points*) methods.

also explain the differences observed in the results that we obtained compared to those computed by Garcia *et al.* (2005) using HFR and AST.

4.2 Plasma effects on the atomic structure, K-shell radiative and Auger processes in oxygen ions

In this section, we evaluate the plasma environment effects on various atomic parameters involved in K-line formation in all the ionization stages of oxygen ions, namely the ionization potentials, the K-shell thresholds, the radiative K-line wavelengths and rates, and the K-vacancy state Auger widths. As explained in Chapter 3, we examine those effects by using a Debye-Hückel potential in the framework of the MCDF/RATIP method where we consider plasma screening parameters μ ranging from 0 a.u. to 0.25 a.u. (see Table 3.1). In particular, we will concentrate on the differences between the results obtained for the isolated ion (0 a.u.) and, on the one hand, for $\mu = 0.1$ a.u. (which corresponds to $T = 10^5$ K and $n_e = 10^{21}$ cm^{-3} or $T = 10^6$ K and $n_e = 10^{22}$ cm^{-3}, for instance), and on the other hand for $\mu = 0.25$ a.u (*i.e.* $T = 10^5$ K and $n_e = 10^{22}$ cm^{-3}).

4.2.1 Ionization potentials and K thresholds

Table 4.4 shows the ionization potentials $E_0(\mu)$ of oxygen ions computed by MCDF/ RATIP for $\mu = 0$ a.u., $\mu = 0.1$ a.u. and $\mu = 0.25$ a.u. The fourth column lists the ionization potentials computed by considering only the screening of the electron–nucleus interaction for $\mu = 0.1$ a.u., thus neglecting the electron–electron screening. As discussed in Section 3.3, it is clear by looking at this table that the screening of the electron–electron interaction cannot be neglected: otherwise, the continuum lowering appears to be overestimated, even leading to an unphysical negative IP value for O I. We therefore stress again that the Debye-Hückel electron–electron screening is essential and must be considered in the computations. As expected, a substantial lowering of the ionization potential absolute values is observed, which is already significant for $\mu = 0.1$ a.u. and is much larger for $\mu = 0.25$ a.u. In the latter case (for the most "extreme" plasma conditions), the ionization potentials are found to be reduced by about 6.5 eV (O I) to 46.5 eV (O VII), which correspond to relative variation of 6% (for O VII) to almost 50% (for O I). The IP depression is thus a very large effect that cannot be neglected, even for $\mu = 0.1$ a.u., for which variations up to ~ 25 % (*i.e.* up to ~ 20 eV) are found.

Figure 4.3 and 4.4 respectively show the ionization potential lowering ($\Delta E_0 = E_0(\mu) - E_0(\mu = 0)$) as a function of the screening parameter μ for all the ionization stages of oxygen and as a function of the effective ionic charge, $Z_{\text{eff}} = Z - N + 1$, for three different values of μ. The ionization potential depression is found to be linear with the plasma screening parameter μ, while the trends of the IP lowering with Z_{eff} is practically linear except for $Z_{\text{eff}} = 7$ (O VII). Actually, the broken trend observed for the latter is due to the absence of electron–electron plasma screening

Table 4.4: Plasma screening effects on the ionization potentials $E_0(\mu)$ (in eV, μ in a.u.) in oxygen ions determined with the MCDF/RATIP method.

Ion	$E_0(0)$	$E_0(0.1)$	$E_0(0.1^a)$	$E_0(0.25)$
O I	13.07	10.33	-6.85	6.42
O II	35.00	29.68	14.65	22.30
O III	54.80	46.90	34.26	36.12
O IV	77.31	66.82	56.60	52.52
O V	112.81	99.75	92.04	82.14
O VI	138.04	122.41	117.21	101.37
O VII	739.86	720.99	718.32	693.36

[a] Without considering the screening of the electron–electron interaction.

Figure 4.3: Ionization potential depression (in eV), $\Delta E_0 = E_0(\mu) - E_0(\mu = 0)$, as function of the plasma screening parameter, μ (in a.u.) for all the oxygen ions considered in this study. Dots: MCDF calculations; triangles: Debye-Hückel limit, *i.e.* $\Delta E_0^{\text{DH}} = -Z_{\text{eff}}\mu$; black: O I; blue: O II; green: O III; red: O IV; yellow: O V; cyan: O VI; magenta: O VII.
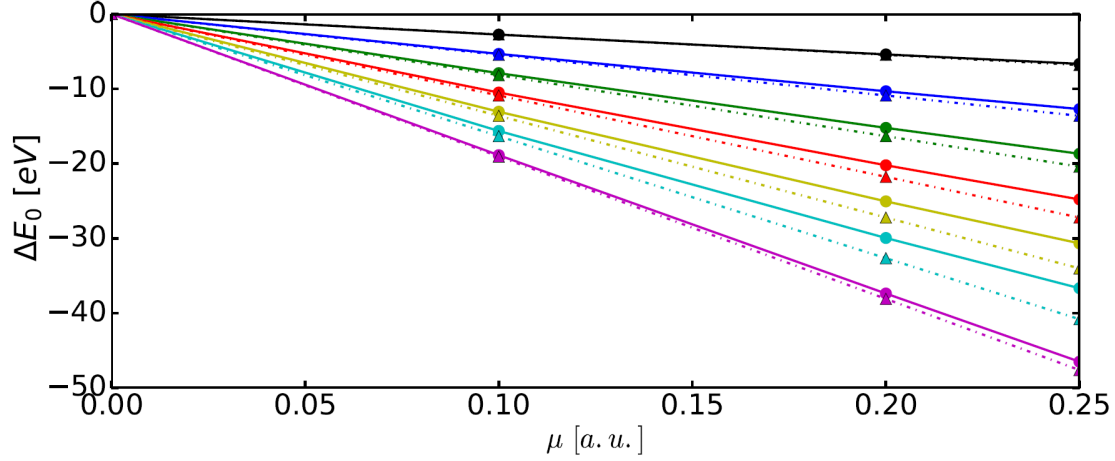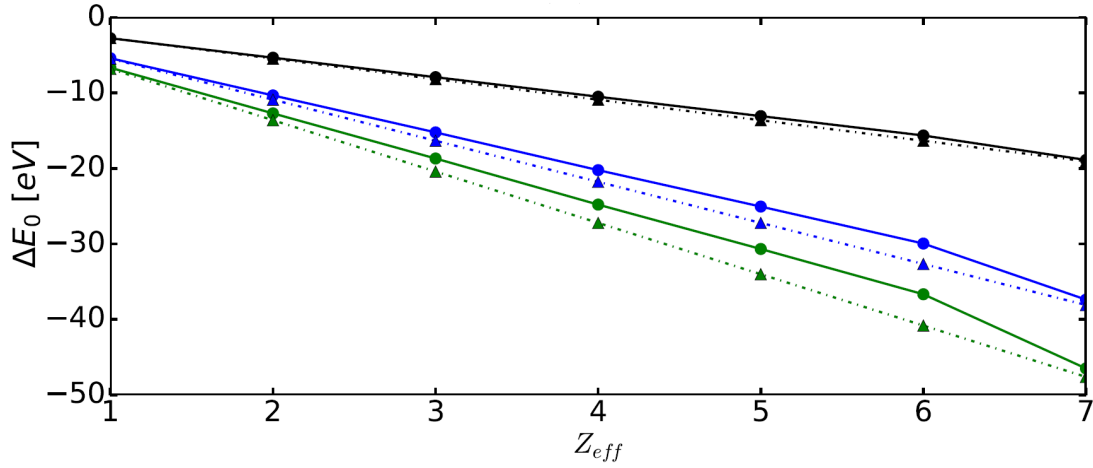

Figure 4.4: Ionization potential depression (in eV), $\Delta E_0 = E_0(\mu) - E_0(\mu = 0)$, as function of the effective ionic charge, $Z_{\text{eff}} = Z - N + 1$, for three different values of μ. Dots: MCDF calculations; triangles: Debye-Hückel limit, *i.e.* $\Delta E_0^{\text{DH}} = -Z_{\text{eff}}\mu$; black: $\mu = 0.1$ a.u.; blue: $\mu = 0.2$ a.u.; green: $\mu = 0.25$ a.u.

Table 4.5: Comparison between the ionization potential lowering (in eV) obtained by MCDF/RATIP and by AST in O IV - O VII for two values of the plasma screening parameter μ (in a.u.).

Ion	MCDF/RATIP		AST	
	ΔE_0	ΔE_0	ΔE_0	ΔE_0
	$\mu = 0.1$	$\mu = 0.25$	$\mu = 0.1$	$\mu = 0.25$
O IV	-10.49	-24.79	-10.34	-24.00
O V	-13.06	-30.67	-12.97	-30.26
O VI	-15.63	-36.67	-15.62	-36.63
O VII	-18.87	-46.50	-18.82	-46.37

in the ground state of O VIII that contributes to the ionization potential of O VII. We also include for each species the DH limit $\Delta E_0^{\mathrm{DH}} = -Z_{\mathrm{eff}}\mu$ as $\Gamma \rightarrow 0$ determined by Stewart & Pyatt (1966) and Crowley (2014), which actually fits our results quite well. For example, in O VII, $\Delta E_0^{\mathrm{DH}} = -47.6$ eV is close to the lowering that we obtained with our method (-46.5 eV).

We also used the AUTOSTRUCTURE method that has been modified to include a DH potential (as described in Section 2.2) in order to estimate the ionization potential lowering for a selected sample of oxygen ions in a comparison purpose. The same CI models have been considered in AST than in MCDF/RATIP. The IP potential depressions obtained by both methods are displayed in Table 4.5 for two values of the screening parameter ($\mu = 0.1$ a.u. and $\mu = 0.25$ a.u.). A very good agreement is found for the IP lowering obtained by both the MCDF/RATIP and the AST methods, as they agree within 1% for $\mu = 0.1$ a.u. and within 3% for $\mu = 0.25$ a.u. These results thus confirm that the Debye-Hückel potential has been correctly implemented in both MCDF/RATIP and AST, since these two methods rely on very different approaches and seem to both produce results in good agreement.

The effects of the plasma screening on the K thresholds of all the oxygen ions are shown in Table 4.6, where are displayed the oxygen ion K-threshold energies for $\mu = 0$ a.u., $\mu = 0.1$ a.u. and $\mu = 0.25$ a.u. It can be easily noticed that, for each oxygen ion, the K-threshold lowering is very similar to the IP one. The same conclusions thus also stand for the K-threshold depression, as a lowering of about 8 eV to 46.5 eV is observed for $\mu = 0.25$ a.u. In particular, the same goes for the linear trends observed for the IP depression that are also obtained for the

Table 4.6: Plasma screening effects on the K threshold $E_K(\mu)$ (in eV, μ in a.u.) in oxygen ions computed with MCDF/RATIP.

Ion	$E_K(0)$	$E_K(0.1)$	$E_K(0.25)$
O I	543.58	540.62	535.47
O II	570.89	565.31	556.49
O III	593.27	585.08	572.74
O IV	626.49	615.64	599.52
O V	664.10	650.57	630.58
O VI	699.64	683.44	659.64
O VII	739.86	720.99	693.36

K-threshold lowering with respect to both the plasma screening parameter and the effective charge, as it can be seen in Figure 4.5 and Figure 4.6. This finding is significant inasmuch as the DH screened photoionization cross sections will only involve approximately constant downward energy shifts of the thresholds leading to resonance series truncations rather than variant line wavelengths and resonance energy positions (this is further discussed in Chapter 5).
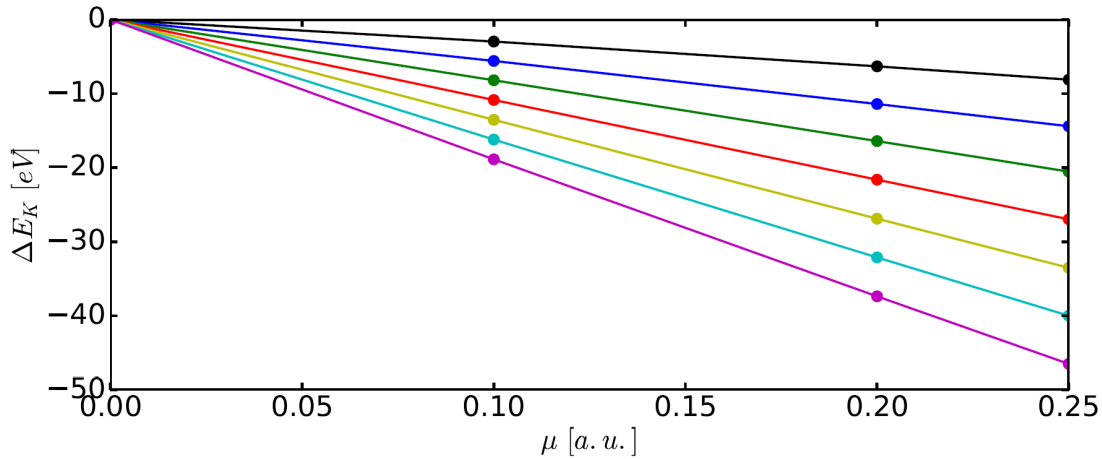
Figure 4.5: K-threshold depression, $\Delta E_K = E_K(\mu) - E_K(\mu = 0)$, (in eV) as function of the plasma screening parameter, μ (in a.u.) for all the oxygen ions considered in this study. Black: O I; blue: O II; green: O III; red: O IV; yellow: O V; cyan: O VI; magenta: O VII.
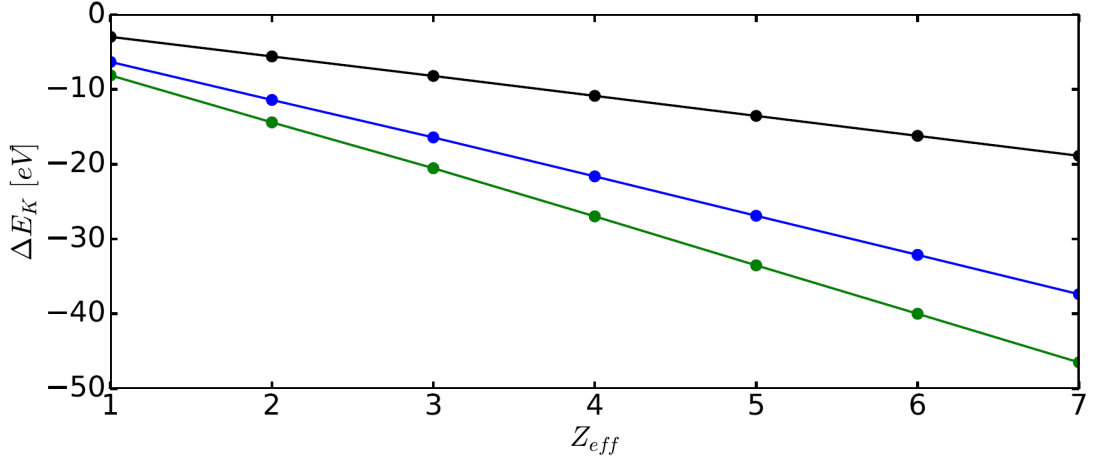
Figure 4.6: K-threshold lowering, $\Delta E_K = E_K(\mu) - E_K(\mu = 0)$, (in eV) as function of the effective ionic charge, $Z_{\text{eff}} = Z - N + 1$, for three different values of μ. Black: $\mu = 0.1$ a.u.; blue: $\mu = 0.2$ a.u.; green: $\mu = 0.25$ a.u.

4.2.2 K-line radiative data

The plasma environment effects on the K-line radiative parameters are reported in Table 4.7 for O I, O II, O III, O IV, O V, O VI and O VII. In this table are displayed the radiative wavelengths (λ) and the corresponding transition probabilities (A_{ki}) for the most intense K lines in the oxygen ions ($A \geq 10^{10}$ s^{-1}) and for three different values of μ, namely $\mu = 0$ a.u. (isolated atomic system), $\mu = 0.1$ a.u. and $\mu = 0.25$ a.u.

Plasma effects on the radiative wavelengths are found to be small for $\mu = 0.1$ a.u., but a little more conspicuous for $\mu = 0.25$ a.u. (although they are still rather small), as it can be seen in Figure 4.7, where the radiative wavelength shifts obtained for $\mu = 0.1$ and $\mu = 0.25$ are represented as a function of the effective charge. Actually, the K-line wavelengths appear to be redshifted by about 10–20 mÅ for $\mu = 0.1$ a.u. and by 50–100 mÅ for $\mu = 0.25$ with respect to the isolated ion ($\mu = 0$), with an increasing trend as a function of the ion effective charge (see Figure 4.7). For $\mu = 0.25$, this corresponds to relative variations up to 0.5%. Although small, such wavelength shifts can be resolved by present and next-generation satellite-borne X-ray spectrometers (such as the X-ray microcalorimeter of XRISM, see Section 1.6). Besides, Figure 4.8 shows the trend of the radiative wavelength with the plasma screening parameter μ for the 1s2s2p ^{2}P$_{1/2}$ - 1s^{2}2s ^{2}S$_{1/2}$ K line in O VI, that is found to be non-linear, unlike the IP and K-threshold variations due to plasma effects.
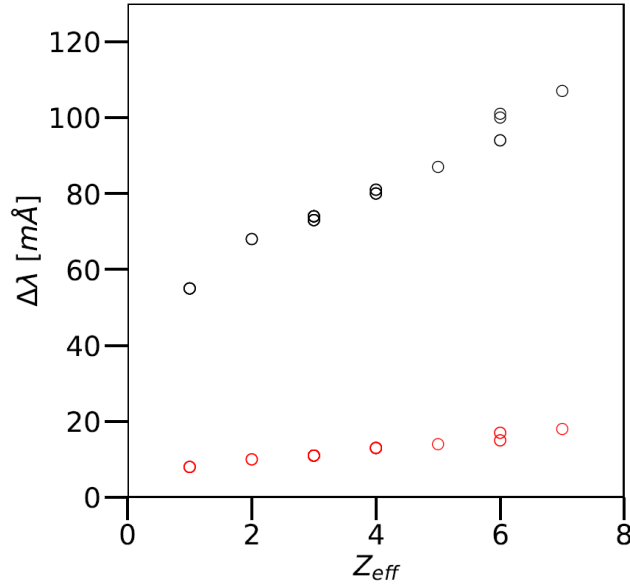
Figure 4.7: MCDF/RATIP wavelength shift $\Delta\lambda = \lambda(\mu) - \lambda(\mu = 0)$ for oxygen K lines as a function of the effective charge $Z_{\text{eff}} = Z - N + 1$ for two different values of the screening parameter μ (in a.u.), namely $\mu = 0.1$ a.u. (*red*) and $\mu = 0.25$ a.u. (*black*)
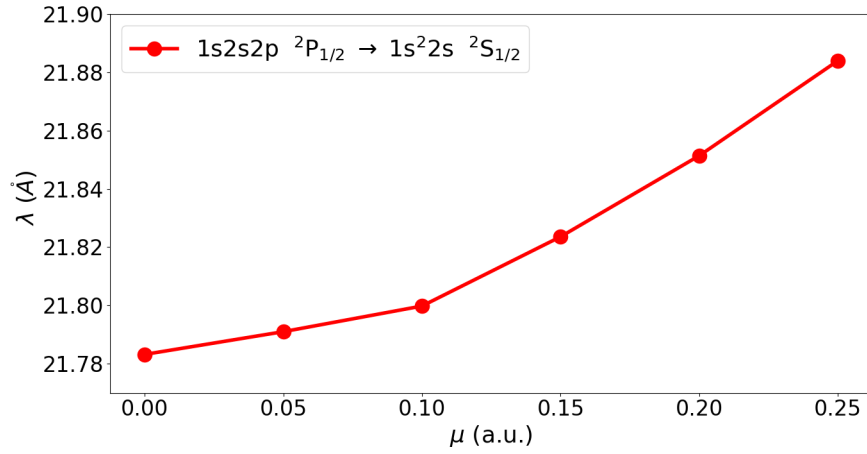
Figure 4.8: MCDF/RATIP radiative wavelength of a K line in O VI as a function of the screening parameter μ
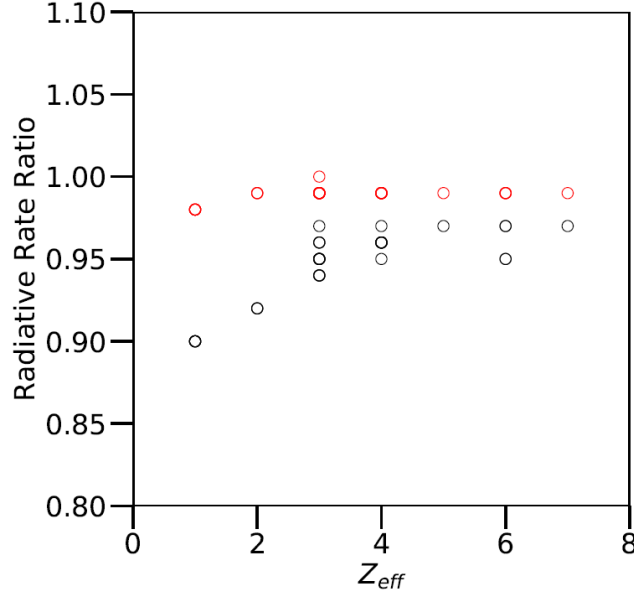
Figure 4.9: MCDF/RATIP radiative rate ratio $A_{ki}(\mu)/A_{ki}(\mu = 0)$ the most intense for oxygen K lines as a function of the effective charge $Z_{\text{eff}} = Z - N + 1$ for two different values of the screening parameter μ (in a.u.), namely $\mu = 0.1$ a.u. (*red*) and $\mu = 0.25$ a.u. (*black*)

The K-line radiative rates also are only slightly modified. All the transition probabilities are actually reduced by a few percents, 5% on average for $\mu = 0.25$ a.u. (up to 10% for a very few number of K lines in the neutral oxygen). This is illustrated in Figure 4.9, where are displayed the ratio $A_{ki}(\mu)/A_{ki}(\mu = 0)$ as a function of the effective charge, respectively for $\mu = 0.1$ and $\mu = 0.25$. Anyway, the variations observed for the radiative rates are too weak to produce significant differences in astrophysical modeling.

We also wanted to test our MCDF/RATIP method concerning plasma effects on the K-line radiative parameters by comparing the results obtained with those computed by the AST method in a few selected cases. Table 4.8 and Table 4.9 show a comparison between the radiative wavelengths and rates obtained by both methods for the most intense K lines ($A \geq 10^{12}$ s^{-1}) in O VI and O VII for the isolated ion and for $\mu = 0.1$ a.u. By looking at these two tables, one can easily note that the wavelength redshift computed by both methods are in very good agreement (15-18 mÅ in both cases), while the very weak variation of the radiative rates (less than 1%) obtained by MCDF/RATIP is confirmed by AST.

78

Table 4.7: Plasma environment effects on radiative wavelengths (λ) and transition probabilities (A_{ki}) of Kα lines in oxygen ions computed with MCDF/RATIP depending on the plasma screening parameter μ (given in a.u.)

Transition	λ (Å)			A_{ki} (s^{-1})		
	$\mu = 0.0$	$\mu = 0.1$	$\mu = 0.25$	$\mu = 0.0$	$\mu = 0.1$	$\mu = 0.25$
O I						
[1s]2p^5 ^{1}P$_1$ - 2p^4 ^{1}D$_2$	23.3180	23.3252	23.3684	2.918E+12	2.885E+12	2.732E+12
[1s]2p^5 ^{3}P$_1$ - 2p^4 ^{3}P$_2$	23.3752	23.3832	23.4301	6.648E+11	6.529E+11	5.993E+11
[1s]2p^5 ^{3}P$_0$ - 2p^4 ^{3}P$_1$	23.3753	23.3833	23.4302	1.597E+12	1.568E+12	1.440E+12
[1s]2p^5 ^{3}P$_1$ - 2p^4 ^{3}P$_1$	23.3759	23.3839	23.4308	3.992E+11	3.921E+11	3.601E+11
[1s]2p^5 ^{3}P$_1$ - 2p^4 ^{3}P$_0$	23.3763	23.3843	23.4311	5.326E+11	5.231E+11	4.806E+11
[1s]2p^5 ^{3}P$_2$ - 2p^4 ^{3}P$_2$	23.3763	23.3843	23.4312	1.197E+12	1.176E+12	1.080E+12
[1s]2p^5 ^{3}P$_2$ - 2p^4 ^{3}P$_1$	23.3770	23.3851	23.4319	3.994E+11	3.924E+11	3.605E+11
[1s]2p^5 ^{1}P$_1$ - 2p^4 ^{1}S$_0$	23.3940	23.4001	23.4382	5.923E+11	5.884E+11	5.704E+11
O II						
[1s]2p^4 ^{2}P$_{1/2}$ - 2p^3 ^{2}D$_{3/2}$	23.1144	23.1241	23.1788	2.534E+12	2.513E+12	2.407E+12
[1s]2p^4 ^{2}P$_{3/2}$ - 2p^3 ^{2}D$_{3/2}$	23.1159	23.1256	23.1802	2.541E+11	2.521E+11	2.426E+11
[1s]2p^4 ^{2}P$_{3/2}$ - 2p^3 ^{2}D$_{5/2}$	23.1159	23.1256	23.1803	2.342E+12	2.321E+12	2.224E+12
[1s]2p^4 ^{2}S$_{1/2}$ - 2p^3 ^{2}P$_{1/2}$	23.1204	23.1303	23.1858	6.302E+11	6.231E+11	5.890E+11
[1s]2p^4 ^{2}S$_{1/2}$ - 2p^3 ^{2}P$_{3/2}$	23.1204	23.1303	23.1858	1.372E+12	1.358E+12	1.289E+12
[1s]2p^4 ^{2}D$_{5/2}$ - 2p^3 ^{2}D$_{3/2}$	23.1636	23.1734	23.2286	9.126E+10	9.033E+10	8.579E+10
[1s]2p^4 ^{2}D$_{5/2}$ - 2p^3 ^{2}D$_{5/2}$	23.1636	23.1734	23.2287	1.389E+12	1.375E+12	1.307E+12
[1s]2p^4 ^{2}D$_{3/2}$ - 2p^3 ^{2}D$_{3/2}$	23.1638	23.1736	23.2288	1.376E+12	1.362E+12	1.293E+12
[1s]2p^4 ^{2}D$_{3/2}$ - 2p^3 ^{2}D$_{5/2}$	23.1638	23.1736	23.2289	1.259E+11	1.247E+11	1.191E+11
[1s]2p^4 ^{2}P$_{1/2}$ - 2p^3 ^{2}P$_{1/2}$	23.1759	23.1852	23.2376	1.054E+12	1.047E+12	1.013E+12
[1s]2p^4 ^{2}P$_{1/2}$ - 2p^3 ^{2}P$_{3/2}$	23.1759	23.1852	23.2376	5.130E+11	5.093E+11	4.910E+11
[1s]2p^4 ^{2}P$_{3/2}$ - 2p^3 ^{2}P$_{1/2}$	23.1774	23.1867	23.2390	2.676E+11	2.657E+11	2.563E+11
[1s]2p^4 ^{2}P$_{3/2}$ - 2p^3 ^{2}P$_{3/2}$	23.1774	23.1867	23.2391	1.237E+12	1.229E+12	1.188E+12
[1s]2p^4 ^{4}P$_{1/2}$ - 2p^3 ^{4}S$_{3/2}$	23.2124	23.2227	23.2807	9.524E+11	9.400E+11	8.801E+11
[1s]2p^4 ^{4}P$_{3/2}$ - 2p^3 ^{4}S$_{3/2}$	23.2131	23.2234	23.2814	9.523E+11	9.399E+11	8.801E+11
[1s]2p^4 ^{4}P$_{5/2}$ - 2p^3 ^{4}S$_{3/2}$	23.2143	23.2246	23.2825	9.521E+11	9.397E+11	8.800E+11
[1s]2p^4 ^{2}D$_{5/2}$ - 2p^3 ^{2}P$_{3/2}$	23.2254	23.2348	23.2877	5.013E+11	4.973E+11	4.781E+11
[1s]2p^4 ^{2}D$_{3/2}$ - 2p^3 ^{2}P$_{1/2}$	23.2256	23.2350	23.2879	3.980E+11	3.949E+11	3.800E+11
[1s]2p^4 ^{2}D$_{3/2}$ - 2p^3 ^{2}P$_{3/2}$	23.2256	23.2350	23.2879	8.319E+10	8.247E+10	7.888E+10
O III						
[1s]2p^3 ^{1}P$_1$ - 2p^2 ^{1}D$_2$	22.8154	22.8267	22.8887	1.982E+12	1.967E+12	1.890E+12
[1s]2p^3 ^{3}S$_1$ - 2p^2 ^{3}P$_0$	22.8748	22.8862	22.9485	4.582E+11	4.554E+11	4.428E+11
[1s]2p^3 ^{3}S$_1$ - 2p^2 ^{3}P$_1$	22.8754	22.8868	22.9491	1.458E+12	1.449E+12	1.405E+12
[1s]2p^3 ^{3}S$_1$ - 2p^2 ^{3}P$_2$	22.8766	22.8880	22.9503	2.736E+12	2.717E+12	2.621E+12
[1s]2p^3 ^{3}P$_1$ - 2p^2 ^{3}P$_0$	22.8897	22.9011	22.9637	4.266E+11	4.225E+11	4.011E+11
[1s]2p^3 ^{3}P$_2$ - 2p^2 ^{3}P$_1$	22.8902	22.9016	22.9642	2.660E+11	2.636E+11	2.515E+11
[1s]2p^3 ^{3}P$_0$ - 2p^2 ^{3}P$_1$	22.8903	22.9017	22.9642	1.143E+12	1.132E+12	1.079E+12
[1s]2p^3 ^{3}P$_1$ - 2p^2 ^{3}P$_1$	22.8903	22.9017	22.9643	3.956E+11	3.918E+11	3.702E+11
[1s]2p^3 ^{1}D$_2$ - 2p^2 ^{1}D$_2$	22.8908	22.9021	22.9636	3.479E+12	3.455E+12	3.340E+12
[1s]2p^3 ^{3}P$_2$ - 2p^2 ^{3}P$_2$	22.8914	22.9028	22.9653	8.768E+11	8.684E+11	8.277E+11
[1s]2p^3 ^{3}P$_1$ - 2p^2 ^{3}P$_2$	22.8915	22.9029	22.9654	3.373E+11	3.342E+11	3.225E+11
[1s]2p^3 ^{1}P$_1$ - 2p^2 ^{1}S$_0$	22.9227	22.9338	22.9943	1.535E+12	1.525E+12	1.480E+12
[1s]2p^3 ^{3}D$_1$ - 2p^2 ^{3}P$_0$	22.9663	22.9776	23.0395	6.370E+11	6.319E+11	6.066E+11

Transition	λ (Å)			A_{ki} (s^{-1})		
	$\mu = 0.0$	$\mu = 0.1$	$\mu = 0.25$	$\mu = 0.0$	$\mu = 0.1$	$\mu = 0.25$
[1s]2p^3 ^{3}D$_2$ - 2p^2 ^{3}P$_1$	22.9669	22.9782	23.0400	8.592E+11	8.522E+11	8.181E+11
[1s]2p^3 ^{3}D$_1$ - 2p^2 ^{3}P$_1$	22.9669	22.9782	23.0401	4.554E+11	4.518E+11	4.341E+11
[1s]2p^3 ^{3}D$_3$ - 2p^2 ^{3}P$_2$	22.9680	22.9792	23.0410	1.119E+12	1.110E+12	1.067E+12
[1s]2p^3 ^{3}D$_2$ - 2p^2 ^{3}P$_2$	22.9681	22.9794	23.0412	2.607E+11	2.587E+11	2.488E+11
[1s]2p^3 ^{3}D$_1$ - 2p^2 ^{3}P$_2$	22.9682	22.9794	23.0413	2.776E+10	2.755E+10	2.651E+10
O IV						
[1s]2p^2 ^{2}S$_{1/2}$ - 2p ^{2}P$_{1/2}$	22.5066	22.5192	22.5869	3.799E+11	3.772E+11	3.636E+11
[1s]2p^2 ^{2}S$_{1/2}$ - 2p ^{2}P$_{3/2}$	22.5087	22.5214	22.5890	9.693E+11	9.607E+11	9.194E+11
[1s]2p^2 ^{2}P$_{3/2}$ - 2p ^{2}P$_{1/2}$	22.5567	22.5695	22.6379	6.296E+11	6.259E+11	6.072E+11
[1s]2p^2 ^{2}P$_{1/2}$ - 2p ^{2}P$_{1/2}$	22.5587	22.5716	22.6399	2.703E+12	2.686E+12	2.602E+12
[1s]2p^2 ^{2}P$_{3/2}$ - 2p ^{2}P$_{3/2}$	22.5588	22.5717	22.6400	3.323E+12	3.303E+12	3.203E+12
[1s]2p^2 ^{2}P$_{1/2}$ - 2p ^{2}P$_{3/2}$	22.5609	22.5737	22.6420	1.246E+12	1.239E+12	1.204E+12
[1s]2p^2 ^{2}D$_{3/2}$ - 2p ^{2}P$_{1/2}$	22.6310	22.6437	22.7113	1.102E+12	1.094E+12	1.058E+12
[1s]2p^2 ^{2}D$_{5/2}$ - 2p ^{2}P$_{3/2}$	22.6330	22.6457	22.7132	1.286E+12	1.277E+12	1.235E+12
[1s]2p^2 ^{2}D$_{3/2}$ - 2p ^{2}P$_{3/2}$	22.6331	22.6458	22.7134	1.862E+11	1.850E+11	1.791E+11
O V						
[1s]2p ^{1}P$_1$ - 2s^2 ^{1}S$_0$	22.2088	22.2229	22.2960	2.884E+12	2.868E+12	2.786E+12
O VI						
[1s]2s2p ^{2}P$_{3/2}$ - 2s ^{2}S$_{1/2}$	21.7832	21.7998	21.8840	6.424E+11	6.368E+11	6.109E+11
[1s]2s2p ^{2}P$_{1/2}$ - 2s ^{2}S$_{1/2}$	21.7836	21.8002	21.8844	6.792E+11	6.735E+11	6.467E+11
[1s]2s2p ^{2}P$_{3/2}$ - 2s ^{2}S$_{1/2}$	21.9706	21.9860	22.0646	2.694E+12	2.680E+12	2.609E+12
[1s]2s2p ^{2}P$_{1/2}$ - 2s ^{2}S$_{1/2}$	21.9730	21.9884	22.0669	2.657E+12	2.643E+12	2.573E+12
O VII						
1s2p ^{1}P$_1$ - 1s^2 ^{1}S$_0$	21.5642	21.5821	21.6707	3.702E+12	3.680E+12	3.574E+12

Table 4.8: Plasma effects on the radiative wavelengths (in Å) for the most intense Kα lines in O VI and O VII computed by MCDF/RATIP and AUTOSTRUCTURE (the screening parameter μ is expressed in a.u.).

Ion	Transition	MCDF/RATIP		AST	
		$\mu = 0.0$	$\mu = 0.1$	$\mu = 0.0$	$\mu = 0.1$
O VI	1s(^{2}S)2s2p(^{3}P) ^{2}P$_{1/2}$ - 1s^{2}2s ^{2}S$_{1/2}$	21.9706	21.9860	22.0743	22.0893
O VI	1s(^{2}S)2s2p(^{3}P) ^{2}P$_{3/2}$ - 1s^{2}2s ^{2}S$_{1/2}$	21.9730	21.9884	22.0723	22.0873
O VII	1s2p ^{1}P$_1$ - 1s^2 ^{1}S$_0$	21.5642	21.5821	21.6595	21.6766

Table 4.9: Plasma effects on the radiative rates (in s^{-1}) for the most intense Kα lines in O VI and O VII computed by MCDF/RATIP and AUTOSTRUCTURE (the screening parameter μ is expressed in a.u.).

		MCDF/RATIP		AST	
Ion	Transition	$\mu = 0.0$	$\mu = 0.1$	$\mu = 0.0$	$\mu = 0.1$
O VI	1s(^{2}S)2s2p(^{3}P) ^{2}P$_{1/2}$ - 1s^{2}2s ^{2}S$_{1/2}$	2.66E+12	2.64E+12	2.66E+12	2.64E+12
O VI	1s(^{2}S)2s2p(^{3}P) ^{2}P$_{3/2}$ - 1s^{2}2s ^{2}S$_{1/2}$	2.69E+12	2.68E+12	2.68E+12	2.67E+12
O VII	1s2p ^{1}P$_1$ - 1s^2 ^{1}S$_0$	3.70E+12	3.68E+12	3.46E+12	3.44E+12

4.2.3   K-vacancy level energies and Auger widths

Table 4.10 reports the data related to the plasma effects on the energies and Auger widths of K-vacancy states in the oxygen ions (O I – O VI). The K-vacancy level energy decrease is found to be small (less than 3 eV) for $\mu = 0.1$ and $\mu = 0.25$, with an increasing trend with Z_{eff}, as illustrated in Figure 4.10. Regarding the K-vacancy Auger widths, one can note by looking at the above-mentioned tables and Figure 4.11 that they are reduced on average by up to 10% for $\mu = 0.25$ a.u., which might have an impact on spectral K-line modeling. The neutral oxygen ($Z_{\text{eff}} = 1$) has a slightly different situation as MCDF/RATIP predicts a 20% decrease for $\mu = 0.25$ a.u. As mentioned in Section 4.1, this may illustrate the difficulty to accurately compute atomic process rates at the neutral end of an isonuclear sequence.

Table 4.10: Plasma environment effects on the energy and Auger widths (A^{a}) of K-vacancy states in oxygen ions

Level	E (eV)			A^{a} (s^{-1})		
	$\mu = 0.0$	$\mu = 0.1$	$\mu = 0.25$	$\mu = 0.0$	$\mu = 0.1$	$\mu = 0.25$
O I						
[1s]2p^5 ^{3}P$_2$	530.39	530.20	529.14	2.606E+14	2.528E+14	2.104E+14
[1s]2p^5 ^{3}P$_1$	530.41	530.23	529.17	2.613E+14	2.536E+14	2.124E+14
[1s]2p^5 ^{3}P$_0$	530.43	530.24	529.18	2.587E+14	2.513E+14	2.110E+14
[1s]2p^5 ^{1}P$_1$	534.13	533.94	532.87	2.086E+14	2.037E+14	1.832E+14
O II						
[1s]2p^4 ^{4}P$_{5/2}$	534.08	533.85	532.52	2.489E+14	2.405E+14	2.202E+14
[1s]2p^4 ^{4}P$_{3/2}$	534.11	533.87	532.54	2.474E+14	2.392E+14	2.191E+14
[1s]2p^4 ^{4}P$_{1/2}$	534.12	533.89	532.55	2.475E+14	2.394E+14	2.194E+14
[1s]2p^4 ^{2}D$_{3/2}$	539.22	538.96	537.51	3.004E+14	2.928E+14	2.680E+14
[1s]2p^4 ^{2}D$_{5/2}$	539.22	538.96	537.51	3.011E+14	2.935E+14	2.686E+14
[1s]2p^4 ^{2}P$_{3/2}$	540.33	540.07	538.63	2.050E+14	1.975E+14	1.804E+14
[1s]2p^4 ^{2}P$_{1/2}$	540.37	540.11	538.66	2.041E+14	1.969E+14	1.798E+14
[1s]2p^4 ^{2}S$_{1/2}$	541.65	541.38	539.85	3.014E+14	2.924E+14	2.578E+14

Table 4.10: (continued)

Transition	E (eV)			A^{a} (s^{-1})		
	$\mu = 0.0$	$\mu = 0.1$	$\mu = 0.25$	$\mu = 0.0$	$\mu = 0.1$	$\mu = 0.25$
O III						
$[1s]2p^3\ ^3D_1$	539.86	539.59	538.14	2.969E+14	2.903E+14	2.719E+14
$[1s]2p^3\ ^3D_2$	539.86	539.59	538.14	2.957E+14	2.891E+14	2.709E+14
$[1s]2p^3\ ^3D_3$	539.86	539.59	538.15	2.974E+14	2.908E+14	2.724E+14
$[1s]2p^3\ ^3P_1$	541.66	541.39	539.92	2.746E+14	2.682E+14	2.500E+14
$[1s]2p^3\ ^3P_0$	541.66	541.39	539.92	2.733E+14	2.669E+14	2.488E+14
$[1s]2p^3\ ^3P_2$	541.66	541.39	539.92	2.746E+14	2.681E+14	2.499E+14
$[1s]2p^3\ ^3S_1$	542.02	541.74	540.27	1.050E+14	1.031E+14	9.827E+13
$[1s]2p^3\ ^1D_2$	544.59	544.30	542.76	2.562E+14	2.505E+14	2.350E+14
$[1s]2p^3\ ^1P_1$	546.38	546.09	544.52	2.389E+14	2.333E+14	2.177E+14
O IV						
$[1s]2p^2\ ^2D_{3/2}$	547.85	547.54	545.91	2.617E+14	2.552E+14	2.392E+14
$[1s]2p^2\ ^2D_{5/2}$	547.86	547.55	545.92	2.622E+14	2.556E+14	2.395E+14
$[1s]2p^2\ ^2P_{1/2}$	549.61	549.29	547.63	1.054E+14	1.033E+14	9.766E+13
$[1s]2p^2\ ^2P_{3/2}$	549.66	549.34	547.68	1.054E+14	1.032E+14	9.762E+13
$[1s]2p^2\ ^2S_{1/2}$	550.88	550.57	548.92	2.239E+14	2.179E+14	2.029E+14
O V						
$[1s]2p\ ^1P_1$	558.26	557.92	556.08	1.196E+14	1.168E+14	1.095E+14
O VI						
$[1s]2s2p\ ^2P_{1/2}$	564.25	563.87	561.86	3.902E+13	3.677E+13	3.360E+13
$[1s]2s2p\ ^2P_{3/2}$	564.32	563.93	561.92	3.651E+13	3.434E+13	3.128E+13
$[1s]2s2p\ ^2P_{1/2}$	569.16	568.73	566.55	9.593E+13	9.544E+13	9.314E+13
$[1s]2s2p\ ^2P_{3/2}$	569.17	568.74	566.56	9.701E+13	9.649E+13	9.414E+13
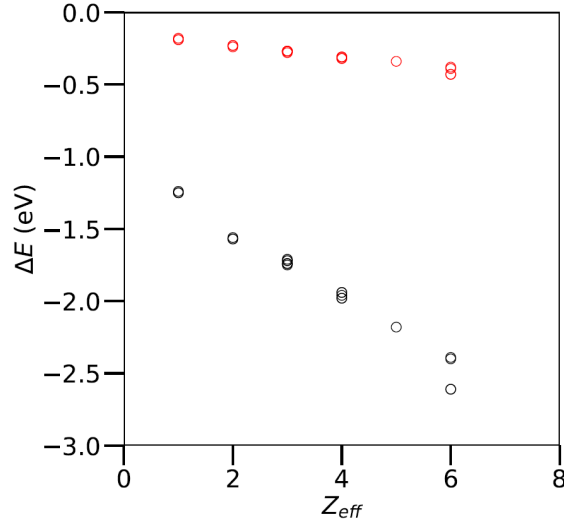
Figure 4.10: MCDF/RATIP computed shift of the K-vacancy level energies ($\Delta E = E(\mu) - E(\mu = 0)$ in oxygen ions as a function of the effective charge $Z_{\text{eff}} = Z - N + 1$ for two different values of the screening parameter μ (in a.u.), namely $\mu = 0.1$ a.u. (*red*) and $\mu = 0.25$ a.u. (*black*)
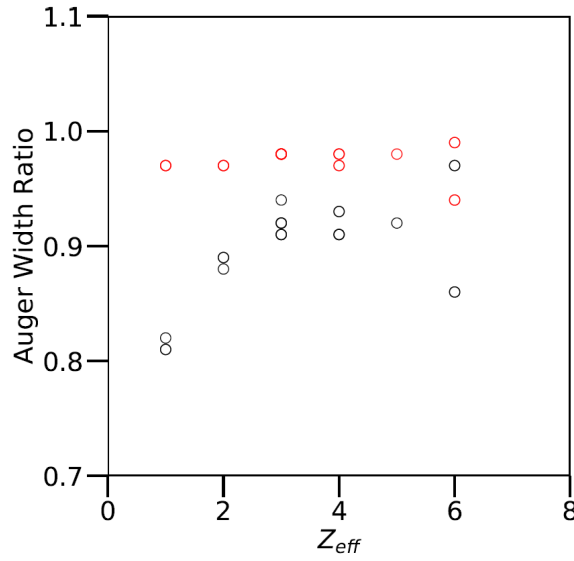
Figure 4.11: MCDF/RATIP Auger width ratio $A^{\text{a}}(\mu)/A^{\text{a}}(\mu = 0)$ for oxygen K-vacancy levels as a function of the effective charge $Z_{\text{eff}} = Z - N + 1$ for two different values of the screening parameter μ (in a.u.), namely $\mu = 0.1$ a.u. (*red*) and $\mu = 0.25$ a.u. (*black*)

4.2.4 Final remarks and summary

In this chapter, we showed that the main effect of the plasma environment on the atomic parameters involved in K-line formation in oxygen ions is the lowering of both the ionization potential and the K-shell threshold. They are both found to decrease by up to about 50 eV for the most "extreme" plasma conditions considered in this work ($\mu = 0.25$ a.u.), which correspond to the expected physical conditions within the accretion disks surrounding black holes. This should modify the ionization balance of the astrophysical plasma, for example. The computed K-line redshifts are small (up to 100 mÅ) but can be detectable by the new generation of X-ray microcalorimeters that will be used in the future astrophysical X-ray observatories. However, the radiative rate variations are too small to imply any modification in the modeling of X-ray astrophysical spectra. Finally, the K-vacancy state Auger widths are reduced by about 10% in the whole, which might have an impact on K-line modeling since it may affect the competition between the fluorescent K-line emission (radiative channel) and the autoionization process (Auger channel). Nevertheless, the precise impact of such findings can only really be estimated through further complex astrophysical modelings that would incorporate the modifications that we computed in this work. Let us also notice that the results obtained in this chapter have recently been published (Deprince *et al.* 2018; Deprince *et al.* 2019a).

Chapter 5

Plasma environment effects on the atomic parameters involving the K shell in iron ions

In this chapter, we present the effects of the plasma environment (for physical conditions such as those expected in accretion disks around black holes) on the atomic parameters involved in K-line emission by iron ions. More precisely, the plasma effects on the ionization potentials, K thresholds, radiative parameters and Auger widths in all the ionization stages of iron ions (from the singly ionized Fe II to the He-like Fe XXV) estimated by our MDCF/RATIP method are discussed in Section 5.1, Section 5.2 and Section 5.3 for the ions Fe XVII – Fe XXV, Fe IX – Fe XVI and Fe II – Fe VIII, respectively. Actually, these three types of ions have been treated with different computational strategies as their atomic structures become more complex due to the successive filling of the 1s, 2s and 2p subshells for Fe XVII – Fe XXV, the 3s and 3p subshells for Fe IX – Fe XVI, and the 3d and 4s subshells for Fe II – Fe VIII. In Section 5.4, the plasma environment effects on the K-shell photoionization cross sections of Fe XXIV are presented. Finally, Section 5.5 presents the main astrophysical (expected or potential) implications of the results we obtained in this work concerning the K-shell processes in iron ions.

5.1   Fe XVII – Fe XXV

The MCDF expansions used to model the atomic structures of Fe XVII – Fe XXV (Ne- through He-like iron ions) have been obtained with the active space (AS) method, using a similar strategy than for the oxygen ions as described in Section 4.1. These AS are built up by considering all the single and double excitations from the spectroscopic configurations, *i.e.* the configurations for which we want

Table 5.1: Reference configurations used to build up the MCDF active spaces (AS) for Fe XVII – Fe XXV and corresponding total number of CSFs within the multiconfiguration model.

Ion	Reference configurations	Number of CSFs
Fe XVII	$1s^22s^22p^6$, $1s^22s^22p^53s$, $1s^22s^22p^53p$, $1s2s^22p^63s$, $1s2s^22p^63p$	12564
Fe XVIII	$1s^22s^22p^5$, $1s2s^22p^6$	2638
Fe XIX	$1s^22s^22p^4$, $1s^22s2p^5$, $1s^22p^6$, $1s2s^22p^5$, $1s2s2p^6$	6013
Fe XX	$1s^22s^22p^3$, $1s^22s2p^4$, $1s^22p^5$, $1s2s^22p^4$, $1s2s2p^5$, $1s2p^6$	7389
Fe XXI	$1s^22s^22p^2$, $1s^22s2p^3$, $1s^22p^4$, $1s2s^22p^3$, $1s2s2p^4$, $1s2p^5$	6730
Fe XXII	$1s^22s^22p$, $1s^22s2p^2$, $1s^22p^3$, $1s2s^22p^2$, $1s2s2p^3$, $1s2p^4$	4107
Fe XXIII	$1s^22s^2$, $1s^22s2p$, $1s^22p^2$, $1s2s^22p$, $1s2s2p^2$, $1s2p^3$	1847
Fe XXIV	$1s^22s$, $1s^22p$, $1s2s2p$, $1s2p^2$	515
Fe XXV	$1s^2$, $1s2s$, $1s2p$	98

to compute the properties, to the $n = 3$ configuration space. The list of reference configurations (*i.e.* the spectroscopic configurations) for each ionic system is specified in Table 5.1, along with the total number of CSFs in the corresponding MCDF expansion. Computations are carried out with the extended average level (EAL) option optimizing a weighted trace of the Hamiltonian using level weights proportional to $(2J + 1)$, and they are completed with the inclusion of the relativistic two-body Breit interaction and the quantum electrodynamic corrections (QED) due to the self-energy and vacuum polarization (see Section 2.1.3). The MCDF ionic bound states generated by GRASP2K are then used in RATIP to compute the atomic structure, the radiative wavelengths and rates and the Auger parameters associated with K-vacancy states, as described in Chapter 2.

The ionization potentials and K thresholds that we computed for the screening parameters $\mu = 0$ a.u. (isolated atomic system), $\mu = 0.1$ a.u. and $\mu = 0.25$ a.u. are respectively reported in Tables 5.2 and Table 5.3. For the isolated ions,

Table 5.2: Computed ionization potentials (eV) for Fe XVII – Fe XXV as a function of the plasma screening parameter μ (a.u.)

Ion	NIST[a]	$\mu = 0.0$	$\mu = 0.1$	$\mu = 0.25$
Fe XVII	1262.7(7)	1260.58	1214.75	1147.80
Fe XVIII	1357.8(1.9)	1357.09	1308.56	1237.68
Fe XIX	1460(3)	1459.12	1407.92	1333.09
Fe XX	1575.6(5)	1573.48	1519.58	1440.80
Fe XXI	1687(1)	1689.13	1632.53	1549.75
Fe XXII	1798.4(8)	1797.82	1738.54	1651.80
Fe XXIII	1950.4(1.8)	1950.49	1888.61	1798.43
Fe XXIV	2045.759(7)	2044.34	1979.79	1885.77
Fe XXV	8828.1875(11)	8836.74	8768.90	8667.86

[a] Kramida *et al.* (2019)

we reproduce the IPs listed in the NIST spectroscopic database with an accuracy better than 0.2%. The inclusion of the DH potential leads to reductions of the IP and K-threshold energies when μ increases. A lowering ranging from $\sim$ 45 to 70 eV for $\mu = 0.1$ a.u. and from about 110 eV to 170 eV for $\mu = 0.25$ a.u. is found, which is a substantial decrease. This corresponds to relative variations of 3–4% and 8–9% for $\mu = 0.1$ and $\mu = 0.25$, respectively, except for Fe XXV, for which the reduction is less than 2% as a consequence of its large IP (about 8800 eV). For the same reason, the K-threshold relative reductions are also only marginal ($< 2\%$), but considerable in an absolute scale.

Table 5.3: Computed K thresholds (eV) for Fe XVII – Fe XXV as a function of the plasma screening parameter μ (a.u.).

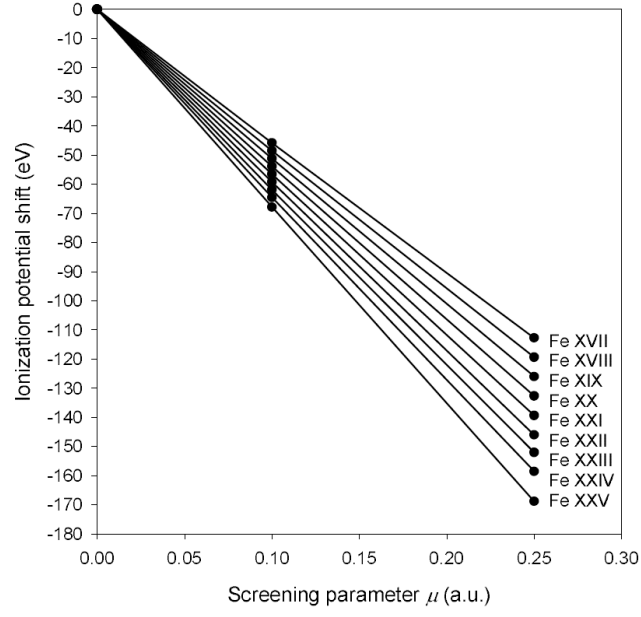| Ion	$\mu = 0.0$	$\mu = 0.1$	$\mu = 0.25$
Fe XVII	7697.64	7651.45	7582.46
Fe XVIII	7827.06	7778.17	7705.19
Fe XIX	7959.86	7908.27	7831.30
Fe XX	8095.41	8041.11	7960.14
Fe XXI	8246.57	8189.56	8104.56
Fe XXII	8398.74	8339.03	8250.02
Fe XXIII	8558.75	8496.29	8403.31
Fe XXIV	8689.49	8624.26	8527.21
Fe XXXV	8836.74	8768.90	8667.86

Figure 5.1: Ionization potential lowering in Fe XVII – Fe XXV as a function of the plasma screening parameter μ.
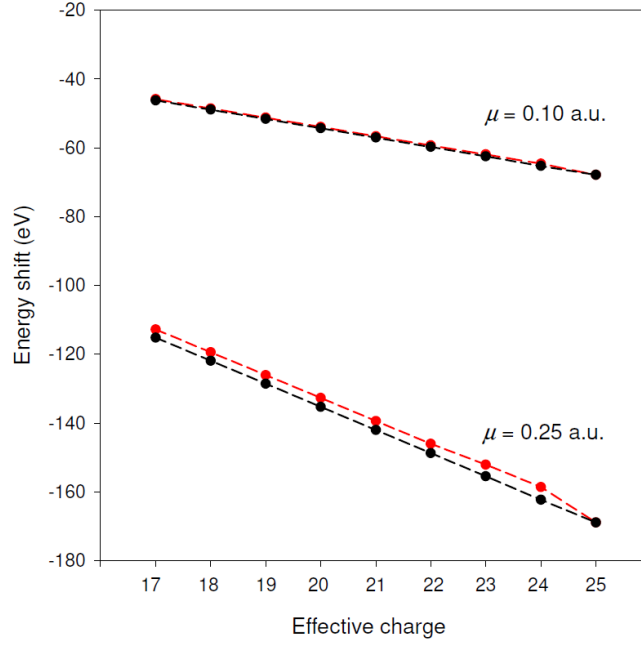
Figure 5.2: Ionization potential (*red points*) and K-threshold (*black points*) energy shifts in Fe XVII – Fe XXV as a function of effective charge Z_{eff} for $\mu = 0.1$ a.u. and $\mu = 0.25$ a.u.

This ionization threshold (IP and K-threshold) lowering is a well-known phenomenon in dense-plasma physics, whose behavior is further illustrated in Figure 5.1 and Figure 5.2. For each of the ionic species considered, the DH potential predicts a linear decrease of the IP downshift with μ, with a steeper slope when the ionic charge is greater (see Figure 5.1). However, as shown in Figure 5.2, the IP-shift variation with effective ionic charge $Z_{\text{eff}} = Z - N + 1$ for a particular μ is only moderate, i.e. $\sim 30\%$. On the other hand, we find that, for any specific ionic species, the IP and K-threshold energy shifts are practically the same (see Figure 5.2).

It is interesting to highlight the fact that the inclusion of the electron–electron Debye screening effect in our calculations, in addition to that of the electron–nucleus, leads to a substantially less pronounced IP lowering, *i.e.* 4% in Fe XXV to 35% in Fe XVII in the case $\mu = 0.25$ a.u., as shown in Table 5.4. As expected, this discrepancy grows inversely with Z_{eff} as the number of interacting electron–electron pairs is larger for the lower charge states. This effect has already been underlined in Chapter 4 for the oxygen isonuclear sequence and in Section 3.3, where we stressed the necessity to take into account the electron–electron screening effect along with the electron–nucleus one.

Computed wavelengths and transition probabilities for the strongest K lines ($A > 10^{13}$ s^{-1}) of Fe XVII – Fe XXV for the three screening parameter values $\mu = 0$ a.u., $\mu = 0.1$ a.u. and $\mu = 0.25$ a.u. are listed in Table 5.5. When comparing our data for the isolated ion ($\mu = 0$) with those taken from Palmeri *et*

Table 5.4: Ionization potentials (eV) for Fe XVII – Fe XXV computed with the DH nucleus–electron screening and with and without the electron–electron screening. The parameters μ_{ne} and μ_{ee} correspond to the screening parameter μ (a.u.) for the electron–nucleus and the electron–electron interactions, respectively

Ion	$\mu_{ne} = 0.1$ $\mu_{ee} = 0.0$	$\mu_{ne} = 0.1$ $\mu_{ee} = 0.1$	$\mu_{ne} = 0.25$ $\mu_{ee} = 0.00$	$\mu_{ne} = 0.25$ $\mu_{ee} = 0.25$
Fe XVII	1190.72	1214.75	1089.22	1147.80
Fe XVIII	1287.21	1308.56	1185.55	1237.68
Fe XIX	1389.10	1407.92	1287.41	1333.09
Fe XX	1503.54	1519.58	1401.59	1440.80
Fe XXI	1619.15	1632.53	1517.02	1549.75
Fe XXII	1727.82	1738.54	1625.57	1651.80
Fe XXIII	1880.58	1888.61	1778.76	1798.43
Fe XXIV	1974.41	1979.79	1872.58	1885.77
Fe XXV	8766.28	8768.90	8661.14	8667.86

al. (2003a) and Mendoza *et al.* (2004), who used the pseudo-relativistic Hartree-Fock (HFR) method, a good agreement is generally found. For the transitions given in Table 5.5, the wavelengths agree to better than 0.1%, while the transition probabilities differ by 10–20%, up to 25% in a few cases. Since we took into account similar configuration-interaction effects in our atomic models as Palmeri *et al.* (2003a) and Mendoza *et al.* (2004), the main discrepancy source must be attributed to relativistic effects, which are strictly and fully treated in the MCDF method (unlike in HFR). Furthermore, we find excellent agreement (within 5%) among our A-values computed in the Babushkin and Coulomb gauges (although only transition probabilities obtained in the Babushkin gauge are reported in Table 5.5).

A close inspection of Table 5.5 brings out the rather small effects of the plasma environment on the K-line radiative parameters. For screening parameters $\mu = 0.1$ a.u. and $\mu = 0.25$ a.u., wavelengths appear to be redshifted by less than 0.1 mÅ and 1 mÅ in comparison to those of the isolated ion, respectively, while the variations of the radiative decay rates do not exceed a few percent. To illustrate this point, we show in Figure 5.3 the reddening of the [1s]3p $^1P_1$ - 2p^6 $^1S_0$ Kβ line in Fe XVII, which amounts to ~ 2 mÅ for $\mu = 0.25$. Similarly, for the [1s]2p^4 $^2D_{3/2}$ - 2p^3 $^2D_{3/2}$ and [1s]2p^4 $^2S_{1/2}$ - 2p^3 $^2P_{3/2}$ Kα lines in Fe XX displayed in Figure 5.4, the reddening is less than 1 mÅ. This illustrates that Kβ line wavelengths appear to be more sensitive to plasma effects compared to Kα line ones, as the Kβ redshifts are actually found to be twice as big as the Kα redshifts. This may be explained by the fact that outer $n = 3$ bound electrons involved in Kβ lines are more perturbed by the surrounding plasma electrons than $n = 2$ bound electrons.

It is shown in Figure 5.5 for the [1s]3p $^3P_0$ - [2p]3p $^3S_1$ and [1s]3p $^1P_1$ - 2p^6 $^1S_0$ lines in Fe XVII that the plasma effects on the radiative transition probabilities (A-values) are less than 1%, although they can increase or decrease their nominal values compared to the isolated ion case ($\mu = 0$). In Fe XXII, the changes are somewhat larger (3%) as illustrated in Figure 5.6 with the 1s2s2p^3 $^4S_{3/2}$ - [2s]2p^2 $^2D_{3/2}$ and 1s2s2p^3 $^2D_{5/2}$ - [2s]2p^2 $^2D_{5/2}$ lines.

The Auger widths computed for the K-vacancy levels for the screening parameters $\mu = 0$ a.u., $\mu = 0.1$, and $\mu = 0.25$ a.u. are tabulated in Table 5.6. Present widths for the isolated ion case ($\mu = 0$ a.u.) are found to be in good agreement (within 5%) with those computed previously with HFR by Palmeri *et al.* (2003a). The DH potential leads to more noticeable reductions of the Auger widths, namely by up to 3% and 10% for $\mu = 0.1$ a.u. and $\mu = 0.25$ a.u., respectively. This variation is exemplified in Figure 5.7 with the 1s2s2p^3 $^2D_{3/2}$ and 1s2s^{2}2p^2 $^4P_{5/2}$ K-vacancy levels in Fe XXII. We also find that the Auger widths for the higher ionization stages of iron seem to be more affected by the plasma environment. However, as shown in Table 5.7 for Fe XVII, Fe XVIII and Fe XIX, because of the
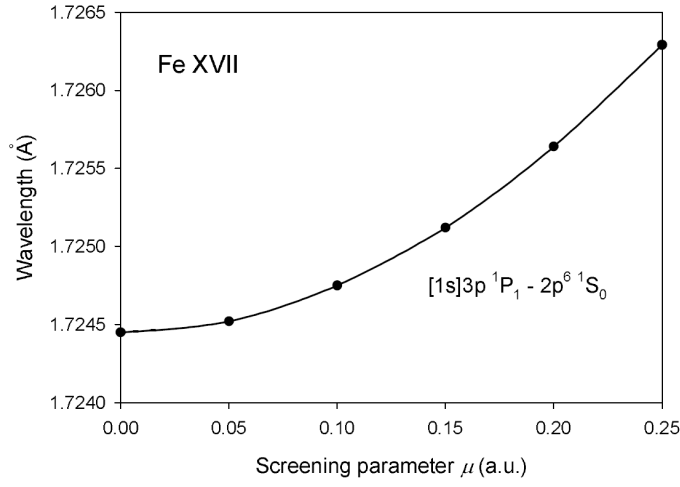
Figure 5.3: Wavelength reddening as a function of the plasma screening parameter μ for the $[1s]3p\ ^1P_1$ - $2p^6\ ^1S_0$ Kβ line in Fe XVII.
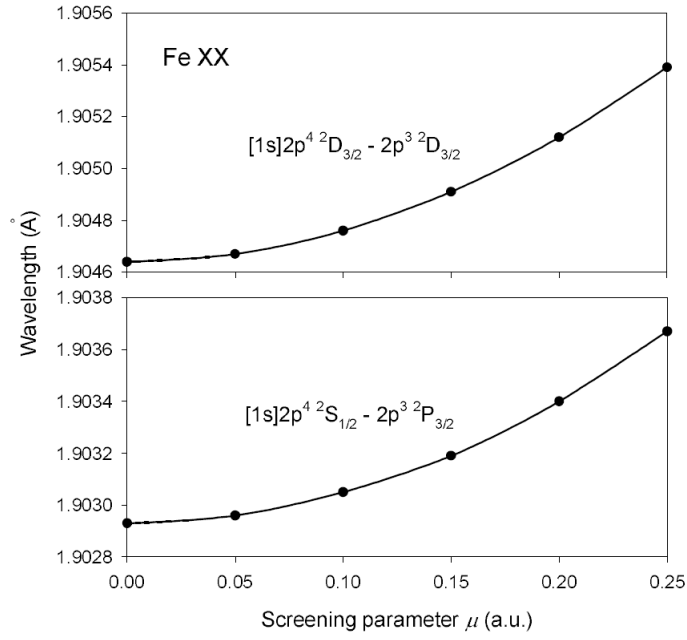
Figure 5.4: Wavelength reddening as a function of the plasma screening parameter μ for the $[1s]2p^4\ ^2D_{3/2}$ - $2p^3\ ^2D_{3/2}$ and $[1s]2p^4\ ^2S_{1/2}$ - $2p^3\ ^2P_{3/2}$ K$_\alpha$ lines in Fe XX.
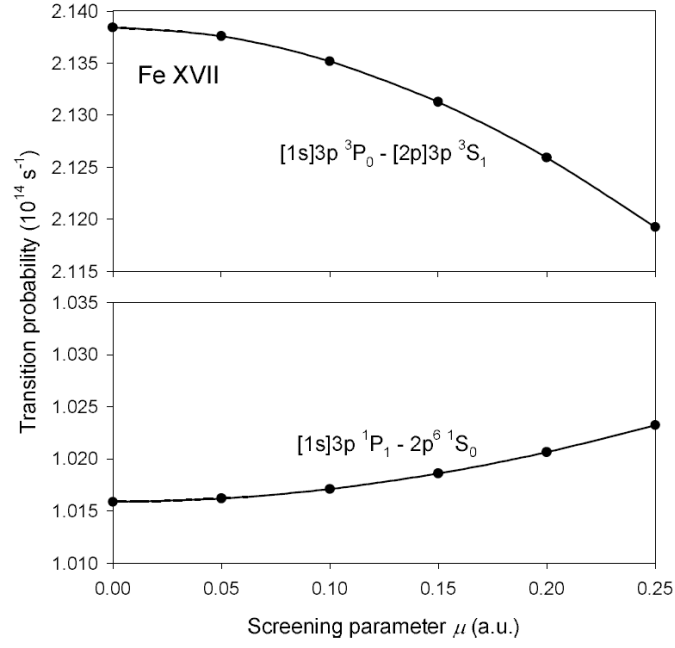
Figure 5.5: Variation of the radiative transition probability (A-value) with the plasma screening parameter μ for the [1s]3p $^3P_0$ - [2p]3p $^3S_1$ and [1s]3p $^1P_1$ - $2p^6$ $^1S_0$ lines in Fe XVII.
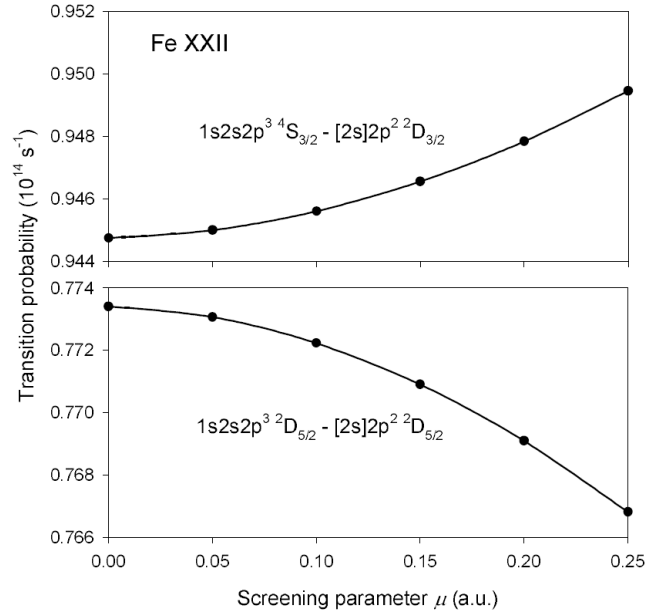
Figure 5.6: Variation of the transition probability (A-value) with the plasma screening parameter μ for the $1s2s2p^3$ $^4S_{3/2}$ - [2s]$2p^2$ $^2D_{3/2}$ and $1s2s2p^3$ $^2D_{5/2}$ - [2s]$2p^2$ $^2D_{5/2}$ lines in Fe XXII.

weak variations of both the radiative rates and Auger widths with μ, the K-line fluorescence yields (as defined in Equation 1.1) in the iron ions considered herein are hardly affected (3% at most).

Let us note that some of the results presented in this section have recently been published (Deprince *et al.* 2019b; Deprince *et al.* 2020a).

Figure 5.7: Variation of the Auger width with the plasma screening parameter μ for two K-vacancy levels in Fe XXII.

Table 5.5: Plasma environment effects on radiative wavelengths (λ) and transition probabilities (A_{ki}) of Kα lines in Fe XVII – Fe XXV computed with MCDF/RATIP depending on the plasma screening parameter μ (given in a.u.)

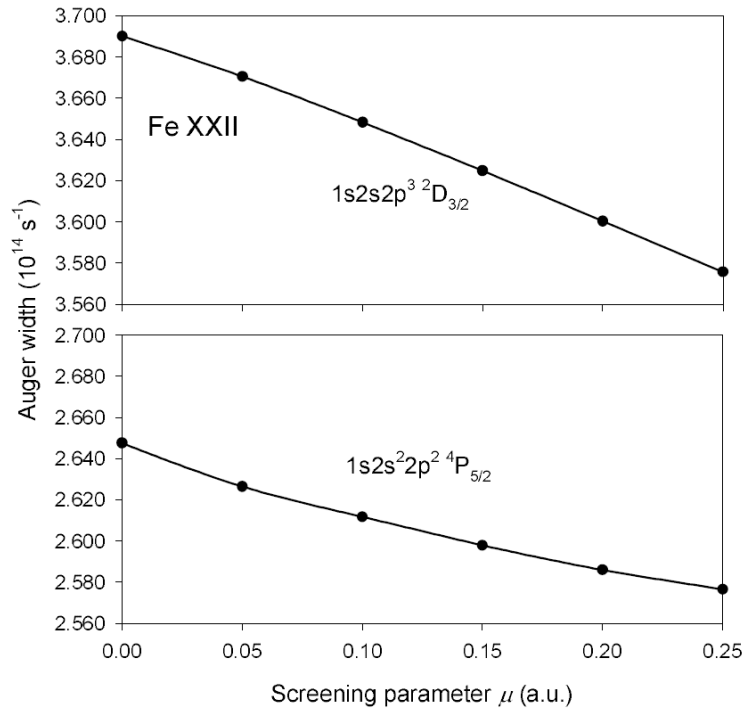| Transition	λ (Å)			A_{ki} (s^{-1})		
	$\mu = 0.0$	$\mu = 0.1$	$\mu = 0.25$	$\mu = 0.0$	$\mu = 0.1$	$\mu = 0.25$
Fe XVII						
[1s]3p ^{1}P$_1$ - 2p^6 ^{1}S$_0$	1.7244	1.7248	1.7263	1.016E+14	1.017E+14	1.023E+14
[1s]3p ^{1}P$_1$ - [2p]3p ^{3}S$_1$	1.9253	1.9254	1.9260	1.131E+13	1.130E+13	1.127E+13
[1s]3p ^{3}P$_2$ - [2p]3p ^{3}S$_1$	1.9263	1.9264	1.9270	2.370E+13	2.373E+13	2.386E+13
[1s]3p ^{1}P$_1$ - [2p]3p ^{3}D$_2$	1.9265	1.9267	1.9273	2.919E+13	2.927E+13	2.964E+13
[1s]3s ^{1}S$_0$ - [2p]3s ^{1}P$_1$	1.9268	1.9269	1.9275	3.225E+14	3.223E+14	3.211E+14
[1s]3p ^{3}P$_1$ - [2p]3p ^{3}S$_1$	1.9270	1.9271	1.9277	8.108E+13	8.109E+13	8.112E+13
[1s]3p ^{3}P$_0$ - [2p]3p ^{3}S$_1$	1.9272	1.9273	1.9279	2.138E+14	2.135E+14	2.119E+14
[1s]3p ^{1}P$_1$ - [2p]3p ^{1}P$_1$	1.9274	1.9275	1.9281	1.108E+14	1.107E+14	1.103E+14
[1s]3s ^{3}S$_1$ - [2p]3s ^{3}P$_2$	1.9278	1.9279	1.9285	3.401E+14	3.400E+14	3.394E+14
[1s]3p ^{3}P$_2$ - [2p]3p ^{3}D$_3$	1.9280	1.9281	1.9287	2.871E+14	2.870E+14	2.865E+14
[1s]3p ^{1}P$_1$ - [2p]3p ^{3}P$_2$	1.9280	1.9281	1.9287	1.505E+14	1.504E+14	1.497E+14
[1s]3p ^{3}P$_1$ - [2p]3p ^{3}D$_2$	1.9283	1.9284	1.9290	3.090E+14	3.088E+14	3.079E+14
[1s]3p ^{3}P$_2$ - [2p]3p ^{1}P$_1$	1.9284	1.9285	1.9291	1.453E+13	1.450E+13	1.435E+13
[1s]3s ^{3}S$_1$ - [2p]3s ^{1}P$_1$	1.9285	1.9286	1.9292	9.717E+13	9.718E+13	9.724E+13
[1s]3p ^{3}P$_2$ - [2p]3p ^{3}P$_2$	1.9290	1.9291	1.9297	9.841E+13	9.840E+13	9.834E+13
[1s]3p ^{3}P$_0$ - [2p]3p ^{1}P$_1$	1.9293	1.9294	1.9300	2.092E+14	2.094E+14	2.102E+14
[1s]3p ^{3}P$_1$ - [2p]3p ^{3}P$_2$	1.9297	1.9298	1.9304	2.434E+13	2.439E+13	2.461E+13
[1s]3p ^{1}P$_1$ - [2p]3p ^{3}P$_0$	1.9297	1.9298	1.9305	1.148E+13	1.143E+13	1.119E+13
[1s]3p ^{1}P$_1$ - [2p]3p ^{3}D$_1$	1.9302	1.9303	1.9309	3.116E+13	3.121E+13	3.145E+13
[1s]3s ^{1}S$_0$ - [2p]3s ^{3}P$_1$	1.9304	1.9305	1.9311	2.896E+14	2.896E+14	2.899E+14
[1s]3p ^{1}P$_1$ - [2p]3p ^{3}P$_1$	1.9312	1.9313	1.9319	5.188E+13	5.184E+13	5.167E+13
[1s]3p ^{1}P$_1$ - [2p]3p ^{3}D$_2$	1.9313	1.9314	1.9320	1.580E+14	1.580E+14	1.577E+14
[1s]3p ^{3}P$_1$ - [2p]3p ^{3}P$_0$	1.9315	1.9316	1.9322	5.507E+13	5.510E+13	5.523E+13
[1s]3s ^{3}S$_1$ - [2p]3s ^{3}P$_0$	1.9316	1.9317	1.9324	6.669E+13	6.667E+13	6.656E+13
[1s]3p ^{3}P$_1$ - [2p]3p ^{3}D$_1$	1.9319	1.9320	1.9327	1.099E+14	1.098E+14	1.093E+14
[1s]3s ^{3}S$_1$ - [2p]3s ^{3}P$_1$	1.9321	1.9322	1.9328	1.042E+14	1.042E+14	1.038E+14
[1s]3p ^{3}P$_0$ - [2p]3p ^{3}D$_1$	1.9321	1.9322	1.9328	1.694E+14	1.693E+14	1.689E+14
[1s]3p ^{3}P$_2$ - [2p]3p ^{3}P$_1$	1.9322	1.9323	1.9329	7.919E+13	7.915E+13	7.896E+13
[1s]3p ^{3}P$_2$ - [2p]3p ^{3}D$_2$	1.9323	1.9324	1.9331	1.014E+14	1.013E+14	1.010E+14
[1s]3p ^{3}P$_0$ - [2p]3p ^{3}P$_1$	1.9331	1.9332	1.9338	1.615E+13	1.619E+13	1.637E+13
[1s]3p ^{1}P$_1$ - [2p]3p ^{1}S$_0$	1.9380	1.9381	1.9388	4.421E+13	4.421E+13	4.421E+13
[1s]3p ^{3}P$_1$ - [2p]3p ^{1}S$_0$	1.9398	1.9399	1.9406	1.056E+13	1.051E+13	1.029E+13
Fe XVIII						
[1s]2p^6 ^{2}S$_{1/2}$ - 2p^5 ^{2}P$_{3/2}$	1.9262	1.9263	1.9268	4.116E+14	4.115E+14	4.103E+14
[1s]2p^6 ^{2}S$_{1/2}$ - 2p^5 ^{2}P$_{1/2}$	1.9301	1.9302	1.9307	2.018E+14	2.017E+14	2.012E+14
Fe XIX						
1s2s2p^6 ^{1}S$_0$ - [2s]2p^5 ^{3}P$_1$	1.9103	1.9105	1.9111	2.103E+13	2.102E+13	2.098E+13
[1s]2p^5 ^{1}P$_1$ - 2p^4 ^{3}P$_1$	1.9115	1.9116	1.9123	1.534E+13	1.533E+13	1.528E+13
[1s]2p^5 ^{3}P$_1$ - 2p^4 ^{3}P$_2$	1.9142	1.9143	1.9150	2.214E+14	2.213E+14	2.209E+14
[1s]2p^5 ^{1}P$_1$ - 2p^4 ^{1}D$_2$	1.9146	1.9147	1.9153	6.307E+14	6.305E+14	6.295E+14
[1s]2p^5 ^{3}P$_0$ - 2p^4 ^{3}P$_1$	1.9152	1.9153	1.9159	4.243E+14	4.241E+14	4.234E+14
[1s]2p^5 ^{3}P$_2$ - 2p^4 ^{3}P$_2$	1.9163	1.9164	1.9170	2.863E+14	2.862E+14	2.858E+14

Table 5.5: (continued)

Transition	λ (Å)			A_{ki} (s^{-1})		
	$\mu = 0.0$	$\mu = 0.1$	$\mu = 0.25$	$\mu = 0.0$	$\mu = 0.1$	$\mu = 0.25$
1s2s2p^6 ^{3}S$_1$ - [2s]2p^5 ^{3}P$_2$	1.9163	1.9164	1.9170	3.520E+14	3.519E+14	3.513E+14
[1s]2p^5 ^{3}P$_1$ - 2p^4 ^{3}P$_0$	1.9170	1.9171	1.9177	1.392E+14	1.392E+14	1.390E+14
[1s]2p^5 ^{3}P$_1$ - 2p^4 ^{3}P$_1$	1.9175	1.9176	1.9182	9.000E+13	8.997E+13	8.984E+13
1s2s2p^6 ^{3}S$_1$ - [2s]2p^5 ^{3}P$_1$	1.9186	1.9187	1.9193	2.022E+14	2.021E+14	2.017E+14
[1s]2p^5 ^{3}P$_2$ - 2p^4 ^{3}P$_1$	1.9196	1.9197	1.9203	1.039E+14	1.039E+14	1.037E+14
[1s]2p^5 ^{1}P$_1$ - 2p^4 ^{1}S$_0$	1.9202	1.9203	1.9209	1.353E+14	1.352E+14	1.350E+14
1s2s2p^6 ^{3}S$_1$ - [2s]2p^5 ^{3}P$_0$	1.9202	1.9203	1.9210	6.896E+13	6.984E+13	6.882E+13
[1s]2p^5 ^{3}P$_1$ - 2p^4 ^{1}D$_2$	1.9206	1.9207	1.9213	3.221E+13	3.218E+13	3.207E+13
1s2s2p^6 ^{1}S$_0$ - [2s]2p^5 ^{1}P$_1$	1.9210	1.9211	1.9217	6.154E+14	6.152E+14	6.141E+14
[1s]2p^5 ^{3}P$_2$ - 2p^4 ^{1}D$_2$	1.9227	1.9228	1.9234	2.959E+13	2.957E+13	2.949E+13
Fe XX						
[1s]2p^4 ^{2}P$_{1/2}$ - 2p^3 ^{2}D$_{3/2}$	1.9014	1.9015	1.9022	3.159E+14	3.158E+14	3.154E+14
1s2s2p^5(^{1}P) ^{2}P$_{3/2}$ - [2s]2p^4 ^{2}D$_{5/2}$	1.9015	1.9017	1.9023	1.585E+14	1.584E+14	1.578E+14
[1s]2p^4 ^{2}P$_{3/2}$ - 2p^3 ^{2}D$_{5/2}$	1.9025	1.9026	1.9033	4.596E+14	4.595E+14	4.588E+14
[1s]2p^4 ^{2}S$_{1/2}$ - 2p^3 ^{2}P$_{3/2}$	1.9029	1.9031	1.9037	5.851E+14	5.848E+14	5.834E+14
[1s]2p^4 ^{4}P$_{1/2}$ - 2p^3 ^{4}S$_{3/2}$	1.9039	1.9040	1.9047	2.234E+14	2.234E+14	2.229E+14
[1s]2p^4 ^{2}D$_{5/2}$ - 2p^3 ^{2}D$_{5/2}$	1.9045	1.9046	1.9052	2.918E+14	2.917E+14	2.913E+14
[1s]2p^4 ^{4}P$_{3/2}$ - 2p^3 ^{4}S$_{3/2}$	1.9046	1.9047	1.9054	2.364E+14	2.363E+14	2.359E+14
[1s]2p^4 ^{2}D$_{3/2}$ - 2p^3 ^{2}D$_{3/2}$	1.9046	1.9048	1.9054	4.714E+14	4.712E+14	4.705E+14
1s2s2p^5 ^{4}P$_{3/2}$ - [2s]2p^4 ^{4}P$_{5/2}$	1.9047	1.9049	1.9055	2.073E+14	2.072E+14	2.068E+14
1s2s2p^5(^{1}P) ^{2}P$_{1/2}$ - [2s]2p^4 ^{2}S$_{1/2}$	1.9047	1.9049	1.9055	6.127E+13	6.125E+13	6.112E+13
1s2s2p^5(^{3}P) ^{2}P$_{1/2}$ - [2s]2p^4 ^{2}D$_{3/2}$	1.9052	1.9053	1.9059	6.987E+14	6.984E+14	6.972E+14
[1s]2p^4 ^{2}P$_{3/2}$ - 2p^3 ^{2}P$_{1/2}$	1.9054	1.9055	1.9062	1.341E+14	1.341E+14	1.339E+14
1s2s2p^5 ^{4}P$_{1/2}$ - [2s]2p^4 ^{4}P$_{3/2}$	1.9055	1.9056	1.9062	3.674E+14	3.672E+14	3.666E+14
[1s]2p^4 ^{2}P$_{1/2}$ - 2p^3 ^{2}P$_{1/2}$	1.9058	1.9060	1.9066	3.462E+14	3.461E+14	3.456E+14
[1s]2p^4 ^{2}D$_{3/2}$ - 2p^3 ^{2}D$_{5/2}$	1.9062	1.9063	1.9069	6.593E+13	6.590E+13	6.574E+13
1s2s2p^5 ^{4}P$_{1/2}$ - [2s]2p^4 ^{4}P$_{1/2}$	1.9063	1.9064	1.9070	7.388E+13	7.385E+13	7.372E+13
1s2s2p^5(^{3}P) ^{2}P$_{3/2}$ - [2s]2p^4 ^{2}D$_{3/2}$	1.9063	1.9064	1.9070	8.524E+13	8.522E+13	8.509E+13
1s2s2p^5(^{1}P) ^{2}P$_{1/2}$ - [2s]2p^4 ^{2}P$_{3/2}$	1.9066	1.9067	1.9073	1.498E+14	1.498E+14	1.496E+14
1s2s2p^5 ^{4}P$_{5/2}$ - [2s]2p^4 ^{4}P$_{5/2}$	1.9068	1.9069	1.9076	2.957E+14	2.956E+14	2.950E+14
1s2s2p^5(^{3}P) ^{2}P$_{3/2}$ - [2s]2p^4 ^{2}D$_{5/2}$	1.9069	1.9071	1.9077	4.883E+14	4.882E+14	4.877E+14
[1s]2p^4 ^{4}P$_{5/2}$ - 2p^3 ^{4}S$_{3/2}$	1.9072	1.9074	1.9080	1.973E+14	1.972E+14	1.969E+14
1s2s2p^5 ^{4}P$_{3/2}$ - [2s]2p^4 ^{4}P$_{3/2}$	1.9072	1.9073	1.9079	5.372E+13	5.370E+13	5.362E+13
1s2p^6 ^{2}S$_{1/2}$ - 1s^{2}2p^5 ^{2}P$_{3/2}$	1.9072	1.9073	1.9080	4.342E+14	4.340E+14	4.333E+14
[1s]2p^4 ^{2}P$_{3/2}$ - 2p^3 ^{2}P$_{3/2}$	1.9078	1.9079	1.9085	1.257E+14	1.257E+14	1.255E+14
1s2s2p^5 ^{4}P$_{3/2}$ - [2s]2p^4 ^{4}P$_{1/2}$	1.9080	1.9081	1.9087	1.778E+14	1.778E+14	1.775E+14
[1s]2p^4 ^{2}P$_{1/2}$ - 2p^3 ^{2}P$_{3/2}$	1.9082	1.9083	1.9089	5.186E+13	5.190E+13	5.208E+13
1s2s2p^5(^{1}P) ^{2}P$_{3/2}$ - [2s]2p^4 ^{2}P$_{3/2}$	1.9082	1.9084	1.9090	2.903E+14	2.903E+14	2.899E+14
1s2s2p^5 ^{4}P$_{5/2}$ - [2s]2p^4 ^{4}P$_{3/2}$	1.9093	1.9094	1.9100	1.266E+14	1.266E+14	1.264E+14
[1s]2p^4 ^{2}D$_{5/2}$ - 2p^3 ^{2}P$_{3/2}$	1.9098	1.9099	1.9105	1.292E+14	1.291E+14	1.290E+14
1s2s2p^5(^{1}P) ^{2}P$_{1/2}$ - [2s]2p^4 ^{2}P$_{1/2}$	1.9101	1.9102	1.9109	2.293E+14	2.293E+14	2.288E+14
1s2s2p^5(^{3}P) ^{2}P$_{1/2}$ - [2s]2p^4 ^{2}S$_{1/2}$	1.9107	1.9108	1.9114	1.156E+14	1.156E+14	1.155E+14
1s2p^6 ^{2}S$_{1/2}$ - 1s^{2}2p^5 ^{2}P$_{1/2}$	1.9112	1.9113	1.9119	2.118E+14	2.117E+14	2.114E+14
1s2s2p^5(^{3}P) ^{2}P$_{3/2}$ - [2s]2p^4 ^{2}S$_{1/2}$	1.9118	1.9119	1.9126	1.254E+14	1.254E+14	1.252E+14
1s2s2p^5(^{1}P) ^{2}P$_{3/2}$ - [2s]2p^4 ^{2}P$_{1/2}$	1.9118	1.9119	1.9125	8.674E+13	8.671E+13	8.657E+13
[1s]2p^4 ^{4}P$_{5/2}$ - 2p^3 ^{2}D$_{3/2}$	1.9124	1.9125	1.9131	1.437E+13	1.436E+13	1.428E+13

Transition	λ (Å)			A_{ki} (s^{-1})		
	$\mu = 0.0$	$\mu = 0.1$	$\mu = 0.25$	$\mu = 0.0$	$\mu = 0.1$	$\mu = 0.25$
1s2s2p^5(^{3}P) ^{2}P$_{1/2}$ - [2s]2p^4 ^{2}P$_{3/2}$	1.9125	1.9126	1.9133	3.027E+13	3.024E+13	3.009E+13
[1s]2p^4 ^{4}P$_{1/2}$ - 2p^3 ^{2}P$_{1/2}$	1.9135	1.9136	1.9143	1.776E+13	1.774E+13	1.762E+13
1s2s2p^5(^{3}P) ^{2}P$_{3/2}$ - [2s]2p^4 ^{2}P$_{3/2}$	1.9137	1.9138	1.9144	5.564E+13	5.558E+13	5.532E+13
[1s]2p^4 ^{4}P$_{5/2}$ - 2p^3 ^{2}D$_{5/2}$	1.9139	1.9140	1.9147	1.622E+13	1.622E+13	1.617E+13
1s2s2p^5(^{3}P) ^{2}P$_{1/2}$ - [2s]2p^4 ^{2}P$_{1/2}$	1.9161	1.9162	1.9168	2.507E+13	2.505E+13	2.494E+13
Fe XXI						
1s2s2p^4 ^{3}P$_2$ - [2s]2p^3 ^{3}D$_3$	1.8881	1.8882	1.8889	8.049E+13	8.042E+13	8.010E13
1s2p^5 ^{1}P$_1$ - 1s^{2}2p^4 ^{3}P$_2$	1.8888	1.8889	1.8897	1.097E+13	1.096E+13	1.094E+13
[1s]2p^3 ^{3}S$_1$ - 2p^2 ^{3}P$_0$	1.8893	1.8894	1.8901	3.165E+13	3.167E+13	3.177E+13
[1s]2p^3 ^{1}P$_1$ - 2p^2 ^{1}D$_2$	1.8898	1.8899	1.8905	4.078E+14	4.077E+14	4.069E+14
1s2s2p^4 ^{3}P$_1$ - [2s]2p^3 ^{3}P$_2$	1.8899	1.8900	1.8906	9.797E+13	9.790E+13	9.756E+13
1s2s2p^4 ^{3}P$_0$ - [2s]2p^3 ^{3}P$_1$	1.8900	1.8901	1.8908	8.534E+13	8.524E+13	8.478E+13
1s2s2p^4 ^{1}D$_2$ - [2s]2p^3 ^{3}P$_2$	1.8901	1.8902	1.8909	1.905E+13	1.904E+13	1.899E+13
[1s]2p^3 ^{3}P$_0$ - 2p^2 ^{3}P$_1$	1.8912	1.8913	1.8919	2.329E+14	2.328E+14	2.324E+14
1s2s2p^4 ^{3}P$_0$ - [2s]2p^3 ^{3}D$_1$	1.8913	1.8914	1.8921	2.512E+14	2.511E+14	2.508E+14
[1s]2p^3 ^{3}P$_1$ - 2p^2 ^{3}P$_2$	1.8914	1.8915	1.8922	4.065E+14	4.063E+14	4.040E+14
[1s]2p^3 ^{3}S$_1$ - 2p^2 ^{3}P$_1$	1.8920	1.8921	1.8928	4.525E+14	4.524E+14	4.517E+14
1s2s2p^4 ^{3}P$_1$ - [2s]2p^3 ^{3}D$_2$	1.8920	1.8921	1.8927	3.215E+14	3.214E+14	3.209E+14
[1s]2p^3 ^{1}D$_2$ - 2p^2 ^{3}P$_2$	1.8921	1.8922	1.8929	3.191E+14	3.190E+14	3.185E+14
1s2s2p^4 ^{1}P$_1$ - [2s]2p^3 ^{1}D$_2$	1.8921	1.8922	1.8928	5.168E+14	5.166E+14	5.157E+14
1s2p^5 ^{1}P$_1$ - 1s^{2}2p^4 ^{3}P$_1$	1.8922	1.8923	1.8929	1.595E+13	1.594E+13	1.590E+13
[1s]2p^3 ^{3}P$_2$ - 2p^2 ^{1}D$_2$	1.8928	1.8929	1.8936	5.164E+14	5.162E+14	5.152E+14
1s2s2p^4 ^{3}S$_1$ - [2s]2p^3 ^{3}P$_1$	1.8929	1.8930	1.8936	8.892E+13	8.888E+13	8.867E+13
1s2s2p^4 ^{3}D$_2$ - [2s]2p^3 ^{3}D$_2$	1.8931	1.8932	1.8938	1.141E+13	1.135E+13	1.103E+13
[1s]2p^3 ^{3}D$_1$ - 2p^2 ^{3}P$_0$	1.8934	1.8935	1.8941	2.711E+14	2.710E+14	2.704E+14
1s2s2p^4 ^{3}S$_1$ - [2s]2p^3 ^{3}P$_2$	1.8936	1.8937	1.8943	3.323E+14	3.323E+14	3.320E+14
[1s]2p^3 ^{3}S$_1$ - 2p^2 ^{3}P$_2$	1.8937	1.8938	1.8944	1.161E+14	1.162E+14	1.167E+14
1s2s2p^4 ^{5}P$_1$ - [2s]2p^3 ^{5}S$_2$	1.8940	1.8941	1.8947	2.295E+14	2.294E+14	2.290E+14
1s2s2p^4 ^{3}D$_2$ - [2s]2p^3 ^{3}D$_3$	1.8941	1.8943	1.8949	3.169E+14	3.170E+14	3.175E+14
[1s]2p^3 ^{1}P$_1$ - 2p^2 ^{1}S$_0$	1.8942	1.8944	1.8950	2.649E+14	2.648E+14	2.645E+14
1s2s2p^4 ^{1}S$_0$ - [2s]2p^3 ^{1}P$_1$	1.8945	1.8947	1.8953	4.142E+14	4.141E+14	4.135E+14
1s2s2p^4 ^{3}D$_3$ - [2s]2p^3 ^{3}D$_3$	1.8946	1.8947	1.8953	2.959E+14	2.958E+14	2.953E+14
1s2s2p^4 ^{3}D$_1$ - [2s]2p^3 ^{3}D$_1$	1.8947	1.8948	1.8954	5.015E+14	5.013E+14	5.002E+14
1s2p^5 ^{3}P$_1$ - 1s^{2}2p^4 ^{3}P$_2$	1.8949	1.8951	1.8957	2.351E+14	2.350E+14	2.346E+14
1s2s2p^4 ^{5}P$_2$ - [2s]2p^3 ^{5}S$_2$	1.8951	1.8952	1.8958	2.277E+14	2.276E+14	2.272E+14
1s2s2p^4 ^{3}P$_2$ - [2s]2p^3 ^{3}D$_1$	1.8952	1.8953	1.8959	4.235E+13	4.233E+13	4.222E+13
1s2s2p^4 ^{3}P$_2$ - [2s]2p^3 ^{3}D$_2$	1.8952	1.8953	1.8960	4.700E+14	4.699E+14	4.694E+14
1s2p^5 ^{1}P$_1$ - 1s^{2}2p^4 ^{1}D$_2$	1.8952	1.8953	1.8960	6.652E+14	6.650E+14	6.640E+14
1s2s2p^4 ^{3}P$_1$ - [2s]2p^3 ^{3}S$_1$	1.8954	1.8955	1.8961	2.228E+14	2.227E+14	2.224E+14
[1s]2p^3 ^{3}D$_2$ - 2p^2 ^{3}P$_1$	1.8955	1.8956	1.8962	2.123E+14	2.122E+14	2.119E+14
1s2s2p^4 ^{1}D$_2$ - [2s]2p^3 ^{3}S$_1$	1.8956	1.8957	1.8963	1.741E+13	1.737E+13	1.717E+13
[1s]2p^3 ^{3}D$_3$ - 2p^2 ^{3}P$_2$	1.8957	1.8958	1.8964	1.711E+14	1.711E+14	1.709E+14
1s2p^5 ^{3}P$_0$ - 1s^{2}2p^4 ^{3}P$_1$	1.8960	1.8961	1.8967	4.485E+14	4.484E+14	4.477E+14
1s2s2p^4 ^{3}P$_0$ - [2s]2p^3 ^{3}S$_1$	1.8962	1.8963	1.8969	2.153E+14	2.152E+14	2.148E+14
1s2s2p^4 ^{3}P$_2$ - [2s]2p^3 ^{3}D$_3$	1.8963	1.8964	1.8971	1.393E+14	1.391E+14	1.381E+14
1s2s2p^4 ^{3}P$_0$ - [2s]2p^3 ^{3}P$_1$	1.8967	1.8968	1.8974	5.741E+14	5.739E+14	5.731E+14

Table 5.5: (continued)

Transition	λ (Å)			A_{ki} (s^{-1})		
	$\mu = 0.0$	$\mu = 0.1$	$\mu = 0.25$	$\mu = 0.0$	$\mu = 0.1$	$\mu = 0.25$
1s2s2p^4 ^{3}P$_1$ - [2s]2p^3 ^{1}D$_2$	1.8967	1.8998	1.8974	4.342E+13	4.340E+13	4.329E+13
[1s]2p^3 ^{1}D$_2$ - 2p^2 ^{1}D$_2$	1.8968	1.8969	1.8975	4.960E+13	4.964E+13	4.986E+13
1s2s2p^4 ^{1}P$_1$ - [2s]2p^3 ^{1}P$_1$	1.8968	1.8969	1.8976	2.984E+14	2.983E+14	2.979E+14
1s2s2p^4 ^{3}P$_1$ - [2s]2p^3 ^{3}P$_0$	1.8969	1.8970	1.8977	2.177E+14	2.177E+14	2.173E+14
1s2s2p^4 ^{1}D$_2$ - [2s]2p^3 ^{1}D$_2$	1.8969	1.8970	1.8977	2.147E+14	2.148E+14	2.150E+14
1s2p^5 ^{3}P$_2$ - 1s^{2}2p^4 ^{3}P$_2$	1.8971	1.8972	1.8978	3.010E+14	3.009E+14	3.005E+14
1s2s2p^4 ^{3}P$_1$ - [2s]2p^3 ^{3}P$_1$	1.8973	1.8974	1.8980	4.408E+13	4.409E+13	4.412E+13
1s2s2p^4 ^{5}P$_3$ - [2s]2p^3 ^{5}S$_2$	1.8975	1.8976	1.8982	2.181E+14	2.180E+14	2.177E+14
[1s]2p^3 ^{3}D$_1$ - 2p^2 ^{3}P$_2$	1.8977	1.8979	1.8985	3.736E+13	3.735E+13	3.727E+13
1s2s2p^4 ^{3}P$_1$ - [2s]2p^3 ^{3}P$_2$	1.8980	1.8981	1.8987	1.347E+14	1.347E+14	1.344E+14
1s2p^5 ^{3}P$_1$ - 1s^{2}2p^4 ^{3}P$_0$	1.8981	1.8983	1.8989	1.487E+14	1.486E+14	1.484E+14
[1s]2p^3 ^{3}S$_1$ - 2p^2 ^{1}D$_2$	1.8983	1.8985	1.8991	1.853E+13	1.854E+13	1.854E+13
1s2p^5 ^{3}P$_1$ - 1s^{2}2p^4 ^{3}P$_1$	1.8983	1.8984	1.8991	9.516E+13	9.513E+13	9.500E+13
1s2s2p^4 ^{3}D$_2$ - [2s]2p^3 ^{3}P$_1$	1.8984	1.8985	1.8992	1.752E+14	1.752E+14	1.749E+14
1s2s2p^4 ^{3}P$_2$ - [2s]2p^3 ^{3}S$_1$	1.8985	1.8986	1.8993	1.747E+14	1.747E+14	1.747E+14
1s2s2p^4 ^{3}D$_2$ - [2s]2p^3 ^{3}P$_2$	1.8991	1.8992	1.8998	5.820E+13	5.823E+13	5.836E+13
1s2s2p^4 ^{3}D$_3$ - [2s]2p^3 ^{3}P$_2$	1.8995	1.8996	1.9002	1.381E+14	1.381E+14	1.379E+14
1s2s2p^4 ^{3}P$_2$ - [2s]2p^3 ^{1}D$_2$	1.8999	1.9000	1.9006	1.138E+14	1.136E+14	1.129E+14
1s2s2p^4 ^{3}D$_1$ - [2s]2p^3 ^{3}P$_1$	1.9001	1.9002	1.9008	1.419E+13	1.418E+13	1.416E+13
[1s]2p^3 ^{3}D$_3$ - 2p^2 ^{1}D$_2$	1.9003	1.9004	1.9011	5.073E+13	5.071E+13	5.059E+13
1s2p^5 ^{3}P$_2$ - 1s^{2}2p^4 ^{3}P$_1$	1.9004	1.9006	1.9012	1.091E+14	1.091E+14	1.089E+14
[1s]2p^3 ^{3}P$_1$ - 2p^2 ^{1}S$_0$	1.9006	1.9007	1.9013	3.297E+13	3.295E+13	3.283E+13
1s2s2p^4 ^{3}D$_1$ - [2s]2p^3 ^{3}P$_2$	1.9007	1.9009	1.9015	3.054E+13	3.051E+13	3.034E+13
1s2s2p^4 ^{3}P$_2$ - [2s]2p^3 ^{3}P$_2$	1.9013	1.9014	1.9020	4.807E+13	4.802E+13	4.779E+13
1s2p^5 ^{3}P$_1$ - 1s^{2}2p^4 ^{1}D$_2$	1.9014	1.9015	1.9021	3.108E+13	3.106E+13	3.099E+13
1s2s2p^4 ^{1}D$_2$ - [2s]2p^3 ^{1}P$_1$	1.9017	1.9018	1.9025	1.288E+14	1.287E+14	1.285E+14
1s2s2p^4 ^{3}P$_0$ - [2s]2p^3 ^{1}P$_1$	1.9023	1.9024	1.9030	2.194E+13	2.192E+13	2.179E+13
1s2s2p^4 ^{3}P$_0$ - [2s]2p^3 ^{3}S$_1$	1.9029	1.9030	1.9036	4.422E+13	4.419E+13	4.403E+13
1s2p^5 ^{3}P$_2$ - 1s^{2}2p^4 ^{1}D$_2$	1.9035	1.9036	1.9042	3.226E+13	3.225E+13	3.219E+13
1s2p^5 ^{1}P$_1$ - 1s^{2}2p^4 ^{1}S$_0$	1.9035	1.9036	1.9042	1.509E+14	1.509E+14	1.506E+14
1s2s2p^4 ^{3}S$_1$ - [2s]2p^3 ^{1}P$_1$	1.9052	1.9053	1.9059	1.729E+13	1.728E+13	1.725E+13
Fe XXII						
1s2s2p^3(^{1}P) ^{2}P$_{3/2}$ - [2s]2p^2 ^{2}D$_{5/2}$	1.8743	1.8745	1.8751	1.035E+13	1.032E+13	1.017E+13
1s2s2p^3 ^{4}S$_{3/2}$ - [2s]2p^2 ^{4}P$_{5/2}$	1.8750	1.8750	1.8756	2.833E+13	2.829E+13	2.809E+13
1s2s2p^3(^{3}P) ^{2}P$_{3/2}$ - [2s]2p^2 ^{2}D$_{5/2}$	1.8779	1.8780	1.8787	2.573E+14	2.573E+14	2.570E+14
[1s]2p^2 ^{2}S$_{1/2}$ - 2p ^{2}P$_{3/2}$	1.8783	1.8785	1.8791	3.059E+14	3.058E+14	3.050E+14
1s2s2p^3 ^{4}P$_{3/2}$ - [2s]2p^2 ^{4}P$_{3/2}$	1.8797	1.8798	1.8804	1.316E+13	1.313E+13	1.296E+13
[1s]2p^2 ^{2}P$_{3/2}$ - 2p ^{2}P$_{3/2}$	1.8799	1.8800	1.8806	6.013E+14	6.012E+14	6.003E+14
1s2s2p^3 ^{2}D$_{5/2}$ - [2s]2p^2 ^{2}D$_{5/2}$	1.8799	1.8800	1.8806	7.734E+13	7.722E+13	7.668E+13
1s2p^4 ^{2}S$_{1/2}$ - 1s^{2}2p^3 ^{2}P$_{1/2}$	1.8800	1.8801	1.8808	1.953E+13	1.950E+13	1.937E+13
1s2s2p^3(^{3}P) ^{2}P$_{1/2}$ - [2s]2p^2 ^{2}D$_{3/2}$	1.8802	1.8804	1.8810	4.002E+14	4.001E+14	3.994E+14
1s2s2p^3 ^{4}P$_{1/2}$ - [2s]2p^2 ^{4}P$_{3/2}$	1.8803	1.8804	1.8811	2.312E+14	2.311E+14	2.307E+14
[1s]2p^2 ^{2}P$_{1/2}$ - 2p ^{2}P$_{1/2}$	1.8806	1.8807	1.8814	5.294E+14	5.293E+14	5.286E+14
1s2s2p^3(^{1}P) ^{2}P$_{1/2}$ - [2s]2p^2 ^{2}P$_{1/2}$	1.8806	1.8807	1.8814	2.321E+14	2.320E+14	2.313E+14
1s2s2p^3 ^{2}S$_{1/2}$ - [2s]2p^2 ^{2}S$_{1/2}$	1.8806	1.8808	1.8814	1.056E+14	1.056E+14	1.052E+14
1s2p^4 ^{2}P$_{1/2}$ - 1s^{2}2p^3 ^{2}D$_{3/2}$	1.8808	1.8809	1.8816	3.777E+14	3.776E+14	3.769E+14

Transition	λ (Å)			A_{ki} (s^{-1})		
	$\mu = 0.0$	$\mu = 0.1$	$\mu = 0.25$	$\mu = 0.0$	$\mu = 0.1$	$\mu = 0.25$
[1s]2p^2 ^{2}D$_{3/2}$ - 2p ^{2}P$_{1/2}$	1.8809	1.8810	1.8817	3.009E+14	3.008E+14	3.004E+14
1s2s2p^3 ^{4}S$_{3/2}$ - [2s]2p^2 ^{4}P$_{1/2}$	1.8811	1.8812	1.8819	8.854E+13	8.856E+13	8.867E+13
1s2s2p^3 ^{2}D$_{3/2}$ - [2s]2p^2 ^{2}D$_{3/2}$	1.8812	1.8813	1.8820	2.272E+14	2.270E+14	2.260E+14
1s2s2p^3 ^{2}S$_{1/2}$ - [2s]2p^2 ^{2}P$_{3/2}$	1.8812	1.8813	1.8820	6.321E+14	6.319E+14	6.307E+14
1s2s2p^3 ^{4}P$_{5/2}$ - [2s]2p^2 ^{4}P$_{5/2}$	1.8817	1.8818	1.8824	2.490E+14	2.489E+14	2.484E+14
1s2s2p^3 ^{4}P$_{3/2}$ - [2s]2p^2 ^{4}P$_{5/2}$	1.8817	1.8818	1.8824	2.689E+14	2.690E+14	2.690E+14
1s2s2p^3 ^{2}D$_{3/2}$ - [2s]2p^2 ^{2}D$_{5/2}$	1.8821	1.8822	1.8828	5.793E+13	5.792E+13	5.780E+13
1s2p^4 ^{2}S$_{1/2}$ - 1s^{2}2p^3 ^{2}P$_{3/2}$	1.8821	1.8822	1.8829	5.108E+14	5.107E+14	5.103E+14
1s2p^4 ^{2}P$_{3/2}$ - 1s^{2}2p^3 ^{2}D$_{5/2}$	1.8824	1.8826	1.8832	4.913E+14	4.911E+14	4.904E+14
1s2s2p^3(^{1}P) ^{2}P$_{3/2}$ - [2s]2p^2 ^{2}P$_{3/2}$	1.8826	1.8827	1.8833	2.184E+14	2.184E+14	2.182E+14
1s2s2p^3 ^{4}S$_{3/2}$ - [2s]2p^2 ^{2}D$_{3/2}$	1.8829	1.8830	1.8836	9.447E+13	9.456E+13	9.495E+13
1s2s2p^3 ^{4}S$_{3/2}$ - [2s]2p^2 ^{4}P$_{3/2}$	1.8831	1.8832	1.8839	4.501E+14	4.499E+14	4.493E+14
1s2s2p^3 ^{4}D$_{1/2}$ - [2s]2p^2 ^{4}P$_{1/2}$	1.8834	1.8836	1.8842	2.313E+14	2.312E+14	2.308E+14
1s2s2p^3 ^{2}D$_{5/2}$ - [2s]2p^2 ^{2}D$_{3/2}$	1.8834	1.8835	1.8841	5.415E+13	5.413E+13	5.404E+13
[1s]2p^2 ^{2}D$_{5/2}$ - 2p ^{2}P$_{3/2}$	1.8835	1.8836	1.8842	2.062E+14	2.061E+14	2.059E+14
1s2p^4 ^{4}P$_{1/2}$ - 1s^{2}2p^3 ^{4}S$_{3/2}$	1.8839	1.8841	1.8847	2.334E+14	2.333E+14	2.330E+14
1s2s2p^3 ^{4}D$_{3/2}$ - [2s]2p^2 ^{4}P$_{1/2}$	1.8840	1.8841	1.8847	2.638E+14	2.636E+14	2.630E+14
1s2s2p^3 ^{2}D$_{5/2}$ - [2s]2p^2 ^{2}D$_{5/2}$	1.8842	1.8843	1.8850	5.425E+14	5.424E+14	5.420E+14
1s2s2p^3(^{3}P) ^{2}P$_{1/2}$ - [2s]2p^2 ^{2}P$_{1/2}$	1.8843	1.8844	1.8851	1.753E+14	1.753E+14	1.755E+14
1s2p^4 ^{2}D$_{5/2}$ - 1s^{2}2p^3 ^{2}D$_{5/2}$	1.8846	1.8847	1.8853	3.065E+14	3.064E+14	3.059E+14
[1s]2p^2 ^{2}P$_{1/2}$ - 2p ^{2}P$_{3/2}$	1.8849	1.8850	1.8856	9.140E+13	9.144E+13	9.162E+13
1s2s2p^3 ^{2}D$_{3/2}$ - [2s]2p^2 ^{2}D$_{3/2}$	1.8849	1.8850	1.8856	3.239E+14	3.238E+14	3.233E+14
1s2p^4 ^{4}P$_{3/2}$ - 1s^{2}2p^3 ^{4}S$_{3/2}$	1.8849	1.8850	1.8857	2.482E+14	2.482E+14	2.478E+14
1s2p^4 ^{2}D$_{3/2}$ - 1s^{2}2p^3 ^{2}D$_{3/2}$	1.8849	1.8851	1.8857	4.849E+14	4.848E+14	4.841E+14
1s2s2p^3 ^{4}S$_{3/2}$ - [2s]2p^2 ^{4}P$_{5/2}$	1.8851	1.8853	1.8859	2.517E+14	2.516E+14	2.510E+14
1s2s2p^3(^{1}P) ^{2}P$_{1/2}$ - [2s]2p^2 ^{2}S$_{1/2}$	1.8851	1.8852	1.8859	1.659E+14	1.659E+14	1.659E+14
[1s]2p^2 ^{2}D$_{3/2}$ - 2p ^{2}P$_{3/2}$	1.8852	1.8853	1.8860	2.440E+13	2.440E+13	2.436E+13
1s2s2p^3 ^{2}D$_{3/2}$ - [2s]2p^2 ^{2}P$_{1/2}$	1.8853	1.8854	1.8860	1.983E+14	1.983E+14	1.981E+14
1s2s2p^3 ^{4}D$_{5/2}$ - [2s]2p^2 ^{4}P$_{3/2}$	1.8856	1.8857	1.8864	2.235E+14	2.235E+14	2.231E+14
1s2s2p^3(^{3}P) ^{2}P$_{3/2}$ - [2s]2p^2 ^{2}S$_{1/2}$	1.8856	1.8857	1.8864	2.577E+14	2.576E+14	2.574E+14
1s2s2p^3 ^{2}D$_{3/2}$ - [2s]2p^2 ^{2}D$_{5/2}$	1.8857	1.8858	1.8865	1.009E+14	1.008E+14	1.004E+14
1s2s2p^3(^{1}P) ^{2}P$_{1/2}$ - [2s]2p^2 ^{2}P$_{3/2}$	1.8857	1.8858	1.8864	2.784E+13	2.784E+13	2.783E+13
1s2s2p^3(^{3}P) ^{2}P$_{3/2}$ - [2s]2p^2 ^{2}P$_{3/2}$	1.8862	1.8863	1.8869	1.216E+13	1.214E+13	1.201E+13
1s2p^4 ^{2}D$_{3/2}$ - 1s^{2}2p^3 ^{2}D$_{5/2}$	1.8862	1.8863	1.8869	6.059E+13	6.058E+13	6.048E+13
1s2s2p^3 ^{4}D$_{7/2}$ - [2s]2p^2 ^{4}P$_{5/2}$	1.8865	1.8866	1.8873	2.186E+14	2.186E+14	2.182E+14
1s2p^4 ^{2}P$_{1/2}$ - 1s^{2}2p^3 ^{2}P$_{1/2}$	1.8871	1.8872	1.8878	3.595E+14	3.594E+14	3.589E+14
1s2p^4 ^{2}P$_{3/2}$ - 1s^{2}2p^3 ^{2}P$_{1/2}$	1.8874	1.8876	1.8882	1.453E+14	1.452E+14	1.449E+14
1s2p^4 ^{4}P$_{5/2}$ - 1s^{2}2p^3 ^{4}S$_{3/2}$	1.8876	1.8877	1.8883	2.107E+14	2.106E+14	2.103E+14
1s2s2p^3 ^{4}D$_{3/2}$ - [2s]2p^2 ^{4}P$_{5/2}$	1.8880	1.8881	1.8888	2.434E+13	2.431E+13	2.416E+13
1s2s2p^3 ^{2}D$_{5/2}$ - [2s]2p^2 ^{2}P$_{3/2}$	1.8881	1.8883	1.8889	2.050E+14	2.050E+14	2.047E+14
1s2s2p^3(^{3}P) ^{2}P$_{1/2}$ - [2s]2p^2 ^{2}S$_{1/2}$	1.8888	1.8889	1.8896	1.029E+14	1.029E+14	1.025E+14
1s2s2p^3 ^{2}D$_{3/2}$ - [2s]2p^2 ^{2}P$_{1/2}$	1.8889	1.8891	1.8897	6.035E+13	6.029E+13	6.002E+13
1s2p^4 ^{2}P$_{1/2}$ - 1s^{2}2p^3 ^{2}P$_{3/2}$	1.8892	1.8893	1.8899	1.221E+14	1.220E+14	1.216E+14
1s2s2p^3(^{3}P) ^{2}P$_{1/2}$ - [2s]2p^2 ^{2}P$_{3/2}$	1.8894	1.8895	1.8901	3.796E+13	3.797E+13	3.801E+13
1s2p^4 ^{2}P$_{3/2}$ - 1s^{2}2p^3 ^{2}P$_{3/2}$	1.8896	1.8897	1.8903	1.432E+14	1.432E+14	1.429E+14
[1s]2p^2 ^{4}P$_{5/2}$ - 2p ^{2}P$_{3/2}$	1.8905	1.8906	1.8913	2.444E+13	2.443E+13	2.439E+13

98

Table 5.5: (continued)

Transition	λ (Å)			A_{ki} (s^{-1})		
	$\mu = 0.0$	$\mu = 0.1$	$\mu = 0.25$	$\mu = 0.0$	$\mu = 0.1$	$\mu = 0.25$
1s2s2p^3 ^{4}P$_{5/2}$ - [2s]2p^2 ^{2}D$_{5/2}$	1.8906	1.8908	1.8914	1.478E+13	1.478E+13	1.473E+13
[1s]2p^2 ^{4}P$_{1/2}$ - 2p ^{2}P$_{1/2}$	1.8907	1.8909	1.8915	2.482E+13	2.480E+13	2.469E+13
1s2p^4 ^{2}D$_{5/2}$ - 1s^{2}2p^3 ^{2}P$_{3/2}$	1.8917	1.8918	1.8925	1.418E+14	1.418E+14	1.415E+14
1s2s2p^3 ^{4}S$_{3/2}$ - [2s]2p^2 ^{2}P$_{3/2}$	1.8920	1.8921	1.8928	2.575E+13	2.573E+13	2.566E+13
1s2s2p^3 ^{2}D$_{5/2}$ - [2s]2p^2 ^{2}P$_{3/2}$	1.8925	1.8927	1.8933	1.676E+13	1.673E+13	1.658E+13
1s2p^4 ^{4}P$_{5/2}$ - 1s^{2}2p^3 ^{2}D$_{3/2}$	1.8928	1.8929	1.8936	1.119E+13	1.118E+13	1.117E+13
1s2p^4 ^{2}D$_{3/2}$ - 1s^{2}2p^3 ^{2}P$_{3/2}$	1.8933	1.8935	1.8941	2.730E+13	2.727E+13	2.712E+13
1s2p^4 ^{4}P$_{5/2}$ - 1s^{2}2p^3 ^{2}D$_{5/2}$	1.8941	1.8942	1.8948	1.679E+13	1.679E+13	1.677E+13
1s2s2p^3 ^{4}D$_{7/2}$ - [2s]2p^2 ^{2}D$_{5/2}$	1.8955	1.8956	1.8963	1.219E+13	1.218E+13	1.215E+13
1s2s2p^3 ^{4}D$_{1/2}$ - [2s]2p^2 ^{2}D$_{3/2}$	1.8956	1.8958	1.8964	1.003E+13	1.002E+13	9.994E+12
Fe XXIII						
1s2s2p^2(^{2}P) ^{3}P$_1$ - 2s2p ^{3}P$_2$	1.8652	1.8653	1.8660	1.764E+14	1.763E+14	1.760E+14
1s2s2p^2(^{2}P) ^{3}P$_0$ - 2s2p ^{3}P$_1$	1.8656	1.8657	1.8664	1.035E+14	1.034E+14	1.030E+14
1s2s2p^2 ^{3}S$_1$ - 2s2p ^{3}P$_1$	1.8659	1.8660	1.8667	3.244E+13	3.239E+13	3.219E+13
1s2s2p^2 ^{1}D$_2$ - 2s2p ^{3}P$_2$	1.8663	1.8664	1.8671	8.236E+13	8.227E+13	8.186E+13
1s2s2p^2 ^{1}S$_0$ - 2s2p ^{1}P$_1$	1.8678	1.8679	1.8686	2.335E+14	2.335E+14	2.331E+14
1s2p^3 ^{1}P$_1$ - 1s^{2}2p^2 ^{1}D$_2$	1.8679	1.8681	1.8687	4.074E+14	4.073E+14	4.068E+14
1s2s2p^2(^{4}P) ^{3}P$_2$ - 2s2p ^{3}P$_1$	1.8680	1.8681	1.8688	4.118E+13	4.120E+13	4.129E+13
[1s]2p ^{1}P$_1$ - 1s^{2}2s^2 ^{1}S$_0$	1.8682	1.8683	1.8690	4.571E+14	4.569E+14	4.563E+14
1s2s2p^2 ^{3}S$_1$ - 2s2p ^{3}P$_2$	1.8692	1.8693	1.8700	9.075E+13	9.074E+13	9.066E+13
1s2p^3 ^{3}S$_1$ - 1s^{2}2p^2 ^{3}P$_0$	1.8696	1.8697	1.8704	5.961E+13	5.958E+13	5.941E+13
1s2s2p^2 ^{1}P$_1$ - 2s2p ^{1}P$_1$	1.8697	1.8698	1.8705	7.036E+14	7.033E+14	7.022E+14
1s2p^3 ^{3}P$_1$ - 1s^{2}2p^2 ^{3}P$_2$	1.8699	1.8700	1.8707	2.958E+14	2.958E+14	2.959E+14
1s2s2p^2 ^{3}D$_1$ - 2s2p ^{3}P$_1$	1.8704	1.8705	1.8712	3.169E+14	3.169E+14	3.168E+14
1s2s2p^2(^{4}P) ^{3}P$_1$ - 2s2p ^{3}P$_0$	1.8710	1.8712	1.8717	4.009E+14	4.007E+14	3.999E+14
1s2s2p^2(^{4}P) ^{3}P$_2$ - 2s2p ^{3}P$_2$	1.8713	1.8714	1.8721	5.189E+14	5.188E+14	5.183E+14
1s2s2p^2 ^{3}D$_2$ - 2s2p ^{3}P$_1$	1.8717	1.8718	1.8724	3.239E+14	3.237E+14	3.230E+14
1s2p^3 ^{1}D$_2$ - 1s^{2}2p^2 ^{3}P$_2$	1.8717	1.8718	1.8725	3.571E+14	3.570E+14	3.564E+14
1s2s2p^2(^{4}P) ^{3}P$_1$ - 2s2p ^{3}P$_1$	1.8721	1.8722	1.8729	2.202E+13	2.194E+13	2.159E+13
1s2p^3 ^{3}S$_1$ - 1s^{2}2p^2 ^{3}P$_1$	1.8721	1.8723	1.8729	4.751E+14	4.750E+14	4.743E+14
1s2p^3 ^{3}P$_2$ - 1s^{2}2p^2 ^{1}D$_2$	1.8722	1.8724	1.8730	4.127E+14	4.127E+14	4.130E+14
1s2s2p^2(^{4}P) ^{3}P$_0$ - 2s2p ^{3}P$_1$	1.8729	1.8730	1.8737	6.221E+14	6.219E+14	6.212E+14
1s2s2p^2(^{2}P) ^{3}P$_2$ - 2s2p ^{1}P$_1$	1.8729	1.8731	1.8737	9.417E+13	9.423E+13	9.447E+13
1s2p^3 ^{3}D$_1$ - 1s^{2}2p^2 ^{3}P$_0$	1.8736	1.8738	1.8744	2.623E+14	2.622E+14	2.619E+14
1s2s2p^2 ^{3}D$_3$ - 2s2p ^{3}P$_2$	1.8737	1.8738	1.8744	2.315E+14	2.314E+14	2.310E+14
1s2s2p^2 ^{3}D$_1$ - 2s2p ^{3}P$_2$	1.8737	1.8738	1.8745	1.074E+14	1.075E+14	1.076E+14
1s2p^3 ^{3}S$_1$ - 1s^{2}2p^2 ^{3}P$_2$	1.8738	1.8740	1.8746	2.443E+14	2.441E+14	2.433E+14
1s2p^3 ^{3}P$_1$ - 1s^{2}2p^2 ^{1}D$_2$	1.8746	1.8748	1.8754	1.598E+13	1.597E+13	1.594E+13
1s2s2p^2 ^{3}D$_2$ - 2s2p ^{3}P$_2$	1.8750	1.8751	1.8758	1.219E+13	1.217E+13	1.205E+13
1s2s2p^2(^{4}P) ^{3}P$_1$ - 2s2p ^{3}P$_2$	1.8754	1.8755	1.8762	7.687E+13	7.677E+13	7.625E+13
1s2p^3 ^{1}P$_1$ - 1s^{2}2p^2 ^{1}S$_0$	1.8756	1.8757	1.8764	3.010E+14	3.009E+14	3.003E+14
1s2p^3 ^{3}D$_2$ - 1s^{2}2p^2 ^{3}P$_1$	1.8757	1.8758	1.8765	2.248E+14	2.247E+14	2.244E+14
1s2s2p^2 ^{1}D$_2$ - 2s2p ^{1}P$_1$	1.8762	1.8763	1.8770	1.388E+14	1.387E+14	1.381E+14
1s2p^3 ^{3}D$_3$ - 1s^{2}2p^2 ^{3}P$_2$	1.8764	1.8765	1.8771	1.783E+14	1.782E+14	1.780E+14
1s2p^3 ^{1}D$_2$ - 1s^{2}2p^2 ^{1}D$_2$	1.8765	1.8766	1.8773	1.783E+14	1.780E+14	1.770E+14
[1s]2p ^{3}P$_1$ - 1s^{2}2s^2 ^{1}S$_0$	1.8773	1.8774	1.8780	2.982E+13	2.982E+13	2.978E+13

Table 5.5: (continued)

Transition	λ (Å)			A_{ki} (s^{-1})		
	$\mu = 0.0$	$\mu = 0.1$	$\mu = 0.25$	$\mu = 0.0$	$\mu = 0.1$	$\mu = 0.25$
1s2p^3 ^{3}D$_1$ - 1s^{2}2p^2 ^{3}P$_2$	1.8779	1.8780	1.8787	4.039E+13	4.038E+13	4.032E+13
1s2p^3 ^{3}S$_1$ - 1s^{2}2p^2 ^{1}D$_2$	1.8786	1.8788	1.8794	3.925E+13	3.920E+13	3.897E+13
1s2s2p^2(^{2}P) ^{3}P$_0$ - 2s2p ^{1}P$_1$	1.8789	1.8790	1.8796	2.873E+13	2.871E+13	2.860E+13
1s2s2p^2 ^{3}S$_1$ - 2s2p ^{1}P$_1$	1.8792	1.8793	1.8799	1.900E+13	1.900E+13	1.896E+13
1s2p^3 ^{3}D$_3$ - 1s^{2}2p^2 ^{1}D$_2$	1.8812	1.8813	1.8819	6.025E+13	6.022E+13	6.006E+13
1s2s2p^2(^{4}P) ^{3}P$_2$ - 2s2p ^{1}P$_1$	1.8813	1.8814	1.8821	1.008E+13	1.006E+13	1.000E+13
1s2p^3 ^{3}D$_2$ - 1s^{2}2p^2 ^{1}D$_2$	1.8822	1.8824	1.8830	1.378E+13	1.377E+13	1.373E+13
1s2p^3 ^{3}P$_1$ - 1s^{2}2p^2 ^{1}S$_0$	1.8823	1.8825	1.8831	2.689E+13	2.688E+13	2.684E+13
[1s]2p ^{1}P$_1$ - 1s^{2}2p^2 ^{1}D$_2$	1.9120	1.9122	1.9132	1.164E+13	1.161E+13	1.139E+13
Fe XXIV						
1s2p^2 ^{2}S$_{1/2}$ - 1s^{2}2p ^{2}P$_{3/2}$	1.8545	1.8546	1.8553	2.554E+14	2.554E+14	2.555E+14
1s2s2p(^{1}P) ^{2}P$_{1/2}$ - 1s^{2}2s ^{2}S$_{1/2}$	1.8550	1.8551	1.8557	2.020E+14	2.020E+14	2.015E+14
1s2p^2 ^{2}P$_{3/2}$ - 1s^{2}2p ^{2}P$_{1/2}$	1.8552	1.8553	1.8560	1.500E+13	1.500E+13	1.499E+13
1s2s2p(^{3}P) ^{2}P$_{3/2}$ - 1s^{2}2s ^{2}S$_{1/2}$	1.8585	1.8586	1.8592	4.944E+14	4.943E+14	4.936E+14
1s2p^2 ^{2}P$_{3/2}$ - 1s^{2}2p ^{2}P$_{3/2}$	1.8598	1.8599	1.8605	6.439E+14	6.437E+14	6.426E+14
1s2p^2 ^{2}P$_{1/2}$ - 1s^{2}2p ^{2}P$_{1/2}$	1.8602	1.8603	1.8609	5.559E+14	5.557E+14	5.550E+14
1s2p^2 ^{2}D$_{3/2}$ - 1s^{2}2p ^{2}P$_{1/2}$	1.8609	1.8610	1.8617	3.227E+14	3.226E+14	3.221E+14
1s2s2p(^{3}P) ^{2}P$_{1/2}$ - 1s^{2}2s ^{2}S$_{1/2}$	1.8612	1.8613	1.8619	3.026E+14	3.026E+14	3.022E+14
1s2p^2 ^{2}D$_{5/2}$ - 1s^{2}2p ^{2}P$_{3/2}$	1.8636	1.8637	1.8643	2.177E+14	2.176E+14	2.173E+14
1s2p^2 ^{2}P$_{1/2}$ - 1s^{2}2p ^{2}P$_{3/2}$	1.8647	1.8649	1.8655	1.577E+14	1.578E+14	1.570E+14
1s2p^2 ^{2}D$_{3/2}$ - 1s^{2}2p ^{2}P$_{3/2}$	1.8655	1.8656	1.8663	2.653E+13	2.652E+13	2.644E+13
1s2p^2 ^{4}P$_{1/2}$ - 1s^{2}2p ^{2}P$_{1/2}$	1.8706	1.8707	1.8713	1.726E+13	1.727E+13	1.733E+13
1s2p^2 ^{4}P$_{5/2}$ - 1s^{2}2p ^{2}P$_{3/2}$	1.8707	1.8709	1.8715	3.004E+13	3.002E+13	2.993E+13
1s2s2p ^{4}P$_{3/2}$ - 1s^{2}2s ^{2}S$_{1/2}$	1.8718	1.8719	1.8725	1.288E+13	1.288E+13	1.284E+13
Fe XXV						
1s2p ^{1}P$_1$ - 1s^2 ^{1}S$_0$	1.8476	1.8478	1.8485	4.843E+14	4.842E+14	4.834E+14
1s2p ^{3}P$_1$ - 1s^2 ^{1}S$_0$	1.8571	1.8572	1.8579	3.555E+13	3.553E+13	3.544E+13

Table 5.6: Plasma environment effects on the Auger widths in Fe XVII - Fe XXIV

Level	Auger width (s^{-1})		
	$\mu = 0.0$	$\mu = 0.1$	$\mu = 0.25$
Fe XVII			
[1s]3s ^{3}S$_1$	7.711E+14	7.647E+14	7.604E+14
[1s]3s ^{1}S$_0$	8.135E+14	8.069E+14	8.027E+14
[1s]3p ^{3}P$_0$	7.610E+14	7.548E+14	7.420E+14
[1s]3p ^{3}P$_1$	7.302E+14	7.243E+14	7.128E+14
[1s]3p ^{3}P$_2$	7.154E+14	7.097E+14	7.069E+14
[1s]3p ^{1}P$_1$	7.244E+14	7.189E+14	7.106E+14

Table 5.6: (continued)

Level	Auger width (s^{-1})		
	$\mu = 0.0$	$\mu = 0.1$	$\mu = 0.25$
Fe XVIII			
[1s]2p^6 ^{2}S$_{1/2}$	1.529E+15	1.523E+15	1.504E+15
Fe XIX			
[1s]2p^5 ^{3}P$_2$	8.058E+14	8.016E+14	7.951E+14
[1s]2p^5 ^{3}P$_1$	7.929e+14	7.890E+14	7.828E+14
[1s]2p^5 ^{3}P$_0$	7.803E+14	7.764E+14	7.699E+14
[1s]2p^5 ^{1}P$_1$	7.512E+14	7.484E+14	7.427E+14
1s2s2p^6 ^{3}S$_1$	7.663E+14	7.623E+14	7.598E+14
1s2s2p^6 ^{1}S$_0$	1.137E+15	1.130E+15	1.115E+15
Fe XX			
[1s]2p^4 ^{4}P$_{5/2}$	5.773E+14	5.721E+14	5.627E+14
[1s]2p^4 ^{4}P$_{3/2}$	5.599E+14	5.548E+14	5.456E+14
[1s]2p^4 ^{4}P$_{1/2}$	5.695E+14	5.643E+14	5.551E+14
[1s]2p^4 ^{2}D$_{3/2}$	6.034E+14	5.976E+14	5.855E+14
[1s]2p^4 ^{2}D$_{5/2}$	6.756E+14	6.694E+14	6.561E+14
[1s]2p^4 ^{2}P$_{1/2}$	5.300E+14	5.241E+14	5.139E+14
[1s]2p^4 ^{2}P$_{3/2}$	5.381E+14	5.327E+14	5.218E+14
[1s]2p^4 ^{2}S$_{1/2}$	5.561E+14	5.497E+14	5.398E+14
1s2s2p^5 ^{4}P$_{5/2}$	5.546E+14	5.509E+14	5.377E+14
1s2s2p^5 ^{4}P$_{3/2}$	5.529E+14	5.492E+14	5.361E+14
1s2s2p^5 ^{4}P$_{1/2}$	5.424E+14	5.387E+14	5.257E+14
1s2s2p^5(^{3}P) ^{2}P$_{3/2}$	7.659E+14	7.548E+14	7.365E+14
1s2s2p^5(^{3}P) ^{2}P$_{1/2}$	6.087E+14	6.020E+14	5.867E+14
1s2s2p^5(^{1}P) ^{2}P$_{3/2}$	6.970E+14	6.907E+14	6.768E+14
1s2s2p^5(^{1}P) ^{2}P$_{1/2}$	8.373E+14	8.270E+14	8.107E+14
1s2p^6 ^{2}S$_{1/2}$	7.350E+14	7.271E+14	7.046E+14
Fe XXI			
[1s]2p^3 ^{5}S$_2$	3.022E+14	3.015E+14	3.004E+14
[1s]2p^3 ^{3}D$_1$	4.445E+14	4.410E+14	4.372E+14
[1s]2p^3 ^{3}D$_2$	4.626E+14	4.588E+14	4.546E+14
[1s]2p^3 ^{3}D$_3$	4.859E+14	4.812E+14	4.765E+14
[1s]2p^3 ^{3}S$_1$	2.965E+14	2.949E+14	2.926E+14
[1s]2p^3 ^{1}D$_2$	4.352E+14	4.326E+14	4.276E+14
[1s]2p^3 ^{3}P$_0$	4.344E+14	4.312E+14	4.273E+14
[1s]2p^3 ^{3}P$_1$	3.652E+14	3.633E+14	3.599E+14
[1s]2p^3 ^{3}P$_2$	4.216E+14	4.182E+14	4.152E+14
[1s]2p^3 ^{1}P$_1$	3.549E+14	3.528E+14	3.495E+14

Table 5.6: (continued)

Level	Auger width (s^{-1})		
	$\mu = 0.0$	$\mu = 0.1$	$\mu = 0.25$
1s2s2p^4 ^{5}P$_3$	2.962E+14	2.907E+14	2.862E+14
1s2s2p^4 ^{5}P$_2$	2.866E+14	2.813E+14	2.769E+14
1s2s2p^4 ^{5}P$_1$	2.898E+14	2.846E+14	2.802E+14
1s2s2p^4 ^{3}P$_2$	4.140E+14	4.081E+14	4.029E+14
1s2s2p^4 ^{3}D$_1$	4.259E+14	4.188E+14	4.133E+14
1s2s2p^4 ^{3}D$_3$	4.550E+14	4.470E+14	4.411E+14
1s2s2p^4 ^{3}D$_2$	4.692E+14	4.627E+14	4.560E+14
1s2s2p^4 ^{3}P$_1$	3.835E+14	3.784E+14	3.735E+14
1s2s2p^4 ^{3}P$_0$	4.007E+14	3.963E+14	3.909E+14
1s2s2p^4 ^{3}S$_1$	4.242E+14	4.201E+14	4.149E+14
1s2s2p^4 ^{3}P$_2$	5.393E+14	5.339E+14	5.260E+14
1s2s2p^4 ^{3}P$_0$	5.254E+14	5.210E+14	5.132E+14
1s2s2p^4 ^{1}D$_2$	6.722E+14	6.655E+14	6.554E+14
1s2s2p^4 ^{3}P$_1$	4.764E+14	4.722E+14	4.655E+14
1s2s2p^4 ^{1}P$_1$	3.587E+14	3.552E+14	3.521E+14
1s2s2p^4 ^{1}S$_0$	6.172E+14	6.127E+14	6.019E+14
1s2p^5 ^{3}P$_2$	5.085E+14	4.987E+14	4.928E+14
1s2p^5 ^{3}P$_1$	5.052E+14	4.956E+14	4.900E+14
1s2p^5 ^{3}P$_0$	4.918E+14	4.826E+14	4.771E+14
1s2p^5 ^{1}P$_1$	5.054E+14	4.973E+14	4.936E+14
Fe XXII			
[1s]2p^2 ^{4}P$_{1/2}$	2.555E+14	2.513E+14	2.478E+14
[1s]2p^2 ^{4}P$_{3/2}$	2.475E+14	2.437E+14	2.405E+14
[1s]2p^2 ^{4}P$_{5/2}$	2.648E+14	2.612E+14	2.577E+14
1s2s2p^3 ^{6}S$_{5/2}$	5.024E+12	5.017E+12	4.942E+12
[1s]2p^2 ^{2}P$_{1/2}$	3.294E+14	3.270E+14	3.204E+14
[1s]2p^2 ^{2}D$_{3/2}$	1.731E+14	1.702E+14	1.668E+14
[1s]2p^2 ^{2}D$_{5/2}$	3.619E+14	3.591E+14	3.520E+14
[1s]2p^2 ^{2}P$_{3/2}$	1.812E+14	1.790E+14	1.753E+14
[1s]2p^2 ^{2}S$_{1/2}$	2.841E+14	2.799E+14	2.768E+14
1s2s2p^3 ^{4}D$_{3/2}$	2.262E+14	2.252E+14	2.229E+14
1s2s2p^3 ^{4}D$_{5/2}$	2.433E+14	2.425E+14	2.397E+14
1s2s2p^3 ^{4}D$_{1/2}$	2.500E+14	2.495E+14	2.468E+14
1s2s2p^3 ^{4}D$_{7/2}$	2.587E+14	2.574E+14	2.554E+14
1s2s2p^3 ^{4}S$_{3/2}$	9.463E+13	9.321E+13	9.090E+13
1s2s2p^3 ^{4}P$_{1/2}$	1.983E+14	1.978E+14	1.944E+14
1s2s2p^3 ^{4}P$_{5/2}$	2.093E+14	2.088E+14	2.047E+14

Table 5.6: (continued)

Level	Auger width (s^{-1})		
	$\mu = 0.0$	$\mu = 0.1$	$\mu = 0.25$
1s2s2p^3 ^{4}P$_{3/2}$	2.057E+14	2.045E+14	2.009E+14
1s2s2p^3 ^{2}D$_{3/2}$	3.690E+14	3.648E+14	3.576E+14
1s2s2p^3 ^{2}D$_{5/2}$	3.521E+14	3.491E+14	3.406E+14
1s2s2p^3 ^{4}S$_{3/2}$	2.643E+14	2.612E+14	2.612E+14
1s2s2p^3 ^{2}D$_{3/2}$	3.181E+14	3.168E+14	3.127E+14
1s2s2p^3(^{3}P) ^{2}P$_{1/2}$	2.441E+14	2.416E+14	2.375E+14
1s2s2p^3 ^{2}D$_{5/2}$	4.129E+14	4.114E+14	4.062E+14
1s2s2p^3(^{3}P) ^{2}P$_{3/2}$	2.972E+14	2.951E+14	2.903E+14
1s2s2p^3(^{1}P) ^{2}P$_{1/2}$	3.330E+14	3.295E+14	3.272E+14
1s2s2p^3(^{1}P) ^{2}P$_{3/2}$	3.886E+14	3.840E+14	3.803E+14
1s2s2p^3 ^{2}S$_{1/2}$	1.561E+14	1.557E+14	1.545E+14
1s2p^4 ^{4}P$_{5/2}$	2.796E+14	2.785E+14	2.733E+14
1s2p^4 ^{4}P$_{3/2}$	2.705E+14	2.693E+14	2.641E+14
1s2p^4 ^{4}P$_{1/2}$	2.704E+14	2.690E+14	2.639E+14
1s2p^4 ^{2}D$_{3/2}$	3.670E+14	3.652E+14	3.565E+14
1s2p^4 ^{2}D$_{5/2}$	4.219E+14	4.207E+14	4.106E+14
1s2p^4 ^{2}P$_{3/2}$	3.174E+14	3.169E+14	3.070E+14
1s2p^4 ^{2}P$_{1/2}$	2.793E+14	2.777E+14	2.686E+14
1s2p^4 ^{2}S$_{1/2}$	2.921E+14	2.890E+14	2.796E+14
Fe XXIII			
[1s]2p ^{3}P$_0$	1.962E+14	1.961E+14	1.959E+14
[1s]2p ^{3}P$_1$	1.991E+14	1.989E+14	1.986E+14
[1s]2p ^{3}P$_2$	2.017E+14	2.014E+14	2.007E+14
1s2s2p^2 ^{5}P$_1$	1.982E+12	1.972E+12	1.956E+12
1s2s2p^2 ^{5}P$_2$	6.627E+11	6.453E+11	6.343E+11
1s2s2p^2 ^{5}P$_3$	6.655E+12	6.504E+12	6.430E+12
[1s]2p ^{1}P$_1$	1.295E+14	1.306E+14	1.314E+14
1s2s2p^2(^{4}P) ^{3}P$_0$	7.895E+13	7.762E+13	7.329E+13
1s2s2p^2(^{4}P) ^{3}P$_1$	9.730E+13	9.574E+13	9.516E+13
1s2s2p^2 ^{3}D$_2$	1.508E+14	1.494E+14	1.484E+14
1s2s2p^2 ^{3}D$_3$	1.165E+14	1.146E+14	1.130E+14
1s2s2p^2 ^{3}D$_1$	1.786E+14	1.779E+14	1.763E+14
1s2s2p^2(^{4}P) ^{3}P$_2$	8.725E+13	8.556E+13	8.283E+13
1s2s2p^2 ^{3}S$_1$	1.560E+14	1.545E+14	1.482E+14
1s2s2p^2(^{2}P) ^{3}P$_0$	1.652E+14	1.640E+14	1.581E+14
1s2s2p^2 ^{1}D$_2$	2.476E+14	2.445E+14	2.386E+14
1s2s2p^2(^{2}P) ^{3}P$_1$	1.288E+14	1.277E+14	1.229E+14

Table 5.6: (continued)

Level	Auger width (s^{-1})		
	$\mu = 0.0$	$\mu = 0.1$	$\mu = 0.25$
1s2p^3 ^{5}S$_2$	7.228E+12	7.080E+12	7.076E+12
1s2s2p^2(^{2}P) ^{3}P$_2$	2.542E+14	2.509E+14	2.437E+14
1s2s2p^2 ^{1}P$_1$	7.024E+13	7.011E+13	6.869E+13
1s2s2p^2 ^{1}S$_0$	2.409E+14	2.358E+14	2.244E+14
1s2p^3 ^{3}D$_1$	2.132E+14	2.095E+14	2.004E+14
1s2p^3 ^{3}D$_2$	2.232E+14	2.194E+14	2.104E+14
1s2p^3 ^{3}D$_3$	2.460E+14	2.417E+14	2.328E+14
1s2p^3 ^{3}S$_1$	5.256E+13	5.174E+13	5.105E+13
1s2p^3 ^{1}D$_2$	2.090E+14	2.061E+14	2.014E+14
1s2p^3 ^{3}P$_0$	1.515E+14	1.492E+14	1.490E+14
1s2p^3 ^{3}P$_1$	1.412E+14	1.392E+14	1.391E+14
1s2p^3 ^{3}P$_2$	1.903E+14	1.882E+14	1.877E+14
1s2p^3 ^{1}P$_1$	1.418E+14	1.415E+14	1.408E+14
Fe XXIV			
1s2s2p ^{4}P$_{1/2}$	2.875E+09	2.488E+09	1.920E+09
1s2s2p ^{4}P$_{3/2}$	2.663E+11	2.779E+11	2.877E+11
1s2s2p ^{4}P$_{5/2}$	6.654E+09	6.715E+09	6.961E+09
1s2s2p(^{3}P) ^{2}P$_{1/2}$	5.781E+13	5.736E+13	5.491E+13
1s2s2p(^{3}P) ^{2}P$_{3/2}$	9.884E+10	6.636E+10	2.746E+10
1s2p^2 ^{4}P$_{1/2}$	1.775E+11	1.778E+11	1.918E+11
1s2s2p(^{1}P) ^{2}P$_{1/2}$	7.824E+13	7.803E+13	7.675E+13
1s2s2p(^{1}P) ^{2}P$_{3/2}$	9.397E+11	9.097E+11	8.113E+11
1s2p^2 ^{4}P$_{3/2}$	1.216E+14	1.212E+14	1.171E+14
1s2p^2 ^{4}P$_{5/2}$	2.117E+13	2.055E+13	2.005E+13
1s2p^2 ^{2}D$_{3/2}$	1.400E+14	1.361E+14	1.339E+14
1s2p^2 ^{2}P$_{1/2}$	2.186E+12	2.178E+12	2.163E+12
1s2p^2 ^{2}D$_{5/2}$	1.510E+14	1.471E+14	1.453E+14
1s2p^2 ^{2}P$_{3/2}$	2.667E+13	2.601E+13	2.576E+13
1s2p^2 ^{2}S$_{1/2}$	3.156E+13	3.130E+13	3.015E+13

Table 5.7: Computed level energies and fluorescence yields (ω_K) for K-vacancy states in Fe XVII–XIX ions as a function of the plasma screening parameter μ (in a.u.)

Ion	Level	Energy (keV)		ω_K (s^{-1})	
		$\mu = 0.0$	$\mu = 0.25$	$\mu = 0.0$	$\mu = 0.25$
Fe XVII	$1s2s^22p^63s\ ^3S_1$	7.151	7.143	0.44	0.44
	$1s2s^22p^63s\ ^1S_0$	7.156	7.148	0.43	0.43
	$1s2s^22p^63p\ ^3P_0$	7.183	7.176	0.44	0.45
	$1s2s^22p^63p\ ^3P_1$	7.184	7.176	0.45	0.45
	$1s2s^22p^63p\ ^3P_2$	7.186	7.179	0.46	0.46
	$1s2s^22p^63p\ ^1P_1$	7.190	7.182	0.49	0.50
Fe XVIII	$1s2s^22p^6\ ^2S_{1/2}$	6.437	6.435	0.29	0.29
Fe XIX	$1s2s^22p^5\ ^3P_2$	6.470	6.468	0.34	0.35
	$1s2s^22p^5\ ^3P_1$	6.477	6.474	0.38	0.38
	$1s2s^22p^5\ ^3P_0$	6.485	6.482	0.35	0.35
	$1s2s^22p^5\ ^1P_1$	6.497	6.495	0.51	0.51
	$1s2s2p^6\ ^3S_1$	6.587	6.585	0.45	0.45
	$1s2s2p^6\ ^1S_0$	6.615	6.613	0.36	0.36

5.2 Fe IX – Fe XVI

The multiconfiguration models used for Fe IX – Fe XVI (Ar- through Na-like Fe ions) are generated using the active space method, whereby electrons from the reference configurations listed in Table 5.8 are singly and doubly excited to configurations that include $n = 3$ and 4s orbitals. The number of CSFs within the MCDF expansion of each ion is also given in this table. Computations are performed with the extended average level (EAL) option optimizing a weighted trace of the Hamiltonian using level weights proportional to $(2J + 1)$. The QED effects listed in Section 2.1.3 are also included in the calculations. The MCDF wavefunctions obtained with GRASP2K are then used in RATIP to compute the atomic structure, the radiative wavelengths and decay rates, and the Auger widths associated with K-vacancy states (as described in Chapter 2 and similarly to the computations of Section 5.1), where the plasma effects are considered through a Debye-Hückel potential with a screening parameter in the range $0 \leq \mu \leq 0.25$ a.u.

The computed ionization potentials (IPs) and K thresholds (E_K) are given in Tables 5.9–5.10, respectively, for plasma screening parameter $\mu = 0.0$, $\mu = 0.1$ and $\mu = 0.25$. As a reminder, the case $\mu = 0.1$ a.u. corresponds for instance to plasma conditions as $T = 10^5$ K and $n_e = 10^{21}$ cm^{-3}, and $\mu = 0.25$ a.u. to $T = 10^5$ K and $n_e = 10^{22}$ cm^{-3}. For the isolated ion case ($\mu = 0.0$ a.u.), the computed IPs

Table 5.8: Reference configurations used to build up the MCDF active space (AS) along with the total number of configuration state functions (CSFs) generated for the MCDF expansions in Fe IX – Fe XVI.

Ion	Reference configurations	Number of CSFs
Fe IX	$3p^6$, $[3p]3d$, $[2p]3d$, $[1s]3d$	20009
Fe X	$3p^5$, $[2p]3p^6$, $[1s]3p^6$	6312
Fe XI	$3p^4$, $[2p]3p^5$, $[1s]3p^5$	12981
Fe XII	$3p^3$, $[2p]3p^4$, $[1s]3p^4$	37967
Fe XIII	$3p^2$, $[2p]3p^3$, $[1s]3p^3$	46771
Fe XIV	$3p$, $[2p]3p^2$, $[1s]3p^2$	35109
Fe XV	$3s^2$, $[2p]3s^23p$, $[1s]3s^23p$	16853
Fe XVI	$3s$, $[2p]3s^2$, $[2p]3s3p$, $[1s]3s^2$, $[1s]3s3p$	25914

are compared in Table 5.9 with the values quoted in the NIST atomic database (Kramida *et al.* 2019), showing an excellent agreement within 0.1%.

Tables 5.9–5.10 also show the IP and K-threshold lowering due to plasma environment for $\mu = 0.1$ a.u. and $\mu = 0.25$ a.u. In agreement with the results of Section 5.1, the absolute IP and K-threshold downshifts for each species are practically similar in magnitude and substantial, the IPs and K thresholds being reduced by about 25 to 45 eV for $\mu = 0.1$ and by about 50 to 110 eV for $\mu = 0.25$. This lowering corresponds to IP relative variations of 9–10% and 21–25%, respectively, while those for the K thresholds, due to their much larger values, are only of 0.4–0.6%

Table 5.9: Computed ionization potentials for Fe IX – Fe XVI as a function of the plasma screening parameter μ (a.u.). NIST values are also listed for comparison.

Ion	IP (eV)			
	NIST[a]	$\mu = 0.0$	$\mu = 0.1$	$\mu = 0.25$
Fe IX	233.6(4)	230.91	206.99	173.48
Fe X	262.10(12)	263.14	236.65	199.74
Fe XI	290.9(4)	294.15	265.04	224.58
Fe XII	330.8(6)	325.81	294.04	249.75
Fe XIII	361.0(7)	356.95	322.54	274.48
Fe XIV	392.2(7)	388.72	351.68	300.03
Fe XV	456.2(5)	457.14	417.57	362.77
Fe XVI	489.312(14)	488.86	446.68	388.34

[a] Kramida *et al.* (2019)

Table 5.10: Computed K-thresholds for Fe IX – Fe XVI as a function of the plasma screening parameter μ (a.u.).

Ion	E_K (eV)		
	$\mu = 0.0$	$\mu = 0.1$	$\mu = 0.25$
Fe IX	7308.25	7283.14	7243.32
Fe X	7351.72	7324.04	7280.88
Fe XI	7393.76	7363.48	7316.89
Fe XII	7434.46	7401.52	7351.12
Fe XIII	7483.90	7448.32	7394.27
Fe XIV	7535.85	7497.64	7439.95
Fe XV	7591.60	7550.76	7489.46
Fe XVI	7639.54	7596.05	7531.05

and 1%. This effect can be further appreciated in Figures 5.8–5.9, where we plot the absolute downshifts as a function of the effective charge, $Z_{\text{eff}} = Z - N + 1$. We also include in these figures the Fe species with $17 \leq Z_{\text{eff}} \leq 25$ from Section 5.1 along with the Debye-Hückel limit $\Delta IP_{\text{DH}} = -Z_{\text{eff}}\,\mu$ (Stewart & Pyatt 1966; Crowley 1984).

Figure 5.8: Ionization potential shifts (ΔIP) in Fe IX – Fe XXV as a function of the effective charge $Z_{\text{eff}} = Z - N + 1$. Red open circles: $\mu = 0.1$ a.u. Black open circles: $\mu = 0.25$ a.u. Open triangles: Debye-Hückel limit $\Delta IP_{\text{DH}} = -Z_{\text{eff}}\,\mu$.
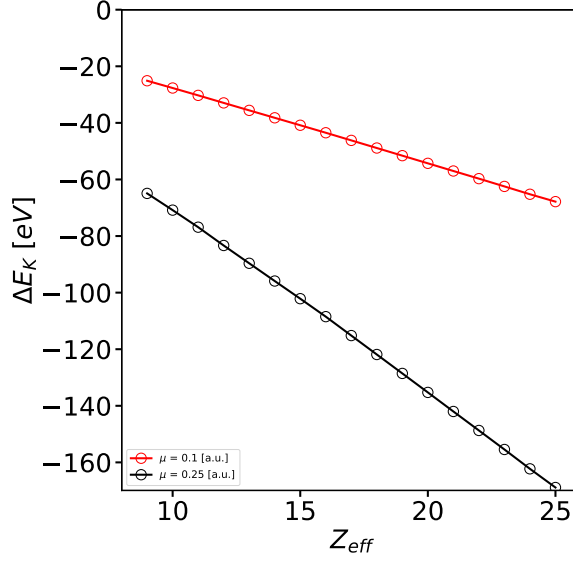
Figure 5.9: K-threshold shifts (ΔE_K) in Fe IX – Fe XXV as a function of the effective charge $Z_{\text{eff}} = Z - N + 1$. Red open circles: $\mu = 0.1$ a.u. Black open circles: $\mu = 0.25$ a.u.

The linear lowerings of both the IP and K threshold, ΔIP and ΔE_K, respectively, with Z_{eff} and their close magnitude for each ion are hereby reiterated. We also verify that the Debye-Hückel limit is a good approximation of the IP lowering except for two discontinuities at $Z_{\text{eff}} = 17$ and $Z_{\text{eff}} = 25$ that are conspicuous for the higher plasma screening parameter value ($\mu = 0.25$), and which are caused by the closing of the L and K shells, respectively. It can be seen in Figure 5.10 that the IP increases linearly with Z_{eff} but two substantial jumps of a factor of 2.6 and 4 occur respectively for the closed L- and K-shell species Fe XVII and Fe XXV, and seem to be slightly attenuated while increasing the screening parameter (the jump observed for Fe XVII is about 771.7, 768.1 and 759.5 eV for $\mu = 0$, $\mu = 0.1$ and $\mu = 0.25$, respectively, and the ones for Fe XXV about 6792.4, 6789.1 and 6782.1 eV). The behavior of the K threshold with effective charge is somewhat different (see Figure 5.11); although it still increases linearly, the slope becomes steeper at $Z_{\text{eff}} = 17$ and no effect is appreciable at $Z_{\text{eff}} = 25$ since the K-shell electron is located deeper close to the nucleus in contrast to the relatively weakly bound valence electron.

In Table 5.11, we tabulate the wavelengths and radiative rates for the strongest K lines ($A_{ki} \geq 10^{13}$ s^{-1}) for $\mu = 0$ a.u., $\mu = 0.1$ a.u. and $\mu = 0.25$ a.u. The present MCDF K-line wavelengths are in excellent agreement with those obtained with the pseudo-relativistic Hartree–Fock (HFR) method by Palmeri *et al.* (2003b) and Mendoza *et al.* (2004), with an average deviation of less than 0.1%, while
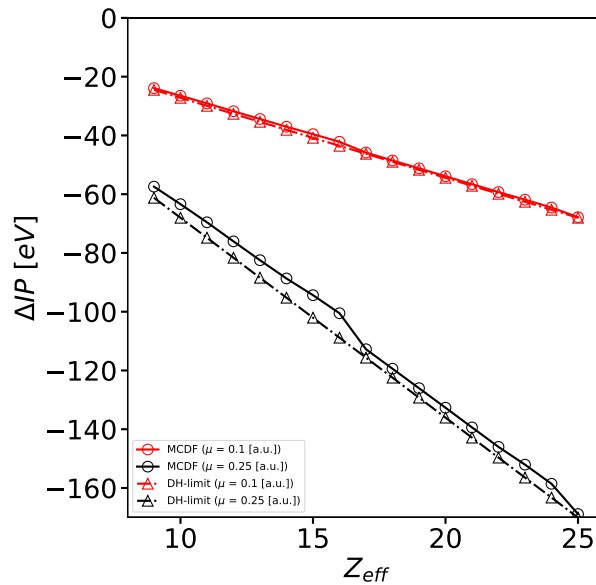
Figure 5.10: Ionization potential (IP) of Fe IX – Fe XXV as a function of the effective charge $Z_{\text{eff}} = Z - N + 1$. Blue open circles: $\mu = 0$ a.u. (isolated atom case). Red open circles: $\mu = 0.1$ a.u. Black open circles: $\mu = 0.25$ a.u. Green open stars: NIST (Kramida *et al.* 2019).

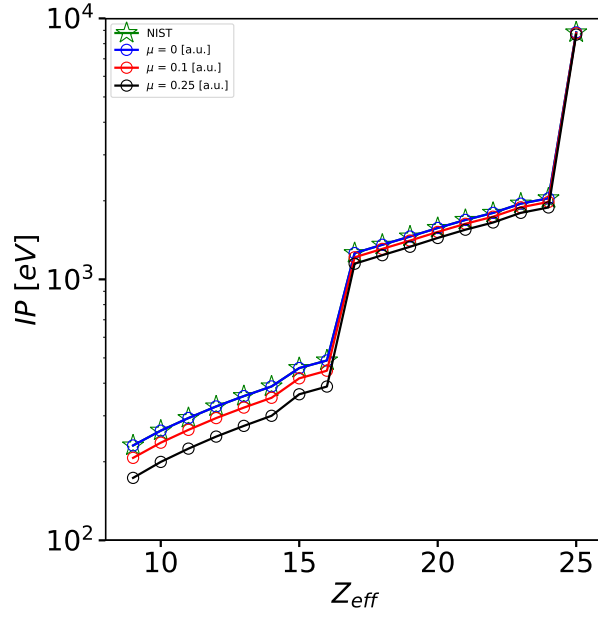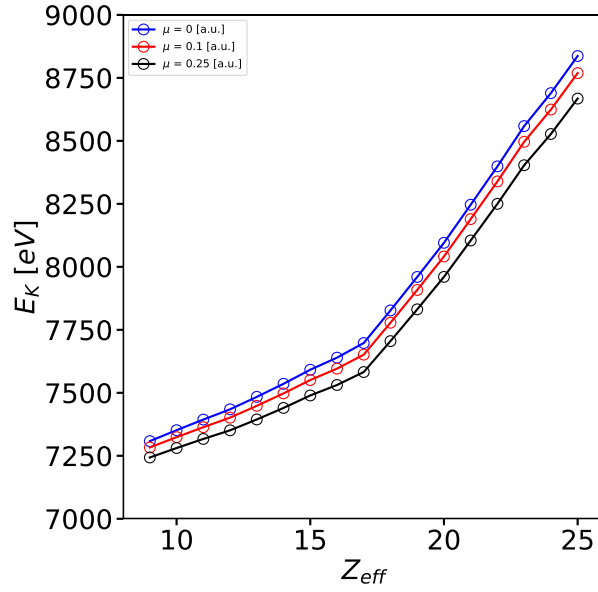Figure 5.11: K thresholds (E_K) of Fe IX – Fe XXV as a function of the effective charge $Z_{\text{eff}} = Z - N + 1$. Blue open circles: $\mu = 0$ a.u. (isolated atom case). Red open circles: $\mu = 0.1$ a.u. Black open circles: $\mu = 0.25$ a.u.

the dispersion of the radiative transition probabilities is not larger than 20%. As discussed in Section 5.1, this discrepancy can mainly be explained by the fully-relativistic framework of our method, unlike the HFR approach.

Regarding plasma effects, it can be noticed in Table 5.11 that both the K-line radiative wavelengths and rates in Fe IX – Fe XVI are hardly modified. Actually, all the K lines are found to be redshifted by $\sim 1-2$ mÅ or less, while the corresponding transition probabilities only vary by a few percent in most cases (up to 15–20% in a handful of transitions). In Figure 5.12, we plot the wavelength shifts as a function of the ionic effective charge $9 \leq Z_{\text{eff}} \leq 25$ for $\mu = 0.1$ a.u. and $\mu = 0.25$ a.u., also including the data from Section 5.1 for Fe XVII – Fe XXV again. We do not see a well-defined trend with Z_{eff}, but for $Z_{\text{eff}} \leq 17$, the Kβ redshifts at $\mu = 0.25$ a.u. are found to be about 2 mÅ, that is a factor of 2 larger than for the Kα lines. This is due to the larger sensibility of the $n = 3$ electrons to the plasma environment with respect to the $n = 2$ electrons, as already discussed in Section 5.1.

The Auger widths for the K-vacancy states we computed for the isolated atom (see Table 5.12) are in good agreement with those obtained by Palmeri *et al.* (2003b) and Mendoza *et al.* (2004), since the differences are not larger than 10–15%. As it can be seen in Table 5.12, and similarly to the radiative rates, our Auger widths are only weakly modified by the plasma environment: the observed reductions at $\mu = 0.25$ a.u. are not greater than a few percent ($< 3\%$) with respect
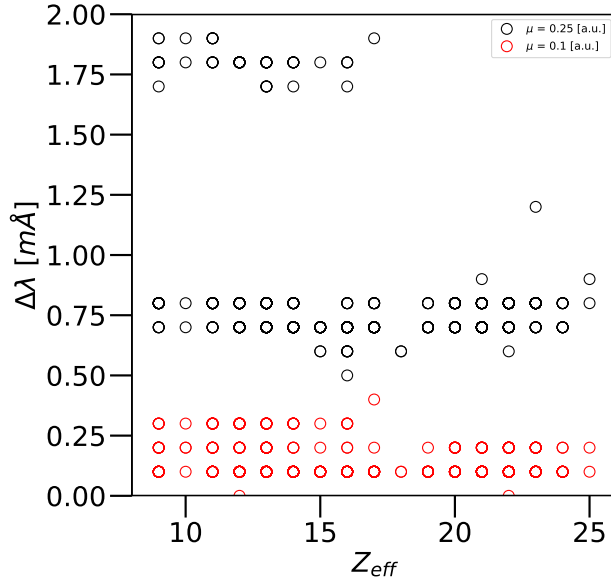

Figure 5.12: Wavelength shifts ($\Delta\lambda$) for K lines in Fe IX – Fe XXV as a function of the effective charge Z_{eff}. Red circles: $\mu = 0.1$ a.u. Black circles: $\mu = 0.25$ a.u.

110

to the isolated atom.

Let us emphasize that the results presented in this section have been published very recently (Deprince *et al.* 2020b).

Table 5.11: Plasma environment effects on radiative wavelengths (λ) and transition probabilities (A_{ki}) of K lines in Fe IX – Fe XVI computed with MCDF/RATIP depending on the plasma screening parameter μ (given in a.u.)

Transition	λ (Å)			A_{ki} (s^{-1})		
	$\mu = 0.0$	$\mu = 0.1$	$\mu = 0.25$	$\mu = 0.0$	$\mu = 0.1$	$\mu = 0.25$
Fe IX						
[1s]3d ^{3}D$_2$ - [2p]3d ^{3}F$_3$	1.7538	1.7541	1.7556	4.143E+13	4.146E+13	4.164E+13
[1s]3d ^{3}D$_1$ - [2p]3d ^{3}F$_2$	1.7540	1.7542	1.7558	5.446E+13	5.450E+13	5.472E+13
[1s]3d ^{1}D$_2$ - [2p]3d ^{3}D$_3$	1.7546	1.7549	1.7565	1.961E+13	1.958E+13	1.943E+13
[1s]3d ^{3}D$_2$ - [2p]3d ^{1}D$_2$	1.7548	1.7550	1.7566	2.961E+13	2.961E+13	2.961E+13
[1s]3d ^{1}D$_2$ - [2p]3d ^{3}D$_2$	1.7548	1.7551	1.7567	2.518E+13	2.518E+13	2.527E+13
[1s]3d ^{3}D$_1$ - [2p]3d ^{3}D$_1$	1.7549	1.7551	1.7567	2.460E+13	2.464E+13	2.480E+13
[1s]3d ^{1}D$_2$ - [2p]3d ^{1}F$_3$	1.7549	1.7552	1.7567	2.334E+13	2.342E+13	2.381E+13
[1s]3d ^{1}D$_2$ - [2p]3d ^{1}P$_1$	1.7588	1.7590	1.7605	1.556E+13	1.559E+13	1.572E+13
[1s]3d ^{3}D$_1$ - [2p]3d ^{3}P$_0$	1.9357	1.9358	1.9365	6.334E+13	6.332E+13	6.322E+13
[1s]3d ^{1}D$_2$ - [2p]3d ^{3}P$_1$	1.9358	1.9359	1.9366	1.997E+13	1.993E+13	1.973E+13
[1s]3d ^{3}D$_1$ - [2p]3d ^{3}P$_1$	1.9359	1.9360	1.9367	1.061E+14	1.060E+14	1.057E+14
[1s]3d ^{3}D$_2$ - [2p]3d ^{3}P$_1$	1.9359	1.9360	1.9367	3.040E+13	3.044E+13	3.064E+13
[1s]3d ^{1}D$_2$ - [2p]3d ^{3}P$_2$	1.9362	1.9363	1.9370	8.137E+13	8.131E+13	8.098E+13
[1s]3d ^{3}D$_1$ - [2p]3d ^{3}P$_2$	1.9363	1.9364	1.9371	2.921E+13	2.912E+13	2.868E+13
[1s]3d ^{3}D$_2$ - [2p]3d ^{3}P$_2$	1.9363	1.9364	1.9371	3.217E+13	3.221E+13	3.239E+13
[1s]3d ^{3}D$_2$ - [2p]3d ^{3}F$_3$	1.9365	1.9366	1.9372	2.690E+14	2.689E+14	2.684E+13
[1s]3d ^{1}D$_2$ - [2p]3d ^{1}D$_2$	1.9367	1.9368	1.9375	4.062E+13	4.062E+13	4.064E+13
[1s]3d ^{3}D$_1$ - [2p]3d ^{1}D$_2$	1.9368	1.9370	1.9376	1.554E+14	1.554E+14	1.555E+14
[1s]3d ^{3}D$_2$ - [2p]3d ^{1}D$_2$	1.9368	1.9369	1.9376	4.873E+13	4.867E+13	4.837E+13
[1s]3d ^{1}D$_2$ - [2p]3d ^{3}D$_3$	1.9369	1.9370	1.9377	1.297E+14	1.297E+14	1.294E+14
[1s]3d ^{1}D$_2$ - [2p]3d ^{3}D$_1$	1.9381	1.9383	1.9389	6.805E+13	6.799E+13	6.765E+13
[1s]3d ^{3}D$_1$ - [2p]3d ^{3}D$_1$	1.9383	1.9384	1.9390	6.597E+13	6.597E+13	6.598E+13
[1s]3d ^{3}D$_1$ - [2p]3d ^{3}F$_2$	1.9402	1.9403	1.9409	1.280E+14	1.280E+14	1.275E+14
[1s]3d ^{3}D$_2$ - [2p]3d ^{3}F$_2$	1.9402	1.9403	1.9409	1.078E+14	1.077E+14	1.075E+14
[1s]3d ^{1}D$_2$ - [2p]3d ^{3}D$_2$	1.9402	1.9403	1.9410	6.681E+13	6.680E+13	6.675E+13
[1s]3d ^{1}D$_2$ - [2p]3d ^{3}F$_3$	1.9403	1.9404	1.9411	1.367E+14	1.366E+14	1.364E+14
[1s]3d ^{1}D$_2$ - [2p]3d ^{1}P$_1$	1.9419	1.9420	1.9427	2.439E+13	2.446E+13	2.479E+13
[1s]3d ^{3}D$_1$ - [2p]3d ^{1}P$_1$	1.9420	1.9421	1.9428	1.776E+13	1.776E+13	1.775E+13
[1s]3d ^{3}D$_2$ - [2p]3d ^{1}P$_1$	1.9420	1.9421	1.9428	7.565E+13	7.555E+13	7.503E+13
Fe X						
[1s]3p^6 ^{2}S$_{1/2}$ - 3p^5 ^{2}P$_{3/2}$	1.7519	1.7521	1.7537	7.603E+13	7.610E+13	7.647E+13
[1s]3p^6 ^{2}S$_{1/2}$ - 3p^5 ^{2}P$_{1/2}$	1.7523	1.7526	1.7542	3.677E+13	3.681E+13	3.698E+13
[1s]3p^6 ^{2}S$_{1/2}$ - [2p]3p^6 ^{2}P$_{3/2}$	1.9367	1.9369	1.9375	3.830E+14	3.828E+14	3.822E+14
[1s]3p^6 ^{2}S$_{1/2}$ - [2p]3p^6 ^{2}P$_{1/2}$	1.9405	1.9406	1.9412	1.880E+14	1.880E+14	1.877E+14
Fe XI						
[1s]3p^5 ^{3}P$_1$ - 3p^4 ^{3}P$_2$	1.7488	1.7491	1.7506	3.773E+13	3.774E+13	3.783E+13
[1s]3p^5 ^{3}P$_0$ - 3p^4 ^{3}P$_1$	1.7489	1.7492	1.7507	8.067E+13	8.074E+13	8.112E+13
[1s]3p^5 ^{3}P$_2$ - 3p^4 ^{3}P$_2$	1.7491	1.7494	1.7509	5.786E+13	5.792E+13	5.825E+13

111

Transition	λ (Å)			A_{ki} (s^{-1})		
	$\mu = 0.0$	$\mu = 0.1$	$\mu = 0.25$	$\mu = 0.0$	$\mu = 0.1$	$\mu = 0.25$
[1s]3p^5 ^{3}P$_1$ - 3p^4 ^{3}P$_1$	1.7492	1.7495	1.7510	1.680E+13	1.684E+13	1.704E+13
[1s]3p^5 ^{3}P$_1$ - 3p^4 ^{3}P$_0$	1.7492	1.7495	1.7511	2.571E+13	2.574E+13	2.589E+13
[1s]3p^5 ^{1}P$_1$ - 3p^4 ^{1}D$_2$	1.7493	1.7496	1.7511	1.191E+14	1.193E+14	1.205E+14
[1s]3p^5 ^{3}P$_2$ - 3p^4 ^{3}P$_1$	1.7494	1.7497	1.7513	1.951E+13	1.953E+13	1.962E+13
[1s]3p^5 ^{3}P$_1$ - 3p^4 ^{1}D$_2$	1.7500	1.7503	1.7519	1.128E+13	1.119E+13	1.078E+13
[1s]3p^5 ^{1}P$_1$ - 3p^4 ^{1}S$_0$	1.7506	1.7509	1.7525	2.513E+13	2.516E+13	2.534E+13
[1s]3p^5 ^{1}P$_1$ - [2p]3p^5 ^{1}P$_1$	1.9341	1.9342	1.9348	7.694E+13	7.723E+13	7.862E+13
[1s]3p^5 ^{3}P$_0$ - [2p]3p^5 ^{1}P$_1$	1.9346	1.9347	1.9354	1.123E+13	1.125E+13	1.132E+13
[1s]3p^5 ^{3}P$_1$ - [2p]3p^5 ^{1}P$_1$	1.9350	1.9351	1.9358	9.933E+13	9.901E+13	9.740E+13
[1s]3p^5 ^{3}P$_2$ - [2p]3p^5 ^{1}P$_1$	1.9353	1.9355	1.9361	1.145E+13	1.144E+13	1.138E+13
[1s]3p^5 ^{3}P$_2$ - [2p]3p^5 ^{3}D$_3$	1.9354	1.9356	1.9362	2.775E+14	2.774E+14	2.771E+14
[1s]3p^5 ^{1}P$_1$ - [2p]3p^5 ^{3}D$_2$	1.9356	1.9357	1.9364	1.016E+14	1.013E+14	9.959E+13
[1s]3p^5 ^{1}P$_1$ - [2p]3p^5 ^{3}S$_1$	1.9358	1.9359	1.9366	3.077E+13	3.066E+13	3.008E+13
[1s]3p^5 ^{3}P$_0$ - [2p]3p^5 ^{3}S$_1$	1.9364	1.9365	1.9371	3.573E+14	3.571E+14	3.561E+14
[1s]3p^5 ^{3}P$_1$ - [2p]3p^5 ^{3}D$_2$	1.9365	1.9367	1.9373	2.224E+14	2.226E+14	2.237E+14
[1s]3p^5 ^{1}P$_1$ - [2p]3p^5 ^{3}P$_2$	1.9365	1.9366	1.9373	5.853E+13	5.834E+13	5.753E+13
[1s]3p^5 ^{3}P$_1$ - [2p]3p^5 ^{3}S$_1$	1.9367	1.9369	1.9375	2.615E+13	2.623E+13	2.661E+13
[1s]3p^5 ^{3}P$_1$ - [2p]3p^5 ^{3}P$_2$	1.9375	1.9376	1.9382	3.365E+13	3.375E+13	3.411E+13
[1s]3p^5 ^{3}P$_2$ - [2p]3p^5 ^{3}P$_2$	1.9378	1.9379	1.9386	1.321E+14	1.320E+14	1.319E+14
[1s]3p^5 ^{3}P$_1$ - [2p]3p^5 ^{3}P$_0$	1.9385	1.9386	1.9392	5.805E+13	5.799E+13	5.773E+13
[1s]3p^5 ^{1}P$_1$ - [2p]3p^5 ^{3}D$_1$	1.9385	1.9386	1.9393	8.811E+13	8.789E+13	8.679E+13
[1s]3p^5 ^{3}P$_0$ - [2p]3p^5 ^{3}D$_1$	1.9390	1.9392	1.9398	1.883E+14	1.883E+14	1.880E+14
[1s]3p^5 ^{3}P$_1$ - [2p]3p^5 ^{3}D$_1$	1.9394	1.9395	1.9402	4.396E+13	4.415E+13	4.507E+13
[1s]3p^5 ^{3}P$_0$ - [2p]3p^5 ^{3}P$_1$	1.9398	1.9399	1.9406	2.225E+13	2.231E+13	2.254E+13
[1s]3p^5 ^{1}P$_1$ - [2p]3p^5 ^{1}D$_2$	1.9399	1.9400	1.9407	1.527E+14	1.530E+14	1.548E+14
[1s]3p^5 ^{3}P$_1$ - [2p]3p^5 ^{3}P$_1$	1.9402	1.9403	1.9410	2.530E+13	2.530E+13	2.526E+13
[1s]3p^5 ^{3}P$_2$ - [2p]3p^5 ^{3}P$_1$	1.9405	1.9407	1.9413	9.137E+13	9.131E+13	9.104E+13
[1s]3p^5 ^{3}P$_1$ - [2p]3p^5 ^{1}D$_2$	1.9409	1.9410	1.9416	6.508E+13	6.471E+13	6.289E+13
[1s]3p^5 ^{3}P$_2$ - [2p]3p^5 ^{1}D$_2$	1.9412	1.9413	1.9420	5.502E+13	5.495E+13	5.459E+13
[1s]3p^5 ^{1}P$_1$ - [2p]3p^5 ^{1}S$_0$	1.9419	1.9420	1.9427	5.655E+13	5.650E+13	5.623E+13
Fe XII						
[1s]3p^4 ^{2}S$_{1/2}$ - 3p^3 ^{2}P$_{1/2}$	1.7457	1.7460	1.7475	1.278E+13	1.283E+13	1.304E+13
[1s]3p^4 ^{4}P$_{1/2}$ - 3p^3 ^{4}S$_{3/2}$	1.7459	1.7461	1.7477	4.385E+13	4.388E+13	4.409E+13
[1s]3p^4 ^{2}S$_{1/2}$ - 3p^3 ^{2}P$_{3/2}$	1.7459	1.7462	1.7477	7.689E+13	7.691E+13	7.706E+13
[1s]3p^4 ^{4}P$_{3/2}$ - 3p^3 ^{4}S$_{3/2}$	1.7460	1.7463	1.7478	4.391E+13	4.394E+13	4.412E+13
[1s]3p^4 ^{2}D$_{3/2}$ - 3p^3 ^{2}D$_{3/2}$	1.7460	1.7463	1.7478	1.987E+13	1.987E+13	1.987E+13
[1s]3p^4 ^{2}D$_{3/2}$ - 3p^3 ^{2}D$_{5/2}$	1.7461	1.7464	1.7479	4.648E+13	4.657E+13	4.709E+13
[1s]3p^4 ^{2}P$_{1/2}$ - 3p^3 ^{2}D$_{3/2}$	1.7462	1.7465	1.7480	7.587E+13	7.602E+13	7.679E+13
[1s]3p^4 ^{2}D$_{5/2}$ - 3p^3 ^{2}D$_{5/2}$	1.7462	1.7465	1.7480	5.860E+13	5.866E+13	5.897E+13
[1s]3p^4 ^{4}P$_{5/2}$ - 3p^3 ^{4}S$_{3/2}$	1.7464	1.7466	1.7482	4.154E+13	4.158E+13	4.180E+13
[1s]3p^4 ^{2}P$_{3/2}$ - 3p^3 ^{2}D$_{3/2}$	1.7466	1.7469	1.7484	6.928E+13	6.934E+13	6.968E+13
[1s]3p^4 ^{2}P$_{3/2}$ - 3p^3 ^{2}D$_{5/2}$	1.7467	1.7470	1.7485	5.529E+13	5.531E+13	5.540E+13
[1s]3p^4 ^{2}D$_{3/2}$ - 3p^3 ^{2}P$_{1/2}$	1.7470	1.7473	1.7488	2.767E+13	2.770E+13	2.788E+13
[1s]3p^4 ^{2}P$_{1/2}$ - 3p^3 ^{2}P$_{1/2}$	1.7472	1.7475	1.7490	5.760E+13	5.763E+13	5.779E+13
[1s]3p^4 ^{2}D$_{5/2}$ - 3p^3 ^{2}P$_{3/2}$	1.7473	1.7476	1.7491	2.507E+13	2.509E+13	2.520E+13
[1s]3p^4 ^{2}P$_{1/2}$ - 3p^3 ^{2}P$_{3/2}$	1.7474	1.7477	1.7492	3.427E+13	3.427E+13	3.427E+13
[1s]3p^4 ^{2}P$_{3/2}$ - 3p^3 ^{2}P$_{3/2}$	1.7478	1.7481	1.7496	2.347E+13	2.356E+13	2.396E+13
[1s]3p^4 ^{2}P$_{1/2}$ - [2p]3p^4 ^{2}S$_{1/2}$	1.9327	1.9328	1.9334	2.674E+13	2.679E+13	2.644E+13

Table 5.11: (continued)

Transition	λ (Å)			A_{ki} (s^{-1})		
	$\mu = 0.0$	$\mu = 0.1$	$\mu = 0.25$	$\mu = 0.0$	$\mu = 0.1$	$\mu = 0.25$
[1s]3p^4 ^{2}P$_{3/2}$ - [2p]3p^4 ^{2}S$_{1/2}$	1.9332	1.9333	1.9339	4.676E+13	4.678E+13	4.690E+13
[1s]3p^4 ^{2}D$_{5/2}$ - [2p]3p^4 ^{4}P$_{5/2}$	1.9332	1.9333	1.9340	1.606E+13	1.609E+13	1.623E+13
[1s]3p^4 ^{2}S$_{1/2}$ - [2p]3p^4 ^{4}S$_{3/2}$	1.9335	1.9336	1.9342	1.979E+13	1.982E+13	1.995E+13
[1s]3p^4 ^{2}D$_{3/2}$ - [2p]3p^4 ^{4}P$_{3/2}$	1.9338	1.9339	1.9346	1.619E+13	1.630E+13	1.685E+13
[1s]3p^4 ^{2}P$_{3/2}$ - [2p]3p^4 ^{4}P$_{5/2}$	1.9339	1.9339	1.9346	7.542E+13	7.547E+13	7.566E+13
[1s]3p^4 ^{2}P$_{1/2}$ - [2p]3p^4 ^{4}P$_{3/2}$	1.9340	1.9341	1.9348	1.933E+13	1.917E+13	1.841E+13
[1s]3p^4 ^{2}D$_{3/2}$ - [2p]3p^4 ^{2}D$_{3/2}$	1.9341	1.9342	1.9348	9.819E+13	9.817E+13	9.802E+13
[1s]3p^4 ^{2}D$_{3/2}$ - [2p]3p^4 ^{2}P$_{1/2}$	1.9341	1.9342	1.9349	1.384E+13	1.382E+13	1.368E+13
[1s]3p^4 ^{2}P$_{3/2}$ - [2p]3p^4 ^{4}D$_{5/2}$	1.9342	1.9343	1.9349	7.464E+13	7.436E+13	7.305E+13
[1s]3p^4 ^{4}P$_{3/2}$ - [2p]3p^4 ^{2}S$_{1/2}$	1.9343	1.9344	1.9350	3.255E+13	3.244E+13	3.188E+13
[1s]3p^4 ^{2}P$_{1/2}$ - [2p]3p^4 ^{2}D$_{3/2}$	1.9343	1.9344	1.9350	1.240E+14	1.240E+14	1.239E+14
[1s]3p^4 ^{2}P$_{1/2}$ - [2p]3p^4 ^{2}P$_{1/2}$	1.9343	1.9344	1.9351	4.715E+13	4.706E+13	4.663E+13
[1s]3p^4 ^{2}P$_{3/2}$ - [2p]3p^4 ^{4}P$_{3/2}$	1.9345	1.9347	1.9353	1.256E+13	1.255E+13	1.247E+13
[1s]3p^4 ^{2}P$_{3/2}$ - [2p]3p^4 ^{2}P$_{1/2}$	1.9348	1.9350	1.9356	2.670E+13	2.676E+13	2.705E+13
[1s]3p^4 ^{4}P$_{5/2}$ - [2p]3p^4 ^{4}D$_{7/2}$	1.9349	1.9350	1.9356	2.663E+14	2.662E+14	2.658E+14
[1s]3p^4 ^{4}P$_{3/2}$ - [2p]3p^4 ^{4}P$_{5/2}$	1.9349	1.9350	1.9356	4.481E+13	4.474E+13	4.442E+13
[1s]3p^4 ^{2}D$_{5/2}$ - [2p]3p^4 ^{2}F$_{7/2}$	1.9350	1.9351	1.9357	2.666E+14	2.666E+14	2.662E+14
[1s]3p^4 ^{2}D$_{3/2}$ - [2p]3p^4 ^{4}S$_{3/2}$	1.9351	1.9352	1.9358	3.109E+13	3.104E+13	3.082E+13
[1s]3p^4 ^{2}S$_{1/2}$ - [2p]3p^4 ^{4}S$_{3/2}$	1.9351	1.9352	1.9359	1.487E+14	1.491E+14	1.504E+14
[1s]3p^4 ^{4}P$_{3/2}$ - [2p]3p^4 ^{4}D$_{5/2}$	1.9352	1.9353	1.9360	2.137E+14	2.139E+14	2.146E+14
[1s]3p^4 ^{4}P$_{5/2}$ - [2p]3p^4 ^{4}P$_{5/2}$	1.9353	1.9354	1.9361	1.038E+14	1.038E+14	1.034E+14
[1s]3p^4 ^{2}P$_{1/2}$ - [2p]3p^4 ^{4}S$_{3/2}$	1.9353	1.9355	1.9361	2.595E+13	2.599E+13	2.619E+13
[1s]3p^4 ^{4}P$_{1/2}$ - [2p]3p^4 ^{4}P$_{3/2}$	1.9354	1.9355	1.9361	2.694E+14	2.693E+14	2.685E+14
[1s]3p^4 ^{2}D$_{3/2}$ - [2p]3p^4 ^{2}D$_{5/2}$	1.9354	1.9355	1.9361	5.912E+13	5.898E+13	5.824E+13
[1s]3p^4 ^{2}D$_{5/2}$ - [2p]3p^4 ^{2}D$_{5/2}$	1.9355	1.9356	1.9362	5.797E+13	5.788E+13	5.743E+13
[1s]3p^4 ^{2}S$_{1/2}$ - [2p]3p^4 ^{2}P$_{3/2}$	1.9356	1.9357	1.9363	5.056E+13	4.990E+13	4.711E+13
[1s]3p^4 ^{4}P$_{1/2}$ - [2p]3p^4 ^{2}P$_{1/2}$	1.9357	1.9358	1.9364	6.773E+13	6.770E+13	6.753E+13
[1s]3p^4 ^{4}P$_{3/2}$ - [2p]3p^4 ^{2}D$_{3/2}$	1.9359	1.9360	1.9366	2.275E+13	2.274E+13	2.274E+13
[1s]3p^4 ^{2}P$_{3/2}$ - [2p]3p^4 ^{2}D$_{5/2}$	1.9361	1.9362	1.9369	2.602E+13	2.615E+13	2.677E+13
[1s]3p^4 ^{2}S$_{1/2}$ - [2p]3p^4 ^{2}D$_{3/2}$	1.9362	1.9363	1.9370	1.143E+14	1.145E+14	1.156E+14
[1s]3p^4 ^{2}D$_{3/2}$ - [2p]3p^4 ^{2}P$_{1/2}$	1.9363	1.9364	1.9370	4.284E+13	4.275E+13	4.228E+13
[1s]3p^4 ^{4}P$_{1/2}$ - [2p]3p^4 ^{4}S$_{3/2}$	1.9367	1.9368	1.9374	5.800E+13	5.784E+13	5.707E+13
[1s]3p^4 ^{2}D$_{3/2}$ - [2p]3p^4 ^{4}S$_{3/2}$	1.9367	1.9368	1.9375	1.065E+13	1.056E+13	1.013E+13
[1s]3p^4 ^{4}P$_{3/2}$ - [2p]3p^4 ^{4}S$_{3/2}$	1.9369	1.9370	1.9377	9.093E+13	9.088E+13	9.064E+13
[1s]3p^4 ^{4}P$_{3/2}$ - [2p]3p^4 ^{2}D$_{5/2}$	1.9372	1.9373	1.9379	2.276E+13	2.273E+13	2.253E+13
[1s]3p^4 ^{2}P$_{3/2}$ - [2p]3p^4 ^{4}S$_{3/2}$	1.9374	1.9375	1.9382	4.048E+13	4.027E+13	3.932E+13
[1s]3p^4 ^{2}P$_{1/2}$ - [2p]3p^4 ^{2}P$_{3/2}$	1.9375	1.9376	1.9383	3.283E+13	3.247E+13	3.086E+13
[1s]3p^4 ^{4}P$_{5/2}$ - [2p]3p^4 ^{2}D$_{5/2}$	1.9376	1.9377	1.9383	6.673E+13	6.681E+13	6.717E+13
[1s]3p^4 ^{2}S$_{1/2}$ - [2p]3p^4 ^{2}D$_{3/2}$	1.9376	1.9377	1.9383	1.596E+13	1.588E+13	1.550E+13
[1s]3p^4 ^{2}P$_{3/2}$ - [2p]3p^4 ^{4}P$_{1/2}$	1.9378	1.9379	1.9385	2.358E+13	2.346E+13	2.288E+13
[1s]3p^4 ^{4}P$_{1/2}$ - [2p]3p^4 ^{2}P$_{1/2}$	1.9379	1.9380	1.9386	9.831E+13	9.839E+13	9.871E+13
[1s]3p^4 ^{2}D$_{5/2}$ - [2p]3p^4 ^{2}D$_{3/2}$	1.9380	1.9381	1.9387	4.693E+13	4.699E+13	4.722E+13
[1s]3p^4 ^{2}P$_{1/2}$ - [2p]3p^4 ^{2}D$_{3/2}$	1.9381	1.9382	1.9388	6.453E+13	6.438E+13	6.365E+13
[1s]3p^4 ^{2}D$_{3/2}$ - [2p]3p^4 ^{2}F$_{5/2}$	1.9382	1.9383	1.9390	2.268E+14	2.267E+14	2.264E+14
[1s]3p^4 ^{4}P$_{1/2}$ - [2p]3p^4 ^{4}S$_{3/2}$	1.9383	1.9384	1.9390	2.913E+13	2.909E+13	2.889E+13
[1s]3p^4 ^{2}D$_{5/2}$ - [2p]3p^4 ^{2}F$_{5/2}$	1.9383	1.9384	1.9391	3.217E+13	3.225E+13	3.258E+13
[1s]3p^4 ^{4}P$_{3/2}$ - [2p]3p^4 ^{4}P$_{1/2}$	1.9388	1.9389	1.9396	6.595E+13	6.604E+13	6.646E+14
[1s]3p^4 ^{4}P$_{5/2}$ - [2p]3p^4 ^{4}S$_{3/2}$	1.9389	1.9390	1.9396	1.579E+13	1.561E+13	1.484E+13

Transition	λ (Å)			A_{ki} (s^{-1})		
	$\mu = 0.0$	$\mu = 0.1$	$\mu = 0.25$	$\mu = 0.0$	$\mu = 0.1$	$\mu = 0.25$
[1s]3p^4 ^{4}P$_{3/2}$ - [2p]3p^4 ^{2}P$_{3/2}$	1.9391	1.9392	1.9398	3.459E+13	3.444E+13	3.374E+13
[1s]3p^4 ^{4}P$_{1/2}$ - [2p]3p^4 ^{2}D$_{3/2}$	1.9395	1.9396	1.9402	1.656E+13	1.651E+13	1.623E+13
[1s]3p^4 ^{2}S$_{1/2}$ - [2p]3p^4 ^{2}P$_{1/2}$	1.9396	1.9397	1.9404	1.171E+14	1.168E+14	1.150E+14
[1s]3p^4 ^{4}P$_{3/2}$ - [2p]3p^4 ^{2}D$_{3/2}$	1.9397	1.9398	1.9404	1.925E+13	1.920E+13	1.897E+13
[1s]3p^4 ^{2}P$_{1/2}$ - [2p]3p^4 ^{2}D$_{5/2}$	1.9398	1.9399	1.9405	5.041E+13	5.019E+13	4.919E+13
[1s]3p^4 ^{2}P$_{3/2}$ - [2p]3p^4 ^{2}D$_{3/2}$	1.9399	1.9400	1.9407	9.955E+13	9.960E+13	9.986E+13
[1s]3p^4 ^{2}S$_{1/2}$ - [2p]3p^4 ^{2}P$_{3/2}$	1.9402	1.9403	1.9410	2.948E+13	2.948E+13	2.946E+13
[1s]3p^4 ^{4}P$_{5/2}$ - [2p]3p^4 ^{2}D$_{3/2}$	1.9414	1.9415	1.9422	3.302E+13	3.293E+13	3.250E+13
[1s]3p^4 ^{2}P$_{1/2}$ - [2p]3p^4 ^{2}P$_{1/2}$	1.9415	1.9416	1.9422	4.902E+13	4.917E+13	4.984E+13
[1s]3p^4 ^{2}D$_{3/2}$ - [2p]3p^4 ^{2}P$_{3/2}$	1.9418	1.9420	1.9426	2.660E+13	2.659E+13	2.659E+13
[1s]3p^4 ^{2}D$_{5/2}$ - [2p]3p^4 ^{2}P$_{3/2}$	1.9419	1.9421	1.9427	5.550E+13	5.543E+13	5.510E+13
[1s]3p^4 ^{2}P$_{1/2}$ - [2p]3p^4 ^{2}P$_{3/2}$	1.9421	1.9422	1.9428	6.493E+13	6.497E+13	6.512E+13
[1s]3p^4 ^{2}P$_{3/2}$ - [2p]3p^4 ^{2}P$_{3/2}$	1.9426	1.9427	1.9433	1.515E+13	1.513E+13	1.506E+13
Fe XIII						
[1s]3p^3 ^{3}P$_0$ - 3p^2 ^{3}P$_1$	1.7415	1.7417	1.7432	4.550E+13	4.554E+13	4.574E+13
[1s]3p^3 ^{3}P$_1$ - 3p^2 ^{3}P$_2$	1.7417	1.7420	1.7434	3.493E+13	3.495E+13	3.509E+13
[1s]3p^3 ^{1}P$_1$ - 3p^2 ^{1}D$_2$	1.7418	1.7421	1.7436	7.524E+13	7.531E+13	7.568E+13
[1s]3p^3 ^{1}D$_2$ - 3p^2 ^{3}P$_2$	1.7420	1.7423	1.7438	3.758E+13	3.756E+13	3.750E+13
[1s]3p^3 ^{3}D$_1$ - 3p^2 ^{3}P$_0$	1.7422	1.7425	1.7440	1.354E+13	1.352E+13	1.341E+13
[1s]3p^3 ^{3}P$_2$ - 3p^2 ^{1}D$_2$	1.7424	1.7427	1.7442	5.627E+13	5.637E+13	5.689E+13
[1s]3p^3 ^{3}D$_2$ - 3p^2 ^{3}P$_1$	1.7425	1.7428	1.7443	4.219E+13	4.222E+13	4.239E+13
[1s]3p^3 ^{3}D$_1$ - 3p^2 ^{3}P$_1$	1.7425	1.7428	1.7443	3.870E+13	3.879E+13	3.930E+13
[1s]3p^3 ^{3}S$_1$ - 3p^2 ^{3}P$_0$	1.7426	1.7428	1.7443	4.325E+13	4.331E+13	4.364E+13
[1s]3p^3 ^{3}D$_3$ - 3p^2 ^{3}P$_2$	1.7427	1.7429	1.7444	4.106E+13	4.111E+13	4.139E+13
[1s]3p^3 ^{3}S$_1$ - 3p^2 ^{3}P$_1$	1.7428	1.7431	1.7446	4.267E+13	4.266E+13	4.258E+13
[1s]3p^3 ^{1}D$_2$ - 3p^2 ^{1}D$_2$	1.7430	1.7433	1.7448	6.975E+13	6.982E+13	7.015E+13
[1s]3p^3 ^{3}S$_1$ - 3p^2 ^{3}P$_2$	1.7431	1.7434	1.7449	7.364E+13	7.372E+13	7.405E+13
[1s]3p^3 ^{1}P$_1$ - 3p^2 ^{1}S$_0$	1.7432	1.7435	1.7450	5.663E+13	5.671E+13	5.710E+13
[1s]3p^3 ^{1}P$_1$ - [2p]3p^3 ^{1}P$_1$	1.9307	1.9308	1.9315	2.099E+13	2.103E+13	2.118E+13
[1s]3p^3 ^{1}D$_2$ - [2p]3p^3 ^{1}P$_1$	1.9322	1.9323	1.9330	6.930E+13	6.923E+13	6.889E+13
[1s]3p^3 ^{3}S$_1$ - [2p]3p^3 ^{5}P$_2$	1.9324	1.9325	1.9331	8.989E+13	8.974E+13	8.890E+13
[1s]3p^3 ^{3}P$_2$ - [2p]3p^3 ^{1}F$_3$	1.9324	1.9325	1.9331	3.593E+13	3.608E+13	3.863E+13
[1s]3p^3 ^{1}P$_1$ - [2p]3p^3 ^{5}P$_1$	1.9324	1.9325	1.9331	1.903E+13	1.913E+13	1.961E+13
[1s]3p^3 ^{3}D$_1$ - [2p]3p^3 ^{3}P$_0$	1.9326	1.9327	1.9334	4.717E+13	4.718E+13	4.732E+13
[1s]3p^3 ^{3}S$_1$ - [2p]3p^3 ^{3}P$_1$	1.9327	1.9328	1.9335	1.252E+14	1.251E+14	1.249E+14
[1s]3p^3 ^{1}P$_1$ - [2p]3p^3 ^{1}P$_1$	1.9328	1.9329	1.9336	7.624E+13	7.599E+13	7.477E+13
[1s]3p^3 ^{1}P$_1$ - [2p]3p^3 ^{3}D$_2$	1.9329	1.9331	1.9337	5.281E+13	5.292E+13	5.344E+13
[1s]3p^3 ^{3}S$_1$ - [2p]3p^3 ^{3}P$_0$	1.9331	1.9332	1.9338	1.871E+13	1.867E+13	1.842E+13
[1s]3p^3 ^{3}D$_3$ - [2p]3p^3 ^{3}D$_3$	1.9331	1.9333	1.9339	6.050E+13	6.063E+13	6.124E+13
[1s]3p^3 ^{1}D$_2$ - [2p]3p^3 ^{1}F$_3$	1.9331	1.9332	1.9339	1.155E+14	1.153E+14	1.147E+14
[1s]3p^3 ^{3}D$_1$ - [2p]3p^3 ^{1}P$_1$	1.9332	1.9333	1.9339	4.242E+13	4.235E+13	4.203E+13
[1s]3p^3 ^{3}D$_2$ - [2p]3p^3 ^{3}D$_3$	1.9333	1.9334	1.9340	1.879E+14	1.875E+14	1.800E+14
[1s]3p^3 ^{3}P$_2$ - [2p]3p^3 ^{3}S$_1$	1.9333	1.9334	1.9340	1.220E+13	1.226E+13	1.255E+13
[1s]3p^3 ^{3}P$_0$ - [2p]3p^3 ^{5}P$_1$	1.9336	1.9337	1.9343	2.111E+13	2.082E+13	1.924E+13
[1s]3p^3 ^{3}P$_1$ - [2p]3p^3 ^{3}S$_1$	1.9336	1.9337	1.9343	7.370E+13	7.370E+13	7.361E+13
[1s]3p^3 ^{3}D$_3$ - [2p]3p^3 ^{3}F$_4$	1.9337	1.9338	1.9344	2.582E+14	2.581E+14	2.577E+14
[1s]3p^3 ^{3}P$_0$ - [2p]3p^3 ^{3}S$_1$	1.9337	1.9338	1.9344	2.414E+14	2.414E+14	2.414E+14
[1s]3p^3 ^{3}P$_1$ - [2p]3p^3 ^{5}P$_2$	1.9337	1.9338	1.9345	2.335E+13	2.344E+13	2.391E+14

Transition	λ (Å)			A_{ki} (s^{-1})		
	$\mu = 0.0$	$\mu = 0.1$	$\mu = 0.25$	$\mu = 0.0$	$\mu = 0.1$	$\mu = 0.25$
[1s]3p^3 ^{3}P$_2$ - [2p]3p^3 ^{3}D$_3$	1.9337	1.9338	1.9345	2.091E+14	2.087E+14	2.068E+14
[1s]3p^3 ^{5}S$_2$ - [2p]3p^3 ^{5}P$_3$	1.9338	1.9340	1.9345	2.801E+14	2.801E+14	2.797E+14
[1s]3p^3 ^{3}D$_2$ - [2p]3p^3 ^{3}D$_2$	1.9338	1.9339	1.9345	8.832E+13	8.831E+13	8.823E+13
[1s]3p^3 ^{3}D$_1$ - [2p]3p^3 ^{3}D$_2$	1.9338	1.9339	1.9346	1.504E+14	1.502E+14	1.493E+14
[1s]3p^3 ^{3}D$_3$ - [2p]3p^3 ^{1}F$_3$	1.9339	1.9340	1.9347	6.054E+13	6.039E+13	5.964E+13
[1s]3p^3 ^{3}P$_0$ - [2p]3p^3 ^{1}P$_1$	1.9340	1.9341	1.9347	4.683E+13	4.700E+13	4.781E+13
[1s]3p^3 ^{3}P$_1$ - [2p]3p^3 ^{3}D$_2$	1.9340	1.9341	1.9348	2.141E+14	2.138E+14	2.123E+14
[1s]3p^3 ^{3}D$_2$ - [2p]3p^3 ^{1}F$_3$	1.9341	1.9342	1.9348	4.581E+13	4.592E+13	4.644E+13
[1s]3p^3 ^{1}D$_2$ - [2p]3p^3 ^{5}P$_2$	1.9341	1.9342	1.9348	2.774E+13	2.764E+13	2.720E+13
[1s]3p^3 ^{1}P$_1$ - [2p]3p^3 ^{3}P$_2$	1.9342	1.9343	1.9349	5.679E+13	5.672E+13	5.634E+13
[1s]3p^3 ^{5}S$_2$ - [2p]3p^3 ^{5}P$_2$	1.9344	1.9345	1.9351	1.246E+14	1.246E+14	1.245E+14
[1s]3p^3 ^{1}D$_2$ - [2p]3p^3 ^{3}D$_3$	1.9344	1.9345	1.9351	6.351E+13	6.377E+13	6.509E+13
[1s]3p^3 ^{1}D$_2$ - [2p]3p^3 ^{3}D$_2$	1.9344	1.9346	1.9352	2.807E+13	2.808E+13	2.814E+13
[1s]3p^3 ^{5}S$_2$ - [2p]3p^3 ^{3}P$_1$	1.9347	1.9348	1.9354	2.711E+13	2.711E+13	2.707E+13
[1s]3p^3 ^{1}P$_1$ - [2p]3p^3 ^{3}P$_1$	1.9347	1.9348	1.9354	2.714E+13	2.716E+13	2.725E+13
[1s]3p^3 ^{3}D$_1$ - [2p]3p^3 ^{5}P$_1$	1.9348	1.9350	1.9356	5.052E+13	5.044E+13	4.997E+13
[1s]3p^3 ^{3}D$_3$ - [2p]3p^3 ^{5}P$_2$	1.9349	1.9350	1.9356	1.560E+13	1.559E+13	1.557E+13
[1s]3p^3 ^{1}P$_1$ - [2p]3p^3 ^{3}D$_2$	1.9349	1.9350	1.9356	1.341E+13	1.338E+13	1.326E+13
[1s]3p^3 ^{3}P$_2$ - [2p]3p^3 ^{3}P$_2$	1.9350	1.9351	1.9357	4.538E+13	4.531E+13	4.496E+13
[1s]3p^3 ^{3}D$_2$ - [2p]3p^3 ^{1}P$_1$	1.9353	1.9354	1.9360	1.528E+13	1.529E+13	1.531E+13
[1s]3p^3 ^{3}D$_1$ - [2p]3p^3 ^{3}D$_2$	1.9354	1.9355	1.9361	1.631E+13	1.638E+13	1.671E+13
[1s]3p^3 ^{3}S$_1$ - [2p]3p^3 ^{5}P$_2$	1.9355	1.9356	1.9362	1.071E+14	1.072E+14	1.077E+14
[1s]3p^3 ^{3}P$_0$ - [2p]3p^3 ^{3}P$_1$	1.9359	1.9360	1.9366	7.341E+13	7.342E+13	7.346E+13
[1s]3p^3 ^{3}P$_1$ - [2p]3p^3 ^{3}D$_2$	1.9359	1.9361	1.9367	3.575E+13	3.578E+13	3.594E+13
[1s]3p^3 ^{3}P$_1$ - [2p]3p^3 ^{3}P$_0$	1.9361	1.9362	1.9368	3.468E+13	3.482E+13	3.546E+13
[1s]3p^3 ^{3}P$_2$ - [2p]3p^3 ^{3}F$_3$	1.9361	1.9362	1.9368	2.827E+13	2.838E+13	2.895E+13
[1s]3p^3 ^{1}D$_2$ - [2p]3p^3 ^{3}P$_1$	1.9362	1.9363	1.9369	2.507E+13	2.508E+13	2.508E+13
[1s]3p^3 ^{1}D$_2$ - [2p]3p^3 ^{3}D$_2$	1.9364	1.9365	1.9371	1.990E+13	1.986E+13	1.968E+13
[1s]3p^3 ^{1}P$_1$ - [2p]3p^3 ^{3}D$_1$	1.9364	1.9365	1.9371	4.421E+13	4.427E+13	4.454E+13
[1s]3p^3 ^{3}D$_3$ - [2p]3p^3 ^{3}P$_2$	1.9365	1.9366	1.9373	1.102E+13	1.101E+13	1.093E+13
[1s]3p^3 ^{3}D$_1$ - [2p]3p^3 ^{3}P$_2$	1.9366	1.9368	1.9374	5.825E+13	5.825E+13	5.827E+13
[1s]3p^3 ^{3}D$_2$ - [2p]3p^3 ^{3}P$_2$	1.9367	1.9368	1.9374	5.951E+13	5.951E+13	5.953E+13
[1s]3p^3 ^{1}P$_1$ - [2p]3p^3 ^{1}D$_2$	1.9367	1.9368	1.9374	1.117E+14	1.119E+14	1.126E+14
[1s]3p^3 ^{1}D$_2$ - [2p]3p^3 ^{3}F$_3$	1.9368	1.9369	1.9375	1.006E+14	1.004E+14	9.927E+13
[1s]3p^3 ^{3}D$_1$ - [2p]3p^3 ^{3}P$_1$	1.9371	1.9372	1.9379	6.371E+13	6.364E+13	6.332E+13
[1s]3p^3 ^{5}S$_2$ - [2p]3p^3 ^{5}P$_1$	1.9372	1.9373	1.9379	5.012E+13	5.018E+13	5.048E+13
[1s]3p^3 ^{3}D$_3$ - [2p]3p^3 ^{3}D$_2$	1.9372	1.9373	1.9380	3.889E+13	3.890E+13	3.908E+13
[1s]3p^3 ^{3}P$_2$ - [2p]3p^3 ^{3}P$_1$	1.9372	1.9374	1.9380	7.174E+13	7.178E+13	7.190E+13
[1s]3p^3 ^{3}D$_2$ - [2p]3p^3 ^{3}D$_2$	1.9373	1.9374	1.9380	3.539E+13	3.541E+13	3.548E+13
[1s]3p^3 ^{3}D$_1$ - [2p]3p^3 ^{3}D$_2$	1.9373	1.9374	1.9381	6.718E+13	6.714E+13	6.699E+13
[1s]3p^3 ^{5}S$_2$ - [2p]3p^3 ^{5}P$_2$	1.9374	1.9375	1.9381	5.843E+13	5.841E+13	5.828E+13
[1s]3p^3 ^{3}D$_1$ - [2p]3p^3 ^{3}P$_0$	1.9374	1.9375	1.9382	1.037E+13	1.032E+13	1.009E+13
[1s]3p^3 ^{3}P$_1$ - [2p]3p^3 ^{3}P$_0$	1.9374	1.9375	1.9382	1.547E+13	1.537E+13	1.492E+13
[1s]3p^3 ^{3}P$_1$ - [2p]3p^3 ^{3}D$_1$	1.9375	1.9376	1.9382	8.741E+13	8.733E+13	8.691E+13
[1s]3p^3 ^{3}P$_2$ - [2p]3p^3 ^{1}D$_2$	1.9375	1.9376	1.9382	7.025E+13	7.038E+13	7.096E+13
[1s]3p^3 ^{3}D$_3$ - [2p]3p^3 ^{3}F$_3$	1.9376	1.9377	1.9383	7.582E+13	7.578E+13	7.559E+13
[1s]3p^3 ^{3}P$_0$ - [2p]3p^3 ^{3}D$_1$	1.9376	1.9377	1.9384	1.748E+14	1.747E+14	1.742E+14
[1s]3p^3 ^{5}S$_2$ - [2p]3p^3 ^{1}P$_1$	1.9377	1.9378	1.9384	2.129E+13	2.142E+13	2.200E+13

Transition	λ (Å)			A_{ki} (s^{-1})		
	$\mu = 0.0$	$\mu = 0.1$	$\mu = 0.25$	$\mu = 0.0$	$\mu = 0.1$	$\mu = 0.25$
[1s]3p^3 ^{3}D$_2$ - [2p]3p^3 ^{3}F$_3$	1.9378	1.9379	1.9385	4.159E+13	4.168E+13	4.210E+13
[1s]3p^3 ^{3}P$_1$ - [2p]3p^3 ^{1}D$_2$	1.9378	1.9379	1.9385	3.952E+13	3.952E+13	3.955E+13
[1s]3p^3 ^{3}S$_1$ - [2p]3p^3 ^{3}P$_0$	1.9379	1.9380	1.9386	1.069E+13	1.061E+13	1.026E+13
[1s]3p^3 ^{1}P$_1$ - [2p]3p^3 ^{1}D$_2$	1.9382	1.9384	1.9390	4.339E+13	4.308E+13	4.174E+13
[1s]3p^3 ^{3}P$_2$ - [2p]3p^3 ^{3}P$_1$	1.9385	1.9386	1.9393	1.549E+13	1.531E+13	1.451E+13
[1s]3p^3 ^{3}P$_0$ - [2p]3p^3 ^{3}P$_1$	1.9389	1.9390	1.9397	2.337E+13	2.337E+13	2.337E+13
[1s]3p^3 ^{3}D$_2$ - [2p]3p^3 ^{3}P$_1$	1.9390	1.9391	1.9397	2.303E+13	2.289E+13	2.228E+13
[1s]3p^3 ^{3}D$_3$ - [2p]3p^3 ^{1}D$_2$	1.9390	1.9391	1.9397	1.020E+13	1.012E+13	9.771E+12
[1s]3p^3 ^{3}P$_2$ - [2p]3p^3 ^{1}D$_2$	1.9390	1.9391	1.9398	1.446E+13	1.432E+13	1.365E+13
[1s]3p^3 ^{3}S$_1$ - [2p]3p^3 ^{3}P$_0$	1.9392	1.9393	1.9400	3.132E+13	3.141E+13	3.184E+13
[1s]3p^3 ^{3}S$_1$ - [2p]3p^3 ^{1}D$_2$	1.9396	1.9397	1.9403	1.891E+13	1.878E+13	1.820E+13
[1s]3p^3 ^{1}D$_2$ - [2p]3p^3 ^{1}D$_2$	1.9397	1.9399	1.9405	4.124E+13	4.131E+13	4.160E+13
[1s]3p^3 ^{1}P$_1$ - [2p]3p^3 ^{1}D$_2$	1.9397	1.9399	1.9405	3.962E+13	3.966E+13	3.983E+13
[1s]3p^3 ^{3}D$_2$ - [2p]3p^3 ^{3}P$_1$	1.9402	1.9403	1.9410	4.006E+13	4.013E+13	4.038E+13
[1s]3p^3 ^{3}P$_2$ - [2p]3p^3 ^{1}D$_2$	1.9405	1.9406	1.9413	3.890E+13	3.895E+13	3.918E+13
[1s]3p^3 ^{3}S$_1$ - [2p]3p^3 ^{3}P$_1$	1.9406	1.9407	1.9413	3.630E+13	3.638E+13	3.668E+13
[1s]3p^3 ^{3}D$_3$ - [2p]3p^3 ^{1}D$_2$	1.9406	1.9407	1.9414	2.794E+13	2.800E+13	2.825E+13
[1s]3p^3 ^{3}S$_1$ - [2p]3p^3 ^{1}D$_2$	1.9411	1.9412	1.9419	7.718E+13	7.729E+13	7.777E+13
[1s]3p^3 ^{1}D$_2$ - [2p]3p^3 ^{1}D$_2$	1.9413	1.9414	1.9420	5.614E+13	5.611E+13	5.594E+13
[1s]3p^3 ^{1}P$_1$ - [2p]3p^3 ^{1}S$_0$	1.9414	1.9415	1.9421	4.447E+13	4.450E+13	4.466E+13
[1s]3p^3 ^{3}D$_3$ - [2p]3p^3 ^{1}D$_2$	1.9421	1.9422	1.9428	2.467E+13	2.461E+13	2.431E+13
[1s]3p^3 ^{3}D$_1$ - [2p]3p^3 ^{1}D$_2$	1.9422	1.9423	1.9430	1.996E+13	1.991E+13	1.970E+13
[1s]3p^3 ^{3}P$_1$ - [2p]3p^3 ^{1}S$_0$	1.9425	1.9426	1.9433	1.292E+13	1.286E+13	1.265E+13
Fe XIV						
[1s]3p^2 ^{2}S$_{1/2}$ - 3p ^{2}P$_{3/2}$	1.7367	1.7370	1.7385	4.382E+13	4.385E+13	4.397E+13
[1s]3p^2 ^{2}P$_{3/2}$ - 3p ^{2}P$_{1/2}$	1.7380	1.7383	1.7398	6.073E+13	6.081E+13	6.119E+13
[1s]3p^2 ^{2}D$_{3/2}$ - 3p ^{2}P$_{3/2}$	1.7380	1.7383	1.7398	8.646E+13	8.664E+13	8.760E+13
[1s]3p^2 ^{2}P$_{1/2}$ - 3p ^{2}P$_{1/2}$	1.7382	1.7385	1.7400	1.011E+14	1.012E+14	1.017E+14
[1s]3p^2 ^{2}D$_{5/2}$ - 3p ^{2}P$_{3/2}$	1.7382	1.7385	1.7400	4.360E+13	4.366E+13	4.392E+13
[1s]3p^2 ^{2}P$_{3/2}$ - 3p ^{2}P$_{3/2}$	1.7386	1.7389	1.7403	3.706E+13	3.700E+13	3.666E+13
[1s]3p^2 ^{2}P$_{1/2}$ - 3p ^{2}P$_{3/2}$	1.7388	1.7391	1.7406	3.396E+13	3.401E+13	3.424E+13
[1s]3p^2 ^{2}S$_{1/2}$ - [2p]3p^2 ^{2}P$_{3/2}$	1.9291	1.9292	1.9298	1.332E+13	1.333E+13	1.337E+13
[1s]3p^2 ^{2}D$_{3/2}$ - [2p]3p^2 ^{4}P$_{1/2}$	1.9299	1.9300	1.9307	1.028E+13	1.030E+13	1.040E+13
[1s]3p^2 ^{2}P$_{3/2}$ - [2p]3p^2 ^{4}P$_{3/2}$	1.9302	1.9303	1.9309	1.321E+13	1.324E+13	1.340E+13
[1s]3p^2 ^{2}D$_{3/2}$ - [2p]3p^2 ^{4}D$_{5/2}$	1.9307	1.9308	1.9314	3.385E+13	3.400E+13	3.474E+13
[1s]3p^2 ^{2}P$_{1/2}$ - [2p]3p^2 ^{4}P$_{1/2}$	1.9309	1.9310	1.9316	6.567E+13	6.558E+13	6.514E+13
[1s]3p^2 ^{2}D$_{5/2}$ - [2p]3p^2 ^{2}P$_{3/2}$	1.9309	1.9310	1.9317	1.829E+13	1.829E+13	1.822E+13
[1s]3p^2 ^{2}D$_{3/2}$ - [2p]3p^2 ^{2}P$_{1/2}$	1.9310	1.9311	1.9317	7.688E+13	7.681E+13	7.649E+13
[1s]3p^2 ^{2}P$_{3/2}$ - [2p]3p^2 ^{4}D$_{5/2}$	1.9314	1.9315	1.9321	7.662E+13	7.639E+13	7.521E+13
[1s]3p^2 ^{2}P$_{3/2}$ - [2p]3p^2 ^{2}P$_{3/2}$	1.9314	1.9315	1.9321	1.175E+14	1.176E+14	1.180E+14
[1s]3p^2 ^{4}P$_{5/2}$ - [2p]3p^2 ^{4}P$_{5/2}$	1.9315	1.9316	1.9322	4.762E+13	4.864E+13	4.906E+13
[1s]3p^2 ^{2}P$_{1/2}$ - [2p]3p^2 ^{2}D$_{3/2}$	1.9316	1.9317	1.9323	2.262E+14	2.261E+14	2.252E+14
[1s]3p^2 ^{4}P$_{3/2}$ - [2p]3p^2 ^{4}P$_{5/2}$	1.9319	1.9320	1.9326	2.264E+14	2.262E+14	2.251E+14
[1s]3p^2 ^{2}D$_{5/2}$ - [2p]3p^2 ^{2}F$_{7/2}$	1.9319	1.9320	1.9327	2.680E+14	2.680E+14	2.676E+14
[1s]3p^2 ^{4}P$_{1/2}$ - [2p]3p^2 ^{4}P$_{3/2}$	1.9322	1.9323	1.9329	3.234E+14	3.231E+14	3.217E+14
[1s]3p^2 ^{2}S$_{1/2}$ - [2p]3p^2 ^{2}P$_{3/2}$	1.9322	1.9324	1.9330	2.492E+14	2.427E+14	2.414E+14
[1s]3p^2 ^{4}P$_{3/2}$ - [2p]3p^2 ^{4}P$_{1/2}$	1.9323	1.9324	1.9330	2.354E+13	2.352E+13	2.341E+13
[1s]3p^2 ^{2}D$_{3/2}$ - [2p]3p^2 ^{2}D$_{5/2}$	1.9323	1.9324	1.9330	1.141E+14	1.139E+14	1.128E+14

116

Transition	λ (Å)			A_{ki} (s^{-1})		
	$\mu = 0.0$	$\mu = 0.1$	$\mu = 0.25$	$\mu = 0.0$	$\mu = 0.1$	$\mu = 0.25$
[1s]3p^2 ^{4}P$_{5/2}$ - [2p]3p^2 ^{4}D$_{7/2}$	1.9324	1.9325	1.9331	2.671E+14	2.671E+14	2.667E+14
[1s]3p^2 ^{2}D$_{5/2}$ - [2p]3p^2 ^{2}D$_{5/2}$	1.9325	1.9326	1.9333	8.313E+13	8.307E+13	8.278E+13
[1s]3p^2 ^{2}S$_{1/2}$ - [2p]3p^2 ^{4}D$_{3/2}$	1.9326	1.9327	1.9333	8.099E+13	8.106E+13	8.150E+13
[1s]3p^2 ^{4}P$_{1/2}$ - [2p]3p^2 ^{4}P$_{1/2}$	1.9327	1.9328	1.9334	4.253E+13	4.254E+13	4.257E+13
[1s]3p^2 ^{4}P$_{5/2}$ - [2p]3p^2 ^{4}D$_{5/2}$	1.9327	1.9328	1.9334	8.678E+13	8.669E+13	8.630E+13
[1s]3p^2 ^{4}P$_{3/2}$ - [2p]3p^2 ^{2}D$_{3/2}$	1.9330	1.9331	1.9337	7.746E+13	7.763E+13	7.865E+13
[1s]3p^2 ^{2}P$_{3/2}$ - [2p]3p^2 ^{2}D$_{5/2}$	1.9330	1.9331	1.9337	6.099E+13	6.118E+13	6.221E+13
[1s]3p^2 ^{4}P$_{3/2}$ - [2p]3p^2 ^{4}D$_{5/2}$	1.9331	1.9332	1.9338	5.828E+13	5.839E+13	5.895E+13
[1s]3p^2 ^{4}P$_{3/2}$ - [2p]3p^2 ^{2}P$_{3/2}$	1.9331	1.9332	1.9338	1.124E+13	1.103E+13	9.832E+12
[1s]3p^2 ^{2}D$_{3/2}$ - [2p]3p^2 ^{4}S$_{3/2}$	1.9333	1.9334	1.9341	4.902E+13	4.890E+13	4.829E+13
[1s]3p^2 ^{4}P$_{1/2}$ - [2p]3p^2 ^{2}P$_{3/2}$	1.9334	1.9335	1.9341	4.153E+13	4.169E+13	4.253E+13
[1s]3p^2 ^{4}P$_{3/2}$ - [2p]3p^2 ^{2}P$_{1/2}$	1.9334	1.9335	1.9341	2.032E+13	2.036E+13	2.057E+13
[1s]3p^2 ^{2}P$_{3/2}$ - [2p]3p^2 ^{4}D$_{1/2}$	1.9336	1.9337	1.9343	2.287E+13	2.198E+13	2.254E+13
[1s]3p^2 ^{2}D$_{3/2}$ - [2p]3p^2 ^{2}P$_{3/2}$	1.9338	1.9339	1.9345	2.556E+13	2.551E+13	2.528E+13
[1s]3p^2 ^{2}S$_{1/2}$ - [2p]3p^2 ^{2}D$_{3/2}$	1.9340	1.9342	1.9348	4.008E+13	4.012E+13	4.033E+13
[1s]3p^2 ^{2}P$_{1/2}$ - [2p]3p^2 ^{4}S$_{3/2}$	1.9343	1.9344	1.9350	4.738E+13	4.736E+13	4.730E+13
[1s]3p^2 ^{2}D$_{3/2}$ - [2p]3p^2 ^{2}D$_{5/2}$	1.9345	1.9346	1.9352	2.944E+13	2.957E+13	3.027E+13
[1s]3p^2 ^{2}P$_{3/2}$ - [2p]3p^2 ^{2}S$_{1/2}$	1.9347	1.9348	1.9354	2.165E+13	2.164E+13	2.162E+13
[1s]3p^2 ^{2}P$_{1/2}$ - [2p]3p^2 ^{2}S$_{1/2}$	1.9350	1.9351	1.9357	3.471E+13	3.473E+13	3.481E+13
[1s]3p^2 ^{2}P$_{1/2}$ - [2p]3p^2 ^{4}D$_{3/2}$	1.9351	1.9352	1.9358	4.742E+13	4.737E+13	4.710E+13
[1s]3p^2 ^{2}P$_{3/2}$ - [2p]3p^2 ^{2}D$_{5/2}$	1.9352	1.9353	1.9359	1.500E+14	1.499E+14	1.492E+14
[1s]3p^2 ^{4}P$_{5/2}$ - [2p]3p^2 ^{4}S$_{3/2}$	1.9353	1.9354	1.9361	2.762E+13	2.776E+13	2.789E+14
[1s]3p^2 ^{4}P$_{1/2}$ - [2p]3p^2 ^{4}D$_{1/2}$	1.9356	1.9357	1.9363	1.346E+14	1.346E+14	1.346E+14
[1s]3p^2 ^{2}D$_{3/2}$ - [2p]3p^2 ^{2}D$_{3/2}$	1.9356	1.9357	1.9363	7.563E+13	7.558E+13	7.531E+13
[1s]3p^2 ^{4}P$_{3/2}$ - [2p]3p^2 ^{4}S$_{3/2}$	1.9357	1.9358	1.9364	5.853E+13	5.854E+13	5.859E+13
[1s]3p^2 ^{2}D$_{3/2}$ - [2p]3p^2 ^{2}F$_{5/2}$	1.9358	1.9359	1.9365	1.217E+14	1.216E+14	1.207E+14
[1s]3p^2 ^{2}S$_{1/2}$ - [2p]3p^2 ^{2}P$_{1/2}$	1.9358	1.9359	1.9365	1.538E+14	1.542E+14	1.558E+14
[1s]3p^2 ^{2}D$_{5/2}$ - [2p]3p^2 ^{2}D$_{3/2}$	1.9359	1.9360	1.9366	5.705E+13	5.702E+13	5.684E+13
[1s]3p^2 ^{2}D$_{5/2}$ - [2p]3p^2 ^{2}F$_{5/2}$	1.9360	1.9361	1.9368	1.084E+14	1.084E+14	1.084E+14
[1s]3p^2 ^{4}P$_{5/2}$ - [2p]3p^2 ^{4}D$_{3/2}$	1.9361	1.9362	1.9368	6.332E+13	6.330E+13	6.314E+13
[1s]3p^2 ^{4}P$_{3/2}$ - [2p]3p^2 ^{2}S$_{1/2}$	1.9363	1.9364	1.9371	4.867E+13	4.860E+13	4.827E+13
[1s]3p^2 ^{4}P$_{3/2}$ - [2p]3p^2 ^{4}D$_{3/2}$	1.9365	1.9366	1.9372	2.118E+13	2.114E+13	2.090E+13
[1s]3p^2 ^{4}P$_{5/2}$ - [2p]3p^2 ^{2}D$_{5/2}$	1.9365	1.9366	1.9372	6.316E+13	6.309E+13	6.274E+13
[1s]3p^2 ^{4}P$_{1/2}$ - [2p]3p^2 ^{4}D$_{3/2}$	1.9369	1.9370	1.9376	2.242E+13	2.246E+13	2.262E+13
[1s]3p^2 ^{4}P$_{3/2}$ - [2p]3p^2 ^{2}D$_{5/2}$	1.9369	1.9370	1.9376	1.655E+13	1.656E+13	1.664E+13
[1s]3p^2 ^{2}S$_{1/2}$ - [2p]3p^2 ^{2}P$_{1/2}$	1.9374	1.9375	1.9381	3.859E+13	3.816E+13	3.776E+13
[1s]3p^2 ^{2}P$_{1/2}$ - [2p]3p^2 ^{2}P$_{1/2}$	1.9384	1.9385	1.9391	1.126E+13	1.110E+13	9.503E+12
[1s]3p^2 ^{2}S$_{1/2}$ - [2p]3p^2 ^{2}P$_{3/2}$	1.9387	1.9388	1.9394	1.763E+13	1.762E+13	1.757E+13
[1s]3p^2 ^{2}P$_{3/2}$ - [2p]3p^2 ^{2}P$_{1/2}$	1.9397	1.9398	1.9404	2.488E+13	2.497E+13	2.521E+13
[1s]3p^2 ^{2}P$_{1/2}$ - [2p]3p^2 ^{2}P$_{1/2}$	1.9400	1.9401	1.9408	7.201E+13	7.214E+13	7.261E+13
[1s]3p^2 ^{2}D$_{3/2}$ - [2p]3p^2 ^{2}P$_{3/2}$	1.9403	1.9404	1.9411	3.371E+13	3.380E+13	3.426E+13
[1s]3p^2 ^{2}D$_{5/2}$ - [2p]3p^2 ^{2}P$_{3/2}$	1.9405	1.9407	1.9413	3.814E+13	3.811E+13	3.797E+13
[1s]3p^2 ^{2}P$_{3/2}$ - [2p]3p^2 ^{2}P$_{3/2}$	1.9410	1.9411	1.9418	3.696E+13	3.687E+13	3.642E+13
[1s]3p^2 ^{2}P$_{1/2}$ - [2p]3p^2 ^{2}P$_{3/2}$	1.9413	1.9414	1.9421	3.498E+13	3.496E+13	3.489E+13
Fe XV						
[1s]3p ^{1}P$_1$ - 3s^2 ^{1}S$_0$	1.7333	1.7336	1.7351	9.035E+13	9.046E+13	9.103E+13
[1s]3p ^{3}P$_2$ - [2p]3p ^{3}S$_1$	1.9291	1.9292	1.9298	1.852E+13	1.856E+13	1.876E+13
[1s]3p ^{1}P$_1$ - [2p]3p ^{3}D$_2$	1.9291	1.9292	1.9298	2.817E+13	2.825E+13	2.863E+13

Transition	λ (Å)			A_{ki} (s^{-1})		
	$\mu = 0.0$	$\mu = 0.1$	$\mu = 0.25$	$\mu = 0.0$	$\mu = 0.1$	$\mu = 0.25$
[1s]3p ^{3}P$_1$ - [2p]3p ^{3}S$_1$	1.9298	1.9299	1.9305	8.120E+13	8.121E+13	8.126E+13
[1s]3p ^{1}P$_1$ - [2p]3p ^{1}P$_1$	1.9299	1.9300	1.9306	1.146E+14	1.145E+14	1.140E+14
[1s]3p ^{3}P$_0$ - [2p]3p ^{3}S$_1$	1.9300	1.9301	1.9307	2.424E+14	2.419E+14	2.398E+14
[1s]3p ^{1}P$_1$ - [2p]3p ^{3}P$_2$	1.9303	1.9304	1.9310	1.473E+14	1.472E+14	1.466E+14
[1s]3p ^{3}P$_2$ - [2p]3p ^{3}D$_3$	1.9304	1.9305	1.9311	2.834E+14	2.834E+14	2.829E+14
[1s]3p ^{3}P$_1$ - [2p]3p ^{3}D$_2$	1.9307	1.9308	1.9314	3.069E+14	3.067E+14	3.058E+14
[1s]3p ^{3}P$_2$ - [2p]3p ^{1}P$_1$	1.9308	1.9309	1.9315	1.679E+13	1.675E+13	1.656E+13
[1s]3p ^{3}P$_2$ - [2p]3p ^{3}P$_2$	1.9312	1.9313	1.9319	9.999E+13	9.997E+13	9.987E+13
[1s]3p ^{3}P$_0$ - [2p]3p ^{1}P$_1$	1.9316	1.9317	1.9323	1.774E+14	1.777E+14	1.792E+14
[1s]3p ^{3}P$_1$ - [2p]3p ^{3}P$_2$	1.9319	1.9320	1.9326	2.020E+13	2.025E+13	2.050E+13
[1s]3p ^{1}P$_1$ - [2p]3p ^{3}P$_0$	1.9320	1.9321	1.9327	1.189E+13	1.184E+13	1.159E+13
[1s]3p ^{1}P$_1$ - [2p]3p ^{3}D$_1$	1.9327	1.9328	1.9334	2.684E+13	2.689E+13	2.714E+13
[1s]3p ^{3}P$_1$ - [2p]3p ^{3}P$_0$	1.9336	1.9337	1.9343	5.369E+13	5.372E+13	5.407E+13
[1s]3p ^{1}P$_1$ - [2p]3p ^{3}P$_1$	1.9336	1.9337	1.9343	5.120E+13	5.118E+13	5.110E+13
[1s]3p ^{1}P$_1$ - [2p]3p ^{3}D$_2$	1.9337	1.9338	1.9344	1.576E+14	1.576E+14	1.573E+14
[1s]3p ^{3}P$_1$ - [2p]3p ^{3}D$_1$	1.9343	1.9344	1.9350	1.113E+14	1.112E+14	1.108E+14
[1s]3p ^{3}P$_0$ - [2p]3p ^{3}D$_1$	1.9345	1.9346	1.9352	1.688E+14	1.687E+14	1.682E+14
[1s]3p ^{3}P$_2$ - [2p]3p ^{3}P$_1$	1.9345	1.9346	1.9352	8.115E+13	8.111E+13	8.090E+13
[1s]3p ^{3}P$_2$ - [2p]3p ^{3}D$_2$	1.9346	1.9348	1.9353	9.786E+13	9.782E+13	9.762E+13
[1s]3p ^{3}P$_0$ - [2p]3p ^{3}P$_1$	1.9354	1.9355	1.9360	1.285E+13	1.290E+13	1.313E+13
[1s]3p ^{1}P$_1$ - [2p]3p ^{1}S$_0$	1.9398	1.9399	1.9404	4.347E+13	4.348E+13	4.353E+13
[1s]3p ^{3}P$_1$ - [2p]3p ^{1}S$_0$	1.9414	1.9415	1.9421	1.107E+13	1.102E+13	1.079E+13
Fe XVI						
[1s]3s3p ^{2}P$_{1/2}$ - 3s^2 ^{2}S$_{1/2}$	1.7274	1.7277	1.7292	3.063E+13	3.069E+13	3.099E+13
[1s]3s3p ^{2}P$_{3/2}$ - 3s^2 ^{2}S$_{1/2}$	1.7274	1.7277	1.7292	1.469E+13	1.472E+13	1.489E+13
[1s]3s3p ^{2}P$_{3/2}$ - 3s^2 ^{2}S$_{1/2}$	1.7295	1.7298	1.7313	8.757E+13	8.763E+13	8.794E+13
[1s]3s3p ^{2}P$_{1/2}$ - 3s^2 ^{2}S$_{1/2}$	1.7300	1.7303	1.7317	7.255E+13	7.258E+13	7.275E+13
[1s]3s3p ^{2}P$_{1/2}$ - [2p]3s3p ^{2}S$_{1/2}$	1.9266	1.9267	1.9273	4.368E+13	4.387E+13	4.473E+13
[1s]3s3p ^{2}P$_{3/2}$ - [2p]3s3p ^{4}D$_{5/2}$	1.9274	1.9275	1.9281	1.784E+13	1.787E+13	1.802E+13
[1s]3s3p ^{4}P$_{5/2}$ - [2p]3s3p ^{4}S$_{3/2}$	1.9282	1.9283	1.9289	2.009E+13	2.012E+13	2.029E+13
[1s]3s3p ^{2}P$_{1/2}$ - [2p]3s3p ^{4}D$_{3/2}$	1.9283	1.9284	1.9290	1.530E+14	1.528E+14	1.522E+14
[1s]3s3p ^{2}P$_{3/2}$ - [2p]3s3p ^{4}P$_{5/2}$	1.9286	1.9288	1.9293	1.022E+14	1.021E+14	1.018E+14
[1s]3s3p ^{2}P$_{1/2}$ - [2p]3s3p ^{4}P$_{1/2}$	1.9286	1.9287	1.9294	4.089E+13	4.057E+13	3.900E+13
[1s]3s3p ^{4}P$_{3/2}$ - [2p]3s3p ^{4}S$_{3/2}$	1.9287	1.9288	1.9294	6.942E+13	6.945E+13	6.960E+13
[1s]3s3p ^{2}P$_{1/2}$ - [2p]3s3p ^{2}P$_{1/2}$	1.9287	1.9288	1.9294	8.825E+13	8.822E+13	8.806E+13
[1s]3s3p ^{2}P$_{3/2}$ - [2p]3s3p ^{2}D$_{3/2}$	1.9287	1.9288	1.9294	1.109E+14	1.109E+14	1.107E+14
[1s]3s3p ^{4}P$_{1/2}$ - [2p]3s3p ^{4}S$_{3/2}$	1.9290	1.9291	1.9295	1.966E+14	1.963E+14	1.948E+14
[1s]3s^2 ^{2}S$_{1/2}$ - [2p]3s^2 ^{2}P$_{3/2}$	1.9291	1.9292	1.9297	4.065E+14	4.064E+14	4.058E+14
[1s]3s3p ^{2}P$_{3/2}$ - [2p]3s3p ^{2}S$_{1/2}$	1.9292	1.9293	1.9298	4.355E+13	4.350E+13	4.329E+13
[1s]3s3p ^{2}P$_{3/2}$ - [2p]3s3p ^{2}D$_{5/2}$	1.9292	1.9293	1.9299	2.726E+14	2.737E+14	2.783E+14
[1s]3s3p ^{2}P$_{1/2}$ - [2p]3s3p ^{2}D$_{3/2}$	1.9293	1.9294	1.9300	6.184E+13	6.189E+13	6.213E+13
[1s]3s3p ^{4}P$_{5/2}$ - [2p]3s3p ^{4}D$_{7/2}$	1.9296	1.9297	1.9303	2.717E+14	2.716E+14	2.712E+14
[1s]3s3p ^{2}P$_{3/2}$ - [2p]3s3p ^{2}D$_{5/2}$	1.9296	1.9297	1.9304	3.222E+13	3.102E+13	2.596E+13
[1s]3s3p ^{4}P$_{3/2}$ - [2p]3s3p ^{4}D$_{5/2}$	1.9299	1.9300	1.9306	2.843E+14	2.842E+14	2.835E+14
[1s]3s3p ^{2}P$_{3/2}$ - [2p]3s3p ^{2}P$_{3/2}$	1.9299	1.9300	1.9306	6.444E+13	6.426E+13	6.334E+13
[1s]3s3p ^{2}P$_{1/2}$ - [2p]3s3p ^{2}P$_{3/2}$	1.9300	1.9301	1.9307	2.397E+14	2.391E+14	2.360E+14
[1s]3s3p ^{4}P$_{3/2}$ - [2p]3s3p ^{4}D$_{3/2}$	1.9302	1.9303	1.9309	5.195E+13	5.186E+13	5.147E+13
[1s]3s3p ^{4}P$_{1/2}$ - [2p]3s3p ^{4}D$_{3/2}$	1.9305	1.9306	1.9312	1.399E+14	1.400E+14	1.408E+14

Transition	λ (Å)			A_{ki} (s^{-1})		
	$\mu = 0.0$	$\mu = 0.1$	$\mu = 0.25$	$\mu = 0.0$	$\mu = 0.1$	$\mu = 0.25$
[1s]3s3p ^{4}P$_{5/2}$ - [2p]3s3p ^{4}P$_{5/2}$	1.9306	1.9307	1.9313	1.242E+14	1.241E+14	1.239E+14
[1s]3s3p ^{4}P$_{5/2}$ - [2p]3s3p ^{2}D$_{3/2}$	1.9307	1.9308	1.9314	2.888E+13	2.884E+13	2.862E+13
[1s]3s3p ^{4}P$_{1/2}$ - [2p]3s3p ^{2}P$_{1/2}$	1.9309	1.9310	1.9316	8.820E+13	8.816E+13	8.794E+13
[1s]3s3p ^{4}P$_{3/2}$ - [2p]3s3p ^{4}P$_{5/2}$	1.9311	1.9313	1.9319	1.430E+13	1.434E+13	1.452E+13
[1s]3s3p ^{4}P$_{1/2}$ - [2p]3s3p ^{2}D$_{3/2}$	1.9315	1.9316	1.9322	3.143E+13	3.143E+13	3.147E+13
[1s]3s3p ^{2}P$_{1/2}$ - [2p]3s3p ^{4}D$_{1/2}$	1.9316	1.9317	1.9323	2.457E+13	2.425E+13	2.265E+13
[1s]3s3p ^{4}P$_{3/2}$ - [2p]3s3p ^{2}S$_{1/2}$	1.9317	1.9318	1.9324	1.912E+13	1.900E+13	1.845E+13
[1s]3s3p ^{2}P$_{1/2}$ - [2p]3s3p ^{4}P$_{1/2}$	1.9319	1.9320	1.9325	4.414E+13	4.443E+13	4.590E+13
[1s]3s3p ^{2}P$_{3/2}$ - [2p]3s3p ^{4}P$_{3/2}$	1.9319	1.9320	1.9326	7.436E+13	7.413E+13	7.299E+13
[1s]3s3p ^{2}P$_{1/2}$ - [2p]3s3p ^{4}D$_{3/2}$	1.9321	1.9322	1.9328	1.675E+14	1.674E+14	1.668E+14
[1s]3s3p ^{2}P$_{3/2}$ - [2p]3s3p ^{2}D$_{5/2}$	1.9323	1.9324	1.9330	1.599E+14	1.606E+14	1.636E+14
[1s]3s3p ^{2}P$_{1/2}$ - [2p]3s3p ^{4}P$_{3/2}$	1.9325	1.9326	1.9332	1.425E+13	1.418E+13	1.382E+13
[1s]3s3p ^{2}P$_{1/2}$ - [2p]3s3p ^{2}P$_{1/2}$	1.9328	1.9329	1.9335	9.744E+13	9.729E+13	9.659E+13
[1s]3s3p ^{2}P$_{3/2}$ - [2p]3s3p ^{2}P$_{1/2}$	1.9328	1.9329	1.9335	4.350E+13	4.360E+13	4.402E+13
[1s]3s^2 ^{2}S$_{1/2}$ - [2p]3s^2 ^{2}P$_{1/2}$	1.9329	1.9330	1.9335	1.993E+14	1.992E+14	1.989E+14
[1s]3s3p ^{2}P$_{1/2}$ - [2p]3s3p ^{2}D$_{3/2}$	1.9332	1.9333	1.9339	1.392E+14	1.392E+14	1.389E+14
[1s]3s3p ^{2}P$_{3/2}$ - [2p]3s3p ^{2}D$_{3/2}$	1.9332	1.9333	1.9339	1.293E+14	1.293E+14	1.291E+14
[1s]3s3p ^{4}P$_{5/2}$ - [2p]3s3p ^{4}D$_{3/2}$	1.9334	1.9335	1.9341	1.534E+13	1.535E+13	1.539E+13
[1s]3s3p ^{4}P$_{3/2}$ - [2p]3s3p ^{4}D$_{1/2}$	1.9336	1.9337	1.9343	3.655E+13	3.691E+13	3.871E+13
[1s]3s3p ^{4}P$_{1/2}$ - [2p]3s3p ^{4}D$_{1/2}$	1.9338	1.9339	1.9345	7.736E+13	7.684E+13	7.414E+13
[1s]3s3p ^{4}P$_{3/2}$ - [2p]3s3p ^{4}P$_{1/2}$	1.9338	1.9339	1.9345	3.105E+13	3.079E+13	2.947E+13
[1s]3s3p ^{4}P$_{5/2}$ - [2p]3s3p ^{4}P$_{3/2}$	1.9339	1.9340	1.9346	6.363E+13	6.351E+13	6.292E+13
[1s]3s3p ^{4}P$_{3/2}$ - [2p]3s3p ^{4}D$_{3/2}$	1.9340	1.9341	1.9347	7.724E+13	7.720E+13	7.702E+13
[1s]3s3p ^{4}P$_{1/2}$ - [2p]3s3p ^{4}P$_{1/2}$	1.9341	1.9342	1.9347	3.096E+13	3.145E+13	3.393E+13
[1s]3s3p ^{4}P$_{1/2}$ - [2p]3s3p ^{4}D$_{3/2}$	1.9343	1.9344	1.9350	2.178E+13	2.177E+13	2.170E+13
[1s]3s3p ^{4}P$_{5/2}$ - [2p]3s3p ^{2}D$_{5/2}$	1.9343	1.9344	1.9350	6.880E+13	6.903E+13	6.995E+13
[1s]3s3p ^{4}P$_{1/2}$ - [2p]3s3p ^{4}P$_{3/2}$	1.9347	1.9348	1.9354	1.307E+13	1.306E+13	1.302E+13
[1s]3s3p ^{2}P$_{3/2}$ - [2p]3s3p ^{2}S$_{1/2}$	1.9373	1.9374	1.9381	2.819E+13	2.807E+13	2.750E+13
[1s]3s3p ^{2}P$_{3/2}$ - [2p]3s3p ^{2}S$_{1/2}$	1.9400	1.9401	1.9408	3.109E+13	3.111E+13	3.119E+13
[1s]3s3p ^{2}P$_{1/2}$ - [2p]3s3p ^{2}S$_{1/2}$	1.9406	1.9407	1.9413	3.238E+13	3.241E+13	3.251E+13

Table 5.12: Plasma environment effects on the Auger widths in Fe IX - Fe XVI

Level	Auger width (s^{-1})		
	$\mu = 0.0$	$\mu = 0.1$	$\mu = 0.25$
Fe IX			
[1s]3d ^{3}D$_1$	1.057E+15	1.054E+15	1.051E+15
[1s]3d ^{3}D$_2$	1.056E+15	1.053E+15	1.050E+15
[1s]3d ^{3}D$_3$	1.056E+15	1.053E+15	1.050E+15
[1s]3d ^{1}D$_2$	1.056E+15	1.053E+15	1.050E+15
Fe X			
[1s]3p^6 ^{2}S$_{1/2}$	9.832E+14	9.789E+14	9.747E+14

Level	Auger width (s^{-1})		
	$\mu = 0.0$	$\mu = 0.1$	$\mu = 0.25$
Fe XI			
$[1s]3p^5\ ^3P_2$	1.252E+15	1.244E+15	1.230E+15
$[1s]3p^5\ ^3P_1$	1.251E+15	1.243E+15	1.230E+15
$[1s]3p^5\ ^3P_0$	1.254E+15	1.246E+15	1.232E+15
$[1s]3p^5\ ^1P_1$	1.235E+15	1.227E+15	1.213E+15
Fe XII			
$[1s]3p^4\ ^4P_{5/2}$	1.257E+15	1.254E+15	1.247E+15
$[1s]3p^4\ ^4P_{3/2}$	1.256E+15	1.254E+15	1.246E+15
$[1s]3p^4\ ^4P_{1/2}$	1.259E+15	1.256E+15	1.248E+15
$[1s]3p^4\ ^2P_{3/2}$	1.231E+15	1.228E+15	1.220E+15
$[1s]3p^4\ ^2P_{1/2}$	1.226E+15	1.224E+15	1.216E+15
$[1s]3p^4\ ^2D_{5/2}$	1.248E+15	1.246E+15	1.238E+15
$[1s]3p^4\ ^2D_{3/2}$	1.247E+15	1.244E+15	1.237E+15
$[1s]3p^4\ ^2S_{1/2}$	1.247E+15	1.244E+15	1.237E+15
Fe XIII			
$[1s]3p^3\ ^5S_2$	1.235E+15	1.230E+15	1.225E+15
$[1s]3p^3\ ^3S_1$	1.193E+15	1.189E+15	1.184E+15
$[1s]3p^3\ ^3D_2$	1.228E+15	1.224E+15	1.218E+15
$[1s]3p^3\ ^3D_1$	1.228E+15	1.223E+15	1.218E+15
$[1s]3p^3\ ^3D_3$	1.227E+15	1.222E+15	1.217E+15
$[1s]3p^3\ ^1D_2$	1.210E+15	1.206E+15	1.201E+15
$[1s]3p^3\ ^3P_0$	1.228E+15	1.224E+15	1.218E+15
$[1s]3p^3\ ^3P_1$	1.227E+15	1.223E+15	1.217E+15
$[1s]3p^3\ ^3P_2$	1.222E+15	1.217E+15	1.212E+15
$[1s]3p^3\ ^1P_1$	1.206E+15	1.201E+15	1.196E+15
Fe XIV			
$[1s]3p^2\ ^4P_{1/2}$	1.205E+15	1.197E+15	1.190E+15
$[1s]3p^2\ ^4P_{3/2}$	1.203E+15	1.194E+15	1.187E+15
$[1s]3p^2\ ^4P_{5/2}$	1.202E+15	1.193E+15	1.186E+15
$[1s]3p^2\ ^2P_{1/2}$	1.168E+15	1.160E+15	1.154E+15
$[1s]3p^2\ ^2P_{3/2}$	1.178E+15	1.170E+15	1.163E+15
$[1s]3p^2\ ^2D_{5/2}$	1.193E+15	1.184E+15	1.178E+15
$[1s]3p^2\ ^2D_{3/2}$	1.184E+15	1.176E+15	1.169E+15
$[1s]3p^2\ ^2S_{1/2}$	1.191E+15	1.183E+15	1.176E+15
Fe XV			
$[1s]3p\ ^3P_0$	1.186E+15	1.178E+15	1.161E+15
$[1s]3p\ ^3P_1$	1.183E+15	1.174E+15	1.158E+15

Table 5.12: (continued)

Level	Auger width (s^{-1})		
	$\mu = 0.0$	$\mu = 0.1$	$\mu = 0.25$
$[1s]3p\ ^3P_2$	1.181E+15	1.173E+15	1.156E+15
$[1s]3p\ ^1P_1$	1.159E+15	1.150E+15	1.134E+15
Fe XVI			
$[1s]3s^2\ ^2S_{1/2}$	1.143E+15	1.131E+15	1.117E+15
$[1s]3s3p\ ^4P_{1/2}$	1.148E+15	1.135E+15	1.122E+15
$[1s]3s3p\ ^4P_{3/2}$	1.146E+15	1.134E+15	1.120E+15
$[1s]3s3p\ ^4P_{5/2}$	1.144E+15	1.131E+15	1.118E+15
$[1s]3s3p\ ^2P_{1/2}$	1.162E+15	1.149E+15	1.135E+15
$[1s]3s3p\ ^2P_{3/2}$	1.152E+15	1.139E+15	1.125E+15
$[1s]3s3p\ ^2P_{1/2}$	1.151E+15	1.139E+15	1.125E+15
$[1s]3s3p\ ^2P_{3/2}$	1.157E+15	1.144E+15	1.130E+15

5.3 Fe II – Fe VIII

The MCDF expansions for Fe II – Fe VIII (Mn- through K-like iron ions) were built up using the AS method, in which we considered all the single and double electron excitations from the reference configurations given in Table 5.13 to configurations including $n = 3$ and 4s orbitals. The final number of CSFs included in the MCDF model of each ion is also reported in this table. Similarly to the computations of Section 5.1 and Section 5.2, the extended average level (EAL) option was used to optimize a weighted trace of the Hamiltonian using level weights proportional to $(2J + 1)$, with the inclusion of the QED effects listed in Section 2.1.3. The combination of the GRASP2K and RATIP programs was used to model the atomic structure and to obtain the radiative wavelengths, the transition probabilities, and the Auger widths associated with K-vacancy states, taking the plasma environment effects into account for a Debye screening parameter in the range $0 \leq \mu \leq 0.25$ a.u.

The computed ionization potentials (IPs) and K thresholds (E_K) are respectively reported in Table 5.14 and Table 5.15 for the plasma screening parameter values $\mu = 0.0$ a.u. (isolated atomic system), $\mu = 0.1$ a.u. and $\mu = 0.25$ a.u. For the isolated ion case, the IPs computed in this work are compared with the values reported in the NIST atomic database (Kramida *et al.* 2019) in Table 5.14, which shows a good overall agreement (within 1%), except for Fe II and Fe III, for which the agreement is only within about 16% and 7%, respectively. This expresses the

Table 5.13: Reference configurations used to build up the MCDF active space (AS) along with the total number of configuration state functions (CSFs) generated for the MCDF expansions in Fe II – Fe VIII.

Ion	Reference configurations	Number of CSFs
Fe II	$3d^64s$, $[3p]3d^74s$, $[3p]3d^64s^2$, $[2p]3d^74s$, $[2p]3d^64s^2$, $[1s]3d^74s$, $[1s]3d^64s^2$	12268
Fe III	$3d^6$, $[3p]3d^7$, $[3p]3d^64s$, $[3p]3d^54s^2$, $[2p]3d^7$, $[2p]3d^64s$, $[2p]3d^54s^2$, $[1s]3d^7$, $[1s]3d^64s$, $[1s]3d^54s^2$	31501
Fe IV	$3d^5$, $[3p]3d^6$, $[2p]3d^6$, $[1s]3d^6$	57189
Fe V	$3d^4$, $[3p]3d^5$, $[2p]3d^5$, $[1s]3d^5$	81237
Fe VI	$3d^3$, $[3p]3d^4$, $[2p]3d^4$, $[1s]3d^4$	85798
Fe VII	$3d^2$, $[3p]3d^3$, $[2p]3d^3$, $[1s]3d^3$	71135
Fe VIII	$3d$, $[3p]3d^2$, $[2p]3d^2$, $[1s]3d^2$	43271

difficulty to model the complex atomic structure of iron ions while approaching the neutral end of the isonuclear sequence, especially when the model is designed for obtaining both an accurate IP and accurate atomic process rates associated with highly-excited K-vacancy states.

The ionization potential and K-threshold lowerings due to plasma effects can

Table 5.14: Computed ionization potentials for Fe II – Fe VIII as a function of the plasma screening parameter μ (a.u.). NIST values are also listed for comparison.

Ion	IP (eV)			
	NIST[a]	$\mu = 0.0$	$\mu = 0.1$	$\mu = 0.25$
Fe II	16.19920(5)	18.89	14.20	7.78
Fe III	30.651(12)	32.93	25.60	16.42
Fe IV	54.91(4)	55.37	44.65	29.64
Fe V	75.0(2)	74.92	61.56	42.83
Fe VI	98.985(15)	98.20	82.20	59.79
Fe VII	124.98(1)	123.60	104.96	78.86
Fe VIII	151.060(12)	151.14	129.85	99.98

[a] Kramida *et al.* (2019)

122

also be inferred from Tables 5.14–5.15 for $\mu = 0.1$ and $\mu = 0.25$. More precisely, the IPs of Fe II - Fe VIII are reduced by 4.7 to 21.3 eV for $\mu = 0.1$ a.u. and by 11.1 to 51.2 eV for $\mu = 0.25$ a.u., while the corresponding K thresholds are decreased by 4.9 to 22.4 eV and by 15.9 to 58.5 eV, respectively. The IP and K-threshold depressions are thus found to be practically the same in magnitude (a difference of a few eV only is observed for $\mu = 0.25$), as already noticed for Fe IX – Fe XXV (see Section 5.1 and Section 5.2). The relative variations observed for the IPs range from 14% to 25% in the case of $\mu = 0.1$ and from 36% to 59% in the case of $\mu = 0.25$. The IP lowering is thus found to be very large. The K-threshold relative reductions, as noticed for Fe IX – Fe XXV (see Sections 5.1-5.2), are much weaker (less than 1%) due to the large energy values of the K-shell thresholds, but the absolute lowering is however noteworthy as it can be as high as around 60 eV.

The IP lowering is linear with both the plasma screening parameter μ and the effective charge, $Z_{\text{eff}} = Z - N + 1$, as shown in Figure 5.13 and Figure 5.14, with the exception of a slight discontinuity between $Z_{\text{eff}} = 3$ and $Z_{\text{eff}} = 4$ (as seen in Figure 5.14) that is clearer for $\mu = 0.25$ a.u. when looking at the IP shift with respect to Z_{eff}. This may be due to the opening of the N-shell ($n = 4$) in Fe III. Such an effect was already observed for the closure of the L- and K-shells in Fe XVII and Fe XXV, respectively (see Section 5.2).

As it can be noticed in Figure 5.15 the ionization potential increases linearly with Z_{eff}, except for one large jump of a factor 1.5 that occurs between $Z_{\text{eff}} = 8$ (Fe VIII) and $Z_{\text{eff}} = 9$ (Fe IX) and that can be attributed to the closure of the 3p subshell (similarly to what happens to the closed L- and K-shell species Fe XVII and Fe XXV, see Section 5.2), and for a change in the slope between $Z_{\text{eff}} = 3$ and $Z_{\text{eff}} = 4$ that should be due to the opening of the N-shell, as discussed above (the IP of Fe IX – Fe XII from Section 5.2 are also represented to illustrate the

Table 5.15: Computed K-thresholds for Fe II – Fe VIII as a function of the plasma screening parameter μ (a.u.).

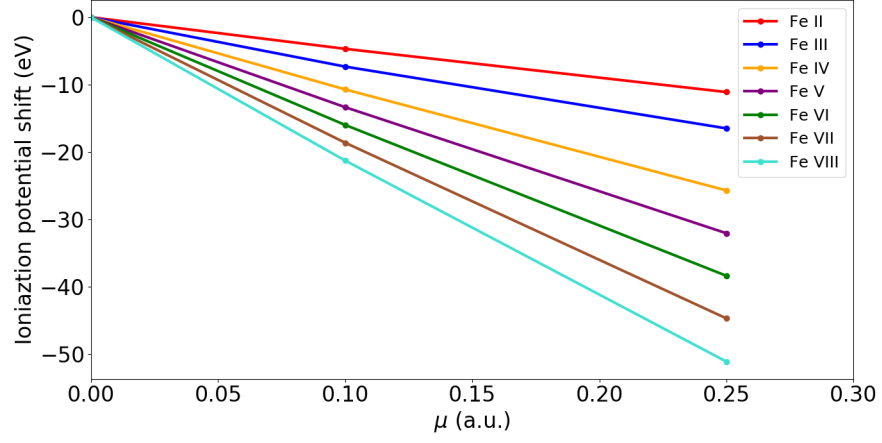| Ion	E_K (eV)		
	$\mu = 0.0$	$\mu = 0.1$	$\mu = 0.25$
Fe II	7131.68	7126.79	7115.77
Fe III	7140.69	7134.10	7119.08
Fe IV	7157.53	7145.57	7123.81
Fe V	7181.20	7166.61	7141.22
Fe VI	7208.68	7191.42	7162.40
Fe VII	7239.44	7219.57	7186.91
Fe VIII	7273.86	7251.42	7215.37

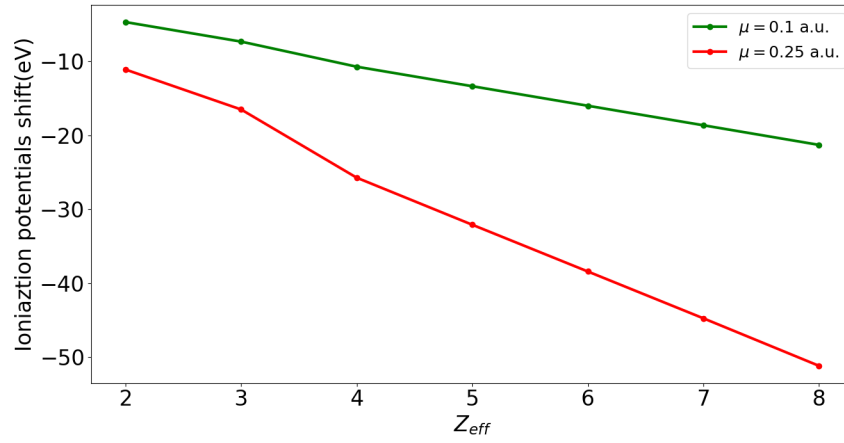Figure 5.13: Ionization potential shifts in Fe II – Fe VIII as a function of the plasma screening parameter μ.

Figure 5.14: Ionization potential shifts in Fe II – Fe VIII as a function of the effective charge $Z_{\text{eff}} = Z - N + 1$.
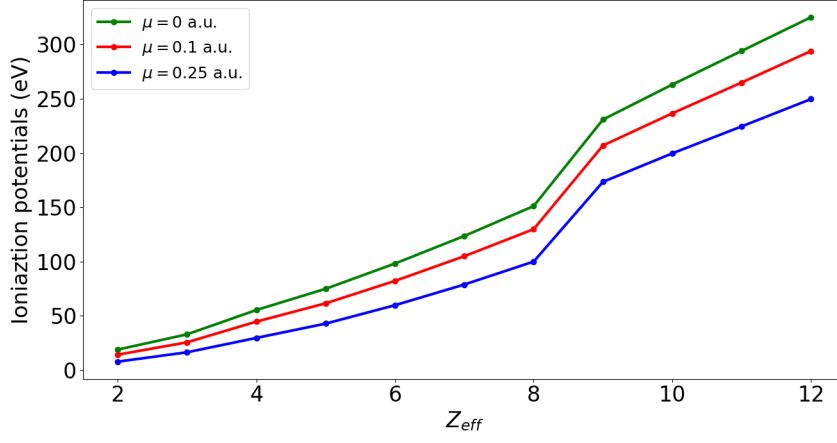
Figure 5.15: Ionization potential of Fe II – Fe XII as a function of the effective charge $Z_{\mathrm{eff}} = Z - N + 1$
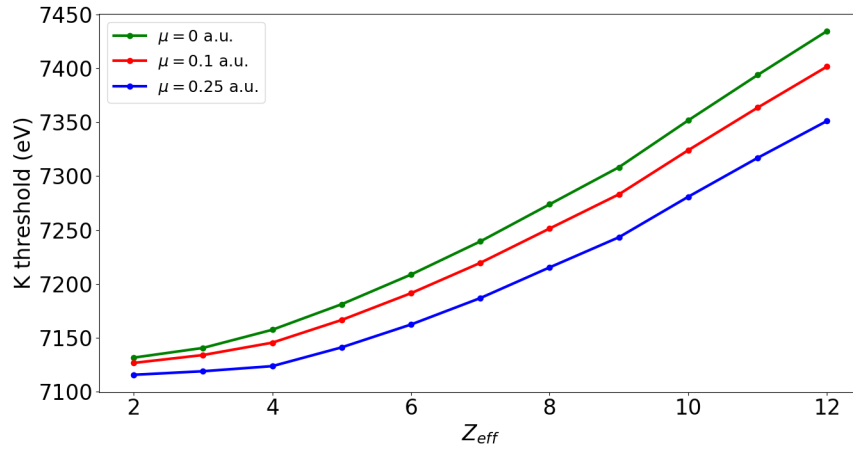

Figure 5.16: K thresholds of Fe II – Fe XII as a function of the effective charge $Z_{\mathrm{eff}} = Z - N + 1$

discontinuity occurring between Fe VIII and Fe IX). However, as already noticed in Section 5.2, the K-threshold trend is a little different since it also increases linearly with Z_{eff} but the slope becomes steeper starting from Fe IV and Fe IX (see Figure 5.16). This is also due to shell opening and closure effects but it is less appreciable than for the IP since the K-shell electron is located deeper close to the nucleus (unlike less bound valence electrons), as mentioned in Section 5.2. Nevertheless, for both the IP and the K threshold, the jump (79.8 eV, 77.1 eV and 73.5 eV for $\mu = 0$, $\mu = 0.1$ and $\mu = 0.25$, respectively) as well as the change of slope are slightly attenuated as the plasma screening parameter increases.

The wavelengths and radiative transition rates for the strongest K lines ($A_{ki} \geq 10^{13}$ s^{-1}) in Fe II - Fe VIII are reported in Table 5.16 for $\mu = 0$ a.u., $\mu = 0.1$ a.u. and $\mu = 0.25$ a.u. Our K-line wavelengths are in very good agreement with the HFR values computed by Mendoza *et al.* (2004) as they differ by less than 0.2% with respect to the latter, while the radiative rates globally agree within 15-20%. Besides, the strong mixing between the states involving both the 3d and 4s orbitals (see *e.g.*, Mendoza *et al.* 2004) increases the complexity to model the atomic structures and process rates of the first ionization stages of iron (Fe II and Fe III) and may induce larger uncertainties in the transition probabilities computed by both the HFR and MCDF methods.

Concerning the plasma environment effects, the K-line redshifts are very weak, that is 1–2 mÅ for $\mu = 0.25$ a.u. and even less for the lowly ionized species (especially Fe II). As seen in Section 5.2, the Kβ lines are more affected than the Kα ones regarding the wavelength redshifts. The radiative rates are also found to be weakly affected by plasma screening effects, as the changes are only about a few percent, except a handful of transitions that are modified by 15-20%, but most of them are relatively weak transitions (these few peculiar large effects might thus be unphysical and could be due to cancellation effects at given values of μ).

Table 5.17 displays the computed Auger widths for the K-vacancy states in Fe II and Fe VIII for $\mu = 0$ a.u., $\mu = 0.1$ a.u. and $\mu = 0.25$ a.u. The Auger widths computed for the isolated atomic system agree within less than 4% with respect to the ones obtained by Mendoza *et al.* (2004) using the HFR method. They are found to be decreased by less than 1% while considering the effects of plasma environment. Let us by the way mention that Auger rate calculations have only been carried out for the ions at both extremes of the Fe II – Fe VIII sequence, as the complexity of these atomic systems makes the computations very long and given the weak effect of the plasma environment on Auger width in these ions.

Table 5.16: Plasma environment effects on the K-line radiative wavelengths (λ) and rates (A_{ki}) in Fe II – Fe VIII

Transition	λ (Å)			A_{ki} (s^{-1})		
	$\mu = 0.0$	$\mu = 0.1$	$\mu = 0.25$	$\mu = 0.0$	$\mu = 0.1$	$\mu = 0.25$
Fe II						
[1s]3d^{6}4s^2 ^{6}D$_{9/2}$ - [3p]3d^{6}4s^2 ^{6}F$_{11/2}$	1.7556	1.7557	1.7560	2.789E+13	2.801E+13	2.854E+13
[1s]3d^{6}4s^2 ^{6}D$_{9/2}$ - [3p]3d^{6}4s^2 ^{6}D$_{9/2}$	1.7560	1.7561	1.7564	1.784E+13	1.788E+13	1.983E+13
[1s]3d^{6}4s^2 ^{6}D$_{9/2}$ - [3p]3d^{6}4s^2 ^{6}P$_{7/2}$	1.7575	1.7576	1.7580	1.598E+13	1.899E+13	2.058E+13
[1s]3d^{6}4s^2 ^{6}D$_{9/2}$ - [2p]3d^{6}4s^2 ^{6}F$_{11/2}$	1.9318	1.9319	1.9323	2.286E+14	1.977E+14	1.693E+14
[1s]3d^{6}4s^2 ^{4}D$_{7/2}$ - [2p]3d^{6}4s^2 ^{4}G$_{9/2}$	1.9319	1.9320	1.9324	5.298E+13	6.126E+13	6.996E+13
[1s]3d^{6}4s^2 ^{6}D$_{7/2}$ - [2p]3d^{6}4s^2 ^{4}G$_{9/2}$	1.9320	1.9321	1.9325	4.409E+13	4.512E+13	4.882E+13
[1s]3d^{6}4s^2 ^{4}D$_{7/2}$ - [2p]3d^{6}4s^2 ^{6}F$_{9/2}$	1.9320	1.9321	1.9325	1.631E+14	1.724E+14	1.894E+14
[1s]3d^{6}4s^2 ^{6}D$_{7/2}$ - [2p]3d^{6}4s^2 ^{6}F$_{9/2}$	1.9321	1.9322	1.9326	4.681E+13	4.599E+13	4.128E+13
[1s]3d^{6}4s^2 ^{4}D$_{7/2}$ - [2p]3d^{6}4s^2 ^{6}D$_{9/2}$	1.9324	1.9325	1.9329	2.512E+13	2.804E+13	3.224E+13
[1s]3d^{6}4s^2 ^{6}D$_{7/2}$ - [2p]3d^{6}4s^2 ^{6}D$_{9/2}$	1.9324	1.9325	1.9329	4.159E+13	4.259E+13	4.449E+13
[1s]3d^{6}4s^2 ^{6}D$_{7/2}$ - [2p]3d^{6}4s^2 ^{6}P$_{5/2}$	1.9324	1.9325	1.9329	6.969E+13	6.722E+13	6.109E+13
[1s]3d^{6}4s^2 ^{6}D$_{9/2}$ - [2p]3d^{6}4s^2 ^{6}D$_{9/2}$	1.9324	1.9325	1.9329	9.011E+13	9.005E+13	8.991E+13
[1s]3d^{6}4s^2 ^{4}D$_{7/2}$ - [2p]3d^{6}4s^2 ^{4}F$_{7/2}$	1.9326	1.9327	1.9331	7.397E+13	7.405E+13	7.498E+13
[1s]3d^{6}4s^2 ^{6}D$_{7/2}$ - [2p]3d^{6}4s^2 ^{4}F$_{7/2}$	1.9326	1.9327	1.9331	2.825E+13	2.799E+13	2.502E+13
[1s]3d^{6}4s^2 ^{6}D$_{7/2}$ - [2p]3d^{6}4s^2 ^{4}D$_{7/2}$	1.9330	1.9331	1.9335	6.469E+13	6.772E+13	7.133E+13
[1s]3d^{6}4s^2 ^{6}D$_{9/2}$ - [2p]3d^{6}4s^2 ^{4}D$_{7/2}$	1.9330	1.9331	1.9335	2.482E+13	2.401E+13	2.289E+13
[1s]3d^{6}4s^2 ^{4}D$_{7/2}$ - [2p]3d^{6}4s^2 ^{4}D$_{5/2}$	1.9331	1.9332	1.9336	3.427E+13	3.393E+13	3.108E+13
[1s]3d^{6}4s^2 ^{6}D$_{7/2}$ - [2p]3d^{6}4s^2 ^{4}D$_{7/2}$	1.9332	1.9333	1.9337	1.211E+13	1.403E+13	1.591E+13
[1s]3d^{6}4s^2 ^{6}D$_{9/2}$ - [2p]3d^{6}4s^2 ^{4}G$_{9/2}$	1.9341	1.9342	1.9346	1.138E+13	1.201E+13	1.399E+13
[1s]3d^{6}4s^2 ^{6}D$_{7/2}$ - [2p]3d^{6}4s^2 ^{4}D$_{5/2}$	1.9341	1.9342	1.9346	1.539E+13	1.591E+13	1.702E+13
[1s]3d^{6}4s^2 ^{4}D$_{7/2}$ - [2p]3d^{6}4s^2 ^{4}F$_{7/2}$	1.9342	1.9343	1.9347	1.812E+13	1.634E+13	1.379E+13
[1s]3d^{6}4s^2 ^{6}D$_{9/2}$ - [2p]3d^{6}4s^2 ^{4}F$_{7/2}$	1.9343	1.9344	1.9348	2.599E+13	2.638E+13	2.812E+13
[1s]3d^{6}4s^2 ^{4}D$_{7/2}$ - [2p]3d^{6}4s^2 ^{4}F$_{5/2}$	1.9344	1.9345	1.9349	1.770E+13	1.711E+13	1.644E+13
[1s]3d^{6}4s^2 ^{4}D$_{7/2}$ - [2p]3d^{6}4s^2 ^{6}F$_{5/2}$	1.9363	1.9364	1.9368	4.827E+13	4.901E+13	5.012E+13
[1s]3d^{6}4s^2 ^{6}D$_{7/2}$ - [2p]3d^{6}4s^2 ^{4}F$_{7/2}$	1.9364	1.9365	1.9369	4.233E+13	4.194E+13	4.058E+13
[1s]3d^{6}4s^2 ^{6}D$_{9/2}$ - [2p]3d^{6}4s^2 ^{4}F$_{7/2}$	1.9364	1.9365	1.9369	3.928E+13	4.079E+13	4.201E+13
[1s]3d^{6}4s^2 ^{4}D$_{7/2}$ - [2p]3d^{6}4s^2 ^{4}F$_{9/2}$	1.9367	1.9368	1.9372	4.639E+13	4.599E+13	4.412E+13
[1s]3d^{6}4s^2 ^{6}D$_{7/2}$ - [2p]3d^{6}4s^2 ^{4}F$_{9/2}$	1.9367	1.9368	1.9372	8.726E+13	8.798E+13	8.911E+13
[1s]3d^{6}4s^2 ^{6}D$_{9/2}$ - [2p]3d^{6}4s^2 ^{4}F$_{9/2}$	1.9368	1.9369	1.9373	3.811E+13	3.759E+13	3.608E+13
[1s]3d^{6}4s^2 ^{4}D$_{7/2}$ - [2p]3d^{6}4s^2 ^{4}D$_{7/2}$	1.9372	1.9373	1.9377	6.131E+13	6.171E+13	6.302E+13
[1s]3d^{6}4s^2 ^{6}D$_{9/2}$ - [2p]3d^{6}4s^2 ^{4}D$_{7/2}$	1.9372	1.9373	1.9377	2.782E+13	2.814E+13	2.967E+13
[1s]3d^{6}4s^2 ^{6}D$_{7/2}$ - [2p]3d^{6}4s^2 ^{4}F$_{9/2}$	1.9380	1.9381	1.9385	1.299E+13	1.332E+13	1.451E+13
Fe III						
[1s]3d^{6}4s ^{7}D$_5$ - [3p]3d^{6}4s ^{7}F$_6$	1.7576	1.7577	1.7582	3.347E+13	3.169E+13	2.289E+13
[1s]3d^{6}4s ^{7}D$_4$ - [3p]3d^{6}4s ^{7}F$_5$	1.7577	1.7579	1.7584	1.807E+13	1.772E+13	1.388E+13
[1s]3d^{6}4s ^{7}D$_5$ - [3p]3d^{6}4s ^{7}D$_5$	1.7580	1.7581	1.7586	2.160E+13	2.166E+13	2.741E+13
[1s]3d^{6}4s ^{7}D$_5$ - [3p]3d^{6}4s ^{7}P$_4$	1.7595	1.7596	1.7601	1.418E+13	1.389E+13	1.058E+13
[1s]3d^{6}4s ^{7}D$_5$ - [2p]3d^{6}4s ^{7}F$_6$	1.9323	1.9324	1.9329	2.278E+14	2.282E+14	2.288E+14
[1s]3d^{6}4s ^{5}D$_4$ - [2p]3d^{6}4s ^{7}F$_5$	1.9324	1.9325	1.9330	2.286E+13	2.322E+13	2.487E+13
[1s]3d^{6}4s ^{7}D$_4$ - [2p]3d^{6}4s ^{7}F$_5$	1.9325	1.9326	1.9331	1.731E+14	1.643E+14	1.506E+13
[1s]3d^{6}4s ^{7}D$_5$ - [2p]3d^{6}4s ^{5}F$_5$	1.9327	1.9328	1.9333	1.655E+13	1.194E+13	2.200E+13
[1s]3d^{6}4s ^{7}D$_4$ - [2p]3d^{6}4s ^{5}F$_4$	1.9328	1.9329	1.9334	3.322E+13	3.295E+13	3.197E+13
[1s]3d^{6}4s ^{5}D$_4$ - [2p]3d^{6}4s ^{5}P$_3$	1.9328	1.9329	1.9334	3.394E+13	3.933E+13	4.802E+13
[1s]3d^{6}4s ^{5}D$_4$ - [2p]3d^{6}4s ^{7}D$_5$	1.9329	1.9330	1.9335	5.481E+13	5.513E+13	5.636E+13
[1s]3d^{6}4s ^{7}D$_4$ - [2p]3d^{6}4s ^{5}P$_3$	1.9329	1.9330	1.9335	2.890E+13	2.832E+13	2.719E+13

Table 5.16: (continued)

Transition	λ (Å)			A_{ki} (s^{-1})		
	$\mu = 0.0$	$\mu = 0.1$	$\mu = 0.25$	$\mu = 0.0$	$\mu = 0.1$	$\mu = 0.25$
[1s]3d^{6}4s ^{7}D$_5$ - [2p]3d^{6}4s ^{7}D$_5$	1.9329	1.9330	1.9335	1.117E+14	9.689E+13	9.102E+13
[1s]3d^{6}4s ^{7}D$_4$ - [2p]3d^{6}4s ^{5}F$_4$	1.9330	1.9331	1.9336	7.524E+13	7.530E+13	7.616E+13
[1s]3d^{6}4s ^{5}D$_4$ - [2p]3d^{6}4s ^{5}D$_4$	1.9334	1.9335	1.9340	4.114E+13	4.260E+13	4.396E+13
[1s]3d^{6}4s ^{7}D$_4$ - [2p]3d^{6}4s ^{5}D$_4$	1.9335	1.9336	1.9341	1.646E+13	1.786E+13	1.882E+13
[1s]3d^{6}4s ^{7}D$_5$ - [2p]3d^{6}4s ^{5}D$_4$	1.9335	1.9336	1.9341	3.034E+13	3.016E+13	2.894E+13
[1s]3d^{6}4s ^{5}D$_4$ - [2p]3d^{6}4s ^{5}D$_3$	1.9335	1.9336	1.9341	2.290E+13	2.312E+13	2.451E+13
[1s]3d^{6}4s ^{7}D$_5$ - [2p]3d^{6}4s ^{5}F$_5$	1.9343	1.9344	1.9349	1.619E+13	1.605E+13	1.576E+13
[1s]3d^{6}4s ^{7}D$_5$ - [2p]3d^{6}4s ^{3}F$_4$	1.9347	1.9348	1.9353	1.881E+13	1.923E+13	2.032E+13
[1s]3d^{6}4s ^{5}D$_4$ - [2p]3d^{6}4s ^{7}D$_3$	1.9367	1.9368	1.9373	1.217E+13	1.199E+13	1.849E+13
[1s]3d^{6}4s ^{7}D$_4$ - [2p]3d^{6}4s ^{7}D$_3$	1.9367	1.9368	1.9373	4.635E+13	4.651E+13	4.788E+13
[1s]3d^{6}4s ^{5}D$_4$ - [2p]3d^{6}4s ^{5}F$_4$	1.9368	1.9369	1.9374	1.187E+13	1.208E+13	1.344E+13
[1s]3d^{6}4s ^{7}D$_5$ - [2p]3d^{6}4s ^{1}G$_4$	1.9369	1.9370	1.9375	1.574E+13	1.517E+13	1.403E+13
[1s]3d^{6}4s ^{7}D$_4$ - [2p]3d^{6}4s ^{5}F$_4$	1.9369	1.9370	1.9375	1.759E+13	1.814E+13	1.923E+13
[1s]3d^{6}4s ^{7}D$_5$ - [2p]3d^{6}4s ^{5}F$_4$	1.9369	1.9370	1.9375	3.091E+13	3.122E+13	3.244E+13
[1s]3d^{6}4s ^{5}D$_4$ - [2p]3d^{6}4s ^{5}F$_5$	1.9371	1.9372	1.9377	8.737E+13	8.699E+13	8.537E+13
[1s]3d^{6}4s ^{7}D$_5$ - [2p]3d^{6}4s ^{5}F$_5$	1.9372	1.9373	1.9378	3.783E+13	3.688E+13	3.542E+13
[1s]3d^{6}4s ^{5}D$_4$ - [2p]3d^{6}4s ^{5}D$_4$	1.9376	1.9377	1.9382	5.508E+13	5.574E+13	5.704E+13
[1s]3d^{6}4s ^{7}D$_5$ - [2p]3d^{6}4s ^{5}D$_4$	1.9376	1.9377	1.9382	2.042E+13	2.016E+13	1.912E+13
[1s]3d^{6}4s ^{5}D$_4$ - [2p]3d^{6}4s ^{5}F$_5$	1.9384	1.9385	1.9390	1.222E+13	1.289E+13	1.394E+13
Fe IV						
[1s]3d^6 ^{6}D$_{9/2}$ - [3p]3d^6 ^{6}F$_{11/2}$	1.7573	1.7575	1.7591	3.383E+13	3.386E+13	3.403E+13
[1s]3d^6 ^{4}D$_{7/2}$ - [3p]3d^6 ^{6}F$_{9/2}$	1.7573	1.7576	1.7592	2.151E+13	2.200E+13	2.432E+13
[1s]3d^6 ^{6}D$_{7/2}$ - [3p]3d^6 ^{6}F$_{9/2}$	1.7573	1.7576	1.7592	1.098E+13	1.052E+13	1.002E+13
[1s]3d^6 ^{6}D$_{9/2}$ - [3p]3d^6 ^{6}D$_{9/2}$	1.7577	1.7580	1.7596	2.511E+13	2.513E+13	2.527E+13
[1s]3d^6 ^{6}D$_{9/2}$ - [3p]3d^6 ^{6}P$_{7/2}$	1.7591	1.7594	1.7610	1.009E+13	1.433E+13	1.786E+13
[1s]3d^6 ^{6}D$_{9/2}$ - [2p]3d^6 ^{6}F$_{11/2}$	1.9332	1.9333	1.9340	2.294E+14	2.294E+14	2.291E+14
[1s]3d^6 ^{4}D$_{7/2}$ - [2p]3d^6 ^{6}F$_{9/2}$	1.9333	1.9334	1.9341	1.327E+14	1.362E+14	1.531E+14
[1s]3d^6 ^{6}D$_{7/2}$ - [2p]3d^6 ^{6}F$_{9/2}$	1.9333	1.9334	1.9341	1.024E+14	9.886E+13	9.201E+13
[1s]3d^6 ^{6}D$_{7/2}$ - [2p]3d^6 ^{6}D$_{5/2}$	1.9336	1.9337	1.9344	2.127E+13	2.074E+13	1.812E+13
[1s]3d^6 ^{4}D$_{7/2}$ - [2p]3d^6 ^{6}D$_{9/2}$	1.9338	1.9339	1.9346	2.232E+13	2.237E+13	2.268E+13
[1s]3d^6 ^{6}D$_{7/2}$ - [2p]3d^6 ^{6}D$_{9/2}$	1.9338	1.9339	1.9346	4.181E+13	4.272E+13	4.493E+13
[1s]3d^6 ^{6}D$_{7/2}$ - [2p]3d^6 ^{6}P$_{5/2}$	1.9338	1.9339	1.9346	4.448E+13	4.403E+13	4.276E+13
[1s]3d^6 ^{6}D$_{9/2}$ - [2p]3d^6 ^{6}D$_{9/2}$	1.9338	1.9339	1.9346	1.111E+14	1.110E+14	1.107E+14
[1s]3d^6 ^{4}D$_{7/2}$ - [2p]3d^6 ^{4}F$_{7/2}$	1.9339	1.9340	1.9347	5.375E+13	5.524E+13	6.240E+13
[1s]3d^6 ^{6}D$_{7/2}$ - [2p]3d^6 ^{4}F$_{7/2}$	1.9339	1.9340	1.9347	4.847E+13	4.692E+13	4.158E+13
[1s]3d^6 ^{6}D$_{9/2}$ - [2p]3d^6 ^{4}D$_{7/2}$	1.9343	1.9344	1.9351	2.257E+13	2.239E+13	2.134E+13
[1s]3d^6 ^{4}D$_{7/2}$ - [2p]3d^6 ^{4}D$_{5/2}$	1.9344	1.9345	1.9352	2.600E+13	2.601E+13	2.607E+13
[1s]3d^6 ^{6}D$_{7/2}$ - [2p]3d^6 ^{4}D$_{7/2}$	1.9345	1.9346	1.9353	1.622E+13	1.594E+13	1.169E+13
[1s]3d^6 ^{4}D$_{7/2}$ - [2p]3d^6 ^{4}F$_{7/2}$	1.9355	1.9356	1.9363	2.084E+13	1.912E+13	1.799E+13
[1s]3d^6 ^{4}D$_{7/2}$ - [2p]3d^6 ^{4}F$_{5/2}$	1.9357	1.9358	1.9365	1.604E+13	1.782E+13	1.902E+13
[1s]3d^6 ^{4}D$_{7/2}$ - [2p]3d^6 ^{6}D$_{5/2}$	1.9376	1.9377	1.9384	5.603E+13	5.422E+13	5.107E+13
[1s]3d^6 ^{6}D$_{7/2}$ - [2p]3d^6 ^{4}F$_{7/2}$	1.9377	1.9378	1.9385	2.581E+13	2.556E+13	1.872E+13
[1s]3d^6 ^{6}D$_{9/2}$ - [2p]3d^6 ^{4}F$_{7/2}$	1.9378	1.9379	1.9386	2.373E+13	2.360E+13	2.295E+13
[1s]3d^6 ^{4}D$_{7/2}$ - [2p]3d^6 ^{4}F$_{9/2}$	1.9380	1.9381	1.9388	3.992E+13	4.011E+13	4.543E+13
[1s]3d^6 ^{6}D$_{7/2}$ - [2p]3d^6 ^{4}F$_{9/2}$	1.9380	1.9381	1.9388	9.162E+13	9.157E+13	8.994E+13
[1s]3d^6 ^{6}D$_{9/2}$ - [2p]3d^6 ^{4}F$_{9/2}$	1.9381	1.9382	1.9389	3.204E+13	3.202E+13	3.188E+13
[1s]3d^6 ^{4}D$_{7/2}$ - [2p]3d^6 ^{4}D$_{7/2}$	1.9385	1.9386	1.9393	6.145E+13	6.320E+13	6.702E+13

Transition	λ (Å)			A_{ki} (s^{-1})		
	$\mu = 0.0$	$\mu = 0.1$	$\mu = 0.25$	$\mu = 0.0$	$\mu = 0.1$	$\mu = 0.25$
[1s]3d^6 ^{6}D$_{9/2}$ - [2p]3d^6 ^{4}D$_{7/2}$	1.9385	1.9386	1.9393	2.422E+13	2.434E+13	2.535E+13
Fe V						
[1s]3d^5 ^{7}S$_3$ - [3p]3d^5 ^{7}P$_4$	1.7572	1.7575	1.7591	3.796E+13	3.800E+13	3.820E+13
[1s]3d^5 ^{7}S$_3$ - [3p]3d^5 ^{7}P$_3$	1.7573	1.7576	1.7592	2.898E+13	2.901E+13	2.918E+13
[1s]3d^5 ^{7}S$_3$ - [3p]3d^5 ^{7}P$_2$	1.7574	1.7577	1.7593	2.052E+13	2.054E+13	2.066E+13
[1s]3d^5 ^{5}S$_2$ - [3p]3d^5 ^{5}P$_2$	1.7633	1.7637	1.7652	2.048E+13	2.045E+13	1.963E+13
[1s]3d^5 ^{5}S$_2$ - [3p]3d^5 ^{5}P$_3$	1.7634	1.7638	1.7653	2.873E+13	2.877E+13	2.891E+13
[1s]3d^5 ^{7}S$_3$ - [2p]3d^5 ^{7}P$_4$	1.9339	1.9340	1.9346	2.452E+14	2.451E+14	2.448E+14
[1s]3d^5 ^{5}S$_2$ - [2p]3d^5 ^{7}P$_3$	1.9344	1.9345	1.9352	6.536E+13	6.532E+13	6.510E+13
[1s]3d^5 ^{7}S$_3$ - [2p]3d^5 ^{7}P$_3$	1.9345	1.9346	1.9352	1.302E+14	1.302E+14	1.300E+14
[1s]3d^5 ^{5}S$_2$ - [2p]3d^5 ^{5}P$_2$	1.9349	1.9350	1.9356	8.580E+13	8.575E+13	8.547E+13
[1s]3d^5 ^{7}S$_3$ - [2p]3d^5 ^{5}P$_2$	1.9349	1.9350	1.9356	3.956E+13	3.953E+13	3.941E+13
[1s]3d^5 ^{5}S$_2$ - [2p]3d^5 ^{5}P$_1$	1.9351	1.9352	1.9358	6.342E+13	6.340E+13	6.325E+13
[1s]3d^5 ^{7}S$_3$ - [2p]3d^5 ^{5}P$_3$	1.9363	1.9364	1.9370	1.734E+13	1.729E+13	1.711E+13
[1s]3d^5 ^{7}S$_3$ - [2p]3d^5 ^{3}D$_2$	1.9365	1.9366	1.9372	1.209E+13	1.289E+13	1.402E+13
[1s]3d^5 ^{7}S$_3$ - [2p]3d^5 ^{5}P$_2$	1.9365	1.9366	1.9372	1.340E+13	1.352E+13	1.399E+13
[1s]3d^5 ^{5}S$_2$ - [2p]3d^5 ^{5}P$_1$	1.9371	1.9372	1.9378	1.836E+13	1.890E+13	1.979E+13
[1s]3d^5 ^{5}S$_2$ - [2p]3d^5 ^{3}P$_2$	1.9381	1.9382	1.9388	1.186E+13	1.184E+13	1.174E+13
[1s]3d^5 ^{5}S$_2$ - [2p]3d^5 ^{3}D$_2$	1.9385	1.9386	1.9392	1.192E+13	1.190E+13	1.179E+13
[1s]3d^5 ^{5}S$_2$ - [2p]3d^5 ^{3}F$_2$	1.9386	1.9387	1.9393	1.899E+13	1.902E+13	1.919E+13
[1s]3d^5 ^{5}S$_2$ - [2p]3d^5 ^{3}D$_2$	1.9388	1.9389	1.9395	3.104E+13	3.189E+13	3.303E+13
[1s]3d^5 ^{7}S$_3$ - [2p]3d^5 ^{3}D$_2$	1.9388	1.9389	1.9395	1.388E+13	1.389E+13	1.398E+13
[1s]3d^5 ^{5}S$_2$ - [2p]3d^5 ^{1}F$_3$	1.9389	1.9390	1.9396	1.802E+13	1.801E+13	1.800E+13
[1s]3d^5 ^{5}S$_2$ - [2p]3d^5 ^{3}G$_3$	1.9391	1.9392	1.9398	2.747E+13	2.429E+13	2.173E+13
[1s]3d^5 ^{5}S$_2$ - [2p]3d^5 ^{5}P$_3$	1.9392	1.9393	1.9399	1.017E+14	1.016E+14	1.013E+14
[1s]3d^5 ^{7}S$_3$ - [2p]3d^5 ^{5}P$_3$	1.9392	1.9393	1.9399	1.788E+13	1.802E+13	1.854E+13
[1s]3d^5 ^{5}S$_2$ - [2p]3d^5 ^{3}D$_3$	1.9405	1.9406	1.9412	1.103E+13	1.099E+13	1.067E+13
Fe VI						
[1s]3d^4 ^{6}D$_{1/2}$ - [3p]3d^4 ^{6}D$_{3/2}$	1.7562	1.7566	1.7582	2.853E+13	2.854E+13	2.860E+13
[1s]3d^4 ^{6}D$_{1/2}$ - [3p]3d^4 ^{6}P$_{3/2}$	1.7576	1.7579	1.7586	1.591E+13	1.595E+14	1.613E+13
[1s]3d^4 ^{4}D$_{1/2}$ - [3p]3d^4 ^{4}F$_{3/2}$	1.7582	1.7585	1.7592	1.547E+13	1.554E+13	1.579E+13
[1s]3d^4 ^{4}D$_{1/2}$ - [3p]3d^4 ^{4}F$_{3/2}$	1.7616	1.7619	1.7626	2.058E+13	2.062E+13	2.084E+13
[1s]3d^4 ^{6}D$_{1/2}$ - [2p]3d^4 ^{6}D$_{3/2}$	1.9344	1.9345	1.9352	3.460E+14	3.461E+14	3.464E+14
[1s]3d^4 ^{4}D$_{1/2}$ - [2p]3d^4 ^{6}D$_{1/2}$	1.9346	1.9347	1.9354	5.120E+13	5.130E+13	5.152E+13
[1s]3d^4 ^{6}D$_{1/2}$ - [2p]3d^4 ^{6}D$_{1/2}$	1.9346	1.9347	1.9354	5.422E+13	5.419E+13	5.402E+13
[1s]3d^4 ^{4}D$_{1/2}$ - [2p]3d^4 ^{6}P$_{3/2}$	1.9350	1.9351	1.9358	8.390E+13	8.399E+13	8.422E+13
[1s]3d^4 ^{4}D$_{1/2}$ - [2p]3d^4 ^{6}P$_{3/2}$	1.9352	1.9353	1.9360	6.331E+13	6.342E+13	6.402E+13
[1s]3d^4 ^{6}D$_{1/2}$ - [2p]3d^4 ^{6}D$_{1/2}$	1.9352	1.9353	1.9360	3.571E+13	3.579E+13	3.598E+13
[1s]3d^4 ^{4}D$_{1/2}$ - [2p]3d^4 ^{4}F$_{3/2}$	1.9353	1.9354	1.9361	3.789E+13	3.779E+13	3.702E+13
[1s]3d^4 ^{6}D$_{1/2}$ - [2p]3d^4 ^{4}D$_{1/2}$	1.9365	1.9366	1.9373	4.298E+13	4.299E+13	4.309E+13
[1s]3d^4 ^{6}D$_{1/2}$ - [2p]3d^4 ^{2}P$_{1/2}$	1.9383	1.9384	1.9391	1.655E+13	1.655E+13	1.658E+13
[1s]3d^4 ^{4}D$_{1/2}$ - [2p]3d^4 ^{6}F$_{3/2}$	1.9392	1.9394	1.9400	7.522E+13	7.517E+13	7.489E+13
[1s]3d^4 ^{6}D$_{1/2}$ - [2p]3d^4 ^{4}D$_{1/2}$	1.9391	1.9392	1.9399	4.822E+13	4.824E+13	4.839E+13
[1s]3d^4 ^{4}D$_{1/2}$ - [2p]3d^4 ^{4}P$_{1/2}$	1.9397	1.9398	1.9405	6.494E+13	6.486E+13	6.456E+13
[1s]3d^4 ^{4}D$_{1/2}$ - [2p]3d^4 ^{4}P$_{3/2}$	1.9403	1.9404	1.9411	2.897E+13	2.899E+13	2.914E+13
[1s]3d^4 ^{4}D$_{1/2}$ - [2p]3d^4 ^{4}D$_{1/2}$	1.9405	1.9406	1.9413	1.404E+13	1.397E+13	1.361E+13
[1s]3d^4 ^{4}D$_{1/2}$ - [2p]3d^4 ^{2}D$_{3/2}$	1.9409	1.9410	1.9417	1.045E+13	1.046E+13	1.051E+13

Transition	λ (Å)			A_{ki} (s^{-1})		
	$\mu = 0.0$	$\mu = 0.1$	$\mu = 0.25$	$\mu = 0.0$	$\mu = 0.1$	$\mu = 0.25$
Fe VII						
[1s]3d^3 ^{5}F$_1$ - [3p]3d^3 ^{5}D$_1$	1.7550	1.7553	1.7570	1.080E+13	1.078E+13	1.072E+13
[1s]3d^3 ^{5}F$_1$ - [3p]3d^3 ^{5}F$_2$	1.7553	1.7556	1.7573	1.720E+13	1.723E+13	1.743E+13
[1s]3d^3 ^{5}F$_1$ - [3p]3d^3 ^{5}F$_1$	1.7553	1.7556	1.7573	1.321E+13	1.322E+13	1.325E+13
[1s]3d^3 ^{5}F$_2$ - [3p]3d^3 ^{5}G$_3$	1.7559	1.7562	1.7579	1.499E+13	1.517E+13	1.611E+13
[1s]3d^3 ^{5}F$_1$ - [3p]3d^3 ^{5}G$_2$	1.7559	1.7562	1.7579	2.099E+13	2.113E+13	2.179E+13
[1s]3d^3 ^{3}F$_2$ - [3p]3d^3 ^{3}G$_3$	1.7572	1.7575	1.7592	1.230E+13	1.301E+13	1.321E+13
[1s]3d^3 ^{3}F$_2$ - [3p]3d^3 ^{3}F$_2$	1.7610	1.7613	1.7630	1.481E+13	1.489E+13	1.528E+13
[1s]3d^3 ^{3}F$_2$ - [2p]3d^3 ^{5}F$_3$	1.9341	1.9343	1.9350	2.295E+13	2.267E+13	2.124E+13
[1s]3d^3 ^{5}F$_1$ - [2p]3d^3 ^{5}D$_2$	1.9342	1.9344	1.9350	7.011E+13	7.014E+13	7.120E+13
[1s]3d^3 ^{5}F$_2$ - [2p]3d^3 ^{5}D$_2$	1.9342	1.9344	1.9350	1.883E+13	1.857E+13	1.729E+13
[1s]3d^3 ^{3}F$_2$ - [2p]3d^3 ^{5}D$_2$	1.9342	1.9344	1.9350	8.529E+13	8.551E+13	8.659E+13
[1s]3d^3 ^{5}F$_2$ - [2p]3d^3 ^{5}F$_3$	1.9342	1.9344	1.9350	7.770E+13	7.761E+13	7.711E+13
[1s]3d^3 ^{5}F$_1$ - [2p]3d^3 ^{5}D$_1$	1.9343	1.9345	1.9351	2.157E+13	2.163E+13	2.196E+13
[1s]3d^3 ^{5}F$_2$ - [2p]3d^3 ^{5}D$_1$	1.9343	1.9345	1.9351	1.300E+14	1.299E+14	1.294E+14
[1s]3d^3 ^{5}F$_1$ - [2p]3d^3 ^{5}D$_0$	1.9344	1.9346	1.9352	5.759E+13	5.757E+13	5.746E+13
[1s]3d^3 ^{3}F$_2$ - [2p]3d^3 ^{3}F$_2$	1.9347	1.9349	1.9355	4.397E+13	4.402E+13	4.424E+13
[1s]3d^3 ^{5}F$_1$ - [2p]3d^3 ^{3}F$_2$	1.9348	1.9350	1.9356	5.932E+13	5.939E+13	5.970E+13
[1s]3d^3 ^{5}F$_2$ - [2p]3d^3 ^{5}G$_3$	1.9348	1.9350	1.9356	8.596E+13	8.589E+13	8.554E+13
[1s]3d^3 ^{5}F$_1$ - [2p]3d^3 ^{5}F$_1$	1.9348	1.9350	1.9356	2.868E+13	2.873E+13	2.897E+13
[1s]3d^3 ^{5}F$_2$ - [2p]3d^3 ^{5}F$_1$	1.9348	1.9350	1.9356	1.527E+13	1.546E+13	1.642E+13
[1s]3d^3 ^{3}F$_2$ - [2p]3d^3 ^{5}F$_1$	1.9348	1.9350	1.9356	5.927E+13	5.902E+13	5.774E+13
[1s]3d^3 ^{3}F$_2$ - [2p]3d^3 ^{3}G$_3$	1.9350	1.9352	1.9358	7.811E+13	7.859E+13	8.096E+13
[1s]3d^3 ^{3}F$_2$ - [2p]3d^3 ^{3}F$_2$	1.9350	1.9352	1.9358	7.176E+13	7.130E+13	6.897E+13
[1s]3d^3 ^{5}F$_2$ - [2p]3d^3 ^{3}G$_3$	1.9350	1.9352	1.9358	1.242E+13	1.240E+13	1.228E+13
[1s]3d^3 ^{3}F$_2$ - [2p]3d^3 ^{3}G$_3$	1.9361	1.9363	1.9369	1.403E+13	1.437E+13	1.457E+13
[1s]3d^3 ^{3}F$_2$ - [2p]3d^3 ^{3}F$_2$	1.9364	1.9366	1.9372	1.100E+13	1.104E+13	1.123E+13
[1s]3d^3 ^{5}F$_2$ - [2p]3d^3 ^{3}G$_3$	1.9364	1.9366	1.9372	5.116E+13	5.133E+13	5.218E+13
[1s]3d^3 ^{5}F$_1$ - [2p]3d^3 ^{3}F$_2$	1.9365	1.9367	1.9373	1.941E+13	1.946E+13	1.972E+13
[1s]3d^3 ^{3}F$_2$ - [2p]3d^3 ^{3}F$_2$	1.9370	1.9372	1.9378	1.199E+13	1.196E+13	1.179E+13
[1s]3d^3 ^{5}F$_1$ - [2p]3d^3 ^{3}F$_2$	1.9370	1.9372	1.9378	1.893E+13	1.897E+13	1.922E+13
[1s]3d^3 ^{3}F$_2$ - [2p]3d^3 ^{5}G$_3$	1.9375	1.9377	1.9383	2.924E+13	2.918E+13	2.894E+13
[1s]3d^3 ^{3}F$_2$ - [2p]3d^3 ^{5}G$_3$	1.9388	1.9390	1.9396	4.561E+13	4.549E+13	4.474E+13
[1s]3d^3 ^{5}F$_2$ - [2p]3d^3 ^{3}D$_1$	1.9390	1.9392	1.9398	4.564E+13	4.550E+13	4.479E+13
[1s]3d^3 ^{5}F$_1$ - [2p]3d^3 ^{5}G$_2$	1.9390	1.9392	1.9398	4.686E+13	4.684E+13	4.667E+13
[1s]3d^3 ^{3}F$_2$ - [2p]3d^3 ^{3}D$_2$	1.9393	1.9395	1.9401	1.856E+13	1.858E+13	1.865E+13
[1s]3d^3 ^{5}F$_1$ - [2p]3d^3 ^{3}D$_2$	1.9394	1.9396	1.9402	1.166E+13	1.157E+13	1.113E+13
[1s]3d^3 ^{5}F$_2$ - [2p]3d^3 ^{3}D$_1$	1.9395	1.9397	1.9403	3.219E+13	3.218E+13	3.209E+13
[1s]3d^3 ^{3}F$_2$ - [2p]3d^3 ^{3}F$_2$	1.9396	1.9398	1.9404	1.030E+13	1.040E+13	1.060E+13
[1s]3d^3 ^{3}F$_2$ - [2p]3d^3 ^{3}F$_3$	1.9400	1.9402	1.9408	1.551E+13	1.557E+13	1.603E+13
[1s]3d^3 ^{5}F$_2$ - [2p]3d^3 ^{3}D$_1$	1.9409	1.9411	1.9417	1.796E+13	1.806E+13	1.829E+13
[1s]3d^3 ^{3}F$_2$ - [2p]3d^3 ^{3}D$_1$	1.9409	1.9411	1.9417	1.931E+13	1.914E+13	1.853E+13
Fe VIII						
[1s]3d^2 ^{4}F$_{3/2}$ - [3p]3d^2 ^{4}D$_{1/2}$	1.7542	1.7545	1.7561	1.362E+13	1.363E+13	1.369E+13
[1s]3d^2 ^{4}F$_{3/2}$ - [3p]3d^2 ^{4}G$_{5/2}$	1.7552	1.7555	1.7571	4.600E+13	4.609E+13	4.654E+13
[1s]3d^2 ^{4}F$_{3/2}$ - [3p]3d^2 ^{4}F$_{3/2}$	1.7554	1.7557	1.7573	1.897E+13	1.904E+13	1.939E+13
[1s]3d^2 ^{4}F$_{5/2}$ - [3p]3d^2 ^{4}F$_{5/2}$	1.7555	1.7558	1.7574	1.256E+13	1.265E+13	1.310E+13
[1s]3d^2 ^{2}F$_{5/2}$ - [3p]3d^2 ^{2}F$_{7/2}$	1.7562	1.7565	1.7581	2.246E+13	2.252E+13	2.289E+13

Transition	λ (Å)			A_{ki} (s^{-1})		
	$\mu = 0.0$	$\mu = 0.1$	$\mu = 0.25$	$\mu = 0.0$	$\mu = 0.1$	$\mu = 0.25$
[1s]3d^2 ^{2}F$_{5/2}$ - [2p]3d^2 ^{4}D$_{3/2}$	1.9352	1.9353	1.9360	2.472E+13	2.464E+13	2.418E+13
[1s]3d^2 ^{4}F$_{3/2}$ - [2p]3d^2 ^{4}D$_{1/2}$	1.9352	1.9353	1.9360	9.009E+13	9.006E+13	8.991E+13
[1s]3d^2 ^{4}F$_{5/2}$ - [2p]3d^2 ^{4}D$_{3/2}$	1.9353	1.9354	1.9361	3.334E+13	3.343E+13	3.393E+13
[1s]3d^2 ^{4}F$_{3/2}$ - [2p]3d^2 ^{4}D$_{3/2}$	1.9353	1.9354	1.9361	8.534E+13	8.527E+13	8.489E+13
[1s]3d^2 ^{2}F$_{5/2}$ - [2p]3d^2 ^{4}D$_{5/2}$	1.9353	1.9354	1.9361	4.500E+13	4.482E+13	4.393E+13
[1s]3d^2 ^{4}F$_{5/2}$ - [2p]3d^2 ^{4}D$_{5/2}$	1.9354	1.9355	1.9363	4.001E+13	4.012E+13	4.067E+13
[1s]3d^2 ^{4}F$_{3/2}$ - [2p]3d^2 ^{4}D$_{5/2}$	1.9354	1.9355	1.9363	2.422E+13	2.417E+13	2.393E+13
[1s]3d^2 ^{2}F$_{5/2}$ - [2p]3d^2 ^{4}D$_{7/2}$	1.9355	1.9356	1.9364	2.093E+13	2.080E+13	2.019E+13
[1s]3d^2 ^{4}F$_{5/2}$ - [2p]3d^2 ^{4}D$_{7/2}$	1.9355	1.9356	1.9364	3.064E+13	3.062E+13	3.055E+13
[1s]3d^2 ^{4}F$_{5/2}$ - [2p]3d^2 ^{4}G$_{7/2}$	1.9358	1.9360	1.9367	2.112E+14	2.111E+14	2.106E+14
[1s]3d^2 ^{2}F$_{5/2}$ - [2p]3d^2 ^{2}F$_{5/2}$	1.9358	1.9360	1.9367	1.529E+13	1.536E+13	1.572E+13
[1s]3d^2 ^{4}F$_{5/2}$ - [2p]3d^2 ^{2}F$_{5/2}$	1.9359	1.9361	1.9368	4.347E+13	4.338E+13	4.289E+13
[1s]3d^2 ^{4}F$_{3/2}$ - [2p]3d^2 ^{2}F$_{5/2}$	1.9359	1.9361	1.9368	9.593E+13	9.592E+13	9.588E+13
[1s]3d^2 ^{2}F$_{5/2}$ - [2p]3d^2 ^{2}G$_{7/2}$	1.9360	1.9363	1.9369	8.601E+13	8.613E+13	8.672E+13
[1s]3d^2 ^{2}F$_{5/2}$ - [2p]3d^2 ^{4}P$_{5/2}$	1.9361	1.9363	1.9370	1.751E+13	1.747E+13	1.728E+13
[1s]3d^2 ^{4}F$_{3/2}$ - [2p]3d^2 ^{2}D$_{3/2}$	1.9362	1.9364	1.9371	2.827E+13	2.827E+13	2.826E+13
[1s]3d^2 ^{2}F$_{5/2}$ - [2p]3d^2 ^{4}D$_{5/2}$	1.9368	1.9370	1.9377	1.465E+13	1.472E+13	1.477E+13
[1s]3d^2 ^{2}F$_{5/2}$ - [2p]3d^2 ^{4}F$_{3/2}$	1.9368	1.9370	1.9377	1.320E+13	1.324E+13	1.345E+13
[1s]3d^2 ^{4}F$_{3/2}$ - [2p]3d^2 ^{4}D$_{5/2}$	1.9369	1.9371	1.9378	1.484E+13	1.542E+13	1.512E+13
[1s]3d^2 ^{4}F$_{3/2}$ - [2p]3d^2 ^{4}F$_{3/2}$	1.9369	1.9371	1.9378	3.114E+13	3.120E+13	3.151E+13
[1s]3d^2 ^{2}F$_{5/2}$ - [2p]3d^2 ^{2}D$_{3/2}$	1.9375	1.9377	1.9384	1.059E+00	1.056E+13	1.047E+13
[1s]3d^2 ^{4}F$_{3/2}$ - [2p]3d^2 ^{2}F$_{5/2}$	1.9376	1.9378	1.9385	3.380E+13	3.380E+13	3.384E+13
[1s]3d^2 ^{2}F$_{5/2}$ - [2p]3d^2 ^{2}F$_{7/2}$	1.9378	1.9380	1.9387	1.381E+13	1.380E+13	1.377E+13
[1s]3d^2 ^{2}F$_{5/2}$ - [2p]3d^2 ^{4}F$_{5/2}$	1.9381	1.9383	1.9390	2.861E+13	2.859E+13	2.853E+13
[1s]3d^2 ^{4}F$_{3/2}$ - [2p]3d^2 ^{4}F$_{5/2}$	1.9381	1.9383	1.9390	2.359E+13	2.354E+13	2.328E+13
[1s]3d^2 ^{2}F$_{5/2}$ - [2p]3d^2 ^{4}F$_{7/2}$	1.9394	1.9396	1.9403	8.605E+13	8.592E+13	8.529E+13
[1s]3d^2 ^{4}F$_{3/2}$ - [2p]3d^2 ^{4}G$_{5/2}$	1.9398	1.9400	1.9407	5.644E+13	5.638E+13	5.603E+13
[1s]3d^2 ^{2}F$_{5/2}$ - [2p]3d^2 ^{2}F$_{7/2}$	1.9399	1.9401	1.9408	4.348E+13	4.343E+13	4.313E+13
[1s]3d^2 ^{2}F$_{5/2}$ - [2p]3d^2 ^{2}F$_{5/2}$	1.9401	1.9403	1.9410	3.629E+13	3.633E+13	3.649E+13
[1s]3d^2 ^{4}F$_{5/2}$ - [2p]3d^2 ^{2}F$_{5/2}$	1.9401	1.9403	1.9410	1.915E+13	1.913E+13	1.902E+13
[1s]3d^2 ^{4}F$_{3/2}$ - [2p]3d^2 ^{2}F$_{5/2}$	1.9401	1.9403	1.9410	2.945E+13	2.937E+13	2.896E+13
[1s]3d^2 ^{4}F$_{5/2}$ - [2p]3d^2 ^{2}P$_{3/2}$	1.9402	1.9403	1.9411	3.419E+13	3.419E+13	3.421E+13
[1s]3d^2 ^{4}F$_{3/2}$ - [2p]3d^2 ^{2}P$_{3/2}$	1.9402	1.9403	1.9411	1.018E+13	1.018E+13	1.020E+13
[1s]3d^2 ^{2}F$_{5/2}$ - [2p]3d^2 ^{2}D$_{5/2}$	1.9414	1.9417	1.9424	1.983E+13	1.986E+13	2.002E+13
[1s]3d^2 ^{2}F$_{5/2}$ - [2p]3d^2 ^{2}D$_{3/2}$	1.9416	1.9419	1.9426	1.699E+13	1.705E+13	1.735E+13
[1s]3d^2 ^{4}F$_{5/2}$ - [2p]3d^2 ^{2}D$_{3/2}$	1.9417	1.9420	1.9427	4.527E+13	4.507E+13	4.402E+13

Table 5.17: Plasma environment effects on the Auger widths in Fe II and Fe VIII

Level	Auger width (s^{-1})		
	$\mu = 0.0$	$\mu = 0.1$	$\mu = 0.25$
Fe II			
[1s]3d^{6}4s^2 ^{6}D$_{9/2}$	1.119E+15	1.117E+15	1.112E+15

Table 5.17: (continued)

Level	Auger width (s^{-1})		
	$\lambda = 0.0$	$\lambda = 0.1$	$\lambda = 0.25$
$[1s]3d^64s^2\ ^6D_{7/2}$	1.119E+15	1.116E+15	1.112E+15
$[1s]3d^64s^2\ ^4D_{7/2}$	1.118E+15	1.116E+15	1.111E+15
Fe VIII			
$[1s]3d^2\ ^4F_{3/2}$	1.224E+15	1.222E+15	1.217E+15
$[1s]3d^2\ ^4F_{5/2}$	1.223E+15	1.220E+15	1.215E+15
$[1s]3d^2\ ^2F_{5/2}$	1.222E+15	1.220E+15	1.215E+15

5.4 K-shell photoionization of Fe XXIV

As a reminder, K-shell photoionization (PI) is a key atomic process in the context of fluorescent K-line emissions by accreting sources since it is the process that is thought to produce the K-vacancy initial states of such radiative transitions (see Chapter 1). In this section, we estimate how the plasma environment can affect the K-shell photoionization cross section of Li-like Fe XXIV.

5.4.1 Direct part of the K-shell photoionization cross section

The direct part of the K-shell photoionization cross section is formed by the absorption of a photon with an energy that is high enough (*i.e.* larger than the K-threshold energy) to pull an electron off the K-shell of a given ion (bound-free process). As a consequence, a very steep increase of the cross section occurs at the energy of the K-shell threshold. As we focus on the photoionization of the atomic K shell, we neglect here the contributions to the total PI cross section coming from the photoionization of the other shells and crudely consider that the cross section is null for photon energies lying below the K threshold.

The MCDF expansion model used for Fe XXIV is the same as the one given in Section 5.1. The RATIP program was then used to obtain the direct part of the photoionization cross section of the Fe XXIV K-shell for $\mu = 0$ a.u. and $\mu = 0.25$ a.u. The computed K-shell PI cross sections are displayed in Figure 5.17 as a function of the incident photon energy. The main visible effect is, as expected, the position of the K-threshold energy that is found to be lowered (by about 162 eV for $\mu = 0.25$ a.u., as seen in Section 5.1, *cf.* Table 5.2) for $\mu = 0.25$ a.u. compared to the isolated atomic system. This arises from the K-threshold lowering effect that
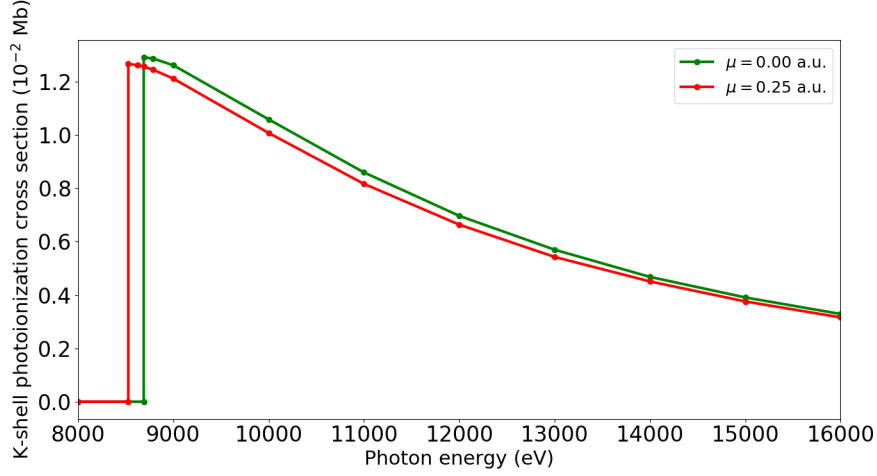
Figure 5.17: Direct part of the K-shell photoionization cross section of Fe XXIV for $\mu = 0$ a.u. (*green*) and for $\mu = 0.25$ a.u. (*red*).

was discussed in Sections 5.1–5.3. The cross section is also decreased in the whole but only by a very few percent. The maximum effect appears at the K-threshold energy, where the cross section is lowered by 2%, but this effect is attenuated as the photon energy grows.

5.4.2 Resonances in the K-shell photoionization cross section

Resonances in the K-shell photoionization cross sections appear at energies lower than the K threshold. They correspond to bound-bound photoexcitations due to the absorption of photons having an energy that coincides with the energy of K inner-shell transitions (1s $\rightarrow$ np, with $n \geq 2$) in a given ion. In this case, the absorbed incident photon can excite the ion in a resonant K-vacancy state, which can in turn autoionize through Auger effect (as explained in Section 1.1). It is thus a two-step photoionization process that can occur through photon resonant absorption. Therefore, the resonant part of the K-shell photoionization cross section is formed by the Rydberg series of K-shell transitions 1s $\rightarrow$ np ($n \geq 2$) whose energies converge toward the K-threshold energy.

Such resonant lines in the K-shell PI cross section can be modeled, in a first approximation, by considering Lorentzian profiles centered on the K-transition energy, with an intensity given by the associated transition probability (in the right units) and a full width at half maximum that coincides with the natural width of the initial K-vacancy state of the transition (*i.e.* the sum of all the radiative and Auger transitions that can de-excite the ion lying in this given K-vacancy state).

133

The RATIP program can thus compute all the required data (radiative transition energies, transition probabilities, Auger rates) to model the resonant part of the K-shell PI cross section of a given ion.

Thereby, we modeled the resonant part of the K-shell PI cross section of Fe XXIV for three given values of plasma screening parameter, that is $\mu = 0$ a.u., $\mu = 0.1$ a.u. and $\mu = 0.25$ a.u. to estimate the effects of the plasma environment on the resonant photoexcitation lines in the cross section. For simplicity reasons, we only considered the two most intense Rydberg series lines, $i.e.$ $1s^2 2s\ ^2S_{1/2} \rightarrow$ $1s2snp\ ^2P_{1/2}$ and $1s^2 2s\ ^2S_{1/2} \rightarrow 1s2snp\ ^2P_{3/2}$, for $2 \le n \le 15$ (n should range from 2 to the infinity but the upper limit $n = 15$ is sufficient to highlight the effect we want to show here). The computed cross sections are illustrated in Figures 5.18–5.20 for the three values of screening parameter above-mentioned, and a zoom around the energies close to the K threshold is also displayed in Figure 5.21 and Figure 5.22 for $\mu = 0.1$ a.u. and $\mu = 0.25$ a.u., respectively.

There are two effects that can be noticed by looking at Figures 5.18–5.22: (i) the redshift of the resonant photoexcitation lines (as discussed in Section 5.1), which is very weak (a few eV) for the weak value of the principal quantum number n but more substantial for high values of n (for instance, for $n = 15$, lines are redshifted by about 25 eV and 100 eV for $\mu = 0.1$ a.u. and $\mu = 0.25$ a.u., respectively); (ii) the K-threshold lowering, as mentioned in Section 5.4.1, which moves the maximum of the PI cross section to lower energies. The combination of these two effects leads to the dissolution of resonances into the continuum, that is the fact that, due to plasma effects, some channels that were resonance transitions for the isolated atomic system become bound-free transitions from a given value of the principal quantum number, since they cross the K-threshold energy and thus contribute to the direct part of the PI cross section instead of the resonant part. This effect can be better appreciated by looking at Figures 5.21–5.22, where it can clearly be noticed that resonances with $n > 14$ and $n > 9$ are diluted into the continuum for $\mu = 0.1$ a.u. and $\mu = 0.25$ a.u., respectively. This is thus a significant effect as it can strongly limit the number of resonant channels that participate to the K-shell photoionization cross section but, in return, the direct part of the PI cross section is enhanced for energies slightly lower than the isolated ion K-threshold energy, within the energy range that corresponds to the K-threshold lowering.

5.4.3 Summary and prospects about K-shell photoionization process in hot dense plasmas

In conclusion, due to plasma screening effects (as they are modeled in our MCDF/ RATIP method), the K-shell photoionization cross section of Fe XXIV is mainly
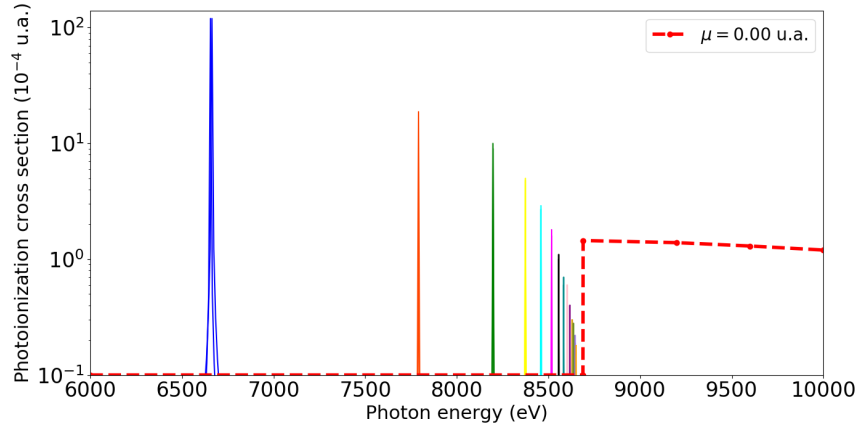
Figure 5.18: K-shell photoionization cross section of Fe XXIV for $\mu = 0$ a.u.
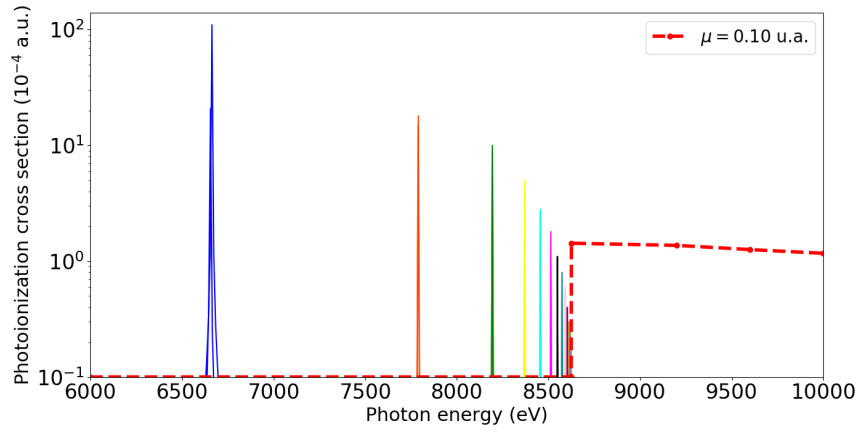

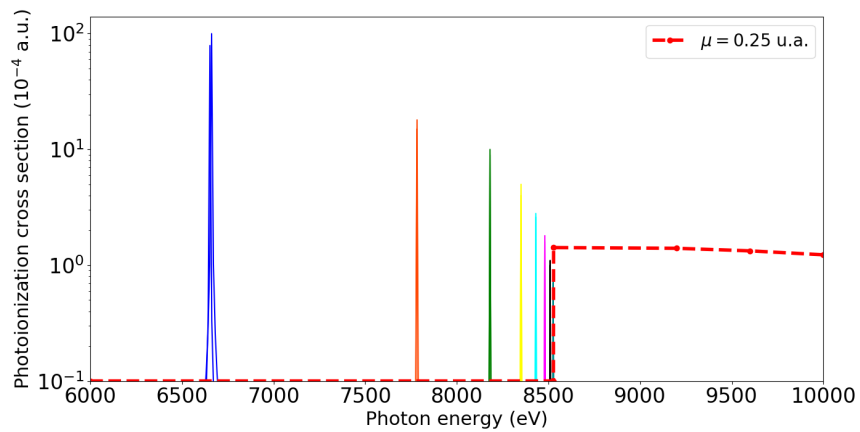Figure 5.19: K-shell photoionization cross section of Fe XXIV for $\mu = 0.1$ a.u.

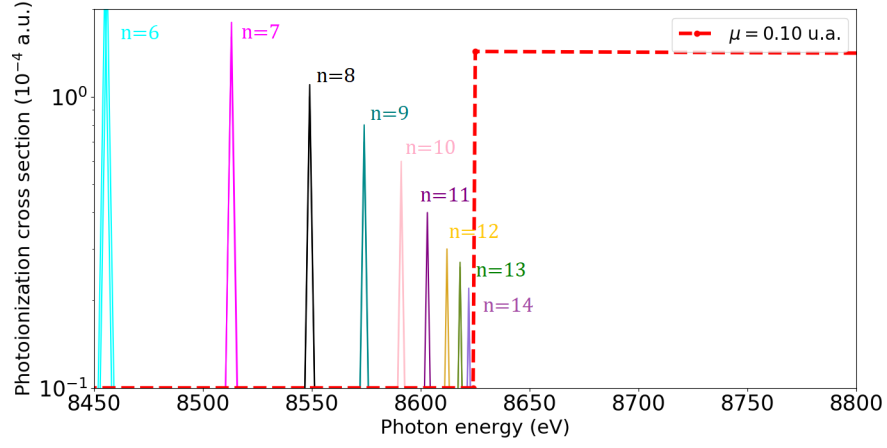Figure 5.20: K-shell photoionization cross section of Fe XXIV for $\mu = 0.25$ a.u.

Figure 5.21: Zoom around the K-threshold energy of the K-shell photoionization cross section of Fe XXIV for $\mu = 0.1$ a.u.
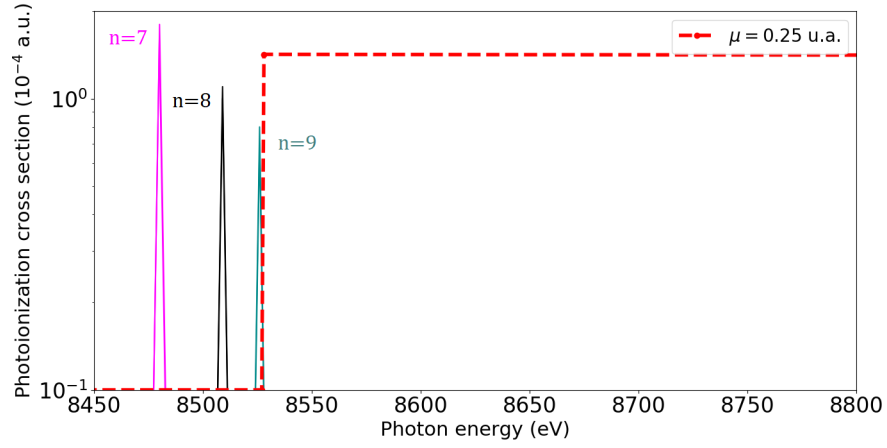

Figure 5.22: Zoom around the K-threshold energy of the K-shell photoionization cross section of Fe XXIV for $\mu = 0.25$ a.u.

affected by the K-threshold lowering and by the dissolution of some resonances into the continuum along with the resonant K-line redshift effect.

Nevertheless, Liu *et al.* (2018) recently highlighted another effect that is not taken into account in our screening model. Actually, they took into consideration the coupling of the continuum electron wavefunction with the plasma environment (due to random collisions with plasma surrounding particles). This coupling gives rise to momentum broadening of the ejected continuum electron (through momentum transfer from the plasma particles to the continuum electron) and hence induces its de-coherence in the processes, while usual models (as ours) generally treat the continuum electron as fully coherent (totally free) in space (which means that there is a probability to find the electron in the whole space). This is thus a transient space localization effect, since the outgoing electron loses coherence when leaving the parent ion, which gives rise to a localized distribution of continuum electrons in space.

Liu *et al.* (2018) developed a formalism to take into account this effect by considering Lorentzian distribution around the unperturbed momentum to model the range of uncertainty around the latter through the exchange of energy with the environment. They found that the photoionization cross section (in the test-case of Fe^{16+}) should be considerably enhanced in the whole, by a factor about 1.5 for $T = 180$ eV and $n_e = 4 \times 10^{22}$ cm^{-3} (corresponding to a screening parameter of $\mu = 0.11$ a.u.), for instance. This effect, if confirmed, would be interesting as it is substantial (much more than the global reduction of the K-shell PI cross section by a very few percent at most observed in Section 5.4.1) and might have an impact on astrophysical modeling. As a prospect, some considerable efforts could be made in the future to implement this kind of effect in our method.

5.5   Astrophysical implications

As mentioned in Chapter 1, the main purpose of the present work is to estimate how the plasma environment can affect the atomic data involved in K-line emission by ions of astrophysical interest (in particular, iron ions). This is of paramount importance in order to implement any potential corrections within the astrophysical modeling programs such as XSTAR and XILLVER (see Section 1.4) to study and interpret at best X-ray spectra from accreting sources. In this section, we discuss the main consequences that would imply modifications in the modeling of astrophysical X-ray spectra from these sources which arise from the results obtained in Sections 5.1–5.4. Actually, the high-density plasma effects presented in this chapter are expected to have a noticeable impact on the modeling of astrophysical environments where the temperature and density are such that the screening parameter μ becomes important. This is the case for relatively low temperatures

$(T \sim 10^5$ K) and high densities ($10^{21} - 10^{22}$ cm^{-3}). These conditions are typically encountered in the inner-most regions of accretion disks around compact objects (white dwarfs, neutron stars, and black holes), from which originates the distorted iron K-line complex (see Chapter 1).

XILLVER (Garcia & Kallman 2010, Garcia *et al.* 2013) is a program that models X-ray reflection spectra from accreting sources, as explained in Chapter 1, and which is based on the XSTAR code (Kallman & Bautista 2001, Bautista & Kallman 2001). The latter is aimed at modeling astrophysical spectra in the case of a photoionized plasma (as mentioned in Chapter 1), that is a plasma in which the ionization balance is determined by an equilibrium (in each point of the plasma) between the photoionization rate induced by an external photoionizing source and the rate of its inverse process, *i.e.* the radiative recombination. The model used in XSTAR consists in considering a spherical shell of gas (plasma) that absorbs and reprocesses the radiation coming from a central point source surrounded by this shell. XSTAR is designed for temperatures ranging from 10^2 K to 10^9 K and densities up to 10^{18}cm^{-3}. It can model the spectra from astrophysical photoionized plasmas along with a lot of other interesting features of the plasma, such as the opacity, temperature (inferred from a thermal balance), the ionization balance (determining the ionization stages of a given species that are present in the plasma), *etc.*

In order to model the emission spectrum from a photoionized plasma, XSTAR needs to compute the emissivity of each line present in the spectrum. In particular, the iron K-line emissivity can be computed by XSTAR within the photoionized plasma model. In the latter, the expression of the iron K-line emissivity, η_z^K, for a K inner-shell radiative transition from a level p to a level q within an iron ion in a charge state z, is given by Kallman *et al.* (2004) as

$$\eta_z^{\mathrm{K}} = E_z^{\mathrm{K}}(p \to q) \int_{E_{z-1}^{\mathrm{K\text{-}Th}}}^{\infty} F_\varepsilon \sum_l n_{z-1}(l)\, \sigma_{z-1}^{\mathrm{K}}(\varepsilon\,;\, l \to p)\, \frac{d\varepsilon}{\varepsilon}\, \omega_z^{\mathrm{K}}(p \to q)\, N y_{\mathrm{Fe}}, \quad (5.1)$$

where $E_z^{\mathrm{K}}(p \to q)$ is the radiative transition energy, $E_{z-1}^{\mathrm{K\text{-}Th}}$ is the K-threshold energy of the parent ion (the iron ion within the charge state $z-1$ that populates by photoionization the initial level of the considered K line), F_ε is the radiation flux emitted by the central source, $n_{z-1}(l)$ is the population of the level l within the parent ion, $\sigma_{z-1}^{\mathrm{K}}(\varepsilon\,;\, l \to p)$ is the K-shell photoionization cross section of the parent ion that is initially in the state l for a given energy ε, N is the plasma density, y_{Fe} is the iron abundance within the plasma and $\omega_z^{\mathrm{K}}(p \to q)$ is the fluorescence yield of the K transition as defined in Equation (1.1). The computation of the iron K-line emissivities thus requires, in one hand, a lot of atomic data (K-threshold energies, K-shell photoionization cross sections, radiative transition energies and rates, Auger widths) and, on the other hand, needs to know the population of each

level of the parent ion that can populate the initial level (a K-vacancy state) of the K line by K-shell photoionization. The determination of the latter (for each level that can populate a K-vacancy state) is a rather difficult task. Actually, in order to accurately determine the population of a given level, one would have to solve the collisional-radiative equations, which are built by considering all the (radiative and non-radiative) atomic processes that can either populate or depopulate this level by unit of time. Solving such a system (as the population of the different levels are coupled with respect to each others), which is also coupled to the ionization balance, is thus a very complex problem (for which approximations are generally considered to limit the number of atomic processes by only taking the dominant ones into account).

As a consequence, the XSTAR program needs to incorporate a lot a atomic data to perform calculations and to model the spectra from photoionized astrophysical plasmas. As aforementioned, the atomic data implemented in XSTAR are only valid for densities up to 10^{18} cm^{-3}. However, in order to model X-ray spectra from accretion disks surrounding black holes, within which densities up to 10^{22} cm^{-3} can be expected (see Chapter 1), it is necessary to update the atomic parameters implemented in XSTAR if the latter are modified due to the high-density plasma environment within the accretion disk.

Firstly, we saw in this chapter that the ionization potentials and K thresholds are substantially lowered with respect to the isolated ion, this effect being the main one highlighted in our work. For instance, for Fe XXV, reductions up to 170 eV are expected for $\mu = 0.25$ a.u., and up to 70 eV for $\mu = 0.1$ a.u. These significant ionization limit lowerings can have several significant consequences in the modeling of X-ray spectra from accretion disks around black holes.

On the one hand, the ionization potential lowering may affect the ionization balance and thus modify the conditions of existence of the different ionization stages of iron ions. As a result, this would induce changes in the iron K-line emissivities since they depend on the level populations of the K-vacancy states (see Equation (5.1)), which are determined by solving the collisional-radiative equations, the latter being actually coupled to the ionization balance. Obviously, the K-line emission by an iron ion in a given charge state also depends on the existence of this charge stage itself within the emitting region, and the conditions of existence could be modified due to the IP depression. More generally, the ionization potential and K-threshold lowerings would modify the ionization rates due to the ionizing radiation field that photoionize the plasma. For simplicity, if we assume a canonical radiation field in the form of an energy power law, the ionizing spectrum illuminating the gas can be crudely represented by a power law $(h\nu)^{-\alpha}$ (see *e.g.* Kallman & Bautista 2001). Therefore, for a flat spectrum in energy ($\alpha = 1$), the rates grow proportionally with the reduction of the IP and

K-threshold energies, leading to a higher ionization rate; moreover, the steeper the spectra is, the larger the change is.

In order to evaluate the influence of the plasma screening effects on the ionization balance, we estimated the fractional abundances of iron ions as a function of the temperature for two values of the electronic density, namely $n_e = 10^{18}$ cm^{-3} and $n_e = 10^{22}$ cm^{-3}. For simplicity, we assumed a local thermodynamic equilibrium (LTE), which is not the case in accretion disks surrounding compact objects (as mentioned above, the ionization balance is determined through an equilibrium between photoionization and radiative recombination processes) but this enables us to simply estimate the fractional abundance by using the Saha equation (see, *e.g.*, Kunze 2009), which reads as

$$\frac{n_{z+1}n_e}{n_z} = 2\,\frac{U_{z+1}(T)}{U_z(T)}\,\frac{1}{\lambda_{\mathrm{dB}}^3}\,\exp\left(-\frac{E_{0,z}}{k_B T}\right),\tag{5.2}$$

where n_z (n_{z+1}) is the density of the iron ion in the charge state z ($z+1$), $U_z(T)$ ($U_{z+1}(T)$) is the partition function of the ion in the charge state z ($z+1$), $E_{0,z}$ is the ionization potential of the ion within the charge state z and λ_{dB} is the electron de Broglie wavelength, which only depends on the temperature. Therefore, it can be clearly seen that the ionization potentials are key atomic parameters to determine the ionization balance between two successive charge stages of a given atomic species. In our estimation, we crudely approximate the partition function of each ion by only considering the ground state of the latter. The fractional ionic abundances are displayed in Figures 5.23–5.25 as a function of the temperature for $n_e = 10^{18}$ cm^{-3} (density for which the IP depression cannot be appreciated since $\mu \approx 0$), for $n_e = 10^{22}$ cm^{-3} without considering the plasma effects and for $n_e = 10^{22}$ cm^{-3} again but considering this time the plasma screening effects that induce the IP lowerings as discussed in this chapter. Zooms of these graphs over a shorter range of temperature ($T = 10^5 - 10^6$ K) are also shown in Figures 5.26–5.28, to better appreciate the changes for the lower charge stages. As one can notice by comparing Figures 5.23 and 5.24 (or Figures 5.26 and 5.27), the effect of the electron density (without considering plasma screening effects) on the ionization balance is obvious: lower charge stages subsist at higher temperature while the electronic density increases. The most interesting comparison for this work concerns Figures 5.24 and 5.25: it can be clearly noticed that, due to IP lowering, a given charge state is created at lower temperature compared to the estimation made without taking plasma screening effect into account. Higher charge stages are thus easily created (at lower temperature) when considering the IP depression due to plasma environment effects. This can be more accurately observed when looking at the zoomed figures (Figures 5.27 and 5.28): for instance, the maximum abundance of Fe X (about 50%) is obtained for $T \approx 5 \times 10^5$ K without considering plasma effects, whereas it happens for $T \approx 4 \times 10^5$ K when
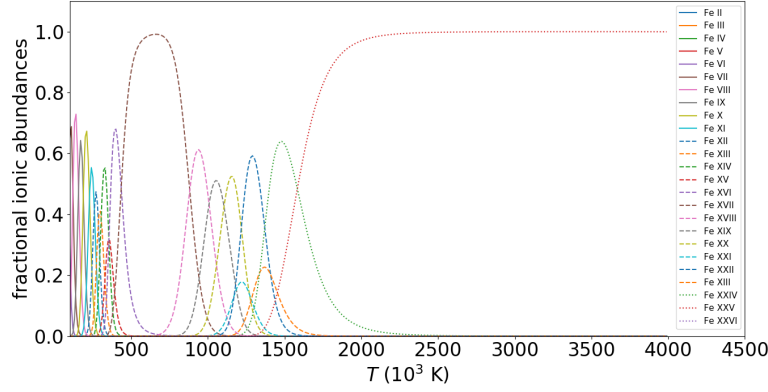
Figure 5.23: Iron ionic abundances for $n_e = 10^{18}$ cm^{-3}
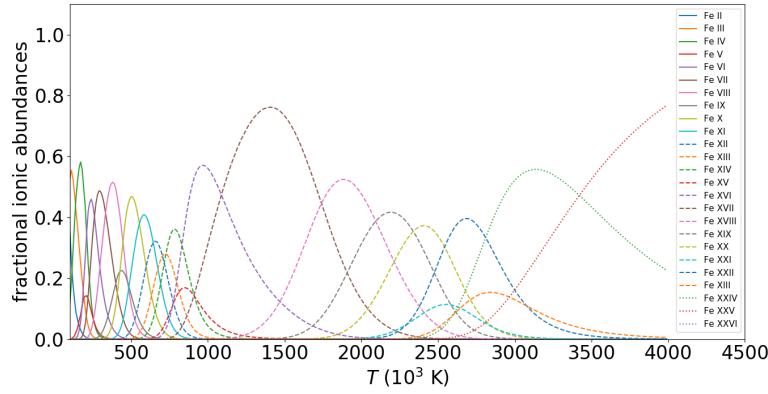

Figure 5.24: Iron ionic abundances for $n_e = 10^{22}$ cm^{-3} *without* consideration of plasma screening effect

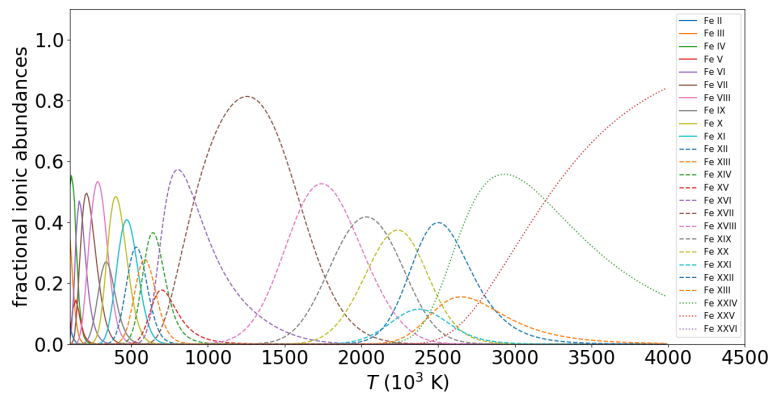

Figure 5.25: Iron ionic abundances for $n_e = 10^{22}$ cm^{-3} *with* consideration of plasma screening effect

141
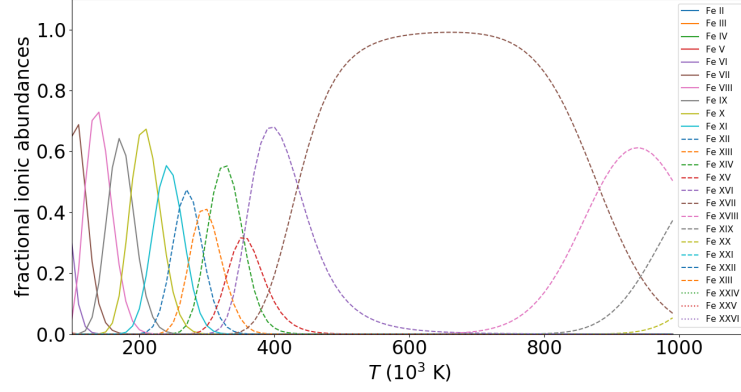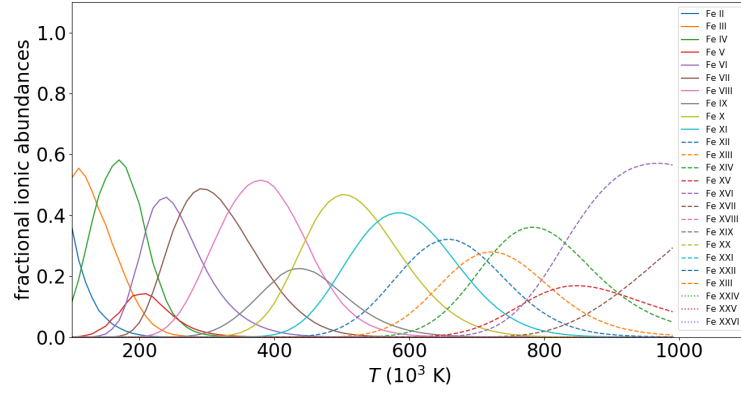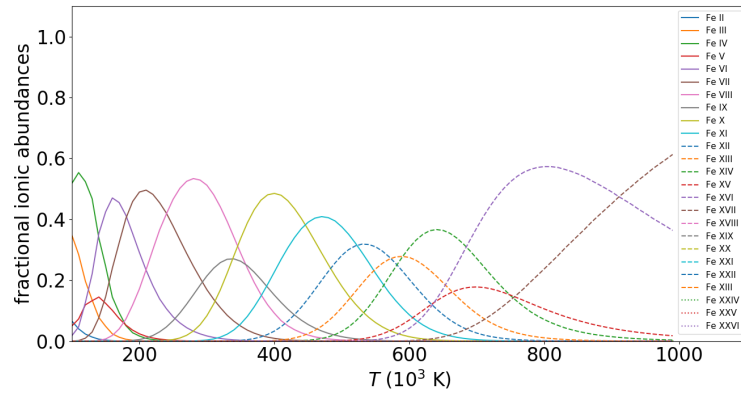
Figure 5.26: Iron ionic abundances for $n_e = 10^{18}$ cm^{-3} (*zoom*)

Figure 5.27: Iron ionic abundances for $n_e = 10^{22}$ cm^{-3} *without* consideration of plasma screening effect (*zoom*)

Figure 5.28: Iron ionic abundances for $n_e = 10^{22}$ cm^{-3} *with* consideration of plasma screening effect (*zoom*)

the IP lowering is considered. Even if this estimation is a crude one, the impact of the IP depression, as computed in our work, is thus clearly noticeable: therefore, it is strongly required to implement the corrections related to IP lowering in the astrophysical modeling codes such as XSTAR.

On the other hand, the K-threshold lowering may also directly affect the iron K-line emissivities since, as it can be noticed by looking at Equation 5.1, the K-threshold energy directly takes part in the calculation of the emissivities *via* the integral lower limit. The K-threshold lowering would thus enlarge the integration domain to compute the K-line emissivities. Besides, the shifts in the K thresholds should be marginally too small to be detected with the available X-ray observatories (at the limit of their detection capability for the highest ionization stages of iron ions and for the largest values of screening parameter μ), but changes in the Fe K-edge position will be resolved with new instruments such as the microcalorimeters aboard the future missions XRISM and ATHENA, which will have a resolution of a few electronvolts only (see Section 1.6). Furthermore, the observed K edge should also be even more smeared due to the density distribution within the plasma of the accretion disk (along with the charge state distribution), inducing a distribution of K-threshold shifts that would make the K edge look smoother and larger.

In order to apply the corrections due to plasma effects to the unperturbed ionization potentials and K thresholds implemented (for instance) in XSTAR, we tried to find simple formulae that fit our data in both cases. For this purpose, we sought a linear dependence for the iron ion IP and K-threshold shifts (ΔE_0 and ΔE_K, respectively, expressed in eV) computed in Sections 5.1–5.3 with respect to both the screening parameter, μ, and the ionic effective charge, Z_{eff}, and we obtained the following fitting formulae:

$$\Delta E_0 = -26.98\mu Z_{\text{eff}} + 35.55\mu^{1.89}, \tag{5.3}$$

and

$$\Delta E_K = -26.5\mu Z_{\text{eff}} - 55.48\mu^{1.89}. \tag{5.4}$$

The graphs representing the fitting formulae and the corresponding data for the IP and K-threshold lowerings are displayed in Figure 5.29 and Figure 5.30, respectively, while the comparisons between our data and the results obtained by using the corresponding fitting formulae are shown in Figures 5.31–5.32. It can be noticed by looking at these figures that the fitting formulae reproduce pretty well our computed data. Furthermore, the results obtained in Chapter 4 concerning the IP and K-threshold lowerings in oxygen ions are also represented in these figures, and it turns out that our fitting formulae actually fit fairly well the computed data for oxygen ions too (a little less concerning the K-thresholds shifts: this is due to the small differences of a few eV between the shifts computed for O
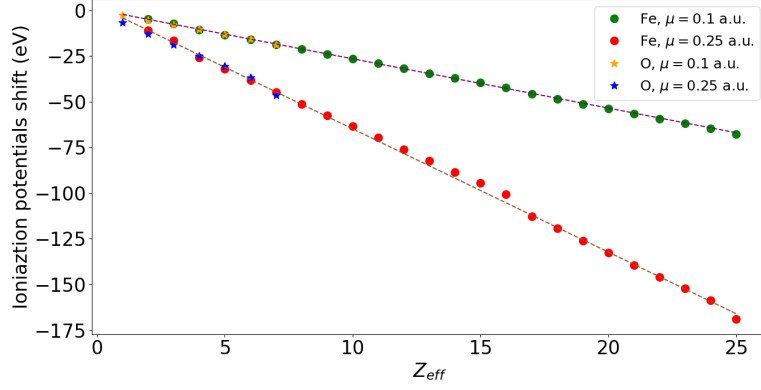
Figure 5.29: Fitting formula for the ionization potentials lowering as a function of the effective charge in iron and oxygen ions for $\mu = 0.1$ a.u. and $\mu = 0.25$ a.u.
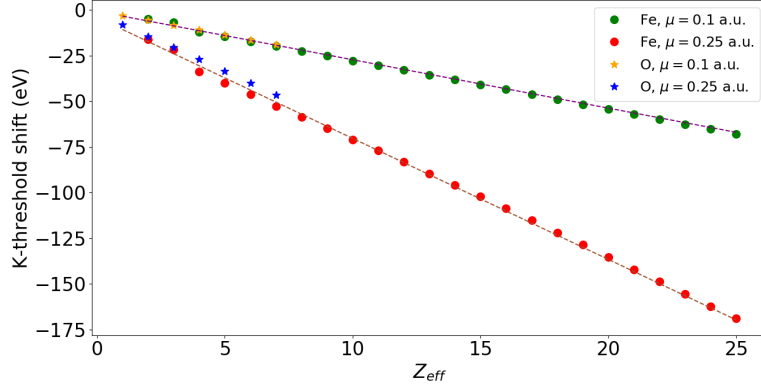

Figure 5.30: Fitting formula for the K-threshold lowering as a function of the effective charge in iron and oxygen ions for $\mu = 0.1$ a.u. and $\mu = 0.25$ a.u.
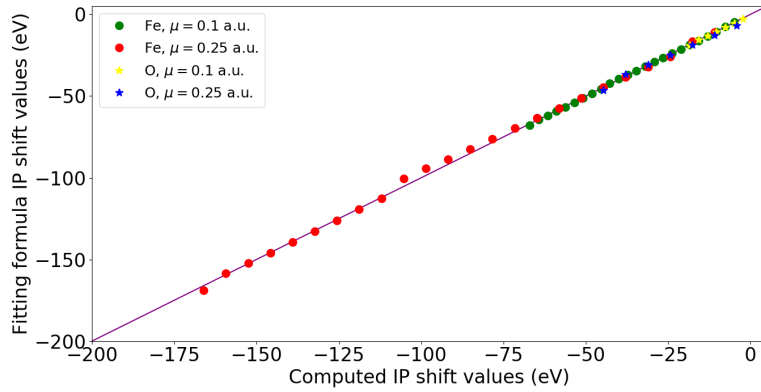

Figure 5.31: Comparison between the ionization potential shifts obtained by the fitting formula and those computed in this work for iron and oxygen ions
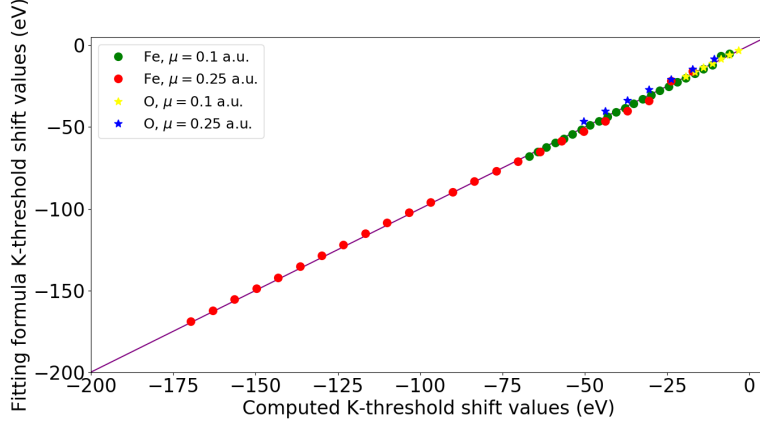
144

Figure 5.32: Comparison between the K-threshold shifts obtained by the fitting formula and those computed in this work for iron and oxygen ions

II – O VII and Fe II – Fe VII). More precisely, the standard deviations between the fitting formula values and our computed ones for both iron and oxygen ions vary from 2% to 6% for the ionization potential lowering and from 4% to 8% for the K-threshold shifts, depending on the screening parameter values. This is thus an important result, as it seems that the IP and K-threshold lowering practically do not depend on Z (*i.e.*, on the element). In a first approximation, the fitting formulae (5.3) and (5.4) could thus be also applied for other elements, namely for elements not considered in our work, which would simplify the implementation of the continuum lowering corrections in XSTAR. Let us however emphasize that more accurate fitting formulae could clearly be obtained by considering each row of iron ions separately. Nevertheless, a slightly less accurate fitting formula that works fairly well for all the ionization stages of iron (and oxygen) is much more convenient to be implemented in XSTAR in order to correct the isolated ion values for the whole isonuclear sequence of a given species. Let us also note that the fitting parameters appearing in the two formulae (5.3) and (5.4) could be improved by further MCDF/RATIP computations of IP and K-threshold lowering in other elements of astrophysical interest.

It is worth mentioning that, unlike the ionization potential and K-threshold energies, the wavelengths of the Kα and Kβ lines are weakly affected by high density plasma effects, as they are redshifted by up to 1 mÅ for Kα lines and up to 2 mÅ for Kβ lines for the largest value of the screening parameter considered in this work ($\mu = 0.25$ a.u.). This corresponds to transition energy variations of a few electronvolts. However, although small, these shifts could be detected by the future X-ray microcalorimeters aboard XRISM and ATHENA, which will be characterized by a resolution of a few eV. Therefore, K-line redshift due to plasma

environment is a small effect but it could be at the limit of detection for the future X-ray satellites and could thus be observed in X-ray spectra in the next few years.

However, both the radiative rates and Auger widths of iron ions are almost unaffected by plasma environment for the physical conditions considered in this work. They are found to be modified by a few percent in most cases, up to 10% for very few transitions, which is not enough to modify significantly the fluorescence yields. As a result, corrections due to plasma effects on such rates do not need to be incorporated in astrophysical modeling codes, unlike (especially) the ionization potentials, K thresholds, and (potentially) the K-line wavelengths.

Finally, K-shell photoionization cross section of Fe XXIV (the test-case studied in this work) is sensitive to plasma screening effects through two different ways. Firstly, the direct part of the PI cross section is mainly modified due to the K-threshold lowering, which shifts the steep rise of the cross section to lower energies. This is closely related to the ionization rate increase discussed above. Secondly, the resonances with a high value of the principal quantum number are diluted in the continuum (due to the combination of the K-threshold lowering and of the resonance redshifts), which cancels some resonant channels that participate to the K-shell photoionization. Nevertheless, the resonant part that contributes to the K-shell PI cross section of Fe XXIV is actually negligible due to Auger and radiative damping (Bautista *et al.* 2003), that is the fact that the K-vacancy states created by photoabsorption will preferably de-excite through one of the other numerous radiative and Auger channels. As a consequence, plasma effects thus contribute to making this resonant part of the cross section even more negligible. Therefore, for the K-shell photoionization cross section of Fe XXIV, the leading correction due the plasma screening effects that has to be considered in the astrophysical modeling program is thus the shift in the bound-free part that is due to the K-edge lowering. The localization effect highlighted by Liu *et al.* (2018) and mentioned in Section 5.4.3 might however bring other substantial changes that should also be implemented (considerable overall enhancement of the cross section), but this effect remains to be tested in the framework of our method.

In conclusion, the atomic parameters that urgently need to be modified in the astrophysical modeling codes (in the case of X-ray emission from accretion disks surrounding black holes) are the ionization potentials, the K thresholds, and the K-shell photoionization cross sections, since the changes observed due to high-density plasma effects should be detectable, especially by the future XRISM and ATHENA X-ray missions. For the two former, it is worth mentioning that the shifts are linear with the screening parameter μ and practically linear (except a few discontinuities or changes of slope when passing from a row of the periodic table to the next one, as discussed in Sections 5.2-5.3) with the ionic effective charge Z_{eff}. The K-line redshifts due to plasma effects are weak but, as they could be at the limit of the

detection capability of both XRISM and ATHENA, modifications could also be implemented in the astrophysical codes such as XSTAR (and, as a consequence, XILLVER) in a second step.

Nevertheless, a comprehensive and deep analysis of the plasma effects on synthetic X-ray astrophysical spectra by implementing all the aforementioned corrections in the astrophysical modeling codes is required to precisely estimate how the plasma environment finally affects the X-ray spectrum of accreting sources. For instance, the formula used to compute the iron ion K-line emissivities (see Equation 5.1) shows how complex the problem is: the net effects due to all the changes in the atomic parameters on the K-line emissivities cannot be clearly estimated without implementing all the corrections in the astrophysical calculations. One of the main prospects of the present work will thus consist in implementing these new atomic data (those that are significantly modified due to plasma effects) in the XSTAR astrophysical modeling code and studying how the reflection spectra of accreting sources modeled by XILLVER would be consequently modified.

Conclusions and prospects

In this work, we have presented our study about the plasma environment effects on the atomic structure and on the radiative and non-radiative processes involving the K shell in ions of astrophysical interest, namely oxygen and iron ions. More precisely, we have focused our work on astrophysical plasmas characterized by physical conditions such as those expected in accretion disks surrounding black holes, where rather high densities (up to $10^{21} - 10^{22}$ cm^{-3}) are suspected to be encountered.

For this purpose, we have modeled the electronic structures of the oxygen and iron ions with the fully-relativistic multiconfiguration Dirac-Fock (MCDF) method by using the GRASP2K computational program. The plasma screening effects have been considered by means of a Debye-Hückel potential as implemented in the RATIP code, which enables the modeling of the atomic structure and the computation of the various parameters that characterize the atomic processes involved in K-line formation by taking the plasma environment effects into account for the ions considered in this work. In some selected cases, our results have been compared with the data obtained using an independent approach based on the Breit-Pauli approximation, as implemented in the AUTOSTRUCTURE (AST) program in which the plasma effects were also included by means of a Debye-Hückel potential.

First of all, we have discussed the validity of our method based on a Debye-Hückel potential. We have shown that our model appears to be suitable to describe a weakly-coupled plasma whose physical conditions correspond to screening parameters as high as those we considered in this work. Indeed, we have been able to reproduce several experimental data and results from other computational approaches, even for high-density plasmas (but still within the limits of coupling parameters lower than unity). We have also highlighted that the electron–electron interaction screening must be considered in addition to the electron–nucleus one; otherwise experimental data cannot be correctly reproduced.

Then, by using our MCDF/RATIP computational approach, we have found that the most significant effect induced by the plasma environment is the lowering of both the ionization potentials and the K-shell thresholds in all the ions considered in this work. For the most extreme physical conditions expected in the

plasma forming the accretion disks around black holes (that is, a density of 10^{22} cm^{-3} along with a temperature of 10^5 K, which correspond to a plasma screening parameter $\mu = 0.25$ a.u.), the ionization potentials and K thresholds of oxygen ions appear to respectively be reduced by 6.5 eV and 8.5 eV to 46.5 eV (the ionization potential of the neutral oxygen is actually lowered by half), while those of iron ions are lowered by about 10 eV and 15 eV to 170 eV. The lowerings of both the ionization potentials and K thresholds are thus found to be practically the same in magnitude and to linearly increase with both the screening parameter and the ionic effective charge. Moreover, a very good agreement is found with the results obtained using the AST method.

The K-line radiative wavelengths appear to be redshifted by only 1–2 mÅ for iron ions and 50-100 mÅ for oxygen ions at most, which is a small variation that can however be detectable with the new-era of X-ray microcalorimeters aboard the future space missions such as XRISM and ATHENA, which will be launched within the next decade (even within a couple of years in the case of XRISM).

Nevertheless, radiative and Auger rates related to K-vacancy states are virtually unaffected by the plasma environment for the physical conditions considered in this work. They are modified by a few percents only and, as a consequence, the K-line fluorescence yields are almost unchanged and do not need to be corrected in the astrophysical modeling codes.

Besides, K-shell photoionization cross sections (which have only be studied in the case of Fe XXIV in this work) are particularly modified through the K-threshold lowering that shifts the cross-section direct part toward lower energies. The dilution of the highest-energy resonances into the continuum is also a noticeable effect. In addition, transient localization effects recently highlighted by Liu *et al.* (2018) could contribute to globally and substantially enhance the K-shell photoionization cross section. An important prospect of this work is thus to implement this effect within our MCDF/RATIP method in order to try to reproduce the results obtained by Liu *et al.* (2018) and to estimate what happens in the particular case of K-shell photoionization for the ions and physical conditions we are interested in.

The results obtained in this work may have several important consequences concerning the astrophysical modeling of X-ray spectra from accreting sources. Firstly, the continuum lowering estimated in this work should significantly modify the ionization balance of the plasma, and thus change the existence conditions of the different ionization stages of a given atomic species. The K-shell threshold reductions may also directly affect the K-line emissivities, as the latter depend on the K-threshold energies since the initial K-vacancy states are populated by K-shell photoionization of the parent ion. The changes in the Fe K-edge position could even be resolved by the instruments aboard the future X-ray space missions.

The linear trend of the ionization potential and K-threshold lowerings with both the screening parameter and the effective charge helps find a simple way to modify these atomic parameters in the astrophysical modeling code such as XSTAR (the standard code used by NASA to model photoionized astrophysical plasmas) by using linear fitting formulae that correct the unperturbed values depending on the plasma conditions and ionization stage. Moreover, the changes do not seem to depend on the atomic species, since the lowerings are found to be practically the same in the cases of both oxygen and iron ions. Therefore, the results that we obtained in this work and, in particular, the fitting formulae derived from them, could also be applied to elements for which computations were not performed. As far as the radiative wavelengths are concerned, the K-line redshifts can be neglected in a first approximation but, as said previously, the weak variations obtained could actually be detected by future X-ray satellites such as XRISM and ATHENA, which will be characterized by spectral resolutions never achieved before in X-ray astrophysics. Corrections to K-line energies could thus be introduced in a second step. Besides, the transient localization effects due to the plasma environment (Liu *et al.*, 2018) should be implemented in our MCDF/RATIP approach in a next step as they may modify significantly the K-shell photoionization cross sections (in addition to the changes that arise from the K-threshold lowering and the resonance dilution into the continuum) and therefore may induce important changes in the K-line emissivities since, as aforementioned, the latter directly depend on them.

Thereby, the results reported in our work represent an important step toward the improvement of the spectral modeling programs currently used in X-ray astrophysics (such as XSTAR and XILLVER), since they clearly highlight the K-line parameters that are most sensitive to the plasma environment effects. However, it is only after the corrections have been included in these modeling programs that it will be possible to precisely assess how X-ray spectra from accretion disks surrounding black holes can be affected by the high-density plasma conditions. Therefore, the main prospect of our work is to implement the corrections due to plasma effects within the XSTAR code and to study how the X-ray spectra modeled by XILLVER are consequently modified. This requirement is even emphasized by the forthcoming launch of XRISM in a couple of years, which will be equipped with a very high-resolution X-ray microcalorimeter that will be able to resolve the Fe K-shell complex as never before. High-precision theoretical atomic data are thus sorely and urgently needed to take advantage of the impending instrumental advances that will bring X-ray astronomy into a very promising and exciting new era.

Bibliography

Badnell N.R., J. Phys. B : At. Mol. Opt. Phys. **30**, 1 (1997)

Badnell N.R., Comput. Phys. Commun. **182**, 1528 (2011)

Balbus S. A. and Hawley J. F., ApJ **376**, 214 (1991)

Bautista M. A., Kallman T. R., Angelini L., Liedahl D. A. & Smits D. P., ApJ **509**, 848 (1998)

Bautista M. A. & Kallman T. R., ApJS **134**, 139 (2001)

Bautista M. A., Mendoza C., Kallman T. R. and Palmeri P., A&A **403**, 339 (2003)

Belkhiri M., Fontes C. J. and Poirier M., Phys. Rev. A **92**, 032501 (2015)

Belkhiri M. and Poirier M., Phys. Rev. A **90**, 062712 (2014)

Berti E. and Volonteri M., ApJ **684**, 822 (2008)

Burke P. G. and Joachain C. J., *Theory of Electron–Atom Collisions*, Springer (1995)

Cackett E. M., Miller J. M., Ballantyne D. R., *et al.*, ApJ **720**, 205 (2010)

Caldwell C. D., Schaphorst S. J., Krause M. O., and Jimenez-Mier J., J. Electron. Spectrosc. Relat. Phenom. **67**, 243 (1994)

Certik O. and Winkler P., Int. J. Quant. Chem. **113**, 2012 (2013)

Chang T. N. and Fang T. K., Phys. Rev. A **88**, 023406 (2013)

Cowan R. D., *The Theory of Atomic Structure and Spectra*, University of California Press, Berkley (1981)

Crowley B. J. B., High Energ. Dens. Phys. **13**, 84 (2014)

Das M., Sahoo B. K. and Pal S., Phys. Rev. A **93**, 052513 (2016)

Debye P. and Hückel E., Physikalische Zeitschrift **24**, No. 9, 185 (1923)

Deprince J., Bautista M. A., Fritzsche S., Garcia J. A., Kallman T. R., Mendoza C., Palmeri P. and Quinet P., Astron. Soc. Pac. Conf. Ser. **515**, 289 (2018)

Deprince J., Bautista M. A., Fritzsche S., Garcia J. A., Kallman T. R., Mendoza C., Palmeri P. and Quinet P., A&A **624**, A74 (2019a)

Deprince J., Bautista M. A., Fritzsche S., Garcia J. A., Kallman T. R., Mendoza C., Palmeri P. and Quinet P., A&A **626**, A83 (2019b)

Deprince J., Bautista M. A., Fritzsche S., Garcia J. A., Kallman T. R., Mendoza C., Palmeri P. and Quinet P., X-Ray Spectrom. **49**, 29 (2020a)

Deprince J., Bautista M. A., Fritzsche S., Garcia J. A., Kallman T. R., Mendoza C., Palmeri P. and Quinet P., A&A **635**, A70 (2020b)

Djenize S., Milosavljevic V. and Sreckovic A., J. Quant. Spectrosc. Radiat. Transf. **59**, 71 (1998)

Eissner W., Jones M. and Nussbaumer H., Comput. Phys. Commun. **8**, 270 (1974)

Eissner W. and Nussbaumer H., J. Phys. B. **2**, 1028 (1969)

Engström L. and Litzen U., J. Phys. B. – At. Mol. Opt. **28**, 2565 (1995)

Fabian A. C., Iwasaka K., Reynolds C. S. and Young A. J., Publ. Astron. Soc. Pac. **112**, 1145 (2000)

Fabian A. C., Rees M. J., Stella L., White N., MNRAS **238**, 729 (1989)

Fabian A. C. and Ross R. R., Space Sci. Rev. **157**, 167 (2010)

Fritzsche S., J. Electron Spec. Relat. Phenom. **114-116**, 1155 (2001)

Fritzsche S., Phys. Scr. T **100**, 37 (2002)

Fritzsche S., Comput. Phys. Commun. **183**, 1523 (2012)

Garcia J., Dauser T., Reynolds C. S., Kallman T. R., McClintock J. E., Wilms J. and Eikmann W., ApJ **768**, 146 (2013)

Garcia J., Fabian A. C., Kallman T. R. *et al.* MNRAS **462**, 751 (2016)

Garcia J. and Kallman T. R., ApJ **718**, 695 (2010)

Garcia J., Kallman T. R., Bautista M. A., Mendoza C., Deprince J., Palmeri P. and Quinet P., Astron. Soc. Pac. Conf. Ser. **515**, 282 (2018)

Garcia J., Mendoza C., Bautista M. A., Gorczyka T. W., Kallman T. R. and Palmeri P., ApJS **158**, 68 (2005)

Gorczyca T. W., Bautista M. A., Hasoglu M. F. *et al.*, ApJ **779**, 78 (2013)

Grant I. P., J. Phys. B : At. Mol. Opt. Phys. **7**; 1458 (1974)

Grant I. P., *Relativistic Quantum Theory of Atoms and Molecules*, Springer (2007)

Greiner W. and Reinhardt J., *Quantum Electrodynamics*, Springer (2002)

Gu M. F., Can. J. Phys. **86**, 675 (2008)

Gu M. F. and Beiersdorfer P., Phys. Rev. A **101**, 032501 (2020)

Guainazzi M. and Tashiro M. S., ArXiv e-prints [arXiv:1807.06903] (2018)

Gupta U. and Rajagopal A. K., J. Phys. B : At. Mol. Phys. **14**, 2309 (1981)

Haardt F. and Maraschi L., ApJL **380**, L51 (1991)

Harrison *et al.*, ApJ **770**, 103 (2013)

Hartman H., Nilsson H., Engström L., Lundberg H., Palmeri P., Quinet P. and Biémont E., Phys. Rev. A **82**, 052512 (2010)

Henke B. L., Gullikson E. M. and Davis J. C., ADNDT **54**, 181 (1993)

The Hitomi Collaboration, Nature **535**, 117 (2016)

Iafrate G. and Mendelsohn, Phys. Rev. **182**, 244 (1969)

Ichimaru S., Rev. Mod. Phys. **54**, 1017 (1982)

Jiang J., Fabian A. C., Wang J. *et al.*, MNRAS **484**, 1972 (2019)

Jönsson P., Gaigalas G., Bieroń J., Froese Fischer C. and Grant I.P., Comput. Phys. Comm. **184**, 2197 (2013)

Juett A. M., Schulz N. S. and Chakrabarty D., ApJ **612**, 308 (2004)

Kaastra J. S., Mewe R., Liedahl D. A., Komossa S. and Brinkman A. C., A&A **354**, L83 (2000)

Kallman T. R. and Bautista M. A., ApJS **133**, 221 (2001) (http://heasarc.nasa.gov/docs/software/xstar/xstar.html)

Kallman T. R., Palmeri P., Bautista M. A., Mendoza C., and Krolik J. H., ApJS **155**, 675 (2004)

Kar S. and Ho Y. K., Phys. Rev. E **70**, 066411 (2004)

Kar S. and Ho Y. K., New J. Phys. **7**, 141 (2005)

Kara E., Zoghbi A., Marinucci A. *et al.* MNRAS **446**, 737 (2015)

Khattak F. Y., O. A. M. B. Percie du Sert , Rosmej F. B. and Riley D., J. Phys. Conf. Ser. **397**, 012020 (2012)

Konjevic N., Lesage A., Fuhr J. R. and Wiese W. L., J. Phys. Chem. Ref. Data **31**, 819 (2002)

Kramida A., Ralchenko Yu., Reader J. and NIST ASD Team (2019). NIST Atomic Spectra Database (ver. 5.7.1), [Online]. Available: https://physics.nist.gov/asd [2020, March 2]

Krause M. O., Nucl. Instrum. Methods Phys. Res. **87**, 178 (1994)

Kunze H.-J., *Introduction to Plasma Spectroscopy*, Springer (2009)

Lee J. C., Ogle P. M., Canizares C. R., Marshall H. L., Schulz N. S., Morales R., Fabian A. C. and Iwasawa K., ApJ **554**, L13 (2001)

Liang E. P. T. & Price R. H., ApJ **218**, 247 (1977)

Liu P., Gao C., Hou Y., Zeng J. and Yuan J., Commun. Phys. **1**, 95 (2018)

Loeb A., Phys. Rev. Lett. **91**, 071103 (2003)

Mendoza C., Kallman T. R., Bautista M. A. and Palmeri P., A&A **414**, 377 (2004)

Meyer D. M., Jura M. and Cardelli J. A., ApJ **493**, 222 (1998)

Miller J. M., ARA&A **45**, 441 (2007)

Miller J. M., Fabian A. C., Wijnands R. *et al.*, ApJ **570**, L69 (2002)

Miller J. M., Miller M. C. and Reynolds C. S., ApJL **731**, L5 (2011)

Miller J. M., Reynolds C. S., Fabian A. C., Miniutti G., Gallo L. C., ApJ **697**, 900 (2009)

Moore C. E., Tables of Spectra of Hydrogen, Carbon, Nitrogen, and Oxygen Atoms and Ions, edited by J. W. Gallagher (Boca Raton, FL: CRC Press) (1998)

Murillo M. S. and Weisheit J. C., Phys. Rep. **302**, 1 (1998)

Nandra K., Barret D., Barcons X. *et al.*, ArXiv e-prints [arXiv:1306.2307] (2013)

Nandra K., Pounds K. A., Steward G. C., Fabian A. C., Rees M. J., MNRAS **236**, 39 (1989)

Nantel M., Ma G., Gu S., Cote C. Y., Itatani J. and Umstadter D., Phys. Rev. Let. **80**, 4442 (1998)

Nguyen H., Koenig M., Benredjem D., Caby M. and Coulaud G., Phys. Rev. A **33**, 1279 (1986)

Page M. J., Soria R., Wu K., Mason K. O., Cordova F. A. and Priedhorsky W. C., MNRAS **345**, 639 (2003)

Palmeri P., Mendoza C., Kallman T. R. and Bautista M. A., A&A **403**, 1175 (2003a)

Palmeri P., Mendoza C., Kallman T. R., Bautista M. A. and Meléndez M., A&A **410**, 359 (2003b)

Piel A., *Plasma Physics. An Introduction to Laboratory, Space and Fusion Plasmas*, Springer (2010)

Pilyugin L. S., A&A **369**, 594 (2001)

Pravdo S. H., Becker R. H., Boldt E. A., Holt S. S., Serlemitsos P. J. and Swank J. H., ApJ **215**, L61 (1977)

Ray D., Phys. Rev. E **62**, 4126 (2000)

Reis R. C. and Miller J. M., ApJ **769**, L7 (2013)

Reynolds C. S., Space Sci. Rev. **183**, 277 (2014)

Reynolds C. S. and Nowak M. A., Phys. Rep. **377**, 389 (2003)

Rogers F. J., Graboske H. C. and Harwood D. J., Phys. Rev. A **1**, 1577 (1970)

Saha B. and Fritzsche S., Phys. Rev. E **73**, 036405 (2006)

Saha B. and Fritzsche S., J. Phys. B : At. Mol. Opt. Phys. **40**, 259 (2007)

Saha B., Mukherjee P. K. and Diercksen G. H. F., A&A **396**, 337 (2002)

Sanford P., Mason K. O., and Ives J., MNRAS **173**, 9P (1975)

Schmidt M., Beiersdorfer P. and Chen H., ApJ **604**, 562 (2004)

Schnittman J. D., Krolik J. H. and Noble S. C., ApJ **769**, 156 (2013)

Serlemitsos P. J., Boldt E. A., Holt S. S., Ramaty R. and Brisken A. F., ApJ
     184, L1 (1973)

Serlemitsos P. J., Smith B. W., Boldt E. A., Holt S. S., and Swank J. H., ApJ
     211, L63 (1977)

Sil A. N., Saha B. and Mukherjee P. K., Int. J. Quantum Chem. **104**, 903 (2005)

Smith R. K. and Brickhouse N. S., Adv. At. Mol. Opt. Phys. **63**, 271 (2014)

Sreckovic A., Djenize S., and Bukvic S., Phys. Scr. **53**, 54 (1996)

Steenbrugge K. C., Kaastra J. S., de Vries C. P. and Edelson R., A&A **402**, 477
     (2003)

Steiner J. F., Reis R. C., Fabian A. C. *et al.*, MNRAS **427**, 2552 (2012)

Stewart J. C. and Pyatt K. D. Jr., ApJ **144**, 1203 (1966)

Tanaka Y. *et al.*, Nature **375**, 659 (1995)

Tashiro M., Maejima H., Toda K. *et al.*, SPIE Conf. Ser. **10699**, 1069922 (2018)

Tomsick J. A., Parker M. L., Garcia J. A. *et al.* ApJ **855**, 3 (2018)

Xie L. Y., Wang J. G., Janev R. K., Qu Y. Z. and Dong C. Z., Eur. Phys. J. D
     66, 125, (2012)

Winkler P., Phys. Rev. E **53**, 5517 (1996)

Xu Y., Harrison F. A., Garcia J. *et al.*, ApJL **852**, L34 (2018)

Yan X.-Z. and Ichimaru S., Phys. Rev. A **34**, 2173 (1986)

Zhang L. and Winkler P., Int. J. Quantum Chem.: Quantum Chemistry Sym-
     posium **30**, 1643 (1996)